Mathematical modelling of myocardial perfusion: coronary flow and myocardial mechanics

Yingjie Wang

Submitted in fulfilment of the requirements for the
Degree of Doctor of Philosophy

School of Mathematics and Statistics
College of Science and Engineering
University of Glasgow

May 2023

Abstract

Coronary artery disease (CAD) is a condition characterised by the narrowing or blockage of the major blood vessels that supply blood to the heart muscle. This can cause insufficient myocardial perfusion to the heart and deficient cardiac outputs, leading to the possibility of heart failure. CAD is one of the leading causes of morbidity and mortality worldwide. Early and accurate diagnosis and treatment of CAD are essential to minimise the risk of complications, including heart attack or heart failure. In cardiovascular research, computational modelling of coronary circulation is proving to be a valuable tool for gaining insights and information. It enables researchers to isolate the effects of various physiological and pathological conditions on the coronary circulation. Thus, this thesis aimed to develop computational models of one-dimensional (1D) coronary flow and three-dimensional (3D) heart. Both models included detailed geometric information to simulate and predict physiologically realistic results. A one-way coupling of the coronary flow model and the heart model was achieved and produced physiologically accurate myocardial perfusion.

Specifically, we first investigated the effect of intramyocardial pressure (IMP) on coronary flow and developed a 1D finite difference coronary flow model. A coronary network based on experimental data was constructed to simulate coronary flow along the complete path of the coronary vasculature. Utilising an assumed aortic pressure, right atrial pressure, and IMP, our simulated coronary pressure and flow rates were in good agreement with published experimental data. It was observed that the majority of the coronary arterial flow on the left side occurs during diastole, while the flow slows down or even reverses during systole. Secondly, we developed a 3D finite element model of the left ventricle (LV) to obtain a more realistic IMP. The LV model was constructed from a patient-specific geometry. The simulated pressure and volume of the LV cavity in repeated cardiac cycles, as well as the ejection fraction, were all within published physiological ranges. We further analysed the stress distributions within the LV wall. Thirdly, a brief review of experimental IMP, as well as calculations of IMP from lumped parameter models and 3D heart models, were presented. Through analysis, we determined a formula for calculating IMP from our 3D LV model. Additionally, we proposed an assignment scheme of the epicardial coronary arteries to the 17 segments of the LV wall recommended by the American

Heart Association. Based on the assignment, we devised the one-way coupling framework between the coronary flow model and the LV model to investigate myocardial perfusion.

We further developed a bi-ventricular model to investigate the effect of pulmonary regurgitation (PR) on cardiac function. The model provided a computational approach for exploring the influence of PR on right ventricle (RV) dilation and the interaction between LV and RV. Our simulated RV end-diastolic volumes under varying degrees of PR were comparable with published magnetic resonance imaging data. Moreover, from the long-axis and short-axis views of the bi-ventricular geometry, we observed clearly the motion of the interventricular septum from the baseline case to the severe PR case. This bi-ventricular model was intended to further couple with the coronary flow model to investigate the interaction of right coronary arterial flow and left coronary arterial flow. However, due to time constraints, this has not yet been undertaken.

The computational models of the coronary flow and heart developed in this thesis exhibit promising capabilities for providing physiologically accurate predictions of coronary flow and myocardial mechanics. Further application of these models has the potential to deepen our understanding of the underlying mechanisms in physiological coronary flow and various CAD.

Contents

List of Abbreviations

1D: One-dimensional
3D: Three-dimensional
FE: Finite element
CAD: Coronary artery disease
LV: Left ventricle
LA: Left atrium
RV: Right ventricle
RA: Right atrium
IMP: Intramyocardial pressure
LMCA: Left main coronary artery
LAD: Left anterior descending artery
LCX: Left circumflex artery
MARG: Marginal artery
AM: Acute marginal
RCA: Right coronary artery
PDA: Posterior descending artery
PLA: Posterolateral ventricular branch
CS: Coronary sinus
NA: Not available
HO: Holzapfel and Ogden
AHA: American Heart Association
CMR: Cardiovascular magnetic resonance
DT-CMR: Diffusion tensor cardiovascular magnetic resonance
CT: Computed tomography
PET: Positron emission tomography
ECG: Electrocardiogram
LVP: Left ventricular pressure
RVP: Right ventricular pressure
PV: Pressure-volume
ED: End of diastole

ES: End of systole
EDV: End-diastolic volume
ESV: End-systolic volume
EDP: End-diastolic pressure
ESP: End-systolic pressure
EF: Ejection fraction
MBF: Myocardial blood flow
PR: Pulmonary regurgitation
PRV: Pulmonary regurgitation volume
PRF: Pulmonary regurgitation fraction
BSA: Body surface area
RVEDVi: Right ventricular end-diastolic volume indexed by the body surface area

List of Tables

List of Figures

Acknowledgements

I would like to express my sincere appreciation and respect to my supervisors, Prof. Xiaoyu Luo and Dr. Hao Gao, as well as Prof. Nicholas Hill, for their guidance throughout my doctoral journey at the University of Glasgow. Under their guidance, my academic pursuits steered toward the enlightening field of coronary circulation research. Their extensive knowledge and assistance have helped me a lot in the advancement of my research work and thesis writing process. Furthermore, I would like to extend my gratitude to my annual reviewers, Prof. Nigel Mottram, Dr. Katarzyna Kowal, and Dr. Robert Teed, for their insightful suggestions and genuine interest in my research career. I also want to thank Dr. Debao Guan, Liuyang Feng, Xin Zhuan, and Scott Richardson for their support and contributions to my research. Moreover, I would like to express my utmost appreciation for the Ph.D. scholarship granted by the Chinese Scholarship Council.

I express my heartfelt gratitude to my beloved family, especially my parents, for their unwavering trust and support. Their boundless love and understanding have been instrumental in enabling me to successfully embark on and complete this journey. I extend my sincerest thanks to Xueqing Yin for her invaluable support and ceaseless encouragement, especially during challenging times, and for consistently brightening my spirits. Additionally, I am deeply grateful to Douglas Robertson, who has not only been a true friend but has also demonstrated the utmost kindness and a broad-minded perspective toward the world. Furthermore, I would like to express my appreciation to all my friends who have shared moments of intense anxiety as well as moments of excitement with me. Their presence has truly made my time studying and staying in Glasgow an unforgettable and enriching experience.

Like a solitary droplet amidst the boundless expanse of the ocean, I consider myself fortunate to have crossed paths with genuine souls who becoming true friends and bearing profound influence upon my growth and development. Without their presence and support, I would not have found the strength and resilience to overcome numerous challenges in both my research and personal interactions. I will carry with me the lessons I have learned and share these pearls of wisdom with others, as I continue to pursue personal and academic growth.

Declaration

I declare that this thesis has been written by me, and has not been submitted previously as part of any application for a degree. With the exception of introductory materials in this thesis, all work was carried out by the author unless otherwise explicitly stated by reference or acknowledgment. Portions of Chapters 3 and 5 have been published in journal papers. Additionally, sections from Chapters 3 and 4 are presently submitted to a journal.

Chapter 1

Introduction

1.1 Background

1.1.1 The heart and blood circulatory system

The heart is an essential organ in mammals and birds, including humans. The human heart beats about 100,000 times a day. It is a muscular organ that is responsible for pumping blood throughout the body while transporting oxygen, nutrients, and other essential substances and removing waste products (Sperelakis, 2000; Marieb and Hoehn, 2007; Caro et al., 2012). The blood travels through blood vessels in the blood circulatory system, which was first described by William Harvey (Schultz, 2002). Harvey discovered that the heart pumps out blood to the whole body through its contraction, while the blood circulates around the body before returning to the heart. Nowadays, it is well known that the blood circulatory system, also known as the cardiovascular system, nourishes all organs, tissues, and cells in the body.

There are three types of circulatory system: pulmonary circulation, systemic circulation, and coronary circulation (Guyton et al., 1986; Formaggia et al., 2010; Klabunde, 2011; Caro et al., 2012). The pulmonary circulation carries deoxygenated blood from the heart to the lungs, where it is oxygenated, before returning the oxygen-rich blood back to the heart. The systemic circulation, on the other hand, passes oxygenated blood from the heart to the rest of the body and then picks up deoxygenated blood to the heart. The coronary circulation is part of the systemic circulation and perfuses the myocardial tissues.

In humans, the heart is located in the chest cavity between the lungs and is enclosed by a fibro-serous sac called the pericardium. The pericardium consists of two layers, an outer fibrous layer and an inner serosal layer, which produces a lubricating fluid that reduces friction as the heart beats. Fig. 1.1 provides a visual representation of the heart's structure. It is comprised of four chambers: the left and right atria, or upper chambers,

and the left and right ventricles, or lower chambers. The right atrium (RA) and ventricle (RV) are separated from the left atrium (LA) and ventricle (LV) by a muscular wall called the interventricular septum. The heart's four-chamber structure is a defining feature that allows it to efficiently pump and circulate blood throughout the body. Specifically, the RA receives deoxygenated blood from the systemic circulation through the venae cavae (including the superior vena cava and inferior vena cava) and from the coronary circulation through the coronary sinus (CS) and passes it through the tricuspid valve into the RV which pumps deoxygenated blood to the lungs through the pulmonary valve, where the blood is oxygenated. The LA receives oxygenated blood from the lungs through the pulmonary veins. The blood then flows through the mitral valve into the LV, which pumps the blood through the aortic valve and into the systemic circulation.

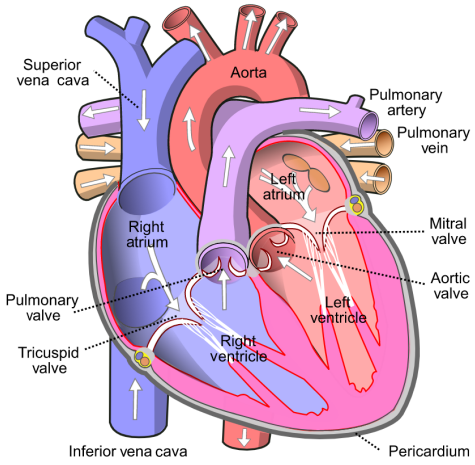

Figure 1.1: Diagram of the heart showing four chambers, valves, and main arteries and veins. The white arrows show the normal direction of blood flow. Source: https://en.wikipedia.org/wiki/Heart, accessed May 10, 2023.

The walls of the two ventricles are much thicker than those of the two atria, as they are responsible for generating the force required to pump blood through the systemic and pulmonary circulations. The LV wall is the thickest and most muscular chamber of the heart because it needs to generate enough force to pump blood throughout the entire body. The heart wall is composed of three distinct layers: the outer epicardium, the middle myocardium, and the inner endocardium. Kawel et al. (2012) provided values of the heart wall thickness for middle-aged and older individuals, reporting that the average maximum thickness of the LV myocardium at mid-cavity was 7-9 mm (long axis) and 7-8 mm (short axis) for women and men, respectively. The epicardium and endocardium are two thin membranes with an approximate thickness of 100 μm. The myocardium, the thickest and functionally the most important tissue of the heart wall, is primarily composed of two types of cells: cardiomyocytes and fibroblasts. Fibroblasts, which are the predominant

cells in the myocardium, synthesise and regulate the composition of the extracellular matrix (Fedak et al., 2005). Cardiomyocytes, which occupy over two-thirds of the total myocardial volume, are the fundamental cells responsible for generating contractile force and providing effective pump function (Woodcock and Matkovich, 2005).

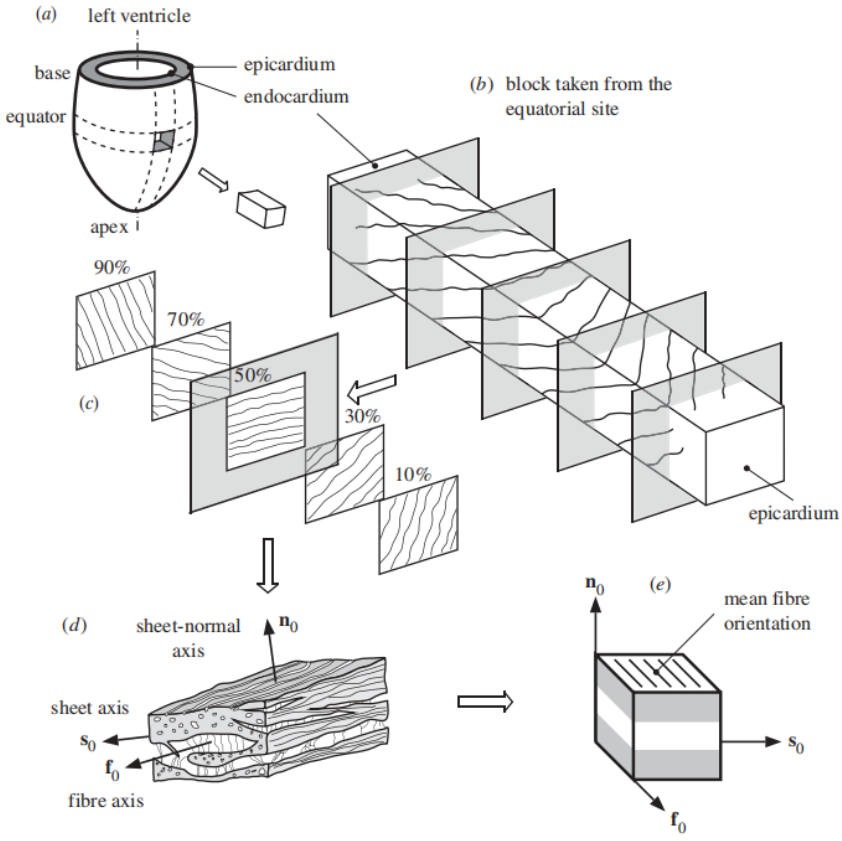

Figure 1.2: Diagram of an imaginary ellipsoid left ventricle and a cutout from the equator of the left ventricle (a); five longitudinal-cut sections from 10% to 90% of the wall thickness of the block (b, c), which shows the transmural variation of the myofibre direction and distribution; microstructure of the myocardium in a sheet (d), where a right-handed orthonormal coordinate system is defined with the myofibre direction $\mathbf{f}_0$, sheet direction $\mathbf{s}_0$, and sheet-normal direction $\mathbf{n}_0$; and a cube of layered tissue (e) with local material coordinates which used for derivation of the HO model (Holzapfel and Ogden, 2009). Source: (Holzapfel and Ogden, 2009), reprint with permission.

The cardiac microstructure in the heart is complex with a three-dimensional (3D) arrangement of cardiomyocytes. According to experimental findings (LeGrice et al., 1995, 1997; Sands et al., 2005), the myocardium exhibits a hierarchical structure, with myocytes arranged in discrete layers or sheets that are typically four to five cells thick, with extensive cleavage planes between muscle layers. The heart wall thus can be considered a composite of layers of parallel myocytes, which occupy approximately 70% of the volume (Holzapfel and Ogden, 2009). It is now widely accepted that the myocardium has a helically-oriented myofibre structure, which is formed by groups of cardiomyocytes along their long axis

direction. As shown in Fig. 1.2, Holzapfel and Ogden (2009) illustrated the distribution of the myofibre structure and developed a fibre-reinforced constitutive model describing the passive response of the myocardium. The arrangement of myofibres within the sheet plane is parallel, and separated by cleavage planes. This microstructure can be described by a local right-handed orthonormal coordinate system. These consist of the unit vector $\mathbf{f}_0$, which is aligned with the average myofibre direction; the unit vector $\mathbf{s}_0$, located within the sheet plane and perpendicular to the myofibre direction; and the unit vector $\mathbf{n}_0$, oriented normal to the sheet plane.

Non-invasive techniques such as diffusion tensor cardiovascular magnetic resonance (DT-CMR) (Basser et al., 1994; Reese et al., 1995; Ferreira et al., 2014; Nielles-Vallespin et al., 2017) have been used to assess the in vivo myofibre and sheet structure of the myocardium. DT-CMR measures the diffusion of water molecules in the myocardium and computes the diffusion tensor, with the maximum eigenvalue of the diffusion tensor being associated with the orientation of the myofibre. Reported values of the helix angle (defined as the angle between the myofibre direction and the ventricular radial direction or the circumferential direction) from DT-CMR measurements differ across several studies: $-30^\circ \sim 55^\circ$ in (Toussaint et al., 2013), $-60^\circ \sim 60^\circ$ in (Nielles-Vallespin et al., 2013), and $-90^\circ \sim 90^\circ$ in (Tseng et al., 2000). However, the most commonly used method to reconstruct the myofibre structure in computational models of the heart is the rule-based method (Bayer et al., 2012; Wang et al., 2013; Wong and Kuhl, 2014), in which it is assumed that the orientation of the myofibre structure varies from the left-handed helix with an angle of approximately -60° at the epicardium to the right-handed helix with an angle of approximately 60° at the endocardium (Wang et al., 2013; Sack et al., 2018; Guan et al., 2021).

Normal cardiovascular function is vital to our health, however, there exist various cardiac diseases that can impair the heart's functionality, including but not limited to ischemic heart disease, heart failure, cardiac arrhythmias, and valvular heart disease (Lilly, 2020). For instance, ischemic heart disease arises from the imbalance between myocardial blood supply and demand, often due to coronary artery diseases caused by narrowed or blocked coronary blood vessels. It is the most commonly occurring cardiac disease (Abubakar et al., 2015; James et al., 2018). Valvular heart disease arises when there are abnormalities in the mitral valve, aortic valve, tricuspid valve, or pulmonic valve. In severe cases, valve regurgitation occurs, and valve repair or replacement is imperative (Paul and Das, 2017).

Vasculature

The vasculature is a complex network of blood vessels comprising arteries, arterioles, capillaries, venules, and veins (Berne, 1981; Guyton et al., 1986; Kassab, 2019) as shown

in Fig. 1.3. Arteries are responsible for carrying oxygenated blood away from the heart and distributing it throughout the body's tissues. They have thick, muscular walls that can expand and contract to regulate blood flow and bear the highest blood pressure. The largest artery in the body is the aorta, which carries blood from the LV to the rest of the body. Arterioles are smaller branches of arteries that connect to capillaries. They are responsible for regulating blood flow to specific areas of the body by constricting or dilating their walls. Capillaries are the smallest and thinnest blood vessels in the body, measuring only one cell layer thick from 5 to 10 μm in diameter (Potter and Groom, 1983). They are responsible for facilitating the efficient exchange of oxygen, nutrients, and waste products between the blood and the body's tissues. Capillaries are found in almost every tissue in the body and are essential for maintaining healthy cellular function. Venules are smaller branches of veins that connect to capillaries. They collect deoxygenated blood from the capillaries and transport it back to the larger veins. Veins are blood vessels that collect deoxygenated blood from the body's tissues and return it to the heart. Unlike arteries, veins have thinner walls and less muscular tissue. They rely on one-way valves to prevent blood from flowing backward.

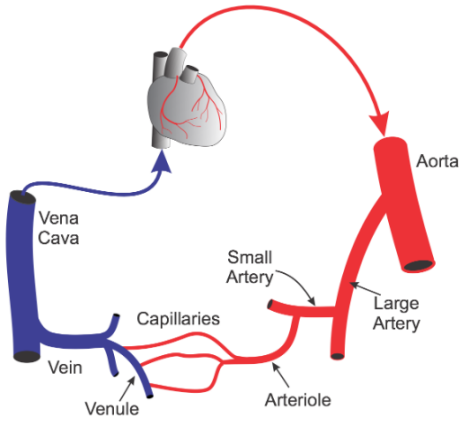

Figure 1.3: Diagram of different types of blood vessels to illustrate arteries, arterioles, capillaries, venules, and veins. Source: https://www.cvphysiology.com, accessed May 10, 2023.

Coronary vasculature supplies blood to the myocardium. As illustrated in Fig. 1.4, coronary vasculature is rather complicated consisting of numerous blood vessels. These vessels in our study are divided into epicardial coronary blood vessels and intramyocardial coronary blood vessels. The epicardial coronary blood vessels, including epicardial arteries and veins, span the surface of the heart. On the other hand, the intramyocardial blood vessels, such as arterioles, capillaries, and venules, are embedded within the myocardium. The intramyocardial coronary blood vessels are very large in number and organised topologically like trees. In contrast, the epicardial coronary arteries and veins are comparatively few in number, which allows for their geometric properties to be studied individually

(Vlodaver et al., 2012; Kassab, 2019; Faletra et al., 2020). Imaging techniques such as X-ray angiography, computed tomography (CT), cardiovascular magnetic resonance (CMR) imaging, and 3D echocardiography have been used to visualise the coronary arteries and detect blockages or other abnormalities (Sato et al., 2010; Loukas et al., 2013; Hirai et al., 2020). Among these techniques, X-ray angiography and CT are currently two common ways of visualising coronary arteries (Moosavi Tayebi et al., 2015). CT involves combining a CT scan with the injection of contrast material into a vein, typically in the hand or arm. The contrast material helps enhance the visibility of blood vessels, and the CT scanner generates cross-sectional images (CT slices) that show cardiac components. CT can create 3D reconstructions of coronary arteries and detect plaque build-up, helping to diagnose and assess coronary artery diseases. On the other hand, X-ray angiography is a real-time imaging procedure. It involves the injection of a radio-opaque contrast agent directly into the coronary arteries. X-ray-based techniques, like fluoroscopy, are then used to capture a series of images called angiograms (or angiographs). X-ray angiography is considered the gold standard in clinical decision making and a detailed review of the X-ray angiography can be found in (Çimen et al., 2016).

American Heart Association (AHA) (Dowe et al., 2013) recommended classification of the epicardial coronary arteries, as shown in Fig. 1.5. The coronary arteries arise from the aorta and consist of three main branches: the left anterior descending artery (LAD) branch, the left circumflex artery (LCX) branch, and the right coronary artery (RCA) branch. The LAD branch is the largest branch of the coronary arteries (Ilia et al., 2001; Dowe et al., 2013; Tarantini et al., 2016). As shown in Fig. 1.6, it runs in the anterior interventricular groove forward toward the apex of the heart and supplies a large part of the myocardium. The LAD branch is also called the 'widowmaker' artery because a blockage in this artery can lead to a severe heart attack. The LCX branch is the second-largest branch of the coronary arteries (Huey et al., 1988; Dowe et al., 2013). It travels under the left atrial appendage and enters the posterior atrioventricular sulcus, corresponding to the base of the mitral valve. The LCX branch has two or three obtuse marginal (OM) branches. The RCA branch is the third and smallest branch of the coronary arteries. It branches into the posterior descending artery (PDA) and the posterolateral ventricular branch (PLV) at its terminal end. The PDA supplies the posterior wall of the heart, while the PLV supplies the lateral wall of the heart.

It is important to acknowledge that the morphology of the coronary vasculature is intricate and varies considerably among individuals. Differences in caliber, alternative branch morphologies, and the type of dominance are some of the variations observed in coronary arteries. Cardiac dominance is an essential variation, whereby the origin of the PDA is from the LCX in left dominance and from the RCA in right dominance (Das et al., 2010; Sakamoto et al., 2013; Khwansang and Chentanez, 2018). Therefore, it is rare to

find similar coronary vascular anatomy in two individuals. Consideration of the artery's morphology and the extent of its perfusion territory is crucial in therapeutic planning. For instance, the presence of a critical stenosis in an artery that supplies a larger myocardial territory warrants consideration of a myocardial revascularization intervention.

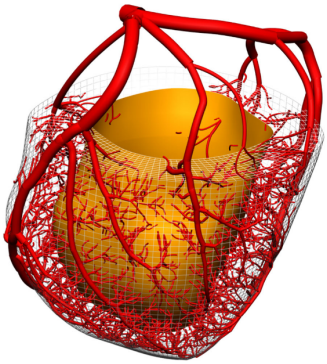

Figure 1.4: Diagram of a coronary vascular tree reconstructed from 50 μm-resolution 3D image stacks of porcine vasculature. Source: (Lee et al., 2016), reprint with permission.

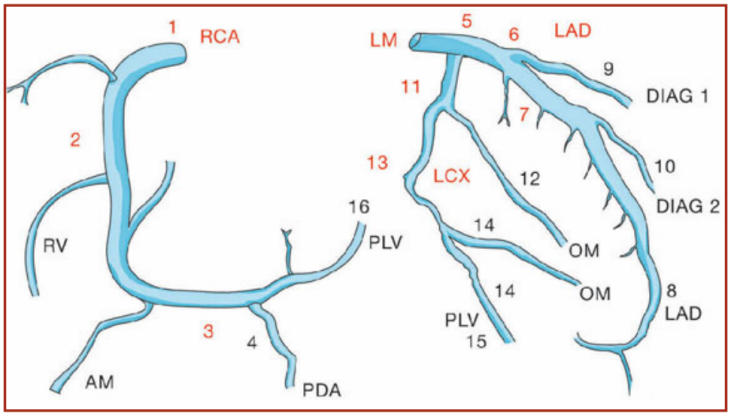

Figure 1.5: A classification of epicardial coronary arteries by the American Heart Association. RCA: right coronary artery; RV: right ventricular branch; AM: acute marginal branch; PLV posterolateral ventricular branch; PDA: posterior descending artery; LM: left main artery; LAD: left anterior descending artery; DIAG 1: first diagonal branch; DIAG 2: second diagonal branch; LCX left circumflex artery; OM: obtuse marginal branches. Source: (Dowe et al., 2013), reprint with permission.

Cardiac cycle

The cardiac cycle is a crucial physiological process that ensures the continuous circulation of blood throughout the body. It is regulated by a complex interplay of electrical, mechanical, and physiological factors, and abnormalities in any of these factors can lead to various cardiovascular diseases (Fukuta and Little, 2008; Caro et al., 2012).

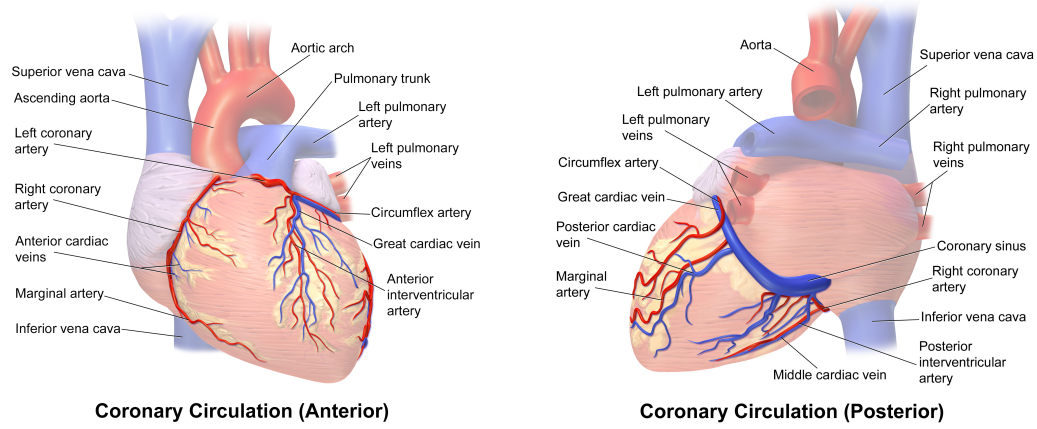

(a) (b)

Figure 1.6: Diagram of distribution of coronary arteries and veins around the heart. Source: https://en.wikipedia.org, accessed May 10, 2023.

In the clinical setting, the heart of a healthy individual typically beats 60-100 times per minute (Umetani et al., 1998). During each heartbeat, a sequence of both mechanical and electrical events occurs (Caro et al., 2012). To illustrate these events, the Wiggers diagram, as shown in Fig. 1.7, is commonly used which shows the contraction and relaxation of the heart chambers, opening and closing of the heart valves, and the corresponding changes in pressure and volume. Systole in this thesis is defined as from the mitral valve closure to the aortic valve closure, with the rest of the cardiac cycle being defined as diastole (Fukuta and Little, 2008).

The contraction of the heart is initiated by electrical signals (depolarization and repolarization) generated by the sinoatrial node (the pacemaker), which is located in the nervous tissues of the right atrial wall. When depolarization occurs in the pacemaker, it spreads at about 1 ms through the myocardial muscles of the right and left atrial walls, causing atrial contraction (Caro et al., 2012). The electrical signals then pass through a discrete nervous pathway that travels through the fibrous tissue around the tricuspid valve ring and into the interventricular septum between the two ventricles, where the signals divide and spread into the myocardium of each ventricle, terminating in a network of fine fibres among the muscle cells. The process of depolarization and repolarization produces an electrocardiogram (ECG) tracing as shown in Fig. 1.7, which consists of three prominent signals: the P wave, the QRS complex, and the T wave. The beginning of the atrial depolarization produces the P wave. After a short time, a larger voltage deflection, the QRS complex, appears. It represents ventricular depolarization. Finally, ventricular repolarization generates the T wave.

Mechanical events include isovolumic contraction and ejection during systole and isovolumic relaxation, rapid inflow, diastasis, and atrial systole during diastole, as shown

in Fig. 1.7. At the onset of the isovolumic contraction, the tension in the LV wall increases rapidly until the pressure within the LV cavity exceeds that in the aorta. Over a short period of time, as the pressure in the LV cavity rises above the pressure in the LA, backflow from the LV to the LA can occur, which is prevented by the closure of the mitral valve. Additionally, during the isovolumic contraction, there is no change in the LV volume since blood is incompressible. Next, the ejection phase commences when the aortic valve opens, allowing the rapid forward acceleration of blood due to the high-pressure difference between the LV and the aorta. Repolarization occurs during about half of this period, leading to a drop in the LV wall tension. The acceleration of blood decreases until the aortic valve closes, leading to the isovolumic relaxation during which the myocardium relaxes and the LV pressure falls further. At the same time, pressure in the LA rises as it fills with blood from the pulmonary veins. When the LA pressure exceeds the LV pressure, the mitral valve reopens, and the ventricular diastole occurs, during which the LV refills with blood following the emptying that occurs during systole. Both the two ventricles and two atria undergo significant passive filling as blood returns from the systemic and pulmonary venous system. Additionally, throughout the diastolic period, the pressure difference between the LA and LV is minimal due to the low resistance offered by an open mitral valve.

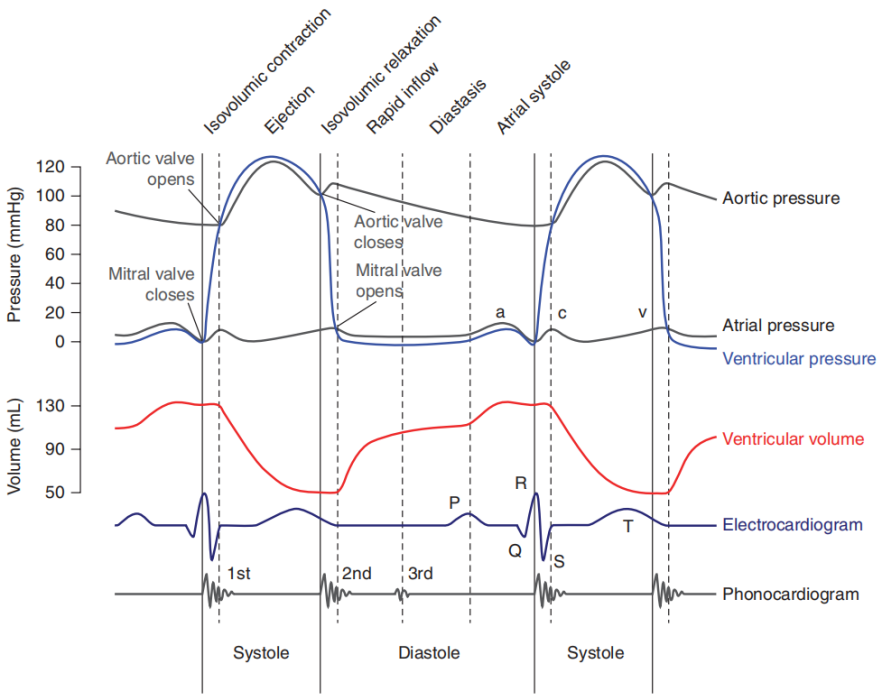

Figure 1.7: A Wiggers diagram to illustrate electrical and mechanical events in one cardiac cycle. Electrical events are indicated by the phonocardiogram, and mechanical events are depicted by the pressure and volume changes in one cardiac cycle. Source: https://en.wikipedia.org, accessed May 10, 2023.

1.2 Computational models of the heart

The computational models of the heart discussed in this context are rooted in the anatomy and biomechanics of the heart, encompassing the soft tissue mechanics of the myocardium, interactions with the circulatory system, and propagation of the electrical signals (Baillargeon et al., 2014; Quarteroni et al., 2017; Sack et al., 2018). These models have been made possible by advancements in continuum mechanics, the finite element (FE) method, high-performance computing, and clinical imaging techniques (Hunter and Smaill, 1988; Wang et al., 2013; Baillargeon et al., 2014; Quarteroni et al., 2017; Sack et al., 2018; Gray and Pathmanathan, 2018; Niederer et al., 2019). For instance, creating a detailed and personalised computational model of the heart requires the utilisation of diverse clinical imaging techniques, such as echocardiography, electrocardiography, CMR, genetics, and blood-pressure measurements.

1.2.1 Geometries of the heart

To perform a quantitative analysis of many aspects of cardiac function, it is necessary to have a geometrical model that provides accurate descriptions of the geometry of the heart, as well as the organisation of myofibres within the myocardium. Woods (1892), for the first time, simplified the LV as a thin-walled spherical shell. Guccione et al. (1991) later adopted an idealised cylindrical model of the LV as shown in Fig. 1.8. More complex models of the LV in studies (Dieudonné, 1969; Streeter Jr and Hanna, 1973; Land et al., 2015) assumed that the epicardial and endocardial surfaces of the LV-free wall can be regarded as confocal ellipsoids of revolution. Due to its capacity to be both representative and simplified, it was adopted in some benchmark models (Land et al., 2015). Nielsen et al. (1991) reconstructed the first mathematical representation of a full 3D left and right ventricular geometry and myofibre orientation from a canine heart arrested in diastole and fixed at zero transmural pressure. Their ventricular geometry was represented by a 24-element mesh, with a fitted description of epicardial and endocardial surfaces. The myofibre orientation was also fitted with a 60-element mesh obtained by subdividing the ventricular mesh.

MRI imaging is the most commonly used technique to reconstruct personalised 3D heart geometries for recent computational modelling studies of the heart. For instance, Sun et al. (2009) reconstructed a 3D LV geometry of a male adult sheep using the endocardial and epicardial contours obtained from CMR images. Wang et al. (2013) reconstructed a human LV geometry by using seven short-axis CMR slices of a healthy volunteer. Biventricular geometries of porcine subjects in healthy and diseased states were reconstructed by (Sack et al., 2018). Moreover, a human heart with all four chambers was reconstructed by Zygote Media Group and Inc (2013) and adopted for computational simulations by

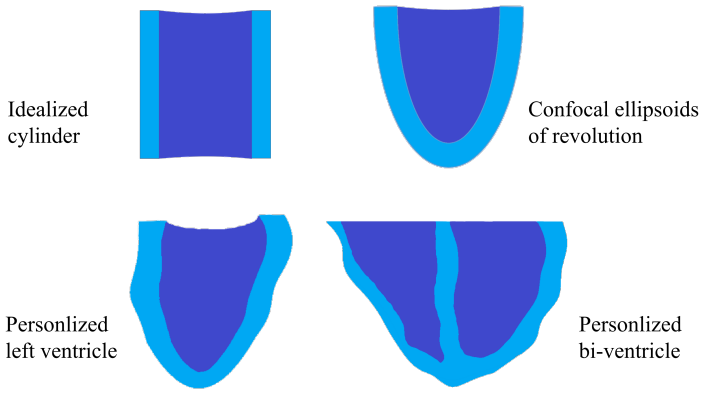

Figure 1.8: Geometries of the heart employed in the computational models of the heart. Through the use of noninvasive imaging techniques, it is possible to obtain personalised reconstructions of the left ventricle, bi-ventricle, and whole heart.

Baillargeon et al. (2014). More sophisticated and automatic reconstruction techniques can be found in (Burton et al., 2006; Lamata et al., 2011; Fonseca et al., 2011; Zhang et al., 2012). Specifically, (Burton et al., 2006) presented a way for the automated construction of an individualised heart, combining MRI imaging and serial histology obtained from representative samples. Lamata et al. (2011) developed a generalist method for cubic Hermite mesh construction by mapping a predefined high-quality template to MRI imaging data via a variational warping step. Additionally, Fonseca et al. (2011) and Zhang et al. (2012) developed the atlas-based geometry pipeline to reconstruct patient-specific hearts.

As for the reconstruction of the myofibre architecture, two methods have been developed for estimating myofibre orientations on the basis of individual geometries of the ventricles. The first is an atlas-based approach, which estimates the patient's myofibre orientation by morphing an atlas of heart anatomy generated by ex vivo or in vivo CMR and diffusion tensor CMR onto the patient's heart anatomy (Vadakkumpadan et al., 2012; Peyrat et al., 2007). The second approach uses a rule-based myofibre orientation estimation derived from histological data, which assigns myofibre orientation from the endocardium to the epicardium with prescribed angles in terms of the circumferential direction (Bayer et al., 2012; Wang et al., 2013; Wong and Kuhl, 2014). Specifically, Wang et al. (2013) generated the myofibre orientation by the rule-based method as follows: At first, a normalised thickness parameter e of each node in the mesh of the LV is defined by

$$e = \frac{d_{\text{endo}}}{d_{\text{endo}} + d_{\text{epi}}}, \tag{1.1}$$

where d_{endo} and d_{epi} are two distances from the node to the endocardial and epicardial surfaces, respectively. Therefore, $e = 0$ for the nodes at the endocardial surface of the LV mesh, and $e = 1$ for the nodes at the epicardial surface. Next, the myofibre angle at each

node is assigned by

$$\theta = (1-e)\,\theta^{\text{endo}} + e\,\theta^{\text{epi}}, \tag{1.2}$$

where θ^{endo} and θ^{epi} are prescribed myofibre angles at the endocardial and epicardial surfaces, respectively.

1.2.2 Constitutive laws of the myocardium

Understanding the mechanical behaviour of the myocardium is crucial for developing accurate computational models of the heart. Such models rely on the use of constitutive laws, which establish the relationship between the material's response and external stimuli. Hooke's law represents the simplest and earliest-known constitutive law, describing the relationship between the deformation of a linear elastic material and the applied force. In the context of cardiac mechanics, constitutive laws are utilised to characterise the relationships between strain and stress in the myocardium. In order to establish appropriate constitutive laws, it is essential to conduct experiments using myocardial tissues and obtain comprehensive data on both force and deformation under various deformation modes. Specifically, a combination of bi-axial testing with different loading protocols and shear testing at varying specimen orientations is necessary to effectively capture the direction-dependent, nonlinear material response of the myocardium (Holzapfel and Ogden, 2009; Sommer et al., 2015; Ahmad et al., 2018b). However, a major challenge in this process is the limited availability of experimental data that are suitable for detailed parameter estimation (Holzapfel and Ogden, 2009).

Reviews of existing constitutive models of the passive response of the myocardium can be found in (Holzapfel and Ogden, 2009; Avazmohammadi et al., 2019). To describe different constitutive models, we denote the deformation gradient as $\mathbf{F}$, associated with the right Cauchy-Green tensor $\mathbf{C} = \mathbf{F}^{\mathrm{T}}\mathbf{F}$. The Green-Lagrange strain tensor is defined by $\mathbf{E} = 1/2(\mathbf{C} - \mathbf{I})$, where $\mathbf{I}$ is the identity tensor. Assuming that the myocardial tissue is a continuous medium, phenomenological constitutive models (Guccione et al., 1991; Costa et al., 2001; Holzapfel and Ogden, 2009) are developed based on general empirical observations of myocardial material symmetry. However, such models do not incorporate additional information regarding the specific composition and structural organisation of the myocardium. These models express the energy density function ψ in terms of the deformation gradient tensor $\mathbf{F}$ through the right Cauchy-Green deformation tensor $\mathbf{C}$ or the Green-Lagrange strain tensor $\mathbf{E}$. Furthermore, the strain energy function can be written in the invariant-based forms which utilise the invariants $I_1 = \text{trace}(\mathbf{C})$, $I_2 = 1/2(\text{trace}(\mathbf{C})^2 - \text{trace}(\mathbf{C}^2))$, $I_3 = \det(\mathbf{C})$, $I_4 = \mathbf{f}_0 \cdot (\mathbf{C}\mathbf{f}_0)$, $I_5 = \mathbf{f}_0 \cdot (\mathbf{C}^2\mathbf{f}_0)$ where $\mathbf{f}_0$ is the myofibre direction in the reference configuration.

In early studies (Humphrey and Yin, 1987; Humphrey et al., 1990; Guccione et al.,

1991), the myocardium was assumed to be transversely isotropic. An example of the transversely isotropic model by Humphrey and Yin (1987) is

$$\psi = c\{e^{b(I_1-3)} - 1\} + A\{e^{a(\sqrt{I_4}-1)^2} - 1\}, \tag{1.3}$$

where c, b, A, a are four material parameters that can be determined by experiments. Later studies assume that the myocardium should be orthotropic (Smaill and Hunter, 1991; Costa et al., 2001; Schmid et al., 2006; Holzapfel and Ogden, 2009), relating to the local myofibre, sheet, and sheet-normal directions of the microstructure of the myocardium. Costa et al. (2001) adopted the exponential strain energy function

$$\psi = \frac{1}{2}a(e^Q - 1), \tag{1.4}$$

with

$$Q = b_{\mathrm{ff}}E_{\mathrm{ff}}^2 + b_{\mathrm{ss}}E_{\mathrm{ss}}^2 + b_{\mathrm{nn}}E_{\mathrm{nn}}^2 + 2b_{\mathrm{fs}}E_{\mathrm{fs}}^2 + 2b_{\mathrm{fn}}E_{\mathrm{fn}}^2 + 2b_{\mathrm{sn}}E_{\mathrm{sn}}^2, \tag{1.5}$$

where $a, b_{ij}, i, j \in \{\mathrm{f}, \mathrm{s}, \mathrm{n}\}$ are seven material parameters. Holzapfel and Ogden (2009) later introduced the strain energy function (HO model)

$$\psi = \frac{a}{2b}\exp[b(I_1-3)] + \sum_{i=\mathrm{f,s}} \frac{a_i}{2b_i}\left\{\exp[b_i(\max(I_{4i},1)-1)^2] - 1\right\} + \frac{a_{\mathrm{fs}}}{2b_{\mathrm{fs}}}\left\{\exp[b_{\mathrm{fs}}I_{8\mathrm{fs}}^2] - 1\right\}, \tag{1.6}$$

where $a, b, a_{\mathrm{f}}, a_{\mathrm{s}}, b_{\mathrm{f}}, b_{\mathrm{s}}, a_{\mathrm{fs}}, b_{\mathrm{fs}}$ are eight material parameters and the max() function ensures that the myofibres only bear a stretching load. The HO model and its variations have been extensively utilised in cardiac modelling. One earliest example is the study conducted by Wang et al. (2013), which investigated the effect of myofibre orientation on LV diastolic mechanics using the HO model. Another application of the HO model is demonstrated in the four-chamber human heart model proposed by Baillargeon et al. (2014), known as the living heart project. Gao et al. (2017) also incorporated the HO model into an immersed boundary framework to examine LV biomechanics during both diastole and systole.

The poroelastic model of the myocardium has been developed as a result of recent progress in poromechanics research (Lee et al., 2016; Bociu et al., 2016; Feng et al., 2018). This model takes into account the interactions between fluid and solid constituents of the myocardium by considering the myocardium as a porous medium saturated with fluid. The pore fluid (blood) and solid (skeleton consisting of myocytes and collagen scaffold) components are distinct and can be differentiated using the superscripts f and s where necessary. For the poroelastic model, Darcy's law is most commonly adopted to describe

the motion of the pore fluid flow as

$$\begin{aligned} \mathbf{w} + \mathbf{K}\nabla p &= 0, \\ \mathbf{w} &= \phi(\mathbf{v}^f - \mathbf{v}^s), \\ \nabla \cdot \mathbf{w} &= s^*, \end{aligned} \tag{1.7}$$

where $\mathbf{w}$ is the Darcy velocity, $\mathbf{K}$ is the permeability tensor of the porous medium informing the perfusion rate, p is the pore pressure, ϕ is the porosity which can be determined by the fluid volume fraction, $\mathbf{v}^f$ and $\mathbf{v}^s$ are the velocity fields associated with their respective constituents, and s^* defines a sink/source term related to blood flow.

Chapelle et al. (2010) presented a general poroelastic model applicable to a nearly incompressible porous medium experiencing finite deformations. They extended the model to describe cardiac perfusion of the LV, simplifying the LV as one compartment with a distributed source term. The myocardial volume change caused by the blood perfusion was presented. Cookson et al. (2012) proposed a multi-compartment poroelastic model using cryo-microtome imaging data of myocardial vasculature to determine perfusion regions that were perfused by distinct arterial subnetworks. They derived region-specific porosity and permeability tensors. Lee et al. (2016) conducted a study on coronary wave intensity analysis using a poroelastic LV model and a 1D representation of the coronary network tree. They adopted a distributive Gaussian function as the source term within a volume surrounding the distal end of its perfusing vessel. Richardson et al. (2021) employed an immersed FE framework to model the LV by considering the myocardium as a three-phase poroelastic system. Most recently, Thekkethil et al. (2023) developed a stabilised linear FE method that is suitable for the implicit time integration of poroelastic formulations and applied it to investigate LV dynamics.

1.3 Computational models of blood flow in the circulatory system

1.3.1 One-dimensional blood flow models

In the previous section, we introduced computational models of the heart. However, in order to fully understand coronary circulation, it is also necessary to introduce computational models of blood flow in the coronary circulation. Additionally, given the increasing prevalence of cardiovascular diseases, there is a growing demand for the development and utilisation of accurate and efficient computational models of blood flow within the field of precision medicine. Instead of studying the detailed local blood flow using 3D computational fluid dynamics (CFD), one-dimensional (1D) wave propagation models are often

used to simulate the blood flow in the cardiovascular system, considering a simplified geometry (Reymond et al., 2009; Formaggia et al., 2010; Morris et al., 2016). These 1D models are based on the principles of fluid dynamics and are capable of simulating the propagation of pressure and flow waves through the blood vessels. They have been shown to be effective in simulating blood flow under various physiological and pathological conditions, ranging from regional to systemic and global circulation (Avolio, 1980; Stettler et al., 1981; Olufsen et al., 2000; Huo and Kassab, 2007; Olufsen et al., 2012; Qureshi and Hill, 2015; Duanmu et al., 2019). These models have the potential to enhance our understanding of the mechanisms underlying cardiovascular diseases and enable the development of more targeted and effective treatment strategies. Furthermore, they can be applied to predict blood gases and drug transport in the organism and to study blood flow remodelling resulting from intravascular surgeries such as stenting and shunting.

In this section, we will use the structured-tree model proposed by Olufsen (1998) to exemplify some concepts in the 1D computational models of blood flow. Firstly, we provide a brief overview of the historical development of 1D computational models of blood flow. To begin, considering a long, uniform, and rigid cylindrical tube, the steady laminar flow of an incompressible and Newtonian fluid within the tube is governed by the Poiseuille equation (Stokes, 2007)

$$\Delta p = \frac{8\mu L Q}{\pi r^4}, \tag{1.8}$$

where Δp is the pressure difference between two ends, μ is the dynamic viscosity, L is the length of the tube, Q is the volumetric flow rate and r the tube radius. This equation is often used in the study of fluid mechanics, including the simplification of blood flow through blood vessels in the human body. It helps to understand how the radius and length of blood vessels affect blood flow and pressure. Based on the Poiseuille equation, the resistance of the flow in the tube can be determined by

$$R = \frac{\Delta p}{Q} = \frac{8\mu L}{\pi r^4}, \tag{1.9}$$

which suggests that the greatest component of peripheral resistance resides in the smallest blood vessels Sutera and Skalak (1993).

The elasticity of the large blood vessels, which expand to store more blood when pressure rises, was considered by (Frank, 1899) to develop the two-element Windkessel model. This model is a simplified mathematical representation of the systemic circulation, which is utilised to describe the interplay between the heart, the arterial system, and the peripheral system. Due to its periodic contraction and relaxation, the heart generates a pulsatile flow. The arterial system, on the other hand, is capable of stretching and storing the blood during systole (heart contraction) and releasing it during diastole (heart relaxation). Consequently, the arterial system can be represented by a compliance element.

The compliance value can be estimated by adding the compliances of all vessels in the arterial system and is thus referred to as the total arterial compliance. The formula for computing the compliance, C, is given by

$$C = \frac{\Delta V}{\Delta P}, \tag{1.10}$$

where ΔV is the volume change and ΔP is the corresponding pressure change. Next, the peripheral system provides resistance to the blood flow and can be modelled by a resistance element. The value of the resistance, R, can be determined by

$$R = \frac{\Delta P}{Q_{\text{co}}}, \tag{1.11}$$

where ΔP is the pressure difference between the LV cavity (approximately the same as the aortic pressure) and the venous pressure, and Q_{co} is the cardiac output in terms of flow rate. The resistance is called total peripheral resistance. The inclusion of the compliance element and resistance element in the two-element Windkessel model results in the conversion of pulsatile flow generated by the heart into a more continuous flow at the peripheral outlet to perfuse the organs.

Various lumped parameter models of blood flow have been developed in the literature based on the concepts of the two-element Windkessel model (Stergiopulos et al., 1999; Wang et al., 2003; Westerhof et al., 2009). These models offer a simplified yet valuable understanding of the hemodynamics of blood circulation in the body. They help to comprehend the function of the arterial system and provide a straightforward and reasonably precise estimate of ventricular afterload, which measures the resistance the heart needs to overcome to pump blood out of the ventricle. However, since these models do not account for phenomena occurring inside the arterial system, they are limited in their ability to capture blood flow distribution and wave propagation in the arterial network.

A 1D computational model of the arterial blood flow, referred to as the structured-tree model, was developed by Olufsen (1998) to account for the time-varying nature of blood flow and pressure in the circulatory systems. This model separates the arterial tree into two components: large and small arteries. The large arteries are simulated in detail using a binary tree of compliant, tapering vessels that replicate the actual geometry, including lengths and diameters of the human arterial tree, with blood assumed to be an incompressible Newtonian fluid. In contrast, the small arteries are modelled as binary asymmetric structured trees originating from the terminals of the large arteries. These vessels are represented as straight segments of compliant vessels and do not mimic the actual geometries of the vessels in the human arterial system but are based on general statistical relationships.

The dynamics of the blood flow in the large arteries are governed by the 1D form

of the Navier-Stokes equations of the conservation of mass and momentum, along with the tube law, which characterises the relationship between pressure and cross-sectional area. The fundamental variables are blood pressure, flow rate, and cross-sectional area, and the governing equations derived from them are hyperbolic in nature. A noteworthy achievement by Womersley (1957) is the derivation of analytical solutions for traveling waves in an infinitely long, compliant tube of uniform undisturbed cross-sectional area, which contains an incompressible fluid. The Womersley number is given as

$$\alpha = r\sqrt{\frac{\omega}{\nu}}, \tag{1.12}$$

where r is the radius of the tube, ω is the angular frequency of the oscillations, and ν is the kinematic viscosity. The Womersley number is the ratio of transient inertial forces to viscous forces. When the value of the Womersley number is small (1 or less), viscous forces dominate and it indicates that the frequency of pulsations is low enough for a parabolic velocity profile to fully develop during each cycle. In contrast, when the Womersley number is large (10 or more), inertial forces dominate and it indicates that the frequency of pulsations is high enough to produce a relatively flat or plug-like velocity profile. In addition, for the blood flow in the small arteries, a linearised equation system is solved based on the analytical solution obtained by Womersley (1957). The small arteries serve as outflow boundary conditions for the network of large arteries.

The structured-tree model has the advantage of being able to imitate the wave propagation effect, which sets it apart from the lumped parameter models. Additionally, the structured-tree model is computationally efficient, making it valuable in clinical practice. Olufsen (1998) first utilised this model to examine the blood flow and pressure in the systemic and pulmonary arteries but did not incorporate the venous system. Subsequently, the structured-tree model was extended by Vaughan (2010) and Qureshi (2013) to enable an analysis of both arterial and venous pressure and flow in the pulmonary circulation. They treated the pulmonary venous system as a 'mirror image' of the pulmonary arterial tree, given that the pulmonary veins generally follow the same paths as the pulmonary arteries. Their studies constructed the venous system using the same topology as the arterial system, while still accounting for differing material properties and geometries. Instead of computing an impedance as an outflow condition as in (Olufsen, 1998), their models calculated an impedance matrix that linked pressures and flows at the outlets of the large arteries to pressures and flows at the inlets of the large veins. This approach enabled the imposition of realistic outflow conditions on the venous side.

Details of other 1D models are referred to (Reymond et al., 2009) which presented a summary of the 1D models in the existing literature. Overall, the mentioned models in their paper are all based on simplified 1D forms of the Navier-Stokes equations. These models rely on specific assumptions, including a significantly small ratio of a single ves-

sel's diameter to its length, the velocity field demonstrating a Poiseuille profile at every cross-section, and the vessel being represented as a thin elastic tube. Moreover, these models connect individual vessels to form a network, where each vessel in the network is characterised by its unique geometry, elasticity, and resistance to flow. The flow within each individual vessel is connected to other vessels through boundary conditions at junction points between them. The computational domain for these models is thus the human vascular network, which can be generated using general anatomical data, such as anatomical charts (Olufsen et al., 2000) or patient-specific data (Duanmu et al., 2019). However, differences between these various types of 1D models include their structural complexity, completeness of the systemic arterial tree, modelling of viscoelastic properties of vessel walls, approximation of wall shear stress, and boundary conditions at terminal sites.

1.3.2 Coronary circulation coupled to myocardial mechanics

The coronary circulation comprises a complex network of blood vessels that supply blood to the myocardium. The blood vessels are divided into two major categories: epicardial and intramyocardial. The epicardial vessels are located on the surface of the heart while the intramyocardial vessels are located within the myocardium and are responsible for supplying blood to the deeper layers of the myocardium. The cardiac muscles and the intramyocardial vessels are in close proximity to each other which gives rise to the interaction between the coronary flow and cardiac motion. The interaction was termed as cross-talk by Westerhof et al. (2006) who also explained the mechanisms of the cross-talk in detail. Briefly, the cross-sectional areas of the intramyocardial vessels change with the transmural pressure, which is the difference between the blood pressure within the vessel and the intramyocardial pressure (IMP) generated by the heart muscles. When the heart contracts, the IMP increases and the cross-sectional areas of the vessels decrease, leading to a decrease in the volume of the intramyocardial vascular system. The decreased volume is squeezed into both arterial and venous coronary blood vessels. Therefore, the blood flow in coronary circulation is distinguished from that in the other two circulations by its phasic flow pattern: Most of the coronary flow within the left arterial domain occurs in diastole, while during systole the left-sided coronary arterial flow may slow down or even reverse (Gregg and Green, 1940; Westerhof et al., 2006). Conversely, the right-sided coronary flow exhibits relatively lesser impediments when compared to its left-sided counterpart, due to the disparity in IMP between the RV and LV walls. As found in some experimental data (Duanmu et al., 2019), the peak flow rate in the right-sided coronary flow occurs during systole.

Myocardial perfusion plays a crucial role in the diagnosis and management of various cardiovascular diseases. Impaired myocardial perfusion, often resulting from pathological conditions such as coronary artery disease, can lead to ischemia, which may ultimately

result in myocardial infarction and heart failure. However, the complex spatial and temporal variations in coronary blood flow significantly impact myocardial perfusion (Gould and Johnson, 2018; Kassab, 2019), making it challenging to study in clinical practice. Hence, to accurately predict blood perfusion throughout the heart wall, it is essential to employ a comprehensive model of coronary circulation that accounts for the intricate interaction between the cardiac motion and the coronary perfusion, considering the anatomies and mechanical properties of both the myocardium and the coronary vasculature. Therefore, there has been a growing focus in recent years on the creation of fully integrated electro-mechano-fluidic heart models that incorporate highly detailed mechanical models of the heart, models of blood flow, and the relationship between the ventricles and the coronary blood flow (Smith et al., 2005; Lee et al., 2016; Papamanolis et al., 2021; Namani et al., 2020; Fan et al., 2020). These models are increasingly personalised to the individual patient, providing a more comprehensive understanding of the interactions between various physical processes within the heart.

An integrated model was proposed by Smith et al. (2005) that combined a hyperelastic bi-ventricular heart model with a detailed 1D coronary flow model, which encompassed the six largest generations of the arterial coronary tree. The two models were coupled through a two-step process. Initially, the ventricular model was utilised to compute the IMP. Subsequently, this IMP was integrated into the blood flow model to examine the response of the coronary flow. The primary objective of their study was to determine the energy supply to the heart which can be determined by integrating the product of active tension and myofibre strain throughout the cardiac cycle. In a subsequent study, Lee et al. (2016) established an integrated model that combined a poroelastic LV with a 1D coronary network containing 3,910 vascular segments. They employed wave intensity analysis to investigate the wave dependence on parameters associated with cardiac contraction, cardiac perfusion, and systemic hemodynamic processes. Their findings revealed a significant dependence of the backward suction wave on QRS duration and vascular resistance, the forward pushing wave on the rate of myocyte tension development, and the late forward pushing wave on the dynamics of the aortic valve. Another multiscale patient-specific model was recently developed by Papamanolis et al. (2021) by integrating a 1D coronary flow model with a single-compartment poroelastic model for the myocardium. Patient-specific data of the aorta and epicardial arteries were used to construct the vascular network, and synthetic trees were generated down to the arteriole level. Vascular segments with larger diameters were allocated to larger myocardial territories. Their model was applied to five patients with non-obstructive coronary artery disease, and it was observed that the simulated results closely matched the experimental data.

A hybrid lumped-FE modelling framework was introduced by Shavik et al. (2020), which bidirectionally coupled FE models of the patient-specific bi-ventricle, aorta, and

main pulmonary artery. The results obtained from the FE models were integrated through a closed-loop lumped parameter circulatory model that characterises both systemic and pulmonary circulations. The authors calibrated the model using clinically-measured waveforms, including volumes and pressures of the LV, aorta, and main pulmonary artery. They then applied the model to designed simulation cases to test its effectiveness. Namani et al. (2020) proposed an open-loop framework to model the interaction between hyperelastic left ventricular mechanics, systemic circulation, and coronary microcirculation. The authors integrated a FE model of the idealised geometry of the LV, a lumped parameter model of the systemic circulation, and a lumped parameter model of network flow analysis of the coronary circulation, which consisted of an anatomically realistic left circumflex subtree of 8,634 vessels. They found that the relaxation rate of the myocardium had a significant impact, whereas LV contractility had a marginal effect on both the magnitude and transmural distribution of coronary perfusion. The open-loop simulation framework was extended to a closed-loop system by Fan et al. (2021). Their model consisted of an idealised LV and four coronary microvascular networks, each comprising 400 vessels, located at different transmural positions across the left ventricular wall. Non-linear three-element Windkessel electrical systems of the coronary microvascular networks were resolved, and the coronary flow system was integrated into a lumped parameter model of the systemic circulation. The feedback from the coronary flow to the LV dynamics was accomplished by prescribing an assumed contractility-coronary flow relationship as proposed in (Fan et al., 2020). Their results suggested that an increase in either contractility, preload, wall thickness, or cavity volume of the LV can increase the vulnerability of the subendocardial region to ischemia.

1.4 Objectives and organisation of this thesis

The main objective of this thesis is to enhance our understanding of coronary flow and myocardial perfusion by examining the coupling between blood flow in the coronary circulation and the deformation of the myocardium. To accomplish this objective, we will develop a 1D computational model of coronary blood flow in the human coronary circulation, as well as 3D computational models of the LV and the bi-ventricle, and explore their one-way coupling. We will begin by refining and adapting an existing 1D computational model of the blood flow in the systemic and pulmonary circulations (Olufsen, 1998; Qureshi, 2013). The adapted coronary flow model will be capable of capturing the effect of time-varying IMP on coronary blood flow, which is the most important feature of coronary circulation. The 1D coronary flow model will be used to simulate physiologically realistic pressure and flow rate waveforms in the three main coronary arteries. We will then determine accurate IMP from a 3D FE LV model which is based on previous work

(Guan et al., 2020a). Finally, we will explore myocardial perfusion based on the one-way coupling of the coronary flow model and the LV model. A bi-ventricle model will also be developed for further investigation of pathological studies namely pulmonary regurgitation (PR). Our research goals are explicitly defined, and we will follow the subsequent course of action to achieve them:

- We aim to derive the mathematical relationship between time-varying IMP and coronary flow and solve it numerically. To obtain realistic coronary flow results, we will incorporate a human coronary network into the 1D coronary flow model. This will enable us to simulate pressure and flow rate waveforms at multiple locations along the three main branches of the coronary vasculature throughout an entire cardiac cycle under normal physiological conditions.
- To ensure accuracy, a fine-tuned hyperelastic LV model will be utilised to obtain physiological boundary conditions, including aortic pressure and time-varying IMP.
- A one-way coupling framework will be established to integrate the coronary flow model and the LV model, allowing us to analyse myocardial perfusion.
- To validate the accuracy of the computational models, we will conduct a comparative analysis between the simulated results and relevant published simulated outcomes or experimental data.
- We will explore potential opportunities to leverage our models and simulations for clinical purposes.

This thesis consists of six chapters. The initial chapter offers an overview of the anatomical and physiological aspects of the cardiovascular system, including the human heart and coronary circulation, as well as a brief introduction to computational modelling of the heart and coronary flow. Various existing approaches are referenced, and the significance and clinical implications of the computational models are shown. The following sections outline the structure and contents of the remaining chapters.

Chapter 2 focuses on the development of a 1D coronary flow model of the coronary circulation. Specifically, the structured-tree model developed by Olufsen (1998); Vaughan (2010); Qureshi (2013) is adapted to incorporate the effect of time-varying IMP on coronary flow. This chapter introduces a simplified computational network of the coronary vasculature and presents equations governing the hemodynamics of the blood flow in large and small blood vessels. The structured-tree matching conditions, bifurcation conditions, and boundary conditions are also outlined. Finally, this chapter discusses the results of the computed coronary flow and its validation. Overall, this chapter provides important insights into the phasic patterns of coronary flow and the underlying mechanisms.

Chapter 3 describes the development of a computational model of the LV. This chapter presents details of the LV model's governing equations, boundary conditions, and implementation and solution using ABAQUS. The simulated results of the LV model, including pressure and volume in a complete cardiac cycle and stress distribution in the LV wall, are also summarised. This chapter further presents an investigation of the effects of myofibre rotation and myofibre dispersion on LV pump functions.

Chapter 4 focuses on the development of a one-way coupling framework between the coronary flow model presented in Chapter 2 and the LV model described in Chapter 3. The LV model is fine-tuned to provide physiologically accurate aortic pressure and IMP, which are used as boundary conditions in the coronary flow model. This chapter involves the calculation of the IMP and investigates the reconstruction of the coronary network, especially the right coronary arteries and coronary venous system. Additionally, this chapter covers the assignment of the coronary arteries to different segments of the LV wall. The resulting simulated coronary flow is compared with published experimental data. This chapter concludes with a study of myocardial perfusion based on the one-way coupling framework.

Chapter 5 focuses on a human bi-ventricle model and its application to studying PR. Assessing the severity of PR is challenging, and finding clinically useful indicators for its treatment remains unclear. Computational models have shown potential in simulating and predicting disease cases. Thus, in this chapter, open-loop lumped parameter models representing systemic and pulmonary circulations are designed to achieve realistic cardiac function and control the backflow in PR disease cases. This chapter simulates five different cases of PR, ranging from healthy to severe, and compares the results to normal physiological ranges as well as pathological CMR data reported in the literature. The analysis includes the RV dilation induced by PR at the end of diastole, the interaction of the LV and RV, and the cardiac stress distributions. This chapter demonstrates the potential of the computational bi-ventricle model in simulating PR. Furthermore, the bi-ventricle model will be utilised in future work to study bi-ventricle myocardial perfusion under PR disease conditions.

Chapter 6 provides a summary of the main contributions and findings of this thesis and outlines potential directions for future research based on the models developed in this thesis.

Chapter 2

Mathematical modelling of blood flow in coronary circulation

Modelling blood flow in coronary circulation is important for understanding the underlying physiology and predicting the impact of cardiovascular diseases. A proper understanding of the factors that influence coronary flow, such as intramyocardial pressure (IMP), is essential for the diagnosis and treatment of coronary artery disease (Westerhof et al., 2006). By developing more accurate models of coronary circulation, researchers can gain a better understanding of the normal and abnormal functioning of the heart and the coronary flow, and this knowledge can be used to improve diagnosis, treatment, and overall outcomes for patients with cardiovascular disease. To model the blood flow in the coronary circulation, a number of factors must be considered, including the anatomy of the coronary vasculature, the hemodynamics governing the blood flow, the boundary conditions determining the hemodynamics, and the interaction between the myocardium and the blood vessels. Increasing mathematical models have been developed by making assumptions about these factors to provide important insights into the phasic patterns of coronary blood flow and the underlying mechanisms.

In this chapter, we will modify the structured-tree model developed by Olufsen (1998); Vaughan (2010); Qureshi (2013) to model coronary flow, with a specific emphasis on incorporating time-varying IMP which has not been considered before. The coronary flow model presented in this chapter is based on the realistic anatomy of the coronary arteries, rather than on idealised lumped models. Firstly, a simplified computational network of the coronary vasculature is introduced including both the arteries and veins. Secondly, equations governing the hemodynamics of blood flow in both large and small blood vessels in the network are presented. Thirdly, the structured-tree matching conditions, bifurcation conditions, and boundary conditions are outlined. Additionally, the Lax-Wendorff method for numerically solving the system is briefly described. Finally, the results of the simulated coronary blood flow and its validation are discussed.

2.1 A simplified computational network for coronary circulation

In this section, a simplified computational network for the structured-tree coronary flow model (Olufsen, 1998) is constructed. In terms of computational modelling of the coronary blood flow, a detailed three-dimensional (3D) computational network of the coronary vasculature plays an important role in determining flow and pressure distributions. Anatomic studies of coronary vasculature have a long history (Zamir and Chee, 1986; Anderson et al., 1988; Kassab et al., 1993). Kassab et al. (1993), for the first time, provided a complete data set of the coronary vasculature of healthy young farm pigs of either sex and established a mathematical model (diameter-defined Strahler model) of the treelike arteries for further hemodynamic analysis of the coronary blood flow. Connectivities, vessel radius, and length distributions were provided in their data set, based on which Smith et al. (2000) developed a geometric coronary model with the first six generations of the largest coronary arterial vessels. In a study by Kaimovitz et al. (2005), a comprehensive reconstruction of the coronary arterial network of a porcine heart was performed at a highly detailed level, including down to the capillary level. Subsequently, in later works (Kaimovitz et al., 2010), they expanded on this reconstruction by incorporating a statistical reconstruction of the venous side. Recently, Goyal et al. (2012) developed a model-based radii extraction method to reconstruct 3D coronary vasculature from cryo-microtome images (optical fluorescence microtomography) of an in vivo pig heart. A 3D reconstruction of the porcine coronary vasculature with detected vessels ranging from 0.03-1.9 mm was presented in their study.

The coronary networks reconstructed in the aforementioned studies are characterised by a high level of complexity, primarily due to the presence of a large number of intramyocardial vessels. This presents a significant challenge in the reconstruction of the coronary vasculature, which, in turn, increases the computational cost associated with modelling coronary blood flow (Kassab et al., 1993; Smith et al., 2000). In contrast, the structured-tree coronary flow model proposed by Olufsen (1998) represents and generates the enormous intramyocardial vessels as binary structured trees, where the realistic morphology and topology of these vessels are not necessary. As a result, the reconstruction of the coronary vasculature can be significantly simplified, and computational costs can be reduced. Despite this simplification, the structured-tree model retains the effects of wave propagation in the coronary blood flow of the large arteries. Therefore, to simplify the reconstruction of the coronary vasculature, this study applies the structured-tree model, which divides the coronary vasculature into three parts: the epicardial coronary arteries, the epicardial coronary veins, and all other vessels within the heart wall. In accordance with the terminology and methods introduced by Olufsen (1998), the epicardial coronary

arteries and veins are referred to as large vessels, while all other vessels within the heart wall are classified as small vessels.

Firstly, the geometric information of the epicardial arteries is adopted from Duanmu et al. (2019). This in vivo data was obtained from a male patient (age 61, 80 kg) using GE 16-slice computed tomography (CT) angiography. Medical imaging software (GE, AW) was used for visualization and measuring the geometries of the arteries as shown in Fig. 2.1 (a). The epicardial coronary arteries consist of left and right branches that originate from the aortic root. The left branch includes the left main coronary artery (LMCA), which further bifurcates into the left anterior descending arteries (LAD, LAD1, LAD2, LAD3, and LAD4), the left circumflex arteries (LCX, LCX1, LCX2, and LCX3), and the marginal arteries (MARG1, MARG2, and MARG3). The right branch includes the right coronary artery (RCA), which bifurcates into the posterior descending artery (PDA), and the posterior lateral artery (PLA). In summary, the epicardial coronary arteries are divided into 16 segments (RCA, PDA, PLA, LMCA, LCX, LCX1, LCX2, LCX3, MARG1, MARG2, MARG3, LAD, LAD1, LAD2, LAD3, and LAD4). Table 2.1 summarises the lengths, top radii (proximal radii), and bottom radii (distal radii) of these segments. Note that the RCA is the longest segment (10.9 cm), while the LMCA has the largest top radius of 0.188 cm and the LAD4 has the smallest top radius of 0.088 cm. All the large vessels are tapered with different top and bottom radii. It should be mentioned that there is a trifurcation in the CT imaging data from Duanmu et al. (2019). The LMCA trifurcates into the LAD, LCX, and DIAG branches. The trifurcation can be simplified as two bifurcations as originally adopted in their study (Duanmu et al., 2019). However, for the purpose of our current investigation, we have chosen to omit the DIAG vessel. This decision stems from the considerable morphological variations that exist within the coronary vasculature among individuals, leading us to focus our study solely on the coronary flow dynamics in the two major branches, namely the LCX and LAD arteries.

Secondly, to model the small vessels, i.e. the intramyocardial blood vessels, we employ one-dimensional (1D) asymmetric structured trees as shown in Fig. 2.1 (b). To generate such structured trees, we require the radii and asymmetry relations over a bifurcation. Fig. 2.2 illustrates a parent vessel with a radius of r_p, and the radii of its two daughter vessels are scaled by factors α and β (Olufsen, 1999) as

$$r_{\mathrm{d1}} = \alpha r_{\mathrm{p}}, \tag{2.1}$$

$$r_{\mathrm{d2}} = \beta r_{\mathrm{p}}, \tag{2.2}$$

where the subscript p refers to the parent vessel and the subscript d1 and d2 represent the two daughter vessels, respectively. Note that it is impossible to estimate α and β for every bifurcation, so α and β are assumed to be the same for all bifurcations. In order to

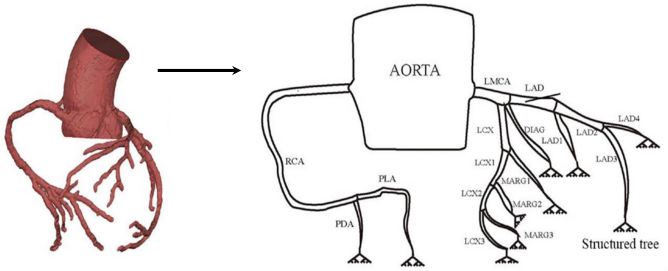

(a)

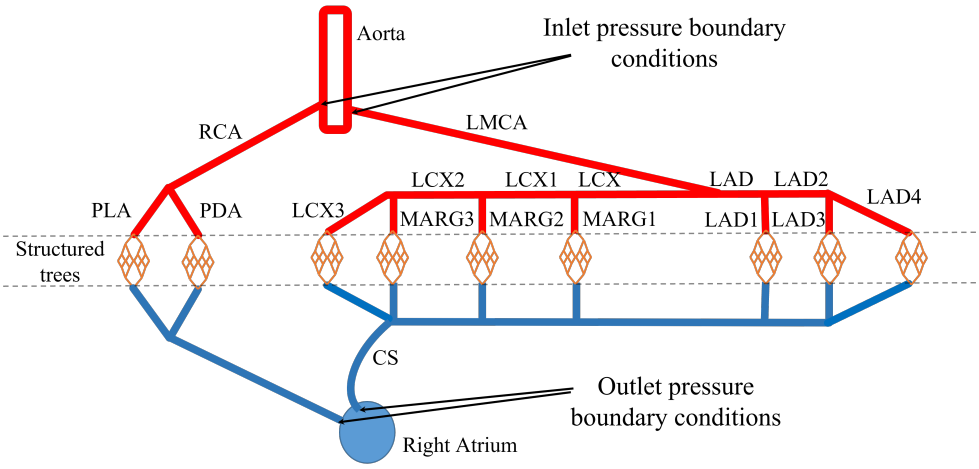

(b)

Figure 2.1: Diagram of epicardial arteries (a) obtained from Duanmu et al. (2019) and a simplified network (b) for the coronary flow model (Olufsen, 1998) reconstructed from (a). LMCA is the left main coronary artery. LAD, LAD1, LAD2, LAD3, and LAD4 are the left anterior descending arteries. LCX, LCX1, LCX2, and LCX3 are the left circumflex arteries. MARG1, MARG2, and MARG3 are the marginal arteries. RCA is the right coronary artery. PDA is the posterior descending artery. PLA is the posterior lateral artery. The structured trees represent intromyocardial blood vessels.

determine realistic α and β, geometric changes over a bifurcation for intramyocardial vessels are necessary. For instance, Murray's law Murray (1926a,b) can be used to determine how the radius changes over an arterial bifurcation. Instead, Olufsen (1999) adopted a more general power law derived by Uylings Uylings (1977), i.e.

$$r_{\mathrm{p}}^{\zeta} = r_{\mathrm{d1}}^{\zeta} + r_{\mathrm{d2}}^{\zeta}, \tag{2.3}$$

where $\zeta = 3.0$ is optimal for laminar flow, and $\zeta = 2.33$ for turbulent flow. In arterial blood flow, a good choice for the exponent is $\zeta = 2.76$ (Kassab et al., 1993; Uylings, 1977; Olufsen, 1998). Then according to (Zamir and Chee, 1986), the area ratio (η) relating the

Table 2.1: Geometric information of the epicardial coronary arteries. Data are provided by Duanmu et al. (2019).

Branch	Length (cm)	Top radius (cm)	Bottom radius (cm)
RCA	10.9	0.151	0.148
PLA	4.20	0.128	0.125
PDA	3.70	0.108	0.105
LMCA	3.20	0.188	0.179
LAD	2.70	0.151	0.145
LAD1	2.90	0.146	0.145
LAD2	6.90	0.138	0.106
LAD3	4.70	0.103	0.103
LAD4	2.20	0.088	0.077
LCX	2.10	0.148	0.147
LCX1	1.60	0.132	0.129
LCX2	2.00	0.115	0.114
LCX3	3.90	0.102	0.099
MARG1	3.50	0.116	0.108
MARG2	3.00	0.098	0.096
MARG3	3.70	0.102	0.100

cross-sectional areas of the two daughter vessels to their parent vessel is

$$\eta = \frac{r_{\mathrm{d1}}^2 + r_{\mathrm{d2}}^2}{r_{\mathrm{p}}^2}, \tag{2.4}$$

and the asymmetry ratio (γ) relating the areas of the two daughter vessels is

$$\gamma = \left(\frac{r_{\mathrm{d2}}}{r_{\mathrm{d1}}}\right)^2. \tag{2.5}$$

The parameters ζ, η, and γ are related by

$$\eta = \frac{1+\gamma}{(1+\gamma^{\zeta/2})^2/\zeta}. \tag{2.6}$$

Using an area ratio $\eta = 1.16$ and an exponent $\zeta = 2.76$, the asymmetry ratio will be $\gamma = 0.41$ (Olufsen, 1998). The scaling parameters α and β now can be calculated by Eq. (2.4) and Eq. (2.5) as

$$\alpha = (1 + \gamma^{\zeta/2})^{-1/\zeta} \approx 0.9, \tag{2.7}$$

and

$$\beta = \alpha\sqrt{\gamma} \approx 0.6. \tag{2.8}$$

The lengths of the small vessels are determined by the relation of the length and diameter reported by Kassab et al. (1993) as

$$L/r = 10, \tag{2.9}$$

where L is the length of a small vessel and r is the radius of the vessel. Details about the parameter choices have been well documented and explained by Olufsen Olufsen (1998, 1999).

Now, the lengths and radii of all vessels in a structured tree can be determined. For example, to obtain a structured tree connected to the large artery LAD1, the bottom radius of LAD1 is the radius of the first parent vessel in the structured tree. According to Eq. (2.1) and Eq. (2.2), the radii of the first two daughter vessels can be determined. Then, the generation of the vessels continues until the radius of the last daughter vessel in the structured tree reaches a cut-off value. The cut-off value (minimum vessel radius) was set to be $r_{\min} = 0.005\,\text{cm}$. The venous side of the structured tree is a 'mirror image' of the arterial side. Next, the lengths of all vessels in the structured tree can be determined according to Eq. (2.9).

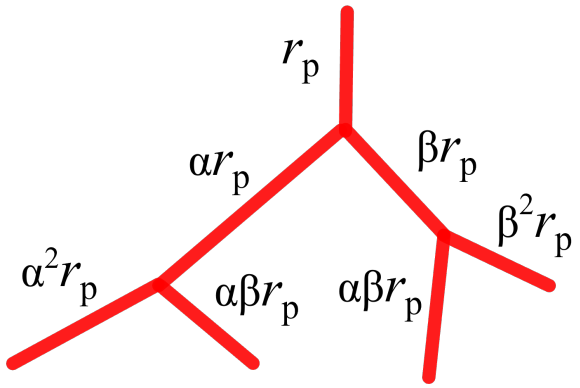

Figure 2.2: A schematic diagram of bifurcation relationship for small blood vessels in a structured tree. At each bifurcation, the radii of the two daughter vessels are scaled by factors α and β, respectively.

Thirdly, geometric information on the epicardial veins is needed. Since data of the

veins are not provided by Duanmu et al. (2019), we here assume that the geometries of the veins are symmetric to that of the arteries, which is based on the observation that the epicardial arteries and veins are basically parallel Vlodaver et al. (2012); Goodwill et al. (2011); Faletra et al. (2020). The same assumption has been used in (Qureshi, 2013; Qureshi and Hill, 2015) for pulmonary circulation modelling.

Finally, a simplified network of coronary vasculature is constructed and shown in Fig. 2.1 (b). It is important to note that the coronary flow in this network is driven by inlet and outlet pressures. The inlet pressure is applied at the proximal point of the LMCA and RCA, while the outlet pressure is applied at the proximal point of the coronary sinus (CS) and the vein that collects flow from the right coronary arteries. In the upcoming sections, the equations and solutions for the coronary flow in this network will be presented. Specifically, based on some assumptions that account for the movement of the blood flow in elastic tapered tubes, we obtain nonlinear equations governing the blood flow in the large vessels, which are reduced from the Navier-Stokes equations, and subsequently solved through numerical methods. On the other hand, the blood flow in the small vessels is governed by linearised equations through linearising the nonlinear equations of the large vessels, which can be solved analytically. This linearity ensures that the effect of the small vessels on the coronary blood flow can be incorporated as dynamic structured-tree matching conditions, which link the pressures and flows of the arterial vessels to those of the venous vessels.

2.2 Hemodynamics of blood flow in large vessels

In this section, we provide the formulation for the hemodynamics of blood flow in the large vessels. These 1D hemodynamics of blood flow in the structured-tree model was developed by Barnard et al. (1966) and Olufsen (1998), which have been widely used and validated in systemic circulation (Olufsen et al., 2000) and pulmonary circulation (Qureshi and Hill, 2015). In the structured-tree model, the large arteries and veins are simplified as elastic tapered tubes. A cylindrical polar coordinate system (r, x, θ) is utilised to determine the position of the points in the vessel as shown in Fig. 2.3, where r represents the radial position, x represents the axial position along the tube, and θ represents the circumferential position. Because of the symmetry of the vessel in terms of the θ direction, the θ variable is omitted in our analysis. Therefore, all variables are dependent on r and x variables, as well as the time variable t. The position of any point inside the vessel can be denoted by (r, x), where $0 \leq r \leq R(x,t)$ and $0 \leq x \leq L$. Here, $R(x,t)$ denotes the radius of the vessel at a fixed x-position and a fixed time, and L represents the length of the vessel. In the initial stress-free state, we have $R(x,t) = R(x,0) = r_0(x)$. The initial vessel radius

$r_0(x)$ along the vessel is determined by the top radius and bottom radius, given as:

$$r_0(x) = r_{\text{Top}} \left(\frac{r_{\text{Bottom}}}{r_{\text{Top}}} \right)^{\frac{x}{L}}, \tag{2.10}$$

where r_{Top} and r_{Bottom} are the initial radii at the proximal and distal ends of the vessel. Assuming the blood flowing within the vessels to be homogeneous, viscous, and incompressible, with a constant density of $\rho = 1.055\,\text{g/cm}^3$ and viscosity of $\mu = 0.49\,\text{g/(cm·s)}$, we consider laminar flow inside the large vessels. Let $p(x,r,t)$ denote the blood pressure inside the vessel, p_0 denote the environmental pressure or external pressure which is called in the following context, and $\mathbf{u}(x,r,t) = (u_x(x,r,t), u_r(x,r,t))$ denote the blood velocity. The mass continuity equation, based on the law of conservation of mass, is given by

$$\frac{\partial \rho}{\partial t} + \nabla \cdot (\rho \mathbf{u}) = 0. \tag{2.11}$$

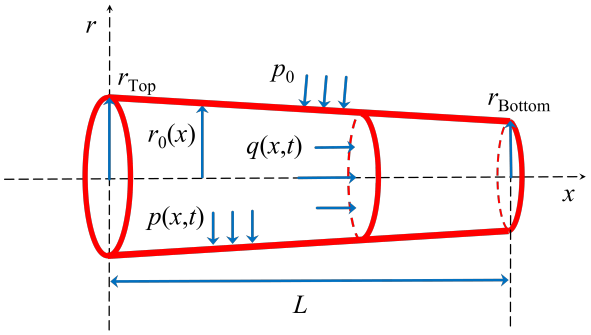

Figure 2.3: Diagram of a tapered tube representing a large vessel. The axial and radial directions of the tube are represented by the coordinate axes x and r, respectively. The unstressed radius along the tube is denoted by $r_0(x)$, while $q(x,t)$ and $p(x,t)$ represent the flow rate and blood pressure at a given axial position and time. Additionally, the constant environmental pressure is denoted as p_0.

For incompressible flow, the blood density remains constant and Eq. (2.11) reduces to

$$\nabla \cdot \mathbf{u} = 0. \tag{2.12}$$

Furthermore,

$$\nabla \cdot \mathbf{u} = \frac{\partial u_x}{\partial x} + \frac{1}{r}\frac{\partial (r u_r)}{\partial r} = 0, \tag{2.13}$$

where $u_x(x,r,t)$ and $u_r(x,r,t)$ are the axial and radial blood flow velocities, respectively. Assuming that the wall of the blood vessel only undergoes transverse motion, the no-slip boundary condition ensures that

$$u_x(x,r,t)|_{r=R(x,t)} = 0, \quad \text{and} \quad u_r(x,r,t)|_{r=R(x,t)} = \frac{\partial R(x,t)}{\partial t}. \tag{2.14}$$

Integrating Eq. (2.13) over the cross-sectional area and using the no-slip boundary condition provides

$$\begin{aligned} 0 &= 2\pi \int_0^R \left(\frac{\partial u_x}{\partial x} + \frac{1}{r} \frac{\partial (r u_r)}{r} \right) r dr \\ &= 2\pi \int_0^R \frac{\partial u_x}{\partial x} r dr + 2\pi \int_0^R \frac{1}{r} \frac{\partial (r u_r)}{r} r dr \\ &= 2\pi \frac{\partial}{\partial x} \int_0^R u_x r dr + 2\pi (r u_r)|_0^R \\ &= 2\pi \frac{\partial}{\partial x} \int_0^R u_x r dr + 2\pi R \frac{\partial R}{\partial t} \\ &= 2\pi \frac{\partial}{\partial x} \int_0^R u_x r dr + \frac{\partial A}{\partial t}, \end{aligned} \tag{2.15}$$

where $A(x,t) = 2\pi R^2(x,t)$ is the cross-sectional area. Here, we introduce the volumetric flow rate

$$q(x,t) = 2\pi \int_0^R u_x r dr. \tag{2.16}$$

Substituting it into Eq. (2.15) gives the 1D equation of continuity of the large blood vessel

$$\frac{\partial q}{\partial x} + \frac{\partial A}{\partial t} = 0. \tag{2.17}$$

The radial and axial balance of momentum equations reduced from the Navier-Stokes equations are

$$\rho \left(\frac{\partial u_r}{\partial t} + u_r \frac{\partial u_r}{\partial r} + u_x \frac{\partial u_r}{\partial x} \right) = -\frac{\partial p}{\partial r} + \mu \left(\frac{\partial^2 u_r}{\partial r^2} + \frac{1}{r} \frac{\partial u_r}{\partial r} - \frac{u_r}{r^2} + \frac{\partial^2 u_r}{\partial x^2} \right), \tag{2.18}$$

and

$$\rho \left(\frac{\partial u_x}{\partial t} + u_r \frac{\partial u_x}{\partial r} + u_x \frac{\partial u_x}{\partial x} \right) = -\frac{\partial p}{\partial x} + \mu \left(\frac{\partial^2 u_x}{\partial r^2} + \frac{1}{r} \frac{\partial u_x}{\partial r} + \frac{\partial^2 u_x}{\partial x^2} \right). \tag{2.19}$$

Since the length of the blood vessel is significantly longer than its radius, it follows that $R(x,t) \ll L$. Moreover, we assume that $u_r(x,r,t) \ll u_x(x,r,t)$, allowing us to introduce an infinitesimal parameter

$$\epsilon = \frac{u_r}{u_x} \ll 1. \tag{2.20}$$

Eliminating ϵ order terms in Eq. (2.18) yields

$$\frac{\partial p}{\partial r} \approx 0, \tag{2.21}$$

which means that the blood pressure only varies along the axial direction as well as time,

i.e. $p(x,r,t) = p(x,t)$. Utilising the same approach, we can simplify Eq. (2.19) to

$$\frac{\partial u_x}{\partial t} + u_r\frac{\partial u_x}{\partial r} + u_x\frac{\partial u_x}{\partial x} = -\frac{1}{\rho}\frac{\partial p}{\partial x} + \nu\left(\frac{\partial^2 u_x}{\partial r^2} + \frac{1}{r}\frac{\partial u_x}{\partial r}\right), \tag{2.22}$$

where $\nu = \mu/\rho$ is the kinematic viscosity. The integration of Eq. (2.22) over the cross-sectional area is given by

$$2\pi\int_0^R\left(\frac{\partial u_x}{\partial t} + u_r\frac{\partial u_x}{\partial r} + u_x\frac{\partial u_x}{\partial x}\right)rdr = -\frac{2\pi}{\rho}\int_0^R\frac{\partial p}{\partial x}rdr + 2\pi\nu\int_0^R\left(\frac{\partial^2 u_x}{\partial r^2} + \frac{1}{r}\frac{\partial u_x}{\partial r}\right)rdr. \tag{2.23}$$

The integration on the left-hand side of Eq. (2.23) is

$$\begin{aligned}
\text{LHS} &= 2\pi\int_0^R\frac{\partial u_x}{\partial t}rdr + 2\pi\int_0^R u_r\frac{\partial u_x}{\partial r}rdr + 2\pi\int_0^R u_x\frac{\partial u_x}{\partial x}rdr \\
&= 2\pi\left(\frac{\partial}{\partial t}\int_0^R u_x rdr - \int_0^R u_x\frac{\partial r}{\partial t}dr\right) + 2\pi\left(\int_0^R u_r u_x rdr - \int_0^R u_x\frac{\partial(u_r r)}{\partial r}dr\right) \\
&\quad + 2\pi\int_0^R u_x\frac{\partial u_x}{\partial x}rdr \\
&= \frac{\partial q}{\partial t} + 2\pi\frac{\partial}{\partial x}\int_0^R u_x^2 rdr,
\end{aligned} \tag{2.24}$$

where we used integration by parts, the continuity equation to replace $\frac{\partial(ru_r)}{\partial r}$, and the no-slip boundary conditions. The integration on the right-hand side of Eq. (2.23) is

$$\text{RHS} = -\frac{A}{\rho}\frac{\partial p}{\partial x} + 2\pi\nu\left(r\frac{\partial u_x}{\partial r}\right)\Big|_{r=R}. \tag{2.25}$$

Thus the momentum equation in the axial direction can be reduced to

$$\frac{\partial q}{\partial t} + 2\pi\frac{\partial}{\partial x}\int_0^R u_x^2 rdr + \frac{A}{\rho}\frac{\partial p}{\partial x} = 2\pi\nu\left(r\frac{\partial u_x}{\partial r}\right)\Big|_{r=R}. \tag{2.26}$$

To determine the integral of u_x^2 (the second term on the left-hand side) and the derivative of u_x in the radial direction (the term on the right-hand side), assumptions on the velocity profile are needed. It has been reported in (Vlachopoulos et al., 2011; Caro et al., 2012) that the velocity profile at the entry region of the aorta was almost flat, and fully developed to a parabolic profile at the resistance arteries. Based on this, Olufsen (1998) introduced the following velocity profile for the blood flow in the large vessels

$$u_x(x,r,t) = \begin{cases} \bar{u}_x(x,t) & \text{for} \quad r \le R-\delta, \\ \bar{u}_x(R-r)/\delta & \text{for} \quad R-\delta < r \le R, \end{cases} \tag{2.27}$$

where $\bar{u}_x(x,t)$ is a constant velocity outside the boundary layer which is a very thin region with thickness δ. Within the boundary layer, the viscous effects are dominant. According to (Lighthill, 1975), the thickness δ can be estimated as

$$\delta = \sqrt{\frac{\nu T}{2\pi}}, \tag{2.28}$$

where T is the period of a cardiac cycle. Using this velocity profile, the integral term on the left-hand side of Eq. (2.26) can be calculated as

$$\begin{aligned} 2\pi \int_0^R u_x^2 r dr &= 2\pi \left(\int_0^{R-\delta} \bar{u}_x^2 r dr + \int_{R-\delta}^R \left(\frac{\bar{u}_x (R-r)}{\delta} \right)^2 \right) \\ &= 2\pi \bar{u}_x^2 \frac{r^2}{2} \Big|_0^{R-\delta} = \bar{u}_x^2 A \left(1 - \frac{4}{3} \frac{\delta}{R} \right) + O(\delta^2). \end{aligned} \tag{2.29}$$

The volumetric flow rate can also be rewritten as

$$q = 2\pi \int_0^R u_x r dr = \bar{u}_x A \left(1 - \frac{\delta}{R} \right) + O(\delta^2). \tag{2.30}$$

Replacing the $\bar{u}_x$ term in Eq. (2.29) with Eq. (2.30), we have

$$2\pi \int_0^R u_x^2 r dr = \frac{q^2}{A} \left(1 + \frac{2}{3} \frac{\delta}{R} \right) + O(\delta^2). \tag{2.31}$$

Using the velocity profile from Eq. (2.27), the derivative term on the right-hand side of Eq. (2.26) is

$$2\pi\nu \left(r \frac{\partial u_x}{\partial r} \right) \Big|_{r=R} = 2\pi\nu \left(-\frac{R\bar{u}_x}{\delta} \right) = -2\pi\nu \frac{R}{\delta} \frac{q}{A} + O(\delta^2). \tag{2.32}$$

Substituting the integral term and the derivative term into Eq. (2.26) and retaining the leading order terms, the final 1D momentum equation is

$$\frac{\partial q}{\partial t} + \frac{\partial}{\partial x} \left(\frac{q^2}{A} \right) + \frac{A}{\rho} \frac{\partial p}{\partial x} = -\frac{2\pi\nu R}{\delta} \frac{q}{A}. \tag{2.33}$$

There are three unknown variables (the pressure $p(x,t)$, the flow rate $q(x,t)$, and the cross-sectional area $A(x,t)$) in the 1D equation of continuity (Eq. (2.17)) and the momentum equation (Eq. (2.33)). To close the governing system of the blood flow in the large blood vessels, we still need another equation.

We assume that the blood vessel wall is thin, elastic, and homogeneous with uniform wall thickness h. Considering the limited motion of the blood vessels within the human body and that their length is much longer than their radii, the transverse motion of the wall is dominant, which further leads to dominant stress and strain in the circumferential

direction. Based on these assumptions and balancing the internal and external pressure and cross-sectional area in an infinitesimal surface element of the vessel wall, Barnard et al. (1966) derived a tube law

$$\mathsf{p}(A) \equiv p(x,t) - p_{\mathrm{L}} = \frac{4}{3}\frac{Eh}{r_0}\left(\sqrt{\frac{A}{A_0}} - 1\right), \tag{2.34}$$

where $\mathsf{p}(A)$ is the transmural pressure, p_{L} is the external pressure of the large vessel, E is Young's modulus, r_0 and A_0 are the initial stress-free radius and cross-sectional area, respectively. Because the large vessels span the surface of the heart, the external pressure on the large vessels is considered to be the pericardium pressure, which is reported not to exceed 2 or 3 mmHg (Shabetai, 1988). In our simulation, the external pressure acting upon the large vessel is negligibly small, effectively setting it to zero. One reason is that a constant external pressure between 0-3 mmHg has a marginal influence on coronary flow. Moreover, this assumption aligns with the utilization of free boundary conditions on the epicardial surface of the LV model as introduced in the subsequent chapter, wherein the pericardium pressure is likewise presumed to be negligible. The Eh/r_0 term is the compliance, which is related to the elastic properties of the blood vessel wall and reflects the flexibility of the vessel wall under pressure. Values of the compliance term should be determined by experimental data. In the pursuit of estimating the compliance of pulmonary blood vessels, Olufsen (1998) put forth an expression

$$\frac{Eh}{r_0} = k_1 \exp(k_2 r_0) + k_3, \tag{2.35}$$

where the constants are $k_1 = 2 \times 10^7 \mathrm{g/s^2/cm}$, $k_2 = -22.53 \mathrm{cm}^{-1}$, $k_3 = 8.65 \times 10^5 \mathrm{g/s^2/cm}$. Later, Qureshi (2013) adopted a constant compliance approach for pulmonary blood vessels, i.e. $k_3 = 2.6 \times 10^5 \mathrm{g/s^2/cm}$ for all the large pulmonary blood vessels and $k_3 = 0.5 \times 10^5 \mathrm{g/s^2/cm}$ for all the small pulmonary blood vessels. In this study, we employ constant compliance values of $k_3 = 1.2 \times 10^6 \mathrm{g/s^2/cm}$ for all the large coronary blood vessels and $k_3 = 2.4 \times 10^5 \mathrm{g/s^2/cm}$ for all the small coronary blood vessels. These chosen values are based on measurements of coronary blood vessel compliance obtained from porcine subjects, as documented by Kassab and Molloi (2001).

2.3 Numerical method

The equations (Eq. (2.17), Eq. (2.33), and Eq. (2.34)) governing the coronary flow in the large vessels are solved by the two-step Lax-Wendroff method. The Lax-Wendroff method is a second-order method and is often adopted to solve compressible fluid dynamics. This method requires that Eq. (2.17) and Eq. (2.33) be written in the conservation forms. For

computational convenience, the following dimensionless variables are introduced to make Eq. (2.17) and Eq. (2.33) dimensionless:

$$x = r_c\tilde{x}, \quad t = \frac{r_c^3}{q_c}\tilde{t}, \quad r = r_c\tilde{r}, \tag{2.36}$$

$$A = r_c^2\tilde{A}, \quad q = q_c\tilde{q}, \quad p = \rho g l_c\tilde{p}. \tag{2.37}$$

where r_c, l_c, and q_c are the characteristic radius, characteristic length, and characteristic average velocity, respectively. Using these quantities, the continuity equation and the momentum equation for the large vessels are transformed into dimensionless forms

$$\frac{\partial\tilde{q}}{\partial\tilde{x}} + \frac{\partial\tilde{A}}{\partial\tilde{t}} = 0, \tag{2.38}$$

and

$$\frac{\partial\tilde{q}}{\partial\tilde{t}} + \frac{\partial}{\partial\tilde{x}}\left(\frac{\tilde{q}^2}{\tilde{A}}\right) + \tilde{A}\frac{\partial\tilde{p}}{\partial\tilde{x}} = -\frac{2\pi\tilde{r}}{\delta\Re}\frac{\tilde{q}}{\tilde{A}}, \tag{2.39}$$

where $\Re = q_c/(\nu r_c)$ is the Reynolds number. In the following context, the tildes are dropped for simplicity. To write the two equations in the conservation forms, we introduce an intermediate variable

$$B(r_0(x), p(x,t)) = \int_{p_0}^{p(x,t)} A(p')dp'. \tag{2.40}$$

Differentiating B with respect to x and substituting it into Eq. (2.39) yields

$$\frac{\partial q}{\partial t} + \frac{\partial}{\partial x}\left(\frac{q^2}{A} + B\right) - \frac{\partial B}{\partial r_0}\frac{dr_0}{dx} = -\frac{2\pi r_0}{\delta\Re}\frac{q}{A}. \tag{2.41}$$

Using the tube law, i.e. Eq. (2.34), the third term in Eq. (2.41) is

$$\frac{\partial B}{\partial r_0}\frac{dr_0}{dx} = \left(2\sqrt{A}\left(\sqrt{\pi}f + \sqrt{A_0}\frac{f}{dr_0}\right) - \frac{f}{dr_0}\right)\frac{dr_0}{dx}, \tag{2.42}$$

where $f = 4Eh/(3r_0)$. Now, the dimensionless momentum equation Eq. (2.41) and the dimensionless continuity equation Eq. (2.38) can be combined as

$$\frac{\partial}{\partial t}\begin{pmatrix} A \\ \\ q \end{pmatrix} + \frac{\partial}{\partial x}\begin{pmatrix} q \\ \\ \frac{q^2}{A} + f\sqrt{A_0 A} \end{pmatrix} = \begin{pmatrix} 0 \\ \\ -\frac{2\pi r}{\delta\Re}\frac{q}{A} + \left(2\sqrt{A}\left(\sqrt{\pi}f + \sqrt{A_0}\frac{df}{dr_0}\right) - A\frac{df}{dr_0}\right)\frac{dr_0}{dx} \end{pmatrix}, \tag{2.43}$$

which is the conservation form of the two equations. The corresponding matrix form is

$$\frac{\partial}{\partial t}\mathbf{U}+\frac{\partial}{\partial x}\mathbf{W}=\mathbf{S}, \tag{2.44}$$

where $\mathbf{U}$, $\mathbf{W}$, and $\mathbf{S}$ are

$$\mathbf{U}=(U_1,U_2)=(A,q), \tag{2.45}$$

$$\mathbf{W}=(W_1,W_2)=(q,\frac{q^2}{A}+f\sqrt{A_0A}), \tag{2.46}$$

$$\mathbf{S}=(S_1,S_2)=(0,-\frac{2\pi r}{\delta\mathfrak{R}}\frac{q}{A}+\left(2\sqrt{A}\left(\sqrt{\pi}f+\sqrt{A_0}\frac{df}{dr_0}\right)-A\frac{df}{dr_0}\right)\frac{dr_0}{dx}). \tag{2.47}$$

After we obtain the conservation form, the variables in Eq. (2.44) are further discretised in spatial and temporal grids. We denote a discretised variable as

$$\boldsymbol{\phi}_m^n=\boldsymbol{\phi}(m\Delta x,n\Delta t), \tag{2.48}$$

where Δx and Δt are the spatial and temporal step sizes, $m\in[0,M]$ and $n\in[0,N]$ denote the current spatial and temporal step position, M is the total spatial grid points, N is the total temporal grid points, and $\boldsymbol{\phi}=\{\mathbf{U},\mathbf{W},\mathbf{S}\}$. For example, one period of 0.8 s can be discretised into 32768 temporal grid points, and the spatial grid points can be set to 10 points per centimeter. We will denote such girds as (32768, 10). For the temporal and spatial grids of (32768, 10), the total temporal grid points are $N=32768$, and the total spatial grid points are $M=50$ for a vessel with a length of 5 cm.

Given the pressure or flow rate at the inlet and the outlet of the computational network, all variables in Eq. (2.44) in the spatial and temporal grids can be numerically solved. In addition, the stability of the Lax-Wendroff numerical scheme requires that the spatial and temporal grids maintain the Courant–Friedrichs–Lewy (CFL) condition, which is determined by

$$\Delta t\leqslant\frac{\Delta x}{|\,c\,|}, \tag{2.49}$$

where c is the wave velocity and $|\cdot|$ is the norm. There is a theorem (Quarteroni and Quarteroni, 2009) ensuring the stability of the Lax-Wendroff numerical method as

Theorem 1 *If the CFL condition, Eq. (2.49), is satisfied, the Lax-Wendroff numerical scheme is strongly stable in the norm* $\|\cdot\|_{\Delta,1}$.

2.4 Hemodynamics of blood flow in small vessels

Considering the large number of small blood vessels, it is computationally challenging to solve non-linear equations for blood flow in these vessels. To address this issue, Olufsen (1999) derived a linearised continuity equation and a linearised axial momentum equation

to analytically solve blood flow in the small vessels based on Womersley's classical theory (Womersley, 1957). Detailed derivations can be found in (Olufsen, 1998). In this section, we briefly present the governing equations obtained by Olufsen (1999) and further consider the effect of the time-varying external pressure on coronary flow.

The same assumptions for the large vessels are adopted for the small vessels, except that the tapering of the small vessels is neglected. We have the axial momentum equation for a large vessel

$$\rho\left(\frac{\partial u_x}{\partial t}+u_r\frac{\partial u_x}{\partial r}+u_x\frac{\partial u_x}{\partial x}\right)=-\frac{\partial p}{\partial x}+\mu\left(\frac{\partial^2 u_x}{\partial r^2}+\frac{1}{r}\frac{\partial u_x}{\partial r}+\frac{\partial^2 u_x}{\partial x^2}\right). \tag{2.50}$$

Because the viscous forces are more dominant than the inertial forces in the small vessels and the small vessels are short and non-tapering, the nonlinear effects may be neglected. Therefore, a linearised version of Eq. (2.50) can be used for modelling the blood flow in the small vessels (Olufsen, 1999), which is

$$\frac{\partial u_x}{\partial t}+\frac{1}{\rho}\frac{\partial p}{\partial x}=\frac{\nu}{r}\frac{\partial}{\partial r}\left(r\frac{\partial u_x}{\partial r}\right), \tag{2.51}$$

where $\nu=\mu/\rho$ is the dynamic viscosity. For the circulatory system, the pressure and flow rate are periodic due to the contraction and relaxation of the heart. Therefore, we assume that all solutions of the coronary flow are periodic with a period time T and an angular frequency $\omega=2\pi/T$. The velocity and pressure can then be expressed as

$$u_x(r,x,t)=\sum_{k=-\infty}^{k=\infty}U_k(r,x)e^{ik\omega t},\qquad\text{and}\qquad p(x,t)=\sum_{k=-\infty}^{k=\infty}P_k(x)e^{ik\omega t}. \tag{2.52}$$

Substituting them into Eq. (2.51) yields

$$ik\omega U_k+\frac{1}{\rho}\frac{dP_k}{dx}=\frac{\nu}{r}\frac{\partial}{\partial r}\left(r\frac{\partial U_k}{\partial r}\right),\quad k=\{\ldots,-2,-1,0,1,2,\ldots\}, \tag{2.53}$$

which can be solved to obtain the kth-component factor in Eq. (2.52). We now transform Eq. (2.53) into a non-dimensional form by multiplying the two sides by r_0^2/ν

$$ik\alpha^2U_k+\frac{r_0^2}{\mu}\frac{dP_k}{dx}=\frac{1}{y}\frac{\partial}{\partial y}\left(y\frac{\partial U_k}{\partial y}\right),\quad k=\{\ldots,-2,-1,0,1,2,\ldots\}, \tag{2.54}$$

where r_0 is the radius of the tube, $y=r/r_0$ and $\alpha^2=r_0^2\omega/\nu$. The quantity α is the Womersley number, which is a dimensionless expression of the pulsatile flow frequency in relation to the viscous effect. The ranges of the Reynolds number and Womersley number in our model are detailed in Table. 2.2. For the small vessels, the Reynolds number is less than one and the Womersley number is less than 0.01, both of which indicate the

dominance of the viscous forces. In fact, due to this prevailing dominance of viscous effects, it is appropriate to neglect the inertial term in Eq. 2.51. However, we are keeping this term for completeness.

Table 2.2: The ranges of the Reynolds number and Womersley number in our model.

Vessel	Reynolds number	Womersley number
Large	50 - 300	1 - 3
Small	< 1	< 0.01

Firstly, we calculate the solutions of the non-zero frequencies in Eq. (2.54), i.e. $k \neq 0$. Womersley (1957) derived that

$$U_k = \frac{r_0^2}{ik\mu\alpha^2}\frac{dP_k}{dx}\left(1 - \frac{J_0(\alpha y i^{3/2})}{J_0(\alpha i^{3/2})}\right), \tag{2.55}$$

where $J_0(x)$ is the zeroth Bessel function of the first kind. The volumetric flow rate can be expanded as

$$q(x,t) = \sum_{k=-\infty}^{k=\infty} Q_k(x) e^{ik\omega t}, \tag{2.56}$$

with the coefficients

$$Q_k = 2\pi \int_0^{r_0} U_k r dr. \tag{2.57}$$

Substituting U_k with Eq. (2.55) gives

$$Q_k = \frac{-A_0}{\rho i k\omega}\frac{dP_k}{dx}(1 - F_J), \tag{2.58}$$

where

$$F_J = \frac{2J_1(k\omega)}{\omega_k J_0(k\omega)}, \tag{2.59}$$

and $J_1(x)$ is the first order Bessel function of the first kind.

The continuity equation and the tube law are the same as that of the large vessels, i.e.

$$\frac{\partial q}{\partial x} + \frac{\partial A}{\partial t} = 0, \tag{2.60}$$

and

$$\mathsf{P}(x,t) = p(x,t) - p^{\text{ext}}(t) = \frac{4}{3}\frac{Eh}{r_0}\left(\sqrt{\frac{A}{A_0}} - 1\right), \tag{2.61}$$

where $p^{\text{ext}}(t)$ is the time-varying external pressure on the small vessels. It should be noted that the external pressure on the large vessels is assumed to be zero. Instead, the small vessels experience external pressure exerted by the myocardium, i.e. the IMP, which

exhibits considerable temporal variation. Combining Eq. (2.60) and Eq. (2.61), we have

$$C\frac{\partial \mathsf{P}}{\partial t}+\frac{\partial q}{\partial x}=0, \tag{2.62}$$

where C is the compliance which can be approximated as

$$C=\frac{\partial A}{\partial \mathsf{P}}=\frac{3A_0r_0}{2Eh}\left(1+\frac{3r_0\mathsf{P}}{4Eh}\right)\approx\frac{3A_0r_0}{2Eh}, \tag{2.63}$$

as $Eh \gg \mathsf{P}r_0$. The transmural and external pressure are

$$\mathsf{P}(x,t)=\sum_{k=-\infty}^{k=\infty}\mathsf{P}_k(x)e^{ik\omega t} \quad \text{and} \quad p^{\text{ext}}(t)=\sum_{k=-\infty}^{k=\infty}P_k^{\text{ext}}e^{ik\omega t}, \tag{2.64}$$

such that Eq. (2.62) can be rewritten as

$$iCk\omega\mathsf{P}_k+\frac{\partial Q_k}{\partial x}=iCk\omega(P_k-P_k^{\text{ext}})+\frac{\partial Q_k}{\partial x}=0. \tag{2.65}$$

Substituting Eq. (2.58) into the above equation leads to

$$\frac{(k\omega)^2}{c^2}Q_k+\frac{\partial^2 Q_k}{\partial x^2}=0, \tag{2.66}$$

where $c=\sqrt{A_0(1-F_J)/\rho C}$ is the wave propagation velocity. Equation (2.66) is simply the equation governing a single-degree-of-freedom system, which has the exact solution

$$Q_k(x)=a_k\cos(k\omega x/c)+b_k\sin(k\omega x/c), \tag{2.67}$$

where a_k and b_k are constants of integration. Substituting Eq. (2.67) into Eq. (2.58) yields

$$\mathsf{P}_k(x)=\frac{1}{iCc}(a_k\sin(k\omega x/c)-b_k\cos(k\omega x/c)). \tag{2.68}$$

Next, we calculate the zero frequency component in Eq. (2.54). When $k=0$, the linearised axial momentum equation in components form i.e. Eq. (2.53), becomes

$$\frac{1}{\rho}\frac{dP_0}{dx}=\frac{\nu}{r}\frac{\partial}{\partial r}\left(r\frac{\partial U_0}{\partial r}\right). \tag{2.69}$$

Integrating Eq. (2.69) with respect to r provides

$$\frac{\partial U_0}{\partial r}=\frac{r}{2\mu}\frac{dP_0}{dx}+\frac{C_1}{r}, \tag{2.70}$$

where C_1 is the constant of integration which can be eliminated by assuming that $\partial U/\partial r$

is finite at $r = 0$. Integrating Eq. (2.70) again with respect to r yields

$$U_0 = \frac{r^2}{2\mu}\frac{dP_0}{dx} + \frac{C_2}{r}, \tag{2.71}$$

where C_2 is the constant of integration which is evaluated using the non-slip condition at the wall $r = r_0$. Thus, we obtain

$$U_0 = \frac{r^2 - r_0^2}{4\mu}\frac{dP_0}{dx}, \tag{2.72}$$

which is a normal Poiseuille flow profile. The volumetric flow rate is

$$Q_0(x) = 2\pi \int_0^{r_0} U_0 r dr = -\frac{\pi}{8\mu}\frac{dP_0}{dx} r_0^4, \tag{2.73}$$

and integration of it gives

$$P_0(x) = -\frac{8\mu C_3}{\pi r_0^4} x + C_4, \tag{2.74}$$

where C_3 and C_4 are constants of integration.

2.5 Structured-tree matching conditions

The structured-tree matching condition serves as a boundary condition, linking the pressure and flow rate at the terminals of the arteries and veins. Such boundary condition was originally suggested by C. S. Peskin. Olufsen (1998), at the first time, developed the structured-tree outflow condition, which only considers the arterial side. Later, Vaughan (2010) extended the structured-tree outflow condition into the structured-tree matching condition, which included the venous side. The structured-tree matching condition was further used in modelling pulmonary circulation by Qureshi (2013).

The admittance concept needs to be introduced in the structured-tree matching condition, based on the analytical solutions of pressure and flow for the small vessels (Olufsen, 1998). In this section, we first calculate the admittance of a single vessel and then assemble them to derive the great admittance of one structured tree. A novel aspect of the method presented here is that we consider the effect of the time-varying external pressure on the great admittance. This concept draws inspiration from Jay Mackenzie, who initially proposed the exploration of both time-varying and spatially varying external pressure.

2.5.1 Admittance matrix for a single vessel in a structured tree

As discussed in section 2.4, the equations governing blood flow in the small vessels are linear. Expanding the flow rate and pressure into the Fourier series, we obtain the following

equations for their Fourier coefficients:

$$Q_k(x) = \frac{1}{q_c}\left(a_k \cos(k\omega x/c) + b_k \sin(k\omega x/c)\right), \tag{2.75}$$

$$\mathfrak{p}_k(x) = \frac{i}{\rho g l C c}(-a_k \sin(k\omega x/c) + b_k \cos(k\omega x/c)), \tag{2.76}$$

$$Q_0(x) = \frac{\Upsilon}{q_c}, \tag{2.77}$$

$$\mathfrak{p}_0(x) = -\frac{1}{\rho g l}\left(\frac{8\mu\Upsilon}{\pi r_0^4}x - \Gamma\right), \tag{2.78}$$

where q_c is the characteristic flow rate and l is the characteristic length to nondimensionalise the flow rate and pressure, g is the acceleration of gravity, and the constants $a_k, b_k, \Upsilon, \Gamma$ are dependent on the specific flow rate and pressure at the inlet and outlet of a vessel.

For the Fourier coefficients of the non-zero frequencies at the inlet, we have

$$Q_k(0) = \frac{a_k}{q_c}, \tag{2.79}$$

$$\mathfrak{p}_k(0) = \frac{i b_k}{\rho g l C c}. \tag{2.80}$$

In the meantime, we have the Fourier coefficients of the zero frequency at the outlet

$$Q_k(L) = \frac{1}{q_c}\left(a_k \cos(k\omega L/c) + b_k \sin(k\omega L/c)\right), \tag{2.81}$$

$$\mathfrak{p}_k(L) = \frac{i}{\rho g l C c}(-a_k \sin(k\omega L/c) + b_k \cos(k\omega L/c)). \tag{2.82}$$

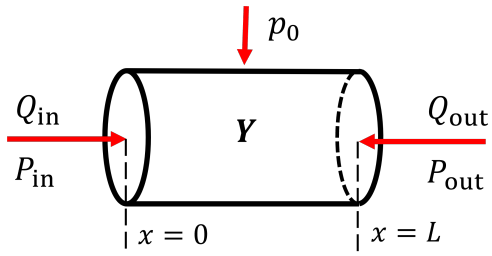

Figure 2.4: Sketch of a single small blood vessel in one structured tree. The Fourier coefficients of the flow rate (Q_{in}, Q_{out}) and pressure (P_{in}, P_{out}) at the inlet point ($x = 0$) and outlet point ($x = L$) of the vessel are depicted. The Fourier coefficients of the external pressure p_0 remain constant along the entirety of the vessel. The symbol $\mathbf{Y}$ denotes the admittance of the single small vessel.

A sketch of a single small blood vessel in one structured tree is shown in Fig. 2.4. We denote that $P_{\text{in}} = \mathfrak{p}_{\text{in}} - p_0 = \mathfrak{p}_k(0) - p_0$, $P_{\text{out}} = \mathfrak{p}_{\text{out}} - p_0 = \mathfrak{p}_k(L) - p_0$, $Q_{\text{in}} = Q_k(0)$,

and $Q_{\text{out}} = Q_k(L)$. The admittance $\mathbf{Y}$ is a 2×2 matrix giving the relation of the Fourier coefficients of flow rate and the transmural pressure at the inlet ($x = 0$) and outlet ($x = L$), specifically

$$\begin{pmatrix} Q_{\text{in}} \\ \\ Q_{\text{out}} \end{pmatrix} = \begin{pmatrix} Y_{11} & Y_{12} \\ \\ Y_{21} & Y_{22} \end{pmatrix} \begin{pmatrix} \mathit{p}_{\text{in}} \\ \\ \mathit{p}_{\text{out}} \end{pmatrix}, \tag{2.83}$$

or in matrix form

$$\mathbf{Q} = \mathbf{Y}\mathit{p}, \tag{2.84}$$

where $\mathbf{Q} = (Q_{\text{in}}, Q_{\text{out}})$ are the flow rate at the inlet and outlet of the vessel, respectively, and $\mathbf{Y}$ is the admittance, $\mathit{p} = (\mathit{p}_{\text{in}}, \mathit{p}_{\text{out}})$ is the transmural pressure, i.e. $\mathit{p}_{\text{in}} = P_{\text{in}} - p_0$ and $\mathit{p}_{\text{out}} = P_{\text{out}} - p_0$. The admittance $\mathbf{Y}$ can be determined by Eqs. (2.79) -(2.82) as

$$Q_{\text{out}} = -Q_{\text{in}} C_L + \frac{i\rho g l C c}{q_c} \mathit{p}_{\text{in}} S_L, \tag{2.85}$$

$$\mathit{p}_{\text{out}} = \mathit{p}_{\text{in}} C_L - \frac{i q_c}{\rho g l C c} Q_{\text{in}} S_L, \tag{2.86}$$

where $C_L \equiv \cos(\omega L/c)$ and $S_L \equiv \sin(\omega L/c)$. This can be rearranged in a matrix form

$$\begin{pmatrix} Q_{\text{in}} \\ \\ Q_{\text{out}} \end{pmatrix} = \frac{iCc}{S_L} \frac{\rho g l}{q_c} \begin{pmatrix} -C_L & 1 \\ \\ 1 & -C_L \end{pmatrix} \begin{pmatrix} \mathit{p}_{\text{in}} \\ \\ \mathit{p}_{\text{out}} \end{pmatrix}. \tag{2.87}$$

Repeating the same procedure for the zero-frequency component yields

$$\begin{pmatrix} Q_{\text{in}} \\ \\ Q_{\text{out}} \end{pmatrix} = \frac{\pi r_0^4}{8\mu L} \frac{\rho g l}{q_c} \begin{pmatrix} 1 & -1 \\ \\ -1 & 1 \end{pmatrix} \begin{pmatrix} \mathit{p}_{\text{in}} \\ \\ \mathit{p}_{\text{out}} \end{pmatrix}. \tag{2.88}$$

Thus, the admittance for a single vessel is

$$\mathbf{Y} = \frac{iCc}{S_L} \frac{\rho g l}{q_c} \begin{pmatrix} -C_L & 1 \\ \\ 1 & -C_L \end{pmatrix} \quad \text{while} \quad k \neq 0, \tag{2.89}$$

and

$$\mathbf{Y} = \frac{\pi r_0^4}{8\mu L} \frac{\rho g l}{q_c} \begin{pmatrix} 1 & -1 \\ \\ -1 & 1 \end{pmatrix} \quad \text{while} \quad k = 0. \tag{2.90}$$

2.5.2 Great admittance of a structured tree

Based on the admittance for a single vessel, in this section, we calculate the great admittance for a whole structured tree. The admittances of two vessels connected in parallel and in series are required.

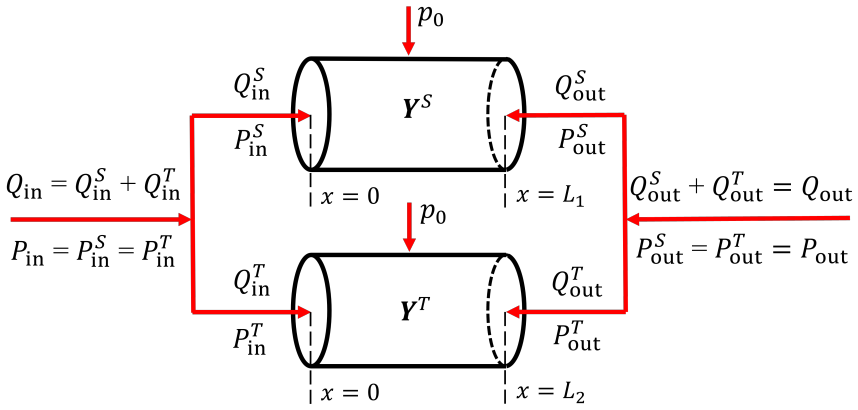

Figure 2.5: Sketch of two parallel small vessels in one structured tree. The Fourier coefficients of the flow rate and pressure at the inlet and outlet of the vessels, along with the flow conservation constraints, are displayed.

At first, we determine the admittance for two vessels connected in parallel. As shown in Fig. 2.5, we have

$$\mathbf{Q}^S = \mathbf{Y}^S \mathbf{P}^S, \tag{2.91}$$

and

$$\mathbf{Q}^T = \mathbf{Y}^T \mathbf{P}^T, \tag{2.92}$$

where S and T denote the two different vessels, $\mathbf{Q}^S = (Q_{\text{in}}^S, Q_{\text{out}}^S)$, $\mathbf{Q}^T = (Q_{\text{in}}^T, Q_{\text{out}}^T)$, $\mathbf{P}^S = (P_{\text{in}}^S - p_0, P_{\text{out}}^S - p_0)$, $\mathbf{P}^T = (P_{\text{in}}^T - p_0, P_{\text{out}}^T - p_0)$. Analogous to the same potential difference across the resistors in parallel combinationton, pressures of the two vessels at the inlet and outlet are

$$\begin{pmatrix} P_{\text{in}} \\ P_{\text{out}} \end{pmatrix} = \begin{pmatrix} P_{\text{in}}^S \\ P_{\text{out}}^S \end{pmatrix} = \begin{pmatrix} P_{\text{in}}^T \\ P_{\text{out}}^T \end{pmatrix}. \tag{2.93}$$

The flow conservation gives us that

$$\begin{pmatrix} Q_{\text{in}} \\ Q_{\text{out}} \end{pmatrix} = \begin{pmatrix} Q_{\text{in}}^S \\ Q_{\text{out}}^S \end{pmatrix} + \begin{pmatrix} Q_{\text{in}}^T \\ Q_{\text{out}}^T \end{pmatrix}. \tag{2.94}$$

As we have only taken into account the time-varying external pressure, the external

pressure remains constant along the vessel at a fixed time. Therefore, we can write

$$\begin{pmatrix} p_{\text{in}} \\ p_{\text{out}} \end{pmatrix} = \begin{pmatrix} p^S_{\text{in}} \\ p^S_{\text{out}} \end{pmatrix} = \begin{pmatrix} p^T_{\text{in}} \\ p^T_{\text{out}} \end{pmatrix}. \tag{2.95}$$

Substituting Eqs. (2.93)-(2.95) into Eq. (2.91) and Eq. (2.92), and then adding them together yields

$$\mathbf{Q} = \mathbf{Y}^{||} p, \tag{2.96}$$

where

$$\mathbf{Y}^{||} = (\mathbf{Y}^S + \mathbf{Y}^T) \tag{2.97}$$

is the admittance matrix for two vessels connected in parallel.

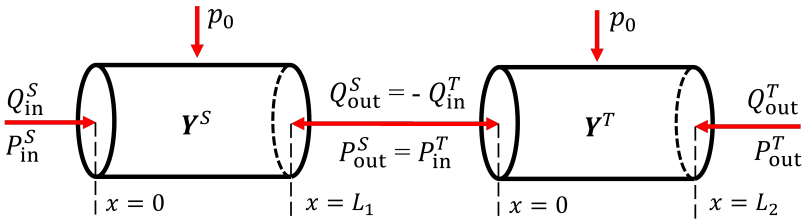

Figure 2.6: Sketch of series small vessels in one structured tree. The Fourier coefficients of the flow rate and pressure at the inlet and outlet of the vessels, along with the flow conservation constraints, are depicted.

Secondly, we determine the admittance for two vessels connected in series. Again for each vessel, as shown in Fig. 2.6, we have

$$\mathbf{Q}^S = \mathbf{Y}^S p^S, \tag{2.98}$$

and

$$\mathbf{Q}^T = \mathbf{Y}^T p^T. \tag{2.99}$$

The expansions of the two equations are

$$Q^S_{\text{in}} = p^S_{\text{in}} Y^S_{11} + p^S_{\text{out}} Y^S_{12}, \tag{2.100}$$

$$Q^S_{\text{out}} = p^S_{\text{in}} Y^S_{21} + p^S_{\text{out}} Y^S_{22}, \tag{2.101}$$

$$Q^T_{\text{in}} = p^T_{\text{in}} Y^T_{11} + p^T_{\text{out}} Y^T_{12}, \tag{2.102}$$

$$Q^T_{\text{out}} = p^T_{\text{in}} Y^T_{21} + p^T_{\text{out}} Y^T_{22}. \tag{2.103}$$

The flow constraints of two vessels connected in series require that

$$\mathit{p}^S_{\text{out}} = \mathit{p}^T_{\text{in}}, \tag{2.104}$$

and

$$Q^S_{\text{out}} = -Q^T_{\text{in}}. \tag{2.105}$$

Introducing $\tilde{\mathit{p}} = \mathit{p}^S_{\text{out}} = \mathit{p}^T_{\text{in}}$ and solving for $\tilde{\mathit{p}}$ using Eq. (2.101) and Eq. (2.102) gives

$$\tilde{\mathit{p}} = -\frac{Y^S_{21}\mathit{p}^S_{\text{in}} + Y^T_{12}\mathit{p}^T_{\text{out}}}{Y^S_{22} + Y^T_{11}}. \tag{2.106}$$

Substituting it into Eq. (2.100) and Eq. (2.103) yields

$$Q^S_{\text{in}} = \left(Y^S_{11} - \frac{Y^S_{21}Y^S_{12}}{Y^S_{22} + Y^T_{11}}\right)\mathit{p}^S_{\text{in}} - \frac{Y^S_{12}Y^T_{12}}{Y^S_{22} + Y^T_{11}}\mathit{p}^T_{\text{out}}, \tag{2.107}$$

and

$$Q^T_{\text{out}} = -\frac{Y^T_{21}Y^S_{21}}{Y^S_{22} + Y^T_{11}}\mathit{p}^S_{\text{in}} + \left(Y^T_{22} - \frac{Y^T_{21}Y^T_{12}}{Y^S_{22} + Y^S_{11}}\right)\mathit{p}^S_{\text{out}}, \tag{2.108}$$

which can be rewritten in a compact form

$$\mathbf{Q} = \mathbf{Y}^{\Leftrightarrow}\mathit{p}, \tag{2.109}$$

where

$$\mathbf{Y}^{\Leftrightarrow} = \begin{pmatrix} Y^S_{11} - \frac{Y^S_{12}Y^S_{21}}{Y^S_{22}+Y^T_{11}} & -\frac{Y^S_{12}Y^T_{12}}{Y^S_{22}+Y^T_{11}} \\ -\frac{Y^S_{21}Y^T_{21}}{Y^S_{22}+Y^T_{11}} & Y^T_{22} - \frac{Y^T_{21}Y^T_{12}}{Y^S_{22}+Y^T_{11}} \end{pmatrix} \tag{2.110}$$

is the admittance of two vessels connected in series.

Finally, we can determine the great admittance for a whole structured tree. Based on the admittance of a single vessel, the admittance of two vessels connected in parallel, and the admittance of two vessels connected in series, we now assemble them together to obtain a great admittance of a whole structured tree. To achieve this, the small veins are assumed to be mirror images of the small arteries in the structured tree. Specifically, the admittance of all single vessels are calculated at first, and then the great admittance is computed according to the combination of the vessels. For instance, given the simplest structured tree as shown in Fig. 2.7, the great admittance is calculated as

$$\mathbf{Y} = \mathbf{Y}^A(0,0) \Leftrightarrow ((\mathbf{Y}^A(1,0) \Leftrightarrow \mathbf{Y}^V(1,0))||(\mathbf{Y}^A(0,1) \Leftrightarrow \mathbf{Y}^V(0,1))) \Leftrightarrow \mathbf{Y}^V(0,0), \tag{2.111}$$

where $\mathbf{Y}^A(0,0)$, $\mathbf{Y}^A(0,1)$, and $\mathbf{Y}^A(1,0)$ are the admittances of the three single arteries, $\mathbf{Y}^V(0,0)$, $\mathbf{Y}^V(0,1)$, and $\mathbf{Y}^V(1,0)$ are the admittances of the three single veins calculated

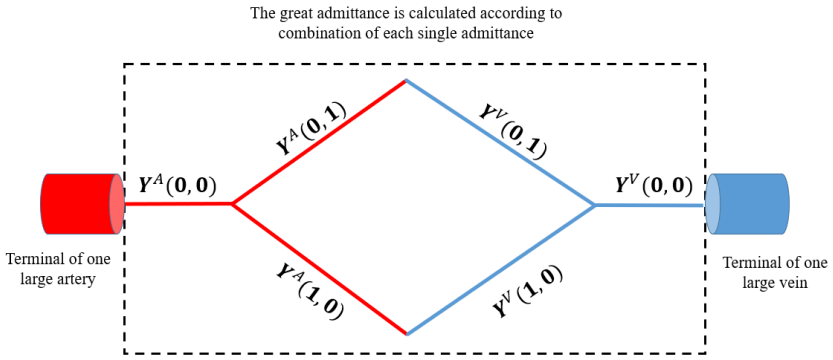

Figure 2.7: A schematic representation depicting the simplest structured tree that connects a large artery to a large vein. This structured tree consists of only a single bifurcation on the arterial side. Each vessel within the structured tree is assigned an index denoted as (i,j), which is utilised to determine its radius based on the expression $r_0^{\alpha^i\beta^j}$. Here, r_0 represents the bottom radius of the large artery, while α and β are scaling factors employed to adjust the radii of the two daughter vessels.

by Eq. (2.89) and Eq. (2.90), the symbols $\Leftrightarrow$ and $||$ represent how two vessels connect and calculated by Eq. (2.110) and Eq. (2.97), respectively. In this way, the recursive algorithm works for more complicated structured trees.

After the great admittance is computed, it serves as a linking condition to relate the frequency-domain transmural pressure $P_k^{TA}(L,t)$ and flow rate $Q_k^{TA}(L,t)$ at the outlet of a large terminal artery with frequency-domain transmural pressure $P_k^{TV}(0,t)$ and flow rate $Q_k^{TV}(0,t)$ at the inlet of a large terminal vein, i.e.

$$\begin{pmatrix} Q_k^{TA}(L) \\ Q_k^{TV}(0) \end{pmatrix} = \mathbf{Y}_k \begin{pmatrix} P_k^{TA}(L) \\ P_k^{TV}(0) \end{pmatrix}. \tag{2.112}$$

Using the convolution integral, the above equation in frequency domain can be transformed into two equations in real domain as

$$q^{TA}(L,t) = \frac{1}{T}\int_{-T/2}^{T/2}(P^{TA}(L,t-\tau)y_{11}(\tau) + P^{TV}(0,t-\tau)y_{12}(\tau))d\tau, \tag{2.113}$$

and

$$q^{TV}(0,t) = \frac{1}{T}\int_{-T/2}^{T/2}(P^{TA}(L,t-\tau)y_{21}(\tau) + P^{TV}(0,t-\tau)y_{22}(\tau))d\tau, \tag{2.114}$$

where $y_{11}(t), y_{12}(t), y_{21}(t), y_{22}(t)$ are the inverse Fourier transforms of the four components of the great admittance $\mathbf{Y}_k$, and T is the time of one cardiac cycle. These two equations give a matching boundary condition connecting the flow from the large arteries to the

large veins. One advantage of this matching condition is that it allows us to investigate the flow effects of the large veins (Qureshi, 2013), which is rarely a concern.

2.6 Boundary conditions and bifurcation conditions

The structured-tree matching condition enables us to avoid making assumptions about the flow at the outlet of the arteries, which is not the case for the original one-side blood flow model (Olufsen, 1998). However, boundary conditions are still required at the inlet of the large arteries and the outlet of the large veins. To simulate the coronary flow in the coronary circulation, we assume that the blood pressure at the inlet of the LMCA and RCA is the same as the aortic pressure, while the blood pressure at the outlet of the veins is the same as the pressure in the right atrium cavity. Hence, for the coronary flow model developed in this chapter, the aortic pressure, IMP, and pressure in the right atrium serve as boundary conditions.

The pressure gradient resulting from the aortic pressure and the pressure in the right atrium provides the driving force for the coronary circulation. In general, patient-specific aortic pressure varies with heart rate, health conditions, and age (Murgo et al., 1980; Denardo et al., 2010). In healthy subjects, normal aortic pressure ranges from 70.0 mmHg to 120.0 mmHg (Erbel et al., 2001; Reymond et al., 2012). The pressure in the right atrium normally ranges from 3.0 mmHg to 8.0 mmHg (Beigel et al., 2013; Lampert, 2018). IMP also significantly affects coronary blood flow. Specifically, during systole, an increase in IMP counteracts the driving force, that is, the pressure gradient within the vessels (Porter, 1898; Krams et al., 1989; Goodwill et al., 2011). Although the aortic pressure remains high during systole, the coronary flow in the coronary arteries can be impeded or even reversed due to high IMP (Gregg and Green, 1940), while the corresponding venous outflow increases. Chapter 4 provides further details about the IMP.

In this section, in the absence of sufficient experimental data, we adopt a lumped parameter heart model following Duanmu et al. (2019) to predict the aortic pressure and IMP of healthy subjects. These two parameters are closely related to the LV pressure which can be determined by (Avanzolini et al., 1988)

$$p_v^L(t) = \begin{cases} p_0^L \sigma(t) + E_v^L (V^L - V_0^L) + R_v^L \dot{V}^L & 0 < t < t_s \quad \text{(systole)}; \\ E_d^L (V^L - V_0^L) & t_s \le t < t_c \quad \text{(diastole)}, \end{cases} \tag{2.115}$$

where p_0^L is the peak isovolumetric pressure at the volume V_0^L, $\sigma(t) = 1 - \cos(2\pi t/t_s)$ is the activation function, $E_v^L = E_d^L + E_s^L \sigma(t)$ is the time-varying elastance, E_d^L is the diastolic passive elastance and E_s^L is the systolic passive elastance, t_s is the time at the

end of systole, t_c is the time at the end of diastole, V is the left ventricular volume, $\dot{V}^L$ is the rate of change in the left ventricular volume, and R_v^L is the resistance of ventricular myocardium. The lumped parameter heart model allows us to compute the LV pressure and aortic pressure for one cardiac cycle, which is 0.7 s. The computed LV pressure ranges from 5.1 mmHg to 125.2 mmHg, while the computed aortic pressure ranges from 71.6 mmHg to 120.6 mmHg, as shown in Fig. 2.8.

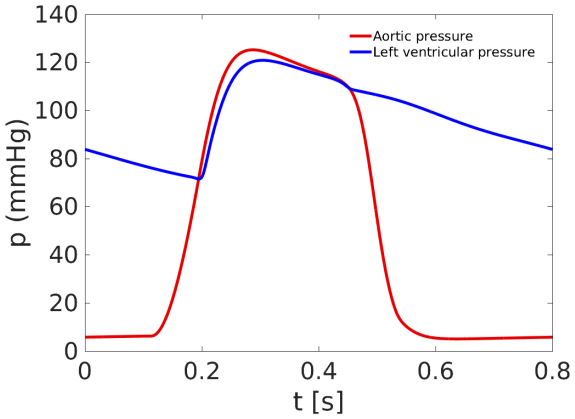

Figure 2.8: Assumed aortic pressure and left ventricular pressure calculated by a lumped parameter model (Avanzolini et al., 1988; Duanmu et al., 2019)

As the distribution of the IMP is related to the heart's contractile function and is not well known, computational heart models (Lee and Smith, 2012; Quarteroni et al., 2017; Kassab, 2019) have been used to determine the spatial and temporal distributions of the IMP. In Chapter 4, a computational LV model will be developed to obtain the IMP. However, in this chapter, to validate the coronary flow model, a homogeneous IMP assumption is made. The heart wall is divided into three regions: LV-free wall, RV-free wall, and septum. It is assumed that the IMP in each of the three regions is homogeneous and proportional to the LV pressure computed from the lumped heart model as

$$\text{IMP} = f_i^{\text{IMP}} \text{LVP}, \quad i = 1, 2, 3, \tag{2.116}$$

where $i = 1$ represents the LV-free wall, $i = 2$ represents the septum and $i = 3$ represents the RV-free wall, f_i^{IMP} is a ratio to be determined for each region, and LVP is the LV cavity pressure.

We assume that the IMP is the highest in the LV-free wall, which should be between the LV pressure (inner wall pressure) and the environment pressure (outer wall pressure) (Nematzadeh et al., 1984; Westerhof et al., 2006). Since the RV-free wall is much thinner than the LV-free wall and the RV pressure is much less than the LV pressure, usually within a range of 1/3 of the LV pressure, the IMP in the RV-free wall is much less than that of the LV-free wall. To reflect these observations, we assign the values $f_1^{\text{IMP}} = 1$, $f_2^{\text{IMP}} = 2/3$, and

$f_3^{\text{IMP}} = 1/3$ to the three regions, respectively. For the computational network shown in Fig. 2.1, the blood vessels LAD4, LCX3, MARG1, MARG2, and MARG3 perfuse the LV-free wall, the blood vessels LAD1 and LCX3 perfuse the septum, and the blood vessels PLA and PDA perfuse the RV-free wall. Accordingly, different structured trees are imposed with different IMPs based on the regions perfused by the large arteries. For example, all the small vessels in the structured tree connected to the LAD4 have an imposed IMP of $\text{IMP} = f_1^{\text{IMP}}\text{LVP}$. The values of f_i^{IMP} and the regions perfused by the large arteries are summarised in Table 2.3.

Table 2.3: Large arteries responsible for perfusing the LV-free wall, septum, and RV-free wall. Additionally, the ratio f_i^{IMP} is introduced to determine the homogeneous intramyocardial pressure (IMP) within these three regions based on the left ventricular pressure.

Location	Perfusing large arteries	f_i^{IMP}
LV-free wall	LAD3, LAD4, MARG1, MARG2, MARG3	$f_1^{\text{IMP}} = 1$
Septum	LAD1, LCX3	$f_2^{\text{IMP}} = 2/3$
RV-free wall	PLA, PDA	$f_3^{\text{IMP}} = 1/3$

Assuming that there is no energy dissipation at each bifurcation of the large vessels in a network, the flow rate and pressure of a parent vessel and its' two daughter vessels satisfy the two bifurcation conditions

$$q_p(L,t) = q_{d1}(0,t) + q_{d2}(0,t), \tag{2.117}$$

and

$$p_p(L,t) = p_{d1}(0,t) = p_{d2}(0,t). \tag{2.118}$$

Finally, the blood flow at any given point in the computational network shown in Fig. 2.1 can be determined by solving Eq. (2.17), Eq. (2.33), and Eq. (2.34), given the inlet and outlet pressure boundary conditions, the IMP, the bifurcation conditions, and the structured-tree matching conditions.

The formulation and method presented in the previous sections have been implemented in C++ and Fortran codes. The code was initially developed by Olufsen et al. (2000) for systemic circulation and later extended by Qureshi and Hill (2015) to include the structured-tree matching conditions for modelling pulmonary circulation. While Duanmu et al. (2019) used the structured-tree model for modelling coronary circulation, they did not include the venous side as Qureshi and Hill (2015) did. Additionally, the IMP in their study was added as a boundary condition for the terminal arteries, which is distinct from our approach. It should be noted that modelling the coronary circulation is different

from modelling the other two circulations because the time-varying IMP has a substantial impact on coronary flow patterns.

2.7 Validation and results of the coronary flow model

In this section, the simulated results of the coronary flow model are presented. As mentioned in Section 2.6, the assumed boundary conditions, including aortic pressure, right atrium pressure, and IMP, are adopted for the simulation.

2.7.1 Validation

To validate the simulated results from the coronary blood flow model, we first take the blood vessel LAD2 for example to show the convergence and periodicity of its pressure and flow rate, and then, we compare the simulated pressures and flow rates in three main branches, i.e. LCX, LAD, and RCA, with published data.

Since the periodic pressure boundary conditions are used and the structured tree model has the ability to preserve wave propagation, stable and periodic numerical solutions are expected. The simulated flow rate and pressure at the midpoint of the LAD2 during the first five periods are shown in Fig. 2.9. At the beginning of the first cycle, the flow rate and pressure are set to be initial values, then they fluctuate during the time 0.0 s to 0.1 s. Quickly, they begin to be stable after the time 0.1 s. After the first cycle, the flow rate profiles and the pressure profiles are overlapping. It can be clearly observed that the flow rate and pressure are stable and periodic after the second cycle. To further quantify the convergence of the solution, the mean squared error of the solutions is defined as

$$\epsilon^2 = \frac{1}{n}\sum_{i=1}^{n}(S_j(i) - S_5(i))^2, \quad j = 1,2,3,4,5, \tag{2.119}$$

where S_j is the solutions in one cycle, S_5 is the reference solutions in the 5th period which is sufficiently stable, and n is the total number of the temporal discretization points in one cycle. As shown in Fig. 2.9 (b), the mean squared error ϵ^2 of the flow rate at the second cycle is less than 1×10^{-3} which can be chosen as a cut-off value. The mean squared error declines steadily in the following cycles. Similarly, the mean squared error of the pressure in Fig. 2.9 (d) is less than the cut-off value after the second cycle. Therefore, solutions in the third cycle are considered sufficiently stable. To reduce computational time, subsequent analyses will focus on the simulated solutions from the third cycle.

We now compare the simulated pressures and flow rates in the three main branches (LAD, LCX, RCA) with experimental data provided by Duanmu et al. (2019). As shown in Fig. 2.10, the simulated results and the experimental data are overall comparable. A perfect match between the simulated results and the experimental data is not our aim

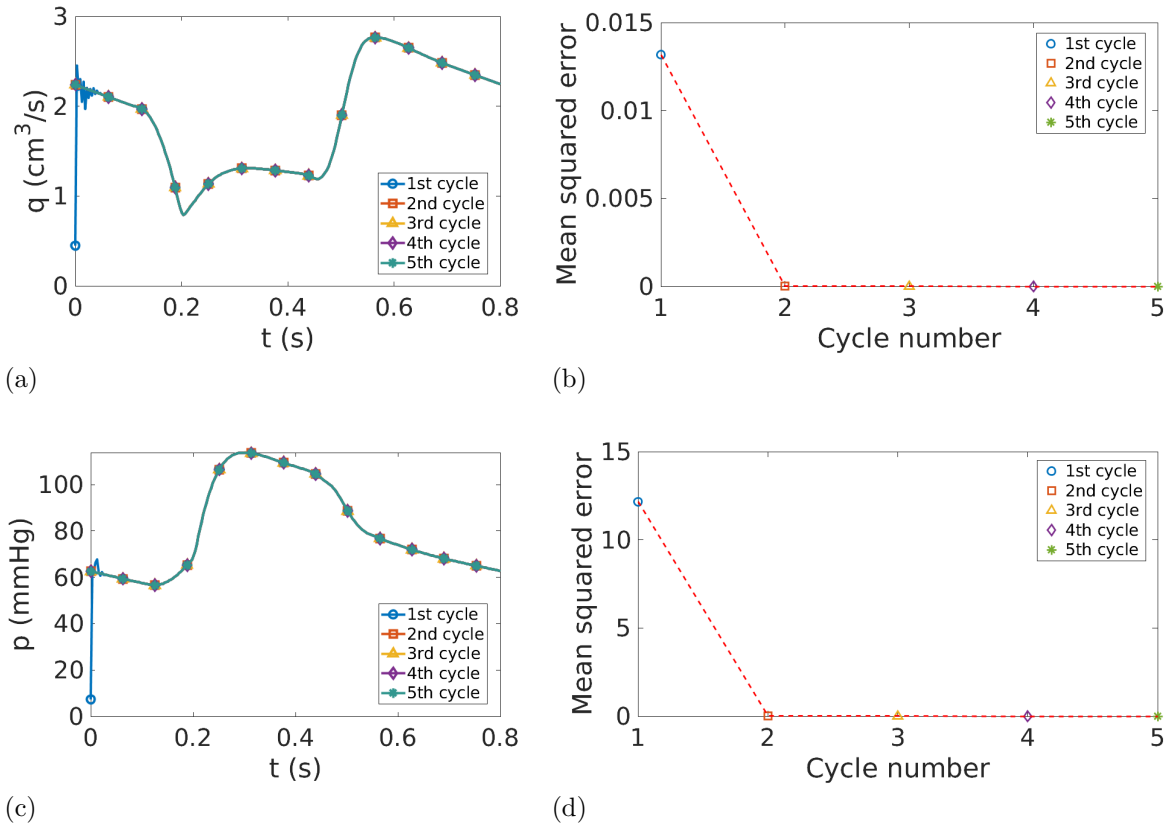

Figure 2.9: Flow rate profiles (a) and pressure profiles (c) at the midpoint of the blood vessel LAD2 in the first five cardiac cycles. Mean squared error calculated by Eq. (2.119) of the flow rates (b) and the pressures (d). The solution in the 5th period is used as a reference.

here. Although we employ the accurate geometries of the epicardial arteries, the geometries of the epicardial veins are assumed and simplified structured trees are utilised to imitate realistic vessel networks within the heart wall. Therefore, our emphasis lies on the magnitude of the values and the flow characteristics of the simulated coronary flow. In Fig. 2.10 (a-f), two y-axes are used to display the IMP profiles, with its axis located on the left side. This is done to enable the direct observation of the effect of the IMP. The maximum IMP values for the LCX, LAD, and RCA are 125.2 mmHg, 82.6 mmHg, and 41.3 mmHg, respectively, due to the utilisation of distinct IMP factors for each vessel, as listed in Table 2.3.

As shown in Fig. 2.10 (a), the simulated pressure at the midpoint of the LCX is from 51.1 mmHg to 113.2 mmHg. The experimental LCX pressure is from 59.6 mmHg to 105.3 mmHg. The minimum values of both the simulated and the experimental pressures are attained near the beginning of the systole which is about 0.12 s, while their maximum values are reached in the middle of the systole which is about 0.26 s. As shown in Fig. 2.10 (b), our simulated LCX flow is from 0.1 cm^3/s to 2.07 cm^3/s. The experimental LCX flow is from 0.82 cm^3/s to 1.81 cm^3/s. During systole (0.12 s - 0.49 s), the IMP is

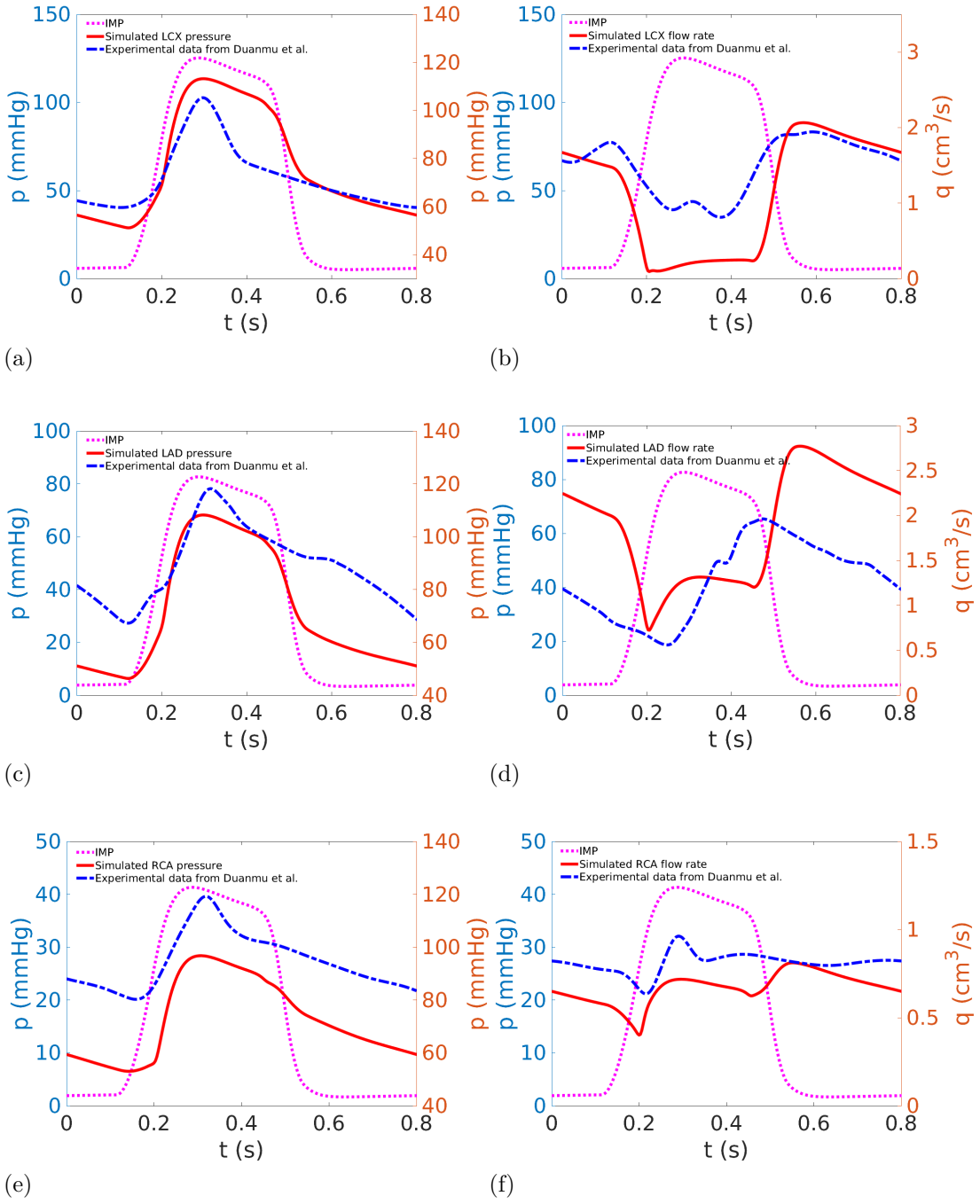

Figure 2.10: In one cardiac cycle, our simulated pressures and flow rates (red solid profiles) are compared with experimental data (blue dashed profiles) from Duanmu et al. (2019). The top two figures show the pressure (a) and flow rate (b) at the midpoint of the LCX, the middle two figures show the pressure (c) and flow rate (d) at the midpoint of the LAD, and the bottom figures show the pressure (e) and flow rate (f) at the midpoint of the RCA. All figures have two y-axes, with the left y-axis indicating the intramyocardial pressure (IMP), which serves as a phase indicator in one cardiac cycle. Note that the IMPs for different branches - LCX, LAD, and RCA are different. The right y-axis is for the simulated and experimental pressures and flow rates.

dominant and the flow in the LCX is reduced significantly both from the experimental measurements and our simulated results. However, the occurrence of the minimum flow in the LCX at 0.21 s is not concurrent with the peak value of the IMP at 0.28 s.

Pressures and flow rates in the LAD are similar to that in the LCX as shown in Fig. 2.10 (c, d). The simulated pressure at the midpoint of the LAD is from 46.4 mmHg to 108.2 mmHg, which is comparable to the experimental LAD pressure from 67.3 mmHg to 118.2 mmHg. As shown in Fig. 2.10 (d), our simulated LAD flow is from 0.73 cm^3/s to 2.77 cm^3/s, also comparable to the experimental LAD flow from 0.56 cm^3/s to 1.96 cm^3/s. Although the simulated LAD pressure is lower than the simulated LCX pressure, the flow in the LAD exceeds that in the LCX. This difference is a result of the impact of the IMP because the peak IMP on the LCX is 51.6% higher than that on the LAD. Another noticeable difference between the flow in the LCX and the LAD is that the peak in the flow of the LCX is more flattened compared to that in the LAD.

For the RCA, as shown in Fig. 2.10 (e), our simulated pressure at the midpoint of the RCA is from 53.1 mmHg to 96.8 mmHg, while the experimental RCA pressure is from 80.3 mmHG to 119.3 mmHg. The peak pressure from the simulation is found to be 18.9% less than the corresponding peak pressure obtained from the experimental data. Similarly, the minimum pressure from the simulation is 33.9% lower than the minimum pressure recorded in the experimental data. This deviation can be attributed to the location from which the data is obtained because the midpoint of the RCA is located at a considerable distance from the aorta and the RCA is the longest blood vessel in our simulation with a length of 10.9 cm. However, the exact location of the experimental RCA pressure is not provided by Duanmu et al. (2019). Additionally, the location has an impact on the flow rate. As shown in Fig. 2.10 (f), our simulated RCA flow is from 0.40 cm^3/s to 0.82 cm^3/s, while the experimental LAD flow is from 0.64 cm^3/s to 0.96 cm^3/s. The peak flow rate from the experimental data occurs during systole. However, in the simulated RCA flow rate profile, the peak flow rate occurs during diastole. This can also be caused by the inaccuracy of the IMP. If we reduce the IMP on the RCA, the peak flow rate occurs during diastole in our further simulations.

2.7.2 Further analysis of the simulations

The pressures and flow rates in the coronary vessels exhibit a pulsatile pattern as a result of the cyclical contraction and relaxation of the heart. In general, the flow rates in the left-side coronary arteries display maximum values during diastole and minimum values during systole (Goodwill et al., 2011; Kassab, 2019). Furthermore, the pressures and flow rates in the coronary arteries vary depending on several factors such as vessel geometry, cardiac function, and the presence of stenosis or occlusion.

In this section, we first present the variations of the pressures and flow rates along

a single vessel, using the RCA as an illustration. Subsequently, we plot the pressures and flow rates at the midpoints of various blood vessels. As shown in Fig. 2.11, we show the pressures and flow rates at five equidistant points (positions 1-5) along the RCA. Position 1 is the proximal point and position 5 is the distal point. The pressures along the RCA decrease from the proximal point to the distal point. At position 5, the maximum pressure is 74.1 mmHg, which is 38.6% lower than the maximum pressure at position 1 (120.6 mmHg). Additionally, the minimum pressure at position 5 is 33.1 mmHg, indicating a drop of 53.8% compared to the minimum pressure at position 1 (71.6 mmHg). The blood flow in RCA is driven by such pressure gradient and thus, despite the significant decline in pressures along the RCA, the flow rates display relatively minimal variations, especially during diastole. However, the difference in the flow rates at different positions is noticeable during systole. At position 1, the maximum flow rate occurs during systole which agrees with the experimental observations (Goodwill et al., 2011). A noteworthy finding is that during the first half of systole, the flow rate at position 1 surpasses that at the other positions, but during the second half of systole, it falls below the flow rate at the other positions. This phenomenon might be explained by the forward and backward wave propagations. Specifically, in the first half of systole, the forward wave dominates the flow at position 1, which is located at the proximal portion of the RCA, making it the highest compared to other positions. Conversely, flow at position 5, situated at the distal portion of the RCA, is the lowest. However, during the second half of systole, the backward wave resulting from the IMP becomes dominant, resulting in the flow at position 5 reaching its peak and flow at position 1 reaching its lowest.

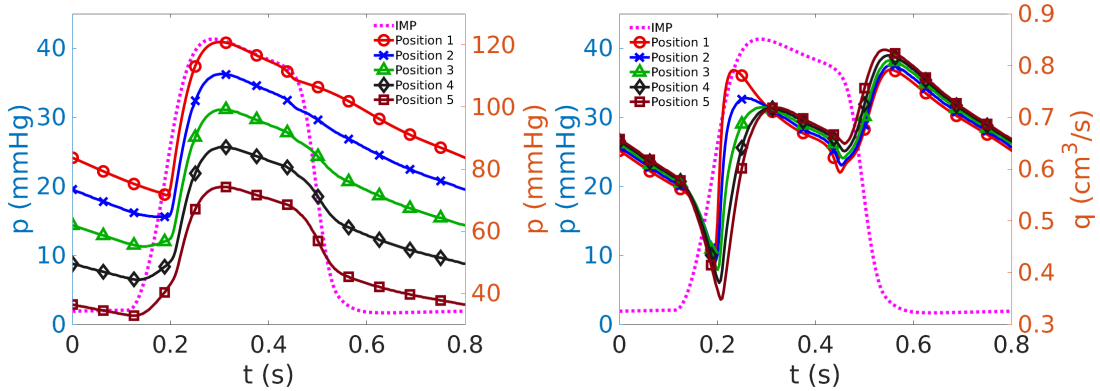

(a) (b)

Figure 2.11: Pressures (a) and flow rates (b) at five equidistant points (positions 1-5) along the RCA. Position 1 is the proximal point and position 5 is the distal point. The intramyocardial pressure (IMP) is plotted as a phase indicator of the cardiac cycle.

Let us now examine the variations of the pressures and flow rates at the midpoints of all the epicardial arteries. Recalling that the entire LCX branch includes the blood vessels

LCX, MARG1, LCX1, MARG2, LCX2, MARG3, and LCX3; the entire LAD branch encompasses the blood vessels LAD, LAD1, LAD2, LAD3, and LAD4; And the entire RCA branch consists of the blood vessels RCA, PLA, and PDA.

Firstly, the pressures and flow rates of the blood vessels in the entire LCX branch are shown in Fig. 2.12 (a, b). Within one cardiac cycle, the pressure within the LCX exhibits the highest values, while the pressure in the LCX3 exhibits the lowest values. This result is rational given that the LCX, as the first branch of the entire LCX branch and its proximity to the aorta, would display higher pressure values. Conversely, the LCX3, being the last branch in the entire LCX branch and situated at a distance from the aorta, would exhibit lower pressure values. The simulated pressures in the other blood vessels fall within the range of pressures observed in both the LCX and LCX3. The minimum pressure in the LCX (51.2 mmHg) shows a decrease of 28.5% compared to the minimum pressure in the aorta, which is 71.6 mmHg as shown in Fig. 2.8. Moreover, the minimum pressure in the LCX3 is 15.4 mmHg, representing a decline of 78.5% in comparison to the minimum pressure in the aorta. Furthermore, the maximum pressure in the LCX (113.2 mmHg) shows a decrease of 6.1% compared to the maximum pressure in the aorta, which is 120.6 mmHg. The maximum pressure in the LCX3 (95.1 mmHg) represents a decline of 21.1% in comparison to the maximum pressure in the aorta. Thus, the presence of the IMP influences the pressure distribution in the entire LCX branch, resulting in a smaller pressure drop during systole as compared to diastole.

With respect to the flow rates of all the vessels in the entire LCX branch, it is observed that during systole (from 0.15 s to 0.45 s), the LCX3 displays the highest values, while the MARG3 displays the lowest flow rates. Note that all vessels exhibit lower flow rates in systole except the LCX3. This phenomenon of the LCX3 having higher flow rates in systole than in diastole is in contrast to the typical flow pattern observed in the coronary circulation (Goodwill et al., 2011). This deviation is attributed to the IMP applied to the LCX3 and its neighboring vessel, i.e. the MARG3, with the magnitude of the IMP on the structured tree connected to the LCX3 being comparatively lower. Consequently, the regional IMP imposed on a single structured tree has not just a localised effect on the vessel it is linked to but also influences blood flow in adjacent vessels.

Secondly, the pressures and flow rates of the blood vessels in the entire LAD branch are shown in Fig. 2.12 (c, d). During diastole, according to the distance to the aorta, the pressure within the LAD exhibits the highest values, while the pressure in the LAD3 exhibits the lowest values. The simulated pressures in the remaining blood vessels fall within the range of pressures in both the LAD and LAD3. The minimum pressure in the LAD is 51.2 mmHg, representing a decrease of 28.5% in comparison to the minimum pressure in the aorta. The minimum pressure in the LAD3 is 11.5 mmHg, a decline of 83.9% in comparison to the minimum pressure in the aorta. The maximum pressure in

the LAD is 108.2 mmHg, representing a decrease of 10.3% in comparison to the maximum pressure in the aorta. The maximum pressure in the LAD3 is 110.6 mmHg, a decline of 8.3% in comparison to the maximum pressure in the aorta. The pressure drop along the entire LAD branch is similar to that along the entire LCX branch. It should be noted that during systole, the LAD3 pressure experiences the greatest increase and reach the highest values since both the LAD3 and the LAD4 are connected to structured trees imposed with the highest IMPs.

In terms of flow rates of all the vessels in the entire LAD branch, as shown in Fig. 2.12 (d), the LAD and LAD1 exhibit higher values, while the LAD2, LAD3, and LAD4 display lower flow rates. The flow rates in all blood vessels are impeded during systole. Furthermore, the flow rates in the LAD and LAD1 are significantly greater than those in the other vessels because the LAD and LAD1 are the trunk vessels of the entire LAD branch, whereas the remaining vessels are terminal vessels.

Thirdly, the pressures and flow rates of the blood vessels in the entire RCA branch are shown in Fig. 2.12 (e, f). The entire RCA branch is comparatively less complex than the LCX and LAD branches, as it consists of only three vessels. The minimum pressure in the RCA is 53.1 mmHg, representing a decrease of 25.8% in comparison to the minimum pressure in the aorta. The minimum pressure in the PLA is 16.2 mmHg, reflecting a decline of 77.4% in comparison to the minimum pressure in the aorta. In the meanwhile, the maximum pressure in the RCA is 96.4 mmHg, representing a decrease of 20.1% in comparison to the maximum pressure in the aorta. The maximum pressure in the PLA is 56.0 mmHg, reflecting a decline of 53.6% in comparison to the maximum pressure in the aorta. The lowest IMP values applied to the structured trees connected to the PLA and PDA result in the largest drop in the maximum pressure from the aorta to the terminal vessels in the entire RCA branch during systole, compared to the drop observed in the LCX and LAD branches. It can also be found that the pressure waveforms in the PLA and PDA during a single cardiac cycle are almost overlapping. However, it must be noted that the flow rates in the two vessels differ significantly. During one cardiac cycle, the flow rate in the PLA is higher than that in the PDA. This can be attributed to the larger radius of the PLA compared to that of the PDA.

In summary, the pressures in the entire LCX, LAD, and RCA branches remain high during systole and low during diastole. Furthermore, the pressure drop during systole is markedly lower than that during diastole due to the influence of the IMP on coronary flow. In contrast, flow rates in these branches exhibit an inverse trend, with low flow rates during systole and high flow rates during diastole, which is consistent with the flow patterns frequently seen in experiments and clinics (Goodwill et al., 2011; Kassab, 2019). This inverse pattern is also caused by the presence of the IMP.

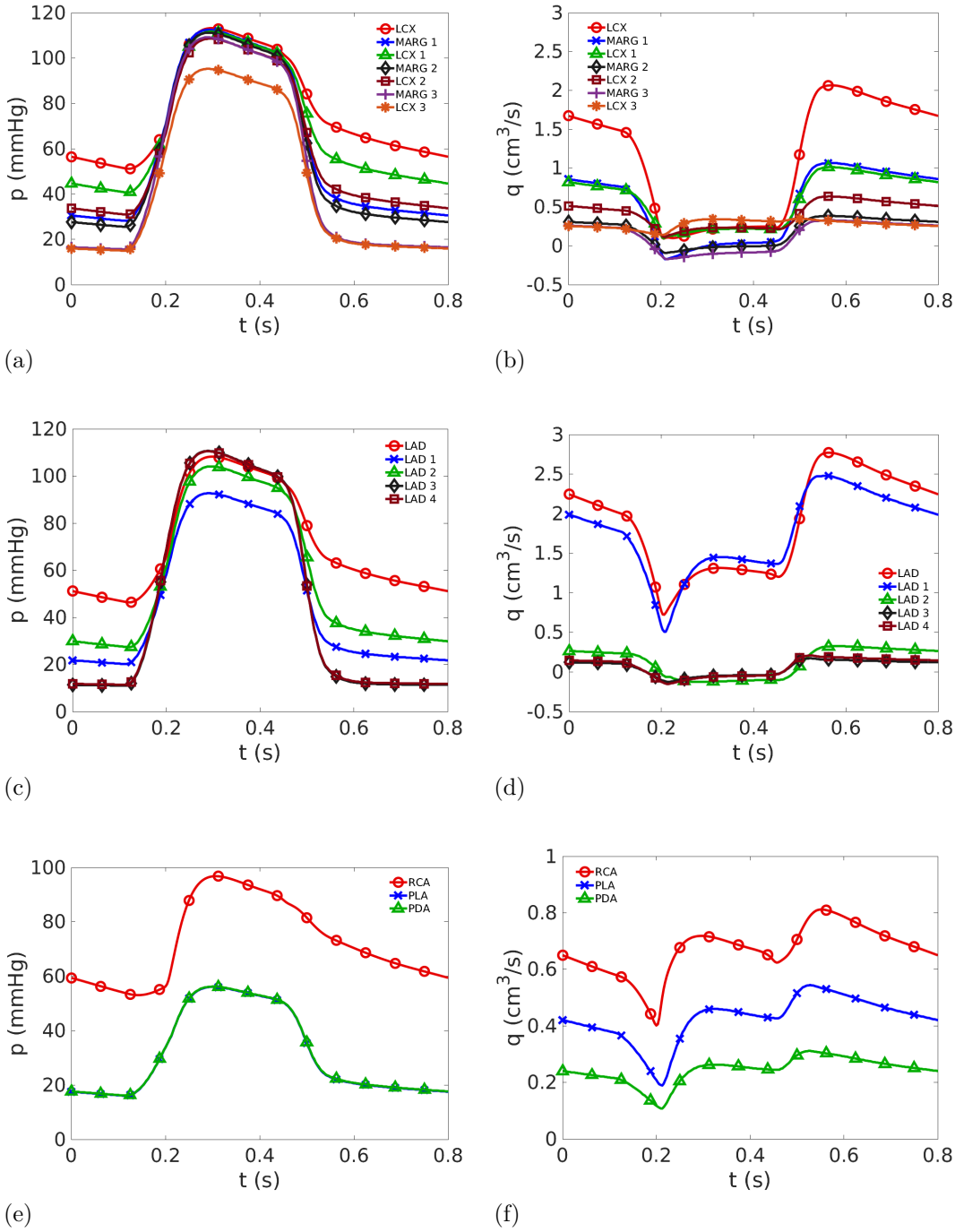

Figure 2.12: The top two figures show the pressures (a) and flow rates (b) at the midpoints of different blood vessels in the entire LCX branch; The middle two figures show the pressures (c) and flow rates (d) at the midpoints of different blood vessels in the entire LAD branch; And the bottom two figures show the pressures (e) and flow rates (f) at the midpoints of different blood vessels in the entire RCA branch.

2.8 Summary

In this chapter, the formulation and simulated results of a coronary flow model have been presented. A simplified network was constructed using patient-specific geometries of human coronary arteries (Duanmu et al., 2019), binary structured trees representing intramyocardial blood vessels, and a symmetrical venous side. The structured-tree model developed by Olufsen (1998); Vaughan (2010); Qureshi (2013) was modified to incorporate the effects of time-varying IMP on coronary flow. Assumed aortic pressure and IMP were adopted for preliminary validation of the model. The solution to this model was achieved using proprietary programs written in C++ and Fortran. Simulations of pressures and flow rates at any position within the simplified computational network are available. Section 2.7 presents detailed results including pressure and flow rate profiles in different coronary arteries.

The aim of this chapter was to develop a reliable coronary flow model for simulating pressures and flows within the coronary arteries. The governing equations for blood flow in both large and small vessels have been employed in systemic and pulmonary circulations. However, the key distinction of coronary circulation from the other two circulations lies in the important role played by the IMP, leading to a reversed flow pattern compared to that in the systemic and pulmonary circulations. Therefore, the effect of the time-varying IMP on the coronary flow was introduced in this chapter in the structured-tree matching conditions. The simulated pressures and flows in the computational network can reach periodic and convergent states. Furthermore, the pressures and flow rates simulated by the coronary flow model in the three main coronary blood vessels (LCX, LAD, and RCA) were comparable with experimental data.

In addition, we have presented the variations in pressure and flow rate along the longest vessel, the RCA, as well as in various vessels. In the RCA, the pressure profile in one cardiac cycle at the proximal end exhibited the largest values while the pressure profile at the distal end displayed the lowest values. There was a noticeable pressure drop along the RCA. However, the variation in flow rates along the RCA was relatively minor, particularly during diastole. Furthermore, the pressures and flow rates of all vessels in the three branches (LCX, LAD, and RCA) were analysed. The magnitude of the IMP had a significant effect on the pressure and flow rate distribution in the three branches. As for the pressure distribution, due to the presence of the IMP, the pressure drop along the three branches was much smaller during systole than diastole. For instance, during systole, the pressure in the distal vessel LAD4 was even higher than the pressure in the corresponding proximal vessel. As for the flow rate distribution, flow rates in all vessels in the three branches were impeded during systole due to the IMP, except for flow rates in the LCX3. Typically, the larger the IMP on the structured tree, the greater the impediment to flow in the vessel connecting the structured tree.

In conclusion, the results of the coronary flow model developed in this chapter are in agreement with experimental data, which provides confidence in further predictions. This coronary flow model offers valuable insights into the mechanisms of coronary circulation, however, it is crucial to acknowledge its limitations. Firstly, the assumption of a proportional relationship between the IMP and LV pressure in the three regions lacks sufficient evidence in the literature. To address this issue, a computational LV model will be introduced in the next chapter to calculate the time-varying IMP. Secondly, the simplification of the intramyocardial blood vessels as binary structured trees and the assumption of symmetrical epicardial veins can not take into account anatomical details and may lead to inaccuracies in simulations. Therefore, in Chapter 4, we will further incorporate details about the structure of the coronary venous system.

Chapter 3

Mathematical modelling of the cardiac dynamics of the left ventricle in a complete cardiac cycle

The use of computational heart models has been a long-term endeavour within the biomedical engineering community. They are important tools for understanding the healthy and diseased functions of the heart. This chapter will introduce the formulation, implementation, and simulated results of an ABAQUS human left ventricle (LV) model. Our focus is to set up an advanced LV model that provides realistic boundary conditions for the coronary flow model as described in the last chapter to establish more accurate predictions of coronary flow. This LV model is built on previous studies by Guan et al. (2020b). In this chapter, we first describe the framework of the LV model, followed by the details of the governing equations of the deformation of the LV. The Holzapfel and Ogden (HO) model (Holzapfel and Ogden, 2009) is employed for describing the passive material property of the myocardium, and a well-established time-varying elastance model is adopted for describing the active force generated by the myofibres during systole. Boundary conditions and implementation of the LV model are presented in section 3.3. In section 3.4, we summarise the results of the LV model with a focus on the pressure and volume of the LV in one cardiac cycle as well as stress distribution in the LV wall. In the last two sections, we investigate the effects of myofibre rotation and myofibre dispersion on the LV cardiac pump functions, which are extended contents.

3.1 A finite element model of the human left ventricle (LV)

There have been a number of ABAQUS models for simulating and predicting the mechanical behaviour of the heart (Wang et al., 2013; Baillargeon et al., 2014; Sack et al., 2018; Guan et al., 2020b). Wang et al. (2013) developed a finite element (FE) human LV model that implemented the passive material model proposed by Holzapfel and Ogden (2009) along with a rule-based myofibre structure. The diastolic functions of the LV were investigated. Their model was compared to similar models with different constitutive models and demonstrated differences in stress and strain distributions. Baillargeon et al. (2014) developed a computational model (the living heart project) to simulate the behaviour of a human heart with all four chambers in a whole cardiac cycle. During systole, an active stress component is added to the total Cauchy stress by a phenomenological representation of active contraction (Guccione and McCulloch, 1993; Guccione et al., 1993; Walker et al., 2005; Göktepe and Kuhl, 2010). In addition, they adopted a lumped parameter system to provide a natural coupling of pressures between the four chambers. Their simulated long-axis shortening and pressure-volume loops agreed well with clinical observations. Moreover, Sack et al. (2018) constructed and validated subject-specific biventricular swine heart models in healthy and diseased states. Their simulated stroke volume, ejection fraction, and strains agreed well with experimental data. Furthermore, reference stress and strain values at multiple time points in one cardiac cycle were reported in their study. Using a bi-ventricular porcine heart model, Guan et al. (2020b) found that the sheet-normal active contraction enhanced the ventricular contraction. Reviews on cardiac modelling can be found in (Quarteroni et al., 2017; Mangion et al., 2018; Peirlinck et al., 2021).

To simulate realistic deformation of the LV, we have developed the following ABAQUS LV model. A schematic diagram of the LV model adopted in this chapter is shown in Fig. 3.1 (c), which consisted of a patient-specific LV geometry, a commonly used myofibre architecture, and a lumped parameter model to represent the systemic circulation. The three-dimensional (3D) human LV geometry was adopted from previous studies in our group (Gao et al., 2017; Guan et al., 2021), as shown in Fig. 3.1 (a). This geometry was reconstructed from short-axis slices from the LV base to the LV apex and three long-axis slices obtained from cardiovascular magnetic resonance (CMR) scans of a healthy volunteer. Details of the reconstruction are referred to Gao et al. (2017).

The FE method has proven to be a valuable tool in the solution of computational models due to its ability to solve partial differential equations over complex geometric domains, making it well-suited for investigating the mechanical performance of the heart. In order to apply the FE method for computation of the deformation of the LV geometry during multiple cardiac cycles, the LV geometry is further discretised into a tetrahedral

mesh consisting of 133,042 elements and 26,010 nodes. Based on the tetrahedral mesh, a rule-based myofibre structure (Bayer et al., 2012; Wong and Kuhl, 2014) is generated. As shown in Fig. 3.1 (b), the myofibre angle varies from $-60°$ at the epicardium to $60°$ at the endocardium. This myofibre rotation angle is widely used in the literature (Wang et al., 2013; Gao et al., 2014; Guan et al., 2022c).

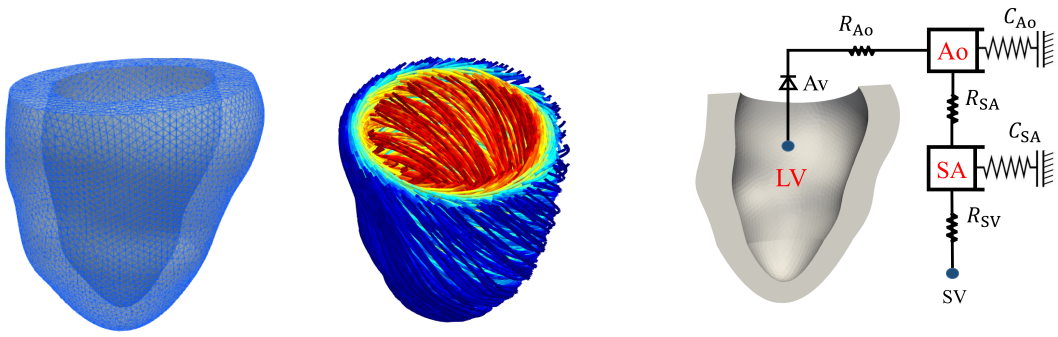

(a) (b) (c)

Figure 3.1: Components of the left ventricle (LV) model. Figure (a) shows the tetrahedral mesh employed to represent the LV wall. The mesh consists of 133,042 linear elements and 26,010 nodes. Figure (b) illustrates a rule-based myofibre structure attached to the LV wall, with the myofibre angle ranging from $-60°$ at the epicardium to $60°$ at the endocardium. In Figure (c), a lumped parameter model is interconnected with the LV cavity, which includes the aorta (Ao), systemic arteries (SA), systemic veins (SV), and aortic valve (Av). The aortic valve is symbolised by the Diode symbol, representing unidirectional flow. The resistances R_{Ao}, R_{SA}, and R_{SV} are associated with the aortic valve, systemic arteries, and trivial resistance allowing drainage of the flow in the systemic circulation, respectively. The compliances C_{Ao} and C_{SA} represent the aortic and systemic arterial compliances, respectively.

The LV cavity pressure is important for determining the deformation of the LV. In this LV model, as shown in Fig. 3.1 (c), a simplified open-loop lumped parameter system representing the systemic circulation is coupled to the LV cavity to provide a physiologically accurate LV cavity pressure. The open-loop lumped parameter system is simpler in that it only focuses on the pressure within the LV cavity and the pressure in the aorta. This simplicity makes the open-loop system easier to calibrate and validate. However, the limitations of this approach include the lack of consideration for the flow conservation between the heart and the circulatory system. On the other hand, closed-loop lumped parameter systems (Baillargeon et al., 2014; Guan et al., 2020b) consider the dynamic exchanges between the heart and the circulatory system, providing a more comprehensive representation of the cardiovascular system. However, closed-loop systems need more heart chamber representations and more compliances and resistances to calibrate. Ultimately, the choice between open-loop and closed-loop lumped parameter systems will

depend on the specific research question and the level of detail required in the computational model. Nevertheless, this type of lumped parameter system corresponds to a two-element Windkessel model (Westerhof et al., 2009).

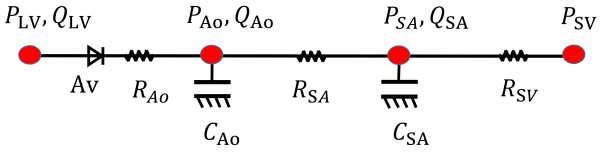

Figure 3.2: Schematic diagram of the lumped parameter system to represent the systemic circulation. LV is the left ventricle. Ao is the aorta. SA is the systemic arteries. SV is the systemic veins. The aortic valve is represented by the Diode symbol to ensure the unidirectional flow. R_{Ao} is the aortic valve resistance and R_{SA} is the resistance of the systemic arteries. R_{SV} is a trivial resistance allowing drainage of the flow in the systemic circulation. C_{Ao} is the aortic compliance and C_{SA} is the compliance of the systemic arteries.

The electrical analog of the lumped parameter system is shown in Fig. 3.2. We consider three cavities: the LV cavity, the aorta (Ao) cavity, and a third cavity representing the systemic arteries (SA). The systemic veins (SV) serve as a boundary condition, which is given a constant pressure of 8 mmHg (Guyton et al., 1954). The compliances of the three cavities are represented by capacitors, and the resistances between the cavities are represented by resistors.

The lumped parameter system is implemented in ABAQUS using the surface-based fluid cavity modulus and the fluid exchanges modulus (Documentation and Manual, 2014). Briefly, each cavity is simplified as a cubic fluid cavity with one face fixed and the opposite face attached to a linear-elastic spring, as shown in Fig. 3.1 (c). If we assume that the spring is along the x-axis, the face attached to the spring is restricted to move only in the x-axis direction. Let the stiffness of the linear spring be k, and the area of one face of the cube be $\tilde{A}$. By ignoring the inertia effect and applying the force balance condition to the face attached to the spring at the current time t_{c}, we have

$$P_{t\mathrm{c}}\,\tilde{A} = k\Delta x_{t\mathrm{c}} \quad \text{and} \quad V_{t\mathrm{c}} = V_0 + \Delta x_{t\mathrm{c}}\tilde{A}, \tag{3.1}$$

where $P_{t\mathrm{c}}$ is the fluid cavity pressure at the current time t_{c}, $\Delta x_{t\mathrm{c}}$ is the displacement that the spring has been compressed, $V_{t\mathrm{c}}$ is the fluid cavity volume at the current time t_{c}, and V_0 is the initial fluid cavity volume. Considering a small time interval Δt, the pressure

and volume of the cube at the next time step ($t_{\mathrm{n}} = t_{\mathrm{c}} + \Delta t$) are

$$P_{t\mathrm{n}}\tilde{A} = k\Delta x_{t\mathrm{n}}, \quad V_{t\mathrm{n}} = V_0 + \Delta x_{t\mathrm{n}}\tilde{A}. \tag{3.2}$$

Thus, the volume change of the cube during Δt is

$$dV = (V_{t\mathrm{n}} - V_{t\mathrm{c}})/(t_{\mathrm{n}} - t_{\mathrm{c}}), \tag{3.3}$$

which can be rewritten as

$$dV = \frac{\Delta x_{t\mathrm{n}} - \Delta x_{t\mathrm{c}}}{t_{\mathrm{n}} - t_{\mathrm{c}}}\tilde{A}. \tag{3.4}$$

By substituting $\Delta x_{t\mathrm{n}} - \Delta x_{t\mathrm{c}} = (P_{t\mathrm{n}} - P_{t\mathrm{c}})\,\tilde{A}/k$ into the above equation, we have

$$dV = \frac{P_{t\mathrm{n}} - P_{t\mathrm{c}}}{t_{\mathrm{n}} - t_{\mathrm{c}}}\frac{\tilde{A}^2}{k}. \tag{3.5}$$

When $\Delta t = t_{\mathrm{n}} - t_{\mathrm{c}} \to 0$, Eq. (3.5) is

$$dV = \tilde{C}\frac{\mathrm{d}P}{\mathrm{d}t}, \tag{3.6}$$

where $\tilde{C} = \tilde{A}^2/k$ is the compliance of the fluid cavity.

According to (Documentation and Manual, 2014), the flow between any two connected cavities is driven by

$$\Delta pA = C_v\dot{m} + C_H\dot{m}|\dot{m}|, \tag{3.7}$$

where Δp is the pressure difference between the two connected cavities, A is the effective area of the fluid exchange, C_v is the viscous resistance coefficient, $\dot{m}$ is the mass flow rate, and C_H is the hydrodynamic resistance coefficient. The hydrodynamic resistance coefficient (C_H) was set to 0. Let ξ be the blood density, we have

$$\dot{m} = \xi\, Q_{c\to c+1}, \tag{3.8}$$

where $Q_{c\to c+1}$ is the flow rate from the first cavity (c) to the next cavity ($c+1$). Eq. (3.7) can now be rewritten as

$$\Delta p\, A = C_v\, \xi\, Q_{c\to c+1}, \tag{3.9}$$

that is

$$Q_{c\to c+1} = \frac{\Delta p}{\xi C_v/A}, \tag{3.10}$$

which means that the fluid exchange between any two connected cavities corresponds to a resistor in the Windkessel model, and the resistance can be calculated as $R = \xi C_v/A$.

Thus, by using the surface-based fluid cavity modulus in ABAQUS, the pressures

(P_{LV}, P_{Ao}, P_{SA}) and volumes (Q_{LV}, Q_{Ao}, Q_{SA}) of the three cavities, as shown in Fig. 3.2, can be determined by following relationship. Derivative of the flow rate in each cavity is

$$\frac{\mathrm{d}Q_e}{\mathrm{d}t} = C_e \frac{\mathrm{d}P_e}{\mathrm{d}t}, \tag{3.11}$$

where $e = \{\mathrm{LV}, \mathrm{Ao}, \mathrm{SA}\}$, C_e is the compliance of each cavity. The flow rate between any two neighboring cavities is driven by

$$Q_{e\to e+1} = \frac{\Delta P_{e\to e+1}}{R_{e\to e+1}}, \tag{3.12}$$

where $\Delta P_{e\to e+1}$ is the pressure difference between the two connected cavities, $R_{e\to e+1}$ is the resistance.

Parameter values of the open-loop systemic circulation are adopted from (Guan et al., 2022c) and listed in Table 3.1. More details about the compliance and resistance in the lumped parameter system can be found in (Hill et al., 2013; Sack et al., 2018).

3.2 Governing equations of the deformation of the LV

To describe the deformation of the LV, we here introduce some necessary notations widely used in continuum mechanics and nonlinear elasticity (Spencer, 1984; Ogden, 2003). Considering a body $\mathcal{B}$, it occupies positions $\mathbf{X}$ at a fixed time such as the initial time. The body at this fixed time can be regarded as a reference configuration and denoted by B_r. At the current time t, the body occupies positions $\mathbf{x}$ and this current configuration is denoted by B_t. The deformation of the body from B_r to B_t is

$$\mathbf{x} = \boldsymbol{\chi}_t(\mathbf{X}), \quad \mathbf{X} = \boldsymbol{\chi}_t^{-1}(\mathbf{x}), \tag{3.13}$$

or

$$\mathbf{x} = \boldsymbol{\chi}(\mathbf{X}, t) \quad \text{for all } \mathbf{X} \in B_r. \tag{3.14}$$

The velocity of the body is defined as

$$\mathbf{v}(\mathbf{x}, t) := \dot{\mathbf{x}}(t) = \frac{\partial}{\partial t}\boldsymbol{\chi}(\mathbf{X}, t). \tag{3.15}$$

The acceleration is

$$\mathbf{a}(\mathbf{x}, t) := \dot{\mathbf{v}}(\mathbf{x}, t) = \ddot{\mathbf{x}}(t) = \frac{\partial^2}{\partial t^2}\boldsymbol{\chi}(\mathbf{X}, t). \tag{3.16}$$

Next, the deformation gradient tensor $\mathbf{F}$ is defined as

$$\mathbf{F}(\mathbf{X}, t) := \mathrm{Grad}\ \mathbf{x} = \mathrm{Grad}\ \boldsymbol{\chi}(\mathbf{X}, t). \tag{3.17}$$

With respect to two chosen bases for the reference configuration and the current configuration, i.e. $\{\ \mathbf{e}_i$ and $\mathbf{E}_i, i = 3$ for 3D space$\}$, we have

$$\mathbf{F} = \frac{\partial}{\partial X_j}(x_i \mathbf{e}_i) \otimes \mathbf{E}_j = \frac{\partial x_i}{\partial X_j} \mathbf{e}_i \otimes \mathbf{E}_j, \tag{3.18}$$

or, in component form

$$F_{ij} = \frac{\partial x_i}{\partial X_j}, \tag{3.19}$$

with $x_i = \chi_i(\mathbf{X}, t)$. Associated with $\mathbf{F}$ are the right and left Cauchy-Green tensors, defined by

$$\mathbf{C} = \mathbf{F}^{\mathrm{T}}\mathbf{F} \quad \text{and} \quad \mathbf{B} = \mathbf{F}\mathbf{F}^{\mathrm{T}}. \tag{3.20}$$

The principal invariants of $\mathbf{C}$ are defined by

$$I_1 = \mathrm{trace}(\mathbf{C}), \tag{3.21}$$

$$I_2 = \frac{1}{2}(\mathrm{trace}(\mathbf{C})^2 - \mathrm{trace}(\mathbf{C}^2)), \tag{3.22}$$

$$I_3 = \det(\mathbf{C}). \tag{3.23}$$

During the movement of the body, the law of the conservation of mass requires

$$\dot{\rho} + \rho \mathrm{div}\mathbf{v} = 0, \tag{3.24}$$

where ρ is the density of the material. This is a local form of the continuity equation in the current configuration. Meanwhile, Newton's Second Law of motion requires

$$\mathrm{div}\boldsymbol{\sigma} + \rho\mathbf{b} = \rho\mathbf{a}, \tag{3.25}$$

and

$$\boldsymbol{\sigma}^{\mathrm{T}} = \boldsymbol{\sigma}, \tag{3.26}$$

where $\boldsymbol{\sigma}$ is the Cauchy stress and $\mathbf{b}$ is the body force. Combined with the continuity equation and the momentum and angular momentum equations, we still need the constitutive equations to solve the motion of a continuous body.

3.2.1 Passive constitutive law of the myocardium

For an elastic incompressible material, the constitutive equation is

$$\boldsymbol{\sigma} = \mathbf{F}\frac{\partial \psi}{\partial \mathbf{F}} - p\mathbf{I}, \tag{3.27}$$

where ψ is the strain energy function, p is the Lagrange multiplier and $\mathbf{I}$ is the second-order identity tensor. The strain energy function proposed by Holzapfel and Ogden (Holzapfel and Ogden, 2009) has been widely used in the computational cardiology community (Wang et al., 2013; Gao et al., 2014; Sack et al., 2018; Wisneski et al., 2020). The HO model treats the myocardium as hyperelastic material and accounts for the layered myofibre architecture with three mutually orthogonal principal directions. The 8-parameter HO model is

$$\psi = \frac{a}{2b}\exp[b(I_1-3)] + \sum_{i=\mathrm{f,s}} \frac{a_i}{2b_i}\left\{\exp[b_i(\max(I_{4i},1)-1)^2]-1\right\} + \frac{a_{\mathrm{fs}}}{2b_{\mathrm{fs}}}\left\{\exp[b_{\mathrm{fs}}I_{8\mathrm{fs}}^2]-1\right\}, \tag{3.28}$$

where $a, b, a_{\mathrm{f}}, a_{\mathrm{s}}, b_{\mathrm{f}}, b_{\mathrm{s}}, a_{\mathrm{fs}}, b_{\mathrm{fs}}$ are eight material constants, $I_{4\mathrm{f}}, I_{4\mathrm{s}}$ and $I_{8\mathrm{fs}}$ are invariants related to the myofibre and sheet directions, i.e.

$$I_{4\mathrm{f}} = \mathbf{f}_0 \cdot (\mathbf{C}\mathbf{f}_0), \quad I_{4\mathrm{s}} = \mathbf{s}_0 \cdot (\mathbf{C}\mathbf{s}_0), \quad I_{8\mathrm{fs}} = \mathbf{f}_0 \cdot (\mathbf{C}\mathbf{s}_0), \tag{3.29}$$

where the fibre-coordinate triads $(\mathbf{f}_0, \mathbf{s}_0, \mathbf{n}_0)$ in the reference configuration are used, i.e. unit vector of the myofibre direction $\mathbf{f}_0$, unit vector of the sheet direction $\mathbf{s}_0$ and unit vector of the sheet-normal direction $\mathbf{n}_0 = \mathbf{f}_0 \times \mathbf{s}_0$. The invariants $I_{4\mathrm{f}}$ and $I_{4\mathrm{s}}$ represent squared stretches along the myofibre direction and the sheet direction, respectively. The max() function ensures that the myofibres only bear a stretching load. Experimental data are needed to calibrate the 8 material parameters. For instance, Guan et al. (2019) have determined the material constants by fitting the HO model to ex vivo myocardial tissue tests of uniaxial tension, biaxial tension, and simple shear (Dokos et al., 2002; Sommer et al., 2015; Ahmad et al., 2018b). Note that the strain energy function depends on the invariants $I_1, I_{4\mathrm{f}}, I_{4\mathrm{s}}$ and $I_{8\mathrm{fs}}$, so the constitutive equation for incompressible materials can be written as

$$\boldsymbol{\sigma} = \mathbf{F}\frac{\partial \psi}{\partial \mathbf{F}} - p\mathbf{I} = \mathbf{F}\sum_{i=1,\mathrm{f,s,fs}} \psi_i \frac{\partial I_i}{\partial \mathbf{F}} - p\mathbf{I}, \tag{3.30}$$

where

$$\psi_i = \frac{\partial \psi}{\partial I_i}. \tag{3.31}$$

This formula can be used to obtain an explicit form of Cauchy stress. The Cauchy stress can also be derived from the Green-Lagrange strain tensor, which is defined as

$$\mathbf{E} = \frac{1}{2}(\mathbf{C}-\mathbf{I}). \tag{3.32}$$

Substituting

$$\frac{\partial I_i}{\partial \mathbf{F}} = \frac{\partial I_i}{\partial \mathbf{E}}\mathbf{F}^{\mathrm{T}}, \tag{3.33}$$

into Eq. (3.30) gives

$$\boldsymbol{\sigma} = \mathbf{F} \sum_{i=1,\mathrm{f,s,fs}} \psi_i \frac{\partial I_i}{\partial \mathbf{E}} \mathbf{F}^{\mathrm{T}} - p\mathbf{I} = \frac{1}{J} \mathbf{F}\mathbf{S}\mathbf{F}^{\mathrm{T}}, \tag{3.34}$$

where

$$\mathbf{S} = \frac{\partial \psi}{\partial \mathbf{E}} - p(\mathbf{I} + 2\mathbf{E})^{-1} = 2\frac{\partial \psi}{\partial \mathbf{C}}, \tag{3.35}$$

is the second Piola-Kirchhoff stress tensor.

For incompressible and nearly incompressible materials, the strain energy function is usually written as

$$\psi = \psi_{\mathrm{dev}} + \psi_{\mathrm{vol}}. \tag{3.36}$$

Such separation ensures that the deviatoric part does not produce any change in volume. By using

$$\bar{\mathbf{F}} = J^{-1/3}\mathbf{F}, \tag{3.37}$$

where $J = \det(\mathbf{F})$, the deviatoric part of the right Cauchy-Green tensor is

$$\bar{\mathbf{C}} = \bar{\mathbf{F}}^{\mathrm{T}}\bar{\mathbf{F}} = J^{-2/3}\mathbf{C}. \tag{3.38}$$

The deviatoric part of the left Cauchy-Green tensor is

$$\bar{\mathbf{B}} = \bar{\mathbf{F}}\bar{\mathbf{F}}^{\mathrm{T}} = J^{-2/3}\mathbf{B}. \tag{3.39}$$

Therefore, the deviatoric parts of the invariants $I_1, I_{4\mathrm{f}}, I_{4\mathrm{s}}, I_{8\mathrm{fs}}$ can be determined. Now, the deviatoric part of the strain energy function in Eq. (3.28) is

$$\psi_{\mathrm{dev}} = \frac{a}{2b}\exp[b(\bar{I}_1 - 3)] + \sum_{i=\mathrm{f,s}} \frac{a_i}{2b_i}\left\{\exp[b_i(\max(\bar{I}_{4i}, 1) - 1)^2] - 1\right\} + \frac{a_{\mathrm{fs}}}{2b_{\mathrm{fs}}}\left\{\exp[b_{\mathrm{fs}}\bar{I}_{8\mathrm{fs}}^2] - 1\right\}, \tag{3.40}$$

and the volumetric part is

$$\psi_{\mathrm{vol}} = \frac{1}{D}\left(\frac{J^2 - 1}{2} - \ln(J)\right), \tag{3.41}$$

where D is the bulk modulus. The second Piola-Kirchhoff stress is

$$\mathbf{S} = 2\frac{\partial \psi}{\partial \mathbf{C}} = 2\left(\frac{\partial \psi_{\mathrm{dev}}}{\partial \mathbf{C}} + \frac{\partial \psi_{\mathrm{vol}}}{\partial \mathbf{C}}\right). \tag{3.42}$$

The second part of the Piola-Kirchhoff stress can be calculated as

$$\frac{\partial \psi_{\mathrm{vol}}}{\partial \mathbf{C}} = \frac{1}{D}(J - J^{-1})\frac{\partial J}{\partial \mathbf{C}} = \frac{1}{2D}(J^2 - 1)\mathbf{C}^{-1}, \tag{3.43}$$

where $\frac{\partial J}{\partial \mathbf{C}} = J\mathbf{C}^{-1}/2$ is used. The first part is

$$\frac{\partial \psi_{\text{dev}}}{\partial \mathbf{C}} = \phi_1 \frac{\partial \bar{I}_1}{\partial \mathbf{C}} + \phi_{4\text{f}} \frac{\partial \bar{I}_{4\text{f}}}{\partial \mathbf{C}} + \phi_{4\text{s}} \frac{\partial \bar{I}_{4\text{s}}}{\partial \mathbf{C}} + \phi_{8\text{fs}} \frac{\partial \bar{I}_{8\text{fs}}}{\partial \mathbf{C}}, \tag{3.44}$$

where

$$\begin{aligned}
\phi_1 &= \frac{\partial \psi_{\text{dev}}}{\bar{I}_1} = \frac{a}{2}\exp[b(\bar{I}_1 - 3)], \\
\phi_{4\text{f}} &= \frac{\partial \psi_{\text{dev}}}{\bar{I}_{4\text{f}}} = a_{4\text{f}}\exp[b_{4\text{f}}(\bar{I}_{4\text{f}} - 1)^2](\bar{I}_{4\text{f}} - 1), \\
\phi_{4\text{s}} &= \frac{\partial \psi_{\text{dev}}}{\bar{I}_{4\text{s}}} = a_{4\text{s}}\exp[b_{4\text{s}}(\bar{I}_{4\text{s}} - 1)^2](\bar{I}_{4\text{s}} - 1), \\
\phi_{8\text{fs}} &= \frac{\partial \psi_{\text{dev}}}{\bar{I}_{8\text{fs}}} = a_{8\text{fs}}\exp[b_{8\text{fs}}\bar{I}_{8\text{fs}}^2]\bar{I}_{8\text{fs}},
\end{aligned}$$

and

$$\begin{aligned}
\frac{\partial \bar{I}_1}{\partial \mathbf{C}} &= \frac{\partial J^{-2/3} I_1}{\partial \mathbf{C}} = \frac{\partial J^{-2/3}}{\partial \mathbf{C}} I_1 + J^{-2/3}\frac{\partial I_1}{\partial \mathbf{C}} = -\frac{1}{3}J^{-2/3} I_1 \mathbf{C}^{-1} + J^{-2/3}\mathbf{I} \\
&= J^{-2/3}\mathbf{I} - \frac{1}{3}\bar{I}_1 \mathbf{C}^{-1}, \\
\frac{\partial \bar{I}_{4\text{f}}}{\partial \mathbf{C}} &= \frac{\partial J^{-2/3} I_{4\text{f}}}{\partial \mathbf{C}} = \frac{\partial J^{-2/3}}{\partial \mathbf{C}} I_{4\text{f}} + J^{-2/3}\frac{\partial I_{4\text{f}}}{\partial \mathbf{C}} = -\frac{1}{3}J^{-2/3} I_{4\text{f}} \mathbf{C}^{-1} + J^{-2/3}\mathbf{f}_0 \otimes \mathbf{f}_0 \\
&= J^{-2/3}\mathbf{f}_0 \otimes \mathbf{f}_0 - \frac{1}{3}\bar{I}_{4\text{f}} \mathbf{C}^{-1}, \\
\frac{\partial \bar{I}_{4\text{s}}}{\partial \mathbf{C}} &= J^{-2/3}\mathbf{s}_0 \otimes \mathbf{s}_0 - \frac{1}{3}\bar{I}_{4\text{s}} \mathbf{C}^{-1}, \\
\frac{\partial \bar{I}_{8\text{fs}}}{\partial \mathbf{C}} &= J^{-2/3}(\mathbf{f}_0 \otimes \mathbf{s}_0 + \mathbf{s}_0 \otimes \mathbf{f}_0) - \frac{1}{3}\bar{I}_{8\text{fs}} \mathbf{C}^{-1}.
\end{aligned}$$

Finally, a passive Cauchy stress tensor derived from the HO strain energy function is

$$\begin{aligned}
\boldsymbol{\sigma}^p = \frac{1}{J}\mathbf{F}\mathbf{S}\mathbf{F}^{\text{T}} =& p_{\text{vol}}\mathbf{I} + 2J^{-1}[\phi_1(\bar{\mathbf{B}} - \frac{1}{3}\bar{I}_1\mathbf{I}) + \phi_{4\text{f}}(\bar{\mathbf{f}}_0 \otimes \bar{\mathbf{f}}_0 - \frac{1}{3}\bar{I}_{4\text{f}}\mathbf{I}) \\
&+ \phi_{4\text{s}}(\bar{\mathbf{s}}_0 \otimes \bar{\mathbf{s}}_0 - \frac{1}{3}\bar{I}_{4\text{s}}\mathbf{I}) + \frac{1}{2}\phi_{8\text{fs}}(\bar{\mathbf{f}}_0 \otimes \bar{\mathbf{s}}_0 + \bar{\mathbf{s}}_0 \otimes \bar{\mathbf{f}}_0 - \frac{2}{3}\bar{I}_{8\text{fs}}\mathbf{I})],
\end{aligned} \tag{3.45}$$

where $p_{\text{vol}} = \frac{1}{D}(J - J^{-1})$ is a Lagrange multiplier to ensure the incompressible constraint, $\phi_i = \partial\psi_{\text{dev}}/\partial\bar{I}_i$, $i \in [1, 4\text{f}, 4\text{s}, 8\text{fs}]$, and $\bar{\mathbf{f}}_0 = \bar{\mathbf{F}}\mathbf{f}_0/|\bar{\mathbf{F}}\mathbf{f}_0|$ and $\bar{\mathbf{s}}_0 = \bar{\mathbf{F}}\mathbf{s}_0/|\bar{\mathbf{F}}\mathbf{s}_0|$ are the unit vector in the current configuration of the myofibre direction and the sheet direction, respectively.

3.2.2 Active stress model

The passive response of the myocardium has been described in the previous section, here, we present a method of modelling the active contraction force of the myocardium. During

systole, contraction of the heart provides sufficient ejection of blood to the whole body. This contraction is controlled by an electrical wave signal, which initiates at the sinoatrial node and propagates throughout the myocardium. There are two common approaches to introduce the active force into the constitutive law of the myocardium: the active stress approach (Gao et al., 2017; Sack et al., 2018; Genet et al., 2014) and the active strain approach (Quarteroni et al., 2017; Rossi et al., 2014; Pandolfi et al., 2016). In the active stress approach, the total stress tensor is decomposed into a passive part and an active part. On the other hand, in the active strain approach, the total deformation gradient tensor is decomposed into a passive part and an active part. Because of the convenience in parameter calibration with experimental stress data, the active stress approach is widely adopted in heart modelling, such as the living heart project (Baillargeon et al., 2014) and some recent studies (Sack et al., 2018; Guan et al., 2020b). Following the active stress approach, the total Cauchy stress is

$$\boldsymbol{\sigma} = \boldsymbol{\sigma}^p + \boldsymbol{\sigma}^a, \tag{3.46}$$

where $\boldsymbol{\sigma}^a$ is the active stress generated by the contraction forces which is

$$\boldsymbol{\sigma}^a = T_{\mathrm{a}} \bar{\mathbf{f}}_0 \otimes \bar{\mathbf{f}}_0, \tag{3.47}$$

where T_{a} is the active tension which can be determined by a well-established time-varying elastance model (Guccione and McCulloch, 1993; Sack et al., 2018),

$$T_{\mathrm{a}}(t,l) = \frac{T_{\max}}{2} \frac{\mathrm{Ca}_0^2}{\mathrm{Ca}_0^2 + \mathrm{ECa}_{50}^2(l)} \left(1 - \cos\left(\omega(t,l)\right)\right), \tag{3.48}$$

in which $T_{\max}$ is the maximum isometric active tension which determines the maximum value of active contraction, Ca_0 is the peak intracellular calcium, and the length-dependent calcium sensitivity (ECa_{50}) is given by

$$\mathrm{ECa}_{50}(l) = \frac{\mathrm{Ca}_{0\max}}{\sqrt{e^{B(l-l_0)} - 1}}, \tag{3.49}$$

where B and $\mathrm{Ca}_{0\max}$ are constants, l_0 is the minimum sarcomere length to produce active stress, and l is the deformed sarcomere length

$$l = l_r \sqrt{2E_{\mathrm{ff}} + 1}, \tag{3.50}$$

where l_r is the stress-free sarcomere length, and E_{ff} is the Lagrange strain in the myofibre direction. The time function after onset of contraction in Eq. (3.48) is

$$\omega(t,l) = \begin{cases} \pi \frac{t}{t_0} & \text{for} \quad 0 \leqslant t \leqslant t_0, \\ \pi \frac{t-t_0+t_r(l)}{t_r} & \text{for} \quad t_0 < t \leqslant t_0 + t_r, \\ 0 & \text{for} \quad t > t_0 + t_r, \end{cases} \tag{3.51}$$

where t_0 is the time to peak tension, and t_r is the duration of relaxation

$$t_r(l) = ml + b, \tag{3.52}$$

where m and b are constants to determine the shape of the linear relaxation duration and sarcomere length relaxation.

3.2.3 Dispersed myofibre modelling and its effect on the strain energy function

In the previous section, the orientations of the myofibres are assumed to vary from -60° at the epicardium to 60° at the endocardium, which is commonly used in the computational studies of the heart (Wang et al., 2013; Sack et al., 2018). Instead of aligning perfectly along their orientations, measurements of the micro-structure of soft tissues by the diffusion tensor magnetic resonance imaging (DT-MRI) technique have shown that myofibres are spatially dispersed around their predominant mean myofibre direction (Helm et al., 2005; Sommer et al., 2015; Ahmad et al., 2018a). Lin and Yin (1998) first reported 40% cross-myofibre active stress in their biaxial contraction tests in rabbit myocardium. Wenk et al. (2012); Genet et al. (2014) also included cross-myofibre active stress in the total stress to better match in vivo cardiac pump function. Later, Sack et al. (2018) added cross-myofibre active tension with cross-myofibre contraction ratios that were inversely determined using a healthy porcine heart and a failing heart. Guan et al. (2021, 2022b,c) recently studied the effects of the myofibre dispersion on the cardiac pump function. They investigated the effects of cross-myofibre active stress on cardiac pump function where a generalised structural tensor (GST) based dispersed active tension model was developed. Their results suggested that cardiac functions during diastolic filling and systolic contraction vary largely while considering different degrees of in-plane and out-of-plane myofibre dispersion. In this section, we summarise the methods for modelling the myofibre dispersion around the mean myofibre direction, based on studies of Guan et al. (2021, 2022b,c). It should be noted that myofibre dispersion in the sheet direction is not considered here,

although it can be added analogously.

The myofibre and sheet directions, f_0 and s_0, can be used to form a local material coordinate system $(\mathrm{f}_0, \mathrm{s}_0, \mathrm{n}_0)$ at each material point, with the normal-sheet direction $\mathrm{n}_0 = \mathrm{s}_0 \times \mathrm{f}_0$. To describe the dispersion of fibres around the mean myofibre direction f_0, as shown in Fig. 3.3 (b), the polar angle Θ (angle with respect to the polar axis) and the azimuthal angle Φ (angle of rotation from the initial meridian plane) are introduced, corresponding to the local material coordinate system. Thus, the polar angle Θ is the angle between the mean myofibre direction f_0 and a single dispersed myofibre direction f_n, and the azimuthal angle Φ is the angle between the sheet-normal direction n_0 and the projected vector of f_n in the $\mathrm{s}_0 - \mathrm{n}_0$ plane. Finally, the direction f_n of a single dispersed myofibre can be described by

$$\mathrm{f}_\mathrm{n}(\Theta, \Phi) = \cos\Theta\,\mathrm{f}_0 + \sin\Theta\cos\Phi\,\mathrm{n}_0 + \sin\Theta\sin\Phi\,\mathrm{s}_0, \tag{3.53}$$

where $\Theta \in [0, \pi/2]$ and $\Phi \in [0, 2\pi]$. Considering that myofibres have the unit length, all the dispersed myofibres at one original point are located within a unit hemisphere $\mathbb{S}_\mathrm{f} = \{(r, \Theta, \Phi) : r = 1,\, \Theta \in [0, \pi/2]\,,\, \Phi \in [0, 2\pi]\}$, as shown in Fig. 3.3 (c).

Here, the distribution of the dispersed fibres needs to be determined. Following Guan et al. (2020b, 2022b,c), a probability density function is adopted to describe the distribution of the dispersed fibres. Specifically, for the dispersed myofibres around f_0, their probability density function is

$$\varrho(\mathrm{f}_0) = \varrho\Big(\Theta, b_1, \Phi, b_2\Big) = G\,\rho_\mathrm{in}(\Theta, b_1)\,\rho_\mathrm{op}(\Phi, b_2), \tag{3.54}$$

where $\rho_\mathrm{in}(\Theta, b_1)$ denotes the in-plane myofibre dispersion and $\rho_\mathrm{op}(\Phi, b_2)$ describes the out-of-plane myofibre dispersion, b_1 and b_2 are the concentration parameters, and G is a constant to ensure

$$\int_\mathbb{S} \rho_\mathrm{in}(\Theta, b_1)\,\rho_\mathrm{op}(\Phi, b_2)\,\mathrm{d}S = 1. \tag{3.55}$$

The concentration parameters b_1 and b_2 can be estimated from measured in-plane and out-of-plane myofibre distributions (Sommer et al., 2015; Ahmad et al., 2018b). The π-periodic von Mises distribution (Holzapfel et al., 2015) is then used to describe ρ_in and ρ_op, i.e.

$$\rho_\mathrm{in}(\Theta, b_1) = \frac{\exp\left(b_1\cos(2\Theta)\right)}{\int_0^\pi \exp\left(b_1\cos(x)\right)\mathrm{d}x}, \tag{3.56}$$

and

$$\rho_\mathrm{op}(\Phi, b_2) = \frac{\exp\left(b_2\cos(2\Phi)\right)}{\int_0^\pi \exp\left(b_2\cos(x)\right)\mathrm{d}x}. \tag{3.57}$$

Note that the distribution of the in-plane dispersion and the distribution of the out-of-plane dispersion are independent.

By taking into account the dispersion of the myofibres, the fibre-related strain energy

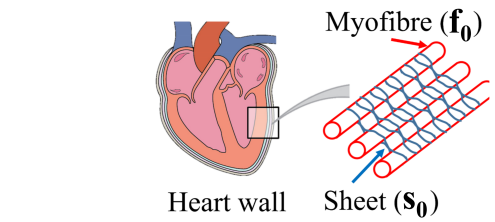

(a)

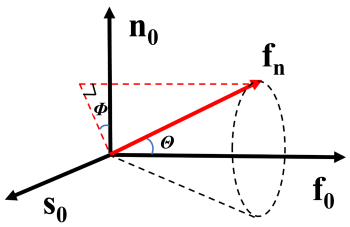

(b)

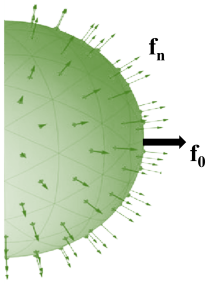

(c)

Figure 3.3: Schematic diagram of the heart (a) showing the microstructural arrangement of the myofibres and sheet fibres in the myocardium. The blue network describes the sheet fibres that connect myofibres (red rods). A local myofibre coordinate system $(\mathrm{f}_0, \mathrm{s}_0, \mathrm{n}_0)$ in (b) showing the unit vector f_n (red) representing the myofibre direction defined by Θ and Φ with respect to the mean myofibre direction f_0. Figure (c) is an illustration of the unit hemisphere domain centralised with the mean myofibre direction f_0 (the black arrow). In the discrete myofibre dispersion method proposed by Li et al. (2018), the hemisphere is divided into N discrete triangular elements with representative myofibre directions f_n (green arrows) at the centroid of each triangular surface. Figures are adapted from (Guan et al., 2022b).

term in Eq. (3.28) is

$$\psi_{\mathrm{Dpf}}^{I_{4\mathrm{f}}*} = \int_{\mathbb{S}_\mathrm{f}} \varrho\big(\Theta, b_1, \Phi, b_2\big)\, \psi_{\mathrm{Dpf}}^{I_{\mathrm{Dpf}}^{4\mathrm{f}}}(I_{\mathrm{Dpf}}^{4\mathrm{f}}(\Theta, \Phi))\, \mathrm{d}S_\mathrm{f}, \tag{3.58}$$

where $I_{\mathrm{Dpf}}^{4\mathrm{f}}(\Theta, \Phi) = \mathrm{f}_n \cdot (\mathbf{C}\,\mathrm{f}_n)$ and $\psi_{\mathrm{Dpf}}^{I_{4\mathrm{f}}}(I_{4\mathrm{f}}(\Theta, \Phi)) = \frac{a_\mathrm{f}}{2b_\mathrm{f}}\Big\{\exp[b_\mathrm{f}(\max(I_{\mathrm{Dpf}}^{4\mathrm{f}}, 1) - 1)^2] - 1\Big\}$. Integration of Eq. (3.58) is achieved by the discrete myofibre dispersion (DFD) method proposed by Li et al. (2018). Details can be found in (Li et al., 2018). In brief, the DFD method divides the surface of the hemisphere space domain $\mathbb{S}_\mathrm{f}$ into N spherical triangle elements with representative myofibre bundles at each triangle element, as shown in Fig. 3.3(c). For the n^{th} spherical triangle element with the triangular area $\Delta\mathbb{S}_n$, the direction of the myofibre at the centroid of this element is defined by a representative myofibre

direction $\mathrm{f}_n(\Theta_n, \Phi_n)$. The myofibre density in this element is approximated as

$$\rho_n = \int_{\Delta\mathbb{S}_n} \varrho(\Theta, b_1, \Phi, b_2) \sin\Theta \,\mathrm{d}\Theta \,\mathrm{d}\Phi, \quad n = 1, \cdots, N, \quad \text{subject to} \quad \sum_{n=1}^{N} \rho_n = 1, \tag{3.59}$$

where N is the total number of the discrete spherical triangle elements of the unit hemisphere. Then, $\psi_{\mathrm{Dpf}}^{I_{4\mathrm{f}}*}$ can be calculated by

$$\psi_{\mathrm{Dpf}}^{I_{4\mathrm{f}}*} \approx \sum_{n=1}^{N} \rho_n \, \psi_{\mathrm{Dpf}}^{I_{4\mathrm{f}}}(I_{4\mathrm{f}}(\Theta_n, \Phi_n)). \tag{3.60}$$

The same procedures can be used to introduce dispersion in the sheet and the sheet-normal direction. Details are referred to (Guan et al., 2022b). Finally, the total strain energy function with dispersed fibres only in the myofibre direction is

$$\begin{aligned}\psi_{\mathrm{Dpf}} =& \frac{a}{2b}\{\exp[b(I_1 - 3)] - 1\} + \psi_{\mathrm{Dpf}}^{I_{4\mathrm{f}}*} + \frac{a_{\mathrm{s}}}{2b_{\mathrm{s}}}\left\{\exp[b_{\mathrm{s}}(\max(I_{4\mathrm{s}}, 1) - 1)^2] - 1\right\} \\ &+ \frac{a_{\mathrm{fs}}}{2b_{\mathrm{fs}}}[\exp(b_{\mathrm{fs}} I_{8\mathrm{fs}}^2) - 1].\end{aligned} \tag{3.61}$$

3.2.4 Effect of myofibre dispersion on the active stress response

If there is no myofibre dispersion, the generated active stress is only along the myofibre direction f_0, that is

$$\boldsymbol{\sigma}^a = T_{\mathrm{a}} \bar{\mathbf{f}}_0 \otimes \bar{\mathbf{f}}_0. \tag{3.62}$$

After introducing the myofibre dispersion, the dispersed active stress approach (Eriksson et al., 2013; Guan et al., 2021) is employed to give

$$\boldsymbol{\sigma}_{\mathrm{Dpf}}^a = n_{\mathrm{f}} T_{\mathrm{a}} \mathbf{f}_0 \otimes \mathbf{f}_0 + n_{\mathrm{s}} T_{\mathrm{a}} \mathbf{s}_0 \otimes \mathbf{s}_0 + n_{\mathrm{n}} T_{\mathrm{a}} \mathbf{n}_0 \otimes \mathbf{n}_0, \tag{3.63}$$

where n_{f}, n_{s} and n_{n} are proportions of the active tension in the myofibre, sheet, and sheet-normal directions, respectively. These parameters can be derived from a generalised structure tensor H (Holzapfel et al., 2015; Eriksson et al., 2013; Gasser et al., 2006), which is defined over the unit hemisphere using the predefined probability density function Eq. (3.54) as

$$\mathrm{H} = \int_{\mathbb{S}} \varrho(\Theta, b_1, \Phi, b_2) \, \mathrm{f}_n \otimes \mathrm{f}_n \,\mathrm{d}S = H_{11} \mathbf{f}_0 \otimes \mathbf{f}_0 + H_{22} \mathbf{s}_0 \otimes \mathbf{s}_0 + H_{33} \mathbf{n}_0 \otimes \mathbf{n}_0, \tag{3.64}$$

where H_{11}, H_{22}, H_{33} are diagonal components with respect to the orthogonal material axes (f_0, s_0 and n_0). The tensor H is diagonal because of the $\pi-$period von Mises probability density functions for the myofibre dispersion and the independence assumption between the in-plane and out-of-plane dispersion. In other words, the myofibre dispersion distri-

bution is symmetrical with respect to (f_0, s_0) plane, (f_0, n_0) plane and (s_0, n_0) plane. We would like to mention that the tensor H may not be diagonal for general myofibre dispersion.

Using the generalised structure tensor, we have

$$n_{\mathrm{f}} = H_{11}, \qquad n_{\mathrm{n}} = H_{22}, \qquad \text{and} \qquad n_{\mathrm{s}} = H_{33}, \tag{3.65}$$

and $n_{\mathrm{f}} + n_{\mathrm{s}} + n_{\mathrm{n}} = 1$. Finally, the total Cauchy stress considering the myofibre dispersion is

$$\sigma_{\mathrm{Dpf}} = \sigma^{\mathrm{p}}_{\mathrm{Dpf}} + \sigma^{\mathrm{a}}_{\mathrm{Dpf}}, \tag{3.66}$$

where $\sigma^{\mathrm{a}}_{\mathrm{Dpf}}$ is given in Eq. (3.63), and $\sigma^{\mathrm{p}}_{\mathrm{Dpf}}$ can be derived from the strain energy function in Eq. (3.61) using the procedures described in section 3.2.1.

Parameters values of the constitutive model and active stress model of a control case have been summarised in Table 3.1.

3.3 Boundary conditions and implementation

In this section, boundary conditions are established to produce a realistic deformation of the LV. The LV surface is divided into three regions, as shown in Fig. 3.4: the basal surface, endocardial surface, and epicardial surface. The nodes on the LV basal surface are only permitted to move radially, while the LV epicardial surface is free to move without any constraints. On the other hand, the LV endocardial surface is subjected to a uniformly time-dependent LV pressure, which is imposed through the fluid cavity modules in ABAQUS. Note that the prescribed LV cavity pressure varies over the course of a single cardiac cycle.

A single cardiac cycle is composed of various phases, including the isovolumetric contraction and ejection phase during systole, and the isovolumetric relaxation, rapid inflow, diastasis, and atrial systole during diastole. This chapter considers a cardiac cycle period time of 0.8 s, equivalent to a heart rate of 75 beats per minute. The systolic phase lasts approximately 0.3 s, while the diastolic phase lasts about 0.5 seconds. To simulate these phases in ABAQUS, the following three steps are introduced in one cardiac cycle:

- A Filling Step: During this step, the LV cavity pressure is gradually increased from 0 mmHg to 8 mmHg over a period of 0.3 s, resulting in the LV geometry reaching its end-diastolic state by the end of this step. The increase in pressure is accomplished through the ramp amplitude of the pressure in ABAQUS.

- A Contraction Step: This step simulates the isovolumetric contraction, systolic ejection phases, and part of the relaxation phase, which is controlled by the active

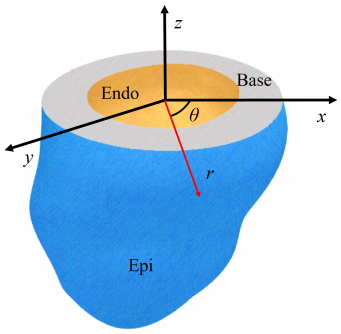

Figure 3.4: Diagram of the boundary conditions of the left ventricle. The surface of the left ventricle is divided into three regions for the imposition of the boundary conditions, namely the basal surface (Base), endocardial surface (Endo), and epicardial surface (Epi). A cylindrical coordinate system is established, denoted as (r, θ, z), wherein (r, θ) designates the polar coordinates of a point in the xy-plane and z refers to the point's projection onto the z-axis. The z-axis direction is the long-axis direction of the left ventricle.

contraction model. The LV cavity pressure during this step is implicitly determined through the fluid cavity modules in ABAQUS, as previously discussed. The duration of this step is set to 0.4 s, with the contraction phase ending around 0.2 s. It is important to note that this step does not capture the rapid isovolumetric relaxation.

- A Recovery Step: In this step, the recovery of the LV is modelled. This step, lasting for 0.1 seconds, enables the LV geometry to be fully unloaded and to reach the end-systolic state.

In ABAQUS, the simulations of multiple cardiac cycles can be performed by repeating the three steps discussed above. Beginning with the second cardiac cycle, only the pressure of the LV cavity needs to be increased linearly from 0 to 8 mmHg in the filling step since the left atrium is not included in the LV model. The rest of the variables will be calculated based on the outcomes of the previous time step. To guarantee that the periodic steady states are reached, the computation is performed in double precision. Using the 'single' precision can result in non-convergence during periodic simulations, such as a persistent decrease in the end-diastolic volume of the LV cavity.

In summary, the deformation of the LV is governed by

$$\begin{cases} \nabla \cdot \sigma = 0, & \text{in the LV wall domain,} \\ \sigma \cdot \mathrm{n} = -P\mathrm{n}, & \text{on the LV endocardial surface,} \\ \sigma \cdot \mathrm{n} = 0, & \text{on the LV epicardial surface,} \\ u_\theta = 0 \quad \text{and} \quad u_z = 0, & \text{on the LV basal surface,} \end{cases} \tag{3.67}$$

where P is the LV cavity pressure, n is the unit vector normal to the LV endocardial surface or to the LV epicardial surface, u_θ and u_z are the displacement along the θ-axis direction and the z-axis direction (the long-axis direction of the heart, as shown in Fig. 3.4) in the global cylindrical coordinate system, respectively. Based on the geometry of the LV, lumped-parameter circulatory system, passive and active material properties, and boundary conditions described previously, an advanced LV model is developed. This LV model is implemented in ABAQUS 2018 (Dassault Systemes, Johnston RI, USA) (Dassault, 2014), with the constitutive law being implemented via the VUMAT user subroutine, which is designed for incorporating user-defined material models. The fluid cavity and fluid exchange modulus in ABAQUS are utilised to simulate the lumped-parameter system. The parameter values for the LV model are obtained from previous studies (Guan et al., 2020b, 2021) conducted by our group and are summarised in Table 3.1. For further information on the ABAQUS software, readers are referred to the official ABAQUS documents (Dassault, 2014; Documentation and Manual, 2014).

Finally, the dynamics of the LV model are solved by the nonlinear FE method via the ABAQUS EXPLICIT solver. In brief, we solve the following dynamic system

$$\mathbb{M}\ddot{\mathrm{x}} + \mathbb{C}\dot{\mathrm{x}} + \mathbb{K}\mathrm{x} = \mathbb{F}_{\mathrm{ext}}, \tag{3.68}$$

where $\mathbb{M}$ is the mass matrix, $\mathbb{C}$ is the damping matrix, $\mathbb{K}(\mathrm{x})$ is the nonlinear stiffness matrix depending on the current configuration, $\mathbb{F}_{\mathrm{ext}}$ is the external force, and x is the displacement field. To eliminate unrealistic transient behaviour, the damping matrix is introduced via Rayleigh damping (Documentation and Manual, 2014), i.e.

$$\mathbb{C} = \alpha\mathbb{M}, \tag{3.69}$$

where α is the damping factor. We find that $\alpha = 160\,\mathrm{s}^{-1}$ can simulate LV dynamics without noticeable oscillation, which is also the value used in the LivingHeart Project (Baillargeon et al., 2015). As previously discussed in section 3.2, the derivation of the deformation tensor, stress, and strain becomes possible once the displacement field is obtained. Additionally, ABAQUS, through its post-processing module, provides convenient access to several relevant variables, including principal stress, principal strain, and logarithmic strain.

3.4 Results of the LV model

In this section, we show the results of the LV model using parameter values in Table 3.1. The objective of reconstructing the LV geometry from the healthy volunteer is not to create a subject-specific model, but rather to develop a healthy LV model that operates within

Table 3.1: Parameter values for the passive constitutive model, the active tension constitutive model, and the lumped circulatory model.

Passive constitutive model (Guan et al., 2020b)									
a_{g} (kPa)	b_{g}	a_{f} (kPa)	b_{f}	a_{s} (kPa)	b_{s}	a_{fs} (kPa)	a_{fs}	b_1	b_2
0.1731	5.1207	1.9344	0.2199	0.2143	0.0005	0.2665	2.5505	4.5	3.9

Active tension constitutive model (Guan et al., 2020b)								
t_0	m	b	l_0	B	Ca_0	$\mathrm{Ca}_{0\max}$	$T_{\max}$	l_r
(s)	($\mathrm{s}\,\mu\mathrm{m}^{-1}$)	(s)	(μm)	($\mu\mathrm{m}^{-1}$)	(μM)	(μM)	(kPa)	(μm)
0.18	1048.9	-1.7	1.58	4.750	4.35	4.35	110	1.85

Lumped circulatory model (Guan et al., 2021)			
Compliance (mL/mmHg)		Resistance (MPa $\cdot$ s/m^3)	
C_{Ao}	C_{SA}	R_{Ao}	R_{SA}
2.5	1.25	2.0	120.0

normal physiological parameters. Hence, the simulated results obtained from our LV model will primarily be compared with physiological ranges reported in clinical observations and studies of healthy subjects, rather than to a specific individual.

3.4.1 LV pressure-volume relationships during multiple cycles

In prior studies of the computational LV models by our research group (Wang et al., 2013; Guan et al., 2020a,b), the implementation of multiple-cycle simulations was not present. Although convergence analysis was performed in terms of mesh size and the results of the first cycle were stable, the outcomes of subsequent cycles may not have been

convergent. As demonstrated in some studies (Baillargeon et al., 2014; Sack et al., 2018), the simulation results from ABAQUS heart models typically converge after three or four cycles. Thus, we extend our previous LV model to incorporate multiple-cycle simulations. The pressure-volume (PV) loops generated from the LV model in these simulations are depicted in Fig. 3.5. Fig. 3.5 (a) shows the PV loops in the first five cardiac cycles. The PV loops of the first and second cycles differ from those of the remaining cycles. The PV loop begins to exhibit stability after the third cycle, highlighting the significance of multiple-cycle simulations for the LV model.

A simulation of five cardiac cycles needs approximately 10 hours on a Linux workstation with 8 cores of 2.3 GHz CPU (Intel(R) Xeon(R) CPU E5-2699 v3) and 128 GB memory. Since the results are stable after the third cycle, we will run the LV model only with three cardiac cycles in the following simulations to reduce the computational time.

Simulated results in the third cardiac cycle are shown in Fig. 3.5 (b). As introduced in section 3.3, we use three steps in one cardiac cycle: the filling step, the contraction step, and the recovery step. The filling step commences at point P_1 as the mitral valve opens and the filling of the LV occurs. The mitral valve closes at point P_2 marking the beginning of the contraction phase. Note that the LV volume at the point P_2 is the end-diastolic volume (EDV). Right after the point P_2, the isovolumetric contraction begins, where the LV cavity volume remains unchanged, but the LV cavity pressure increases rapidly. As we can see from Fig. 3.5 (b), the PV loop curve from the point P_2 to point P_3 is vertical until the LV cavity pressure exceeds the aortic pressure at the point P_3, leading to the opening of the aortic valve. After the opening of the aortic valve, blood is expelled from the LV into the aorta. The LV volume decreases quickly in this period, but the LV pressure remains high due to the continuous contraction generated by the myocardium. The ejection of blood causes an increase in aortic pressure. When the aortic pressure surpasses the LV pressure at the point P_4, the aortic valve closes and the systolic phase ends. The LV volume at the point P_4 is the end-systolic volume (ESV). Finally, there is a relaxation phase where the LV cavity pressure falls until it is below the atrial pressure at the point P_1, marking the commencement of the subsequent filling phase and the initiation of a new cardiac cycle.

The LV pressure, aortic pressure, and LV cavity volume simulated from the LV model are plotted in Fig. 3.6. As illustrated in Fig. 3.6 (a), the LV pressure is linearly increased from 0 to 8 mmHg, from 0 s to 0.3 s which is the filling step. The systolic phase of the LV occurs from 0.3 s to 0.5 s as indicated by the two vertical lines. During this phase, the LV pressure increases rapidly to a peak value of 119.6 mmHg. After the closure of the aortic valve, the LV pressure decreases to 0 corresponding to the recovery phase. It should be noted that the simulation of the relaxation phase in the active contraction model (Guccione and McCulloch, 1993; Sack et al., 2018) is not accurate, causing the

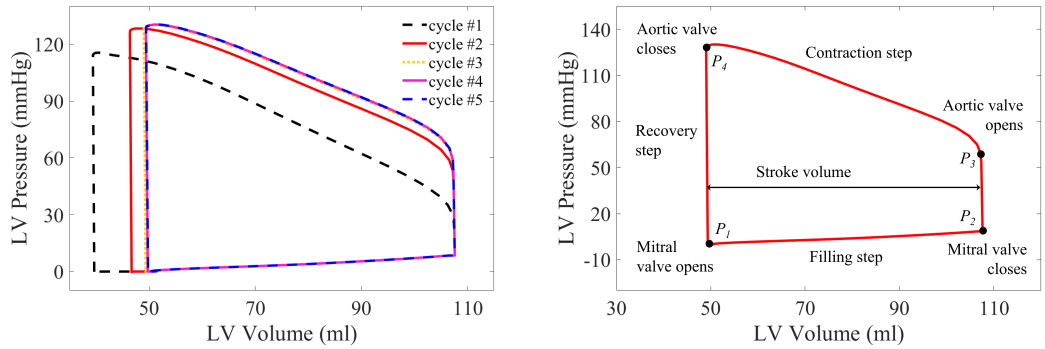

(a) (b)

Figure 3.5: Pressure-volume (PV) loops (a) of the left ventricle (LV) model in the first five consecutive cardiac cycles. Figure (b) is the PV loop in the third cardiac cycle. The three ABAQUS steps (filling step, contraction step, and recovery step) are shown, as well as four critical points (P_1, P_2, P_3, P_4) in a complete cardiac cycle. P_1 marks the opening of the mitral valve. P_2 marks the closing of the mitral valve. P_3 marks the opening of the aortic valve. P_4 marks the closing of the aortic valve.

simulated LV pressure to decrease slowly over a period of 0.16 s. The normal range for the isovolumetric relaxation time is 0.05 s to 0.14 s, with an average of 0.103 $\pm$ 0.022 s (Benchimol and Ellis, 1967; Thomas et al., 1992). Thus, future research requires more realistic modelling of the relaxation phase.

The simulated aortic pressure, as plotted in Fig. 3.6 (a), ranges from 79.8 mmHg to 118.7 mmHg. This result aligns with the reported normal range of aortic pressure in healthy individuals, which is between 80 mmHg and 120 mmHg (Erbel et al., 2001; Reymond et al., 2012). The pressure difference between the LV pressure and the aortic pressure during the ejection phase is within 10 mmHg and is attributed to the resistance posed by the aortic valve. However, if the aortic valve is narrowed or does not open fully, as in the case of aortic stenosis, the pressure difference would be larger. For instance, a mean pressure gradient of 20 mmHg is considered moderate aortic stenosis, while a mean gradient of 40 mmHg is considered severe aortic stenosis (Nishimura et al., 2017; Wisneski et al., 2020). In addition, during diastole, the aortic pressure decreases linearly as the blood stored in the aortic chamber is gradually pushed towards the peripheral vessels, driven by the aortic compliance, which is determined by the lumped parameter system.

The changes in the LV volume during a single cardiac cycle are depicted in Fig. 3.6 (b). As can be seen, the LV volume is increased from 49.2 ml to 109.5 ml during the filling step, occurring between 0 to 0.3 s. During the following isovolumetric contraction phase, from 0.3 s to 0.33 s, the LV volume remains unchanged. In the ejection phase, from 0.33 s to 0.5 s, the LV volume decreases as a result of the ejection of blood. After the closure of the aortic valve, the LV volume remains steady. In the third ABAQUS step (the recovery step), from 0.7 s to 0.8 s, there is a 7% increase in the LV volume due to the manual unloading

of the LV pressure. The end-diastolic volume is 109.5 ml, and the end-systolic volume is 45.9 ml, resulting in an ejection fraction (EF) of the LV of 58.1%, which falls within the normal range of healthy individuals (50% - 65%) (Kumar et al., 2014; Mahadevan et al., 2008; Dokainish et al., 2011; Feher, 2017; Lang et al., 2015).

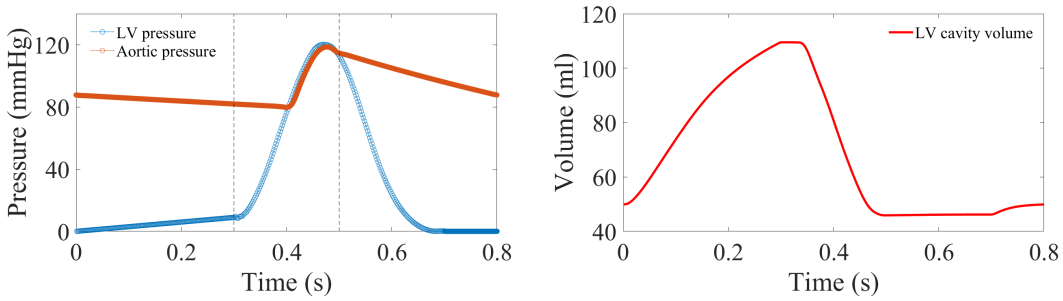

(a) (b)

Figure 3.6: Simulated pressure and volume from the left ventricle (LV) model. Figure (a) presents simulated pressure profiles in the LV and aorta during the third cardiac cycle. The systole period is indicated by the presence of the two vertical dashed lines. Figure (b) displays the corresponding LV cavity volume throughout the third cardiac cycle.

3.4.2 Evaluation of stress distribution in the LV wall

In this section, we analyse the stress distribution in the LV wall. The stresses along the myofibre direction, the sheet direction, and the sheet-normal direction are calculated from the Cauchy stress by

$$\sigma_{\mathrm{ff}} = \bar{\mathbf{f}}_0 \cdot (\boldsymbol{\sigma} \bar{\mathbf{f}}_0), \quad \sigma_{\mathrm{ss}} = \bar{\mathbf{s}}_0 \cdot (\boldsymbol{\sigma} \bar{\mathbf{s}}_0), \quad \text{and} \quad \sigma_{\mathrm{nn}} = \bar{\mathbf{n}}_0 \cdot (\boldsymbol{\sigma} \bar{\mathbf{n}}_0). \tag{3.70}$$

These three stresses are calculated in the deformed configuration. The volumetric-averaged myofibre stress is calculated by

$$\bar{\sigma}_{\mathrm{ff}} = \frac{\sum_{i=1}^{n} (\sigma_{\mathrm{ff}}^{i}) V^{i}}{\sum_{i=1}^{n} V^{i}}, \tag{3.71}$$

where $\sigma_{\mathrm{ff}}^{i} = \bar{\mathbf{f}}_0^{i} \cdot (\boldsymbol{\sigma}^{i} \bar{\mathbf{f}}_0^{i})$ is the myofibre stress at the centroid of i^{th} element, $\boldsymbol{\sigma}^{i}$ is the Cauchy stress at the centroid of i^{th} element, $\bar{\mathbf{f}}_0^{i}$ is the unit vector of the myofibre direction at the centroid of i^{th} element, V^{i} is the volume of i^{th} element, n is the total number of elements occupied by the LV wall. The volumetric-averaged stresses along the sheet direction ($\bar{\sigma}_{\mathrm{ss}}$) and the sheet-normal direction ($\bar{\sigma}_{\mathrm{nn}}$) can be calculated using similar methods.

Volumetric-averaged stresses in one cardiac cycle

In this section, firstly, we illustrate the volumetric-averaged stress curves throughout one cardiac cycle. Secondly, we present the volumetric-averaged stresses at three different time points, namely, ED, peak systole, and ES. These results are in good agreement with previously published data. Lastly, we demonstrate the stress distributions across the entire LV wall at two specific time points, ED and ES.

Volumetric-averaged stresses in one cardiac cycle along the myofibre direction ($\bar{\sigma}_{\mathrm{ff}}$), the sheet direction ($\bar{\sigma}_{\mathrm{ss}}$), and the sheet-normal direction ($\bar{\sigma}_{\mathrm{nn}}$) are shown in Fig. 3.7 (a, b, c). The systolic period is from 0.3 s to 0.5 s, which is between the two vertical dashed lines in those figures. Note that the systolic period is a part of the ABAQUS contraction step.

For $\bar{\sigma}_{\mathrm{ff}}$, as shown in Fig. 3.7 (a), it increases from zero to 3.6 kPa during the filling phase (0 - 0.3 s), followed by a rapid increase to a peak value of 35.4 kPa during the contraction phase (0.3 s - 0.7 s), and then decreases to zero. During the recovery phase (0.7 s - 0.8 s), it remains zero. For $\bar{\sigma}_{\mathrm{ss}}$, as shown in Fig. 3.7 (b), it slightly decreases during the filling phase, then rapidly drops to a minimum value of -3.4 kPa during the contraction phase, and finally increases to zero. It remains zero during the recovery phase. For $\bar{\sigma}_{\mathrm{nn}}$, as shown in Fig. 3.7 (c), it increases from zero to 1.6 kPa during the filling phase. During the contraction phase, it first increases to 3.4 kPa, and then decreases to -0.6 kPa. After the closing of the aortic valve, it starts to increase until it reaches zero during the recovery phase.

The absolute maximum values of $\bar{\sigma}_{\mathrm{ss}}$ is 3.4 kPa, which happens to be the same as the absolute maximum values of $\bar{\sigma}_{\mathrm{nn}}$. However, their maximum values do not occur at the same time. Moreover, they are 90.4% lower than the maximum value of $\bar{\sigma}_{\mathrm{ff}}$. The peak value of $\bar{\sigma}_{\mathrm{ff}}$ occurs during systole due to the dominance of active tension along the myofibre direction as shown in Fig. 3.8. The active tension is governed by the active contraction model. It first reaches its maximum peak of 49.9 kPa and then decreases to zero. Thus, the average stress along the myofibre direction is dominant by the active tension in systole. In general, the volumetric-averaged myofibre stress has the same trend as the active tension. In addition, the maximum values of the myofibre stress and the active tension occurs at the same time during systole.

The volumetric-averaged stresses in one cardiac cycle have rarely been reported in the literature, thus, it is difficult to validate them. However, model-predicted volumetric-averaged myofibre stress at ED and at ES can be found in studies (Genet et al., 2014; Sack et al., 2016, 2018; Fan et al., 2019), which are summarised in Table 3.2. The average myofibre stress at ED is from 1.47 kPa to 2.53 kPa, and the average myofibre stress at ES is from 14.45 kPa to 36.08 kPa. Our average myofibre stresses at ED and at ES are both comparable to simulated results from Fan et al. (2019). Specifically, our average myofibre stress at ED is 3.26 kPa, which is 28.9% higher than theirs, and our average myofibre

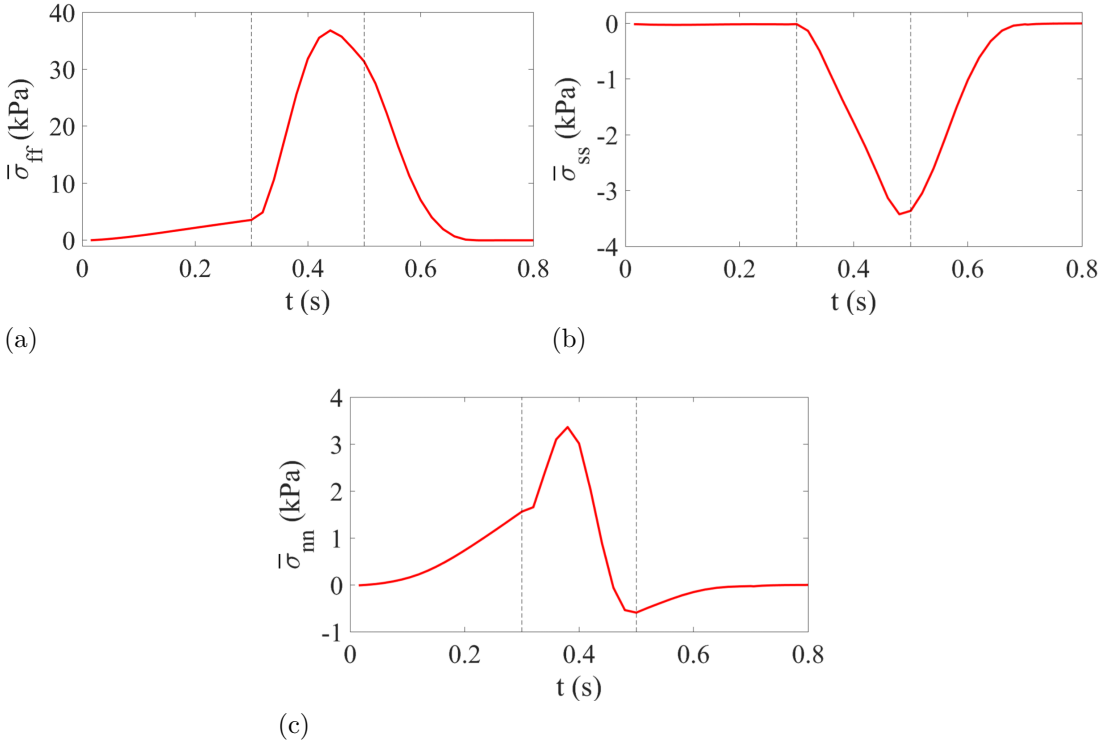

Figure 3.7: Average stresses over the whole LV wall in a cardiac cycle, namely along the myofibre direction $\bar{\sigma}_{\mathrm{ff}}$ in (a), along the sheet direction $\bar{\sigma}_{\mathrm{ss}}$ in (b), and along the sheet-normal direction $\bar{\sigma}_{\mathrm{nn}}$ in (c).

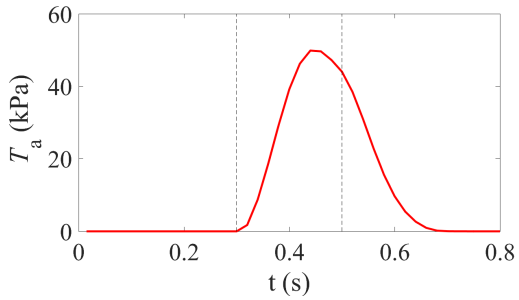

Figure 3.8: Average active tension (T_a) over the whole LV wall in a cardiac cycle.

stress at ES is 27.32 kPa, which is 24.3% lower than theirs. Because of different material models, parameters, and boundary conditions, such differences are expected. Moreover, the stress deviation values exhibit considerable magnitude, indicating a high degree of heterogeneity in the stress distribution. It also happens in other studies (Genet et al., 2014; Sack et al., 2016, 2018; Fan et al., 2019). At ED, this is mainly caused by the high-pressure difference between the LV cavity pressure for the LV endocardial surface and the environment pressure for the LV epicardial surface. At ES, this is caused by the helical orientation of the myofibre structure, especially for a patient-specific geometry.

Table 3.3 provides a summary of the average stresses observed at three specific time points: at ED, at peak systole, and at ES. It can be found that the absolute values of $\bar{\sigma}_{\mathrm{ff}}$

Table 3.2: Comparison of the simulated average myofibre stress (kPa) from the left ventricle model with published data.

	(Genet et al., 2014)	(Sack et al., 2016)	(Sack et al., 2018)
ED	2.21 ± 0.58	1.47 ± 20.72	2.1 ± 4.2
ES	16.54 ± 4.73	14.45 ± 106.72	18.6 ± 14.9
	(Fan et al., 2019)	Ours	
ED	2.53	3.26±16.42	
ES	36.08	27.32±26.33	

are much higher than that of $\bar{\sigma}_{\mathrm{ss}}$ and $\bar{\sigma}_{\mathrm{nn}}$. At the peak systole, $\bar{\sigma}_{\mathrm{ff}}$ reaches its maximum value of 35.40 kPa, which is about 9 times higher than $\bar{\sigma}_{\mathrm{ss}}$, while $\bar{\sigma}_{\mathrm{nn}}$ is neglectable. In fact, due to the high active contraction force in systole, $\bar{\sigma}_{\mathrm{ss}}$ and $\bar{\sigma}_{\mathrm{nn}}$ are both neglectable compared with $\bar{\sigma}_{\mathrm{ff}}$. At ED, the absolute value of $\bar{\sigma}_{\mathrm{ff}}$ is 145.1% higher than that of $\bar{\sigma}_{\mathrm{nn}}$, and the absolute value of $\bar{\sigma}_{\mathrm{ss}}$ is neglectable.

Table 3.3: Simulated average stresses (kPa) from the left ventricle model at three particular time points.

	End-diastole	Peak systole	End-systole
$\bar{\sigma}_{\mathrm{ff}}$	3.26±16.42	35.40±30.71	27.32±26.37
$\bar{\sigma}_{\mathrm{ss}}$	-0.14±16.37	-3.51±27.19	-3.34±23.71
$\bar{\sigma}_{\mathrm{nn}}$	1.33±16.49	-0.42±26.85	-0.77±23.43

In summary, the volumetric-averaged stress along the myofibre direction is dominant. In systole, it is much higher than stresses along the sheet and sheet-normal directions due to the active contraction force.

Stress distribution in the LV wall

From the curves and values of the volumetric-averaged stresses in the last section, we have seen that the average stress along the myofibre direction is the highest. In this section, the stress distributions in the LV wall at ED and at ES in the myofibre direction, in the sheet direction, and in the sheet-normal direction are shown, respectively.

Firstly, distributions of the stresses (σ_{ff}, σ_{ss}, σ_{nn}) at ED are shown in Fig. 3.9. It should be noted that the LV volume is at its maximum at ED in one cardiac cycle.

The stress distributions are heterogeneous, with some regions at the endocardial surface of the LV exhibiting the highest stresses. This distribution is related to the geometric irregularities of the inner surface of the LV and the corresponding variations in the myofibre orientation. The average stresses at ED, as listed in Table 3.3, are 3.26±16.42 kPa for σ_{ff}, -0.14±16.37 kPa for σ_{ss}, and 1.33±16.49 kPa for σ_{nn}. Interestingly, even without active contraction force at ED, σ_{ff} is the highest. Moreover, all three stresses are higher at the endocardial surface than at the epicardial surface, which can be attributed to the pressure difference between the LV and the surrounding environment.

Secondly, distributions of the stresses (σ_{ff}, σ_{ss}, σ_{nn}) at ES are shown in Fig. 3.10. At ES, the LV volume is at its minimum while the LV pressure remains significantly elevated. The LV geometries at ED are depicted as solid black outlines in Fig. 3.10 for comparison purposes, enabling the observation of contraction and long-axis shortening of the LV. The stresses observed at ES are significantly higher than those at ED, primarily due to the high LV cavity pressure and active contraction force. As previously noted, the stress along the myofibre direction (σ_{ff}) is higher than the other two stresses (σ_{ss} and σ_{nn}), given the high active tension along this direction. The stresses σ_{ss} and σ_{nn} exhibit similar distributions, with positive stresses in the epicardial layers that become negative stresses in the endocardial layers. However, the transmural distribution of the myofibre stress is not monotonic. Near the basal and middle regions, σ_{ff} exhibits high positive values in the middle layers of the LV wall and low positive values at the epicardial and endocardial surfaces. In contrast, in the apical regions, highly negative σ_{ff} values exist in the middle layers as well as in both the epicardial and endocardial surfaces.

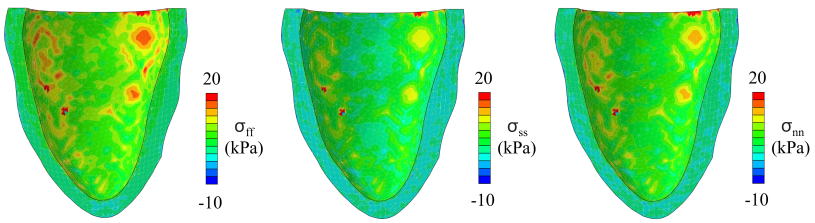

Figure 3.9: Distributions of stresses at the end of diastole along the myofibre direction σ_{ff}, the sheet direction σ_{ss}, and the sheet-normal direction σ_{nn}, respectively.

Stress distribution of the human heart can provide valuable information for clinical diagnoses, such as quantifying myocardial contractility and predicting cardiac growth and remodelling. Despite the limitations of current imaging techniques in capturing this distribution, some computational heart models (Genet et al., 2014; Sack et al., 2018; Wisneski et al., 2020) have been employed to predict the stress distribution in the heart. Genet et al. (2014) utilised MRI data to construct five computational LV models of normal subjects and reported the reference myofibre stresses of the LV wall at both ED and ES.

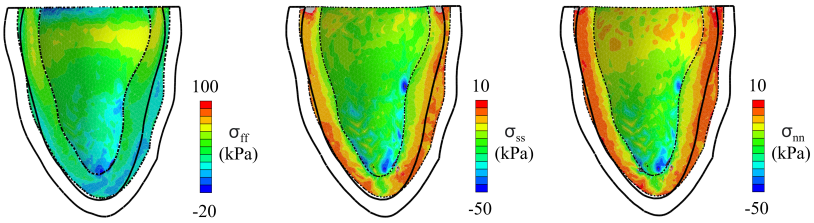

Figure 3.10: Distributions of stresses at the end of systole along the myofibre direction σ_{ff}, the sheet direction σ_{ss}, and the sheet-normal direction σ_{nn}, respectively. The solid black outlines are used for comparison, which are outlines of the LV geometry at the end of the diastole.

They found that their simulated myofibre stress at ED was higher near the subendocardial wall than near the subepicardial wall. Moreover, their myofibre stress at ES was higher in the middle layer of the myocardium and the basal regions. These findings are generally consistent with our results, as shown in Fig. 3.9 (a) and Fig. 3.10 (a). However, it is important to note that they used the transversely isotropic Fung model for the passive material properties, which may impact the stress distribution. Another study by Sack et al. (2018) also demonstrated heterogeneous myofibre stress distribution in a long-axis cut plane of both the LV and RV. At ED, their maximum myofibre stress appeared in the subendocardial and basal regions. At ES, high myofibre stress appeared in the middle and endocardial layers of the LV wall near the basal and middle regions, while myofibre stress was negative near the apical regions. Similarly, Wisneski et al. (2020) showed myofibre stress distribution in a long-axis cut plane of both the LV and RV at ED and peak systole, with predominantly negative myofibre stress appearing in the subendocardial regions at peak systole.

In conclusion, variations in myocardial geometry and material properties lead to variations in myofibre stress distribution across different studies, while the general patterns remain consistent. In specific, most studies have observed higher myofibre stress at ED in the subendocardial layers compared to the subepicardial layers of the LV wall. At ES, the distribution of myofibre stress across the LV wall is non-monotonic, with high positive myofibre stress in the middle layers around the basal and middle regions, and negative myofibre stress in the subendocardial layers near the apical regions.

Volumetric-averaged myofibre stress in the AHA regions

We further computed the volumetric-averaged myofibre stress in the 17 American Heart Association (AHA) regions, which will be described in detail in Section 4.4.1. In brief, the LV wall is partitioned into 17 regions, comprising 6 basal regions, 6 middle regions, and 5 apical regions. As shown in Fig. 3.11, the myofibre stresses in all AHA regions exhibit

similar trends, with differences in peak values and the time taken to reach those peaks. During the filling phase, myofibre stresses increase gradually. In the contraction phase, they first rise rapidly to reach their maximum values before returning to zero. Throughout the recovery phase, myofibre stresses remain at zero. In the basal regions, the peak values of σ_{ff} range from 47.2 kPa (in region 5) to 55.7 kPa (in region 3). In the middle regions, the maximum values of σ_{ff} are between 25.8 kPa (in region 7) and 38.4 kPa (in region 10). For the apical regions, the peak values of σ_{ff} range from 13.9 kPa (in region 17) to 27.3 kPa (in region 15). Therefore, σ_{ff} varies across regions and decreases from the basal to the apical regions. Notably, region 3 has the highest myofibre stress, whereas the apex (region 17) has the lowest myofibre stress.

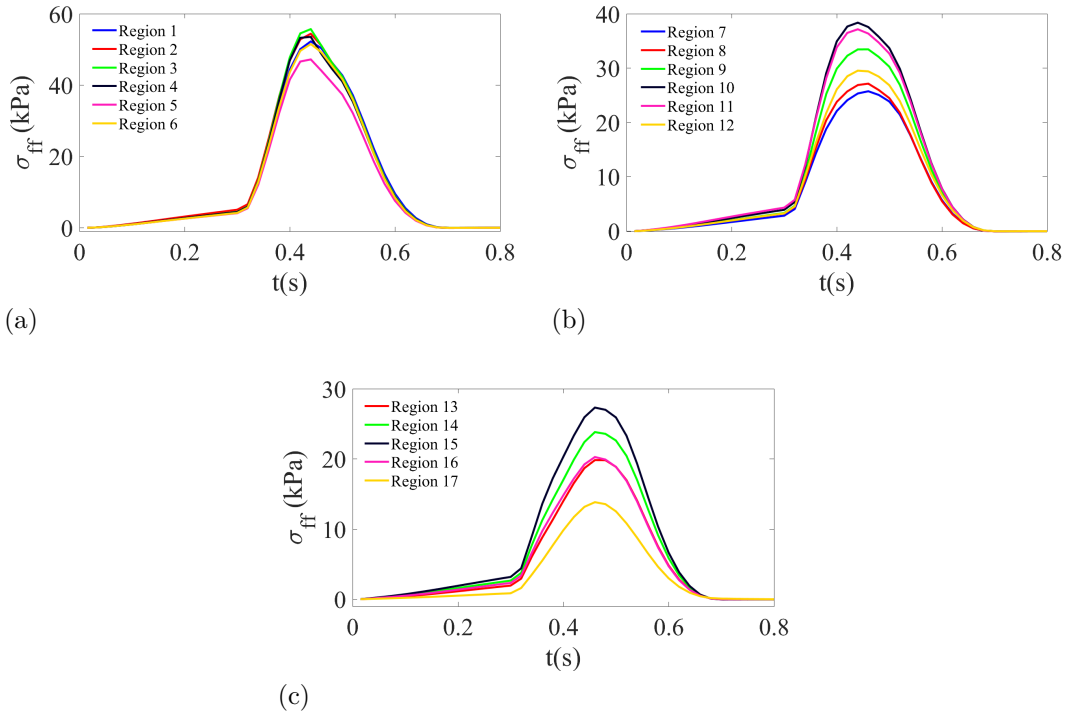

Figure 3.11: Average myofibre stresses in six basal regions (a), six middle regions (b), and five apical regions (c).

Fig. 3.12 shows the average myofibre stresses in the 17 AHA regions at peak systole. In a previous study, Wisneski et al. (2020) reported that the average myofibre stresses in the 17 AHA regions range from 3.89 kPa to 30.03 kPa. However, our average myofibre stresses are higher, ranging from 13.84 kPa to 55.70 kPa. This discrepancy could be due to the differences in geometries, boundary conditions, and material properties used in the two studies. For instance, they used a whole four-chamber human heart model, which may have constrained the deformation of their basal regions more than in our single ventricle model. Furthermore, the interventricular septum regions (regions 2, 3, 8, 9, 14) are under different boundary conditions given that the right ventricle pressure affects the motion of

the septum, whereas we assumed that it moves freely.

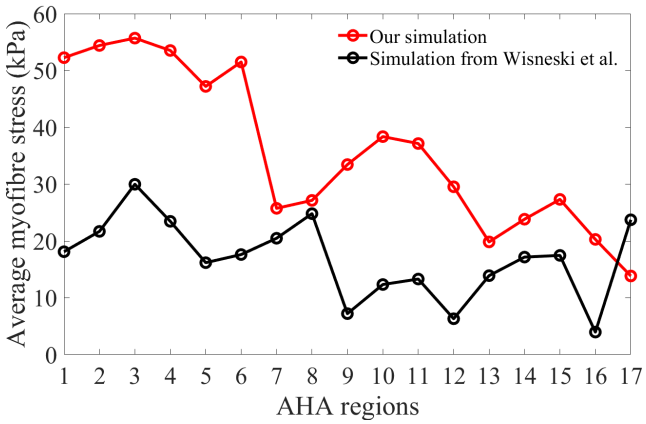

Figure 3.12: Average myofibre stresses in the 17 AHA regions at peak systole. Simulated results from (Wisneski et al., 2020) are adopted for comparison.

3.5 Effects of myofibre rotation on cardiac functions

The LV model described above has been modified to study the impact of myofibre rotations and myofibre dispersion on cardiac dynamics, as published in (Guan et al., 2022c). The subsequent sections present the outcomes of the investigation.

In order to assess the deformation of the LV wall, we now introduce long-axis shortening, radial-axis shortening, and apex twist angle during systole. These parameters have been commonly employed in the literature (Rogers Jr et al., 1991; Alam et al., 1992; Sengupta et al., 2008; Omar et al., 2015) to evaluate the contractile function of the LV. The long-axis shortening (%) is defined by

$$\mathrm{LAS} = (L_t - L_0)/L_0 \times 100, \tag{3.72}$$

where L_0 and L_t are the long-axis lengths of the LV at ED and at the current time t, respectively, and the long-axis length of the LV is the distance between the centre point at the basal plane and the apical point at the endocardial surface as shown in Fig. 3.13. The radial-axis shortening is calculated as the mean radius change of the selected points at the middle region of the LV, i.e.

$$\mathrm{RAS} = (R_t - R_0)/R_0, \tag{3.73}$$

where R_0 is the mean radius of the selected points at the endocardial surface of the middle plane of the LV at ED, and R_t is the mean radius at the current time t.

In this section, we first investigate the LV cardiac functions using different myofibre

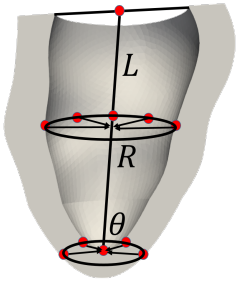

Figure 3.13: Positions of selected nodes (red points) to calculate long axis shortening and apex twist angle. L is the length of the left ventricle from the centre point of the base plane to the endocardial apex point, and R is the mean radius of the selected points at the endocardial surface of the middle plane of the left ventricle. θ is the mean rotation angle of the selected points at the epicardial surface near the apical region with a reference state of their positions at the end of diastole.

rotation angles. Seven cases are considered here with different myofibre rotation angles from the epicardium to the endocardium:

- rot-80: $-40^\circ \sim 40^\circ$, and the rotation angle: 80°;
- rot-100: $-50^\circ \sim 50^\circ$, and the rotation angle: 100°;
- rot-120: $-60^\circ \sim 60^\circ$, and the rotation angle: 120°;
- rot-140: $-70^\circ \sim 70^\circ$, and the rotation angle: 140°;
- rot-160: $-80^\circ \sim 80^\circ$, and the rotation angle: 160°;
- rot-unsym1: $-30^\circ \sim 90^\circ$, and the rotation angle: 120°;
- rot-unsym2: $-90^\circ \sim 30^\circ$, and the rotation angle: 120°.

The diagrams of the corresponding myofibre structures of the seven cases are shown in Fig. 3.14. Cases rot-80 to rot-160 have the same angle to the circumferential direction with opposite signs at the epicardium and the endocardium, denoted as symmetrical rotation cases, and cases rot-unsym1/2 have different angles to the circumferential direction at the epicardium and the endocardium, denoted as unsymmetrical rotation cases. All seven cases consider the same myofibre dispersion distribution. The values of the corresponding scaling factors n_f, n_s and n_n in Eq. (3.63) are 0.879, 0.009, and 0.112, respectively, which were obtained from (Guan et al., 2021).

Fig. 3.15 (a) shows the pressure-volume (PV) loops of the seven cases. The values of the end-diastolic volume (EDV), end-systolic volume (ESV), and ejection fraction (EF) are summarised in Table 3.4. For the symmetrical rotation cases (case rot-80 to case rot-160), EF can be improved when increasing the myofibre rotation angle from 80° (case rot-80) to 140° (case rot-140). The smallest ESV (46.1 ml) appears when the rotation angle is 140°.

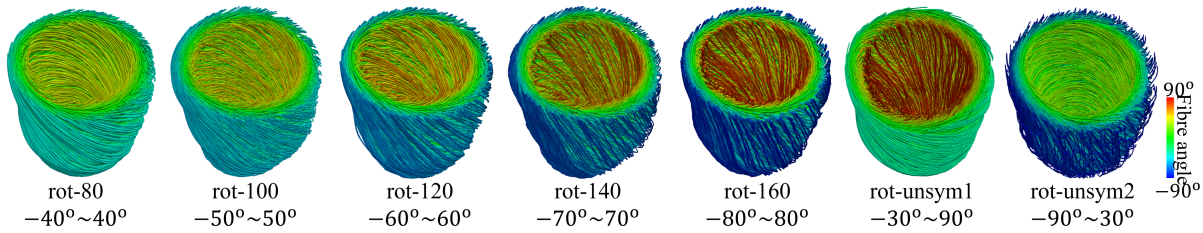

Figure 3.14: Myofibre structures with different transmural rotation angles.

Interestingly, EDV increases approximately by 1.0 ml per 20° increment of the myofibre rotation angle. The EF of the case rot-80 is 46.0% (< 50%), which is abnormal for healthy subjects (Kumar et al., 2014; Mahadevan et al., 2008; Dokainish et al., 2011; Feher, 2017; Lang et al., 2015). In addition, the EF of the unsymmetrical rotation case rot-unsym2 is also lower than normal values.

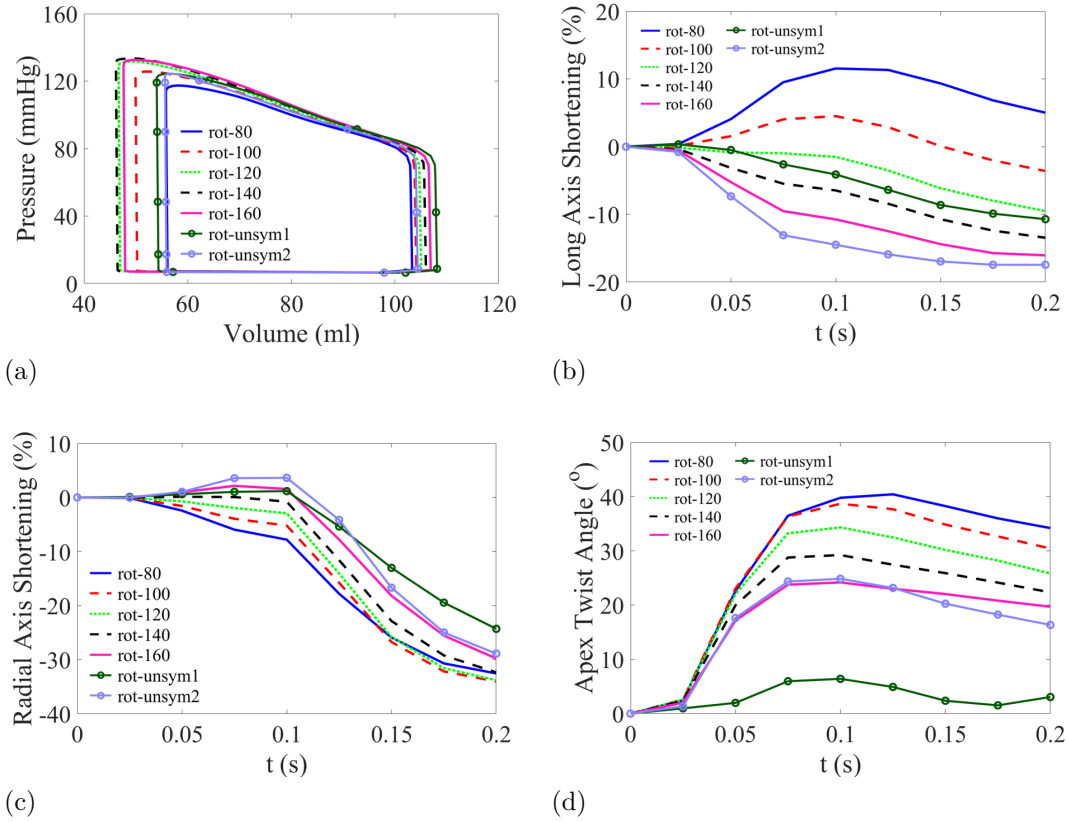

Figure 3.15: Using different myofibre rotation structures in the left ventricle model, pressure-volume loops (a), long-axis shortening (b), radial axis shortening (c), and apex twist angle (d). Results from the end of diastole to the end of systole in one cardiac cycle are shown because active tension plays the primary role in cardiac dynamics during this period (about 0.2 s).

Long-axis shortenings of the seven cases are shown in Fig. 3.15 (b). The greater negative value of the long-axis shortening indicates a larger longitudinal contraction. For

Table 3.4: Cardiac pump functions with different myofibre rotation angles. EDV: end-diastolic volume, ESV: end-systolic volume, EF: ejection fraction, L_r^{ES}: Long-axis shortening at the end of systole (ES), R_r^{ES}: Radial axis shortening at ES, and θ_r^{ES}: Apex twist angle at ES. $\bar{\sigma}_{\mathrm{ff}} \pm \vartheta$ is mean and standard deviation of myofibre stress σ_{ff}.

Rotation case	EDV (ml)	ESV (ml)	EF (%)	L_r^{ES} (%)	R_r^{ES} (%)	θ_r^{ES} (°)	$\bar{\sigma}_{\mathrm{ff}} \pm \vartheta$ (kPa)
rot-80	103.3	55.8	46.0	5.0	-32.4	34.2	33.8±31.1
rot-100	104.1	49.9	52.0	-3.6	-33.8	30.4	34.6±31.1
rot-120	105.0	46.7	55.6	-9.5	-33.8	25.8	34.9±30.7
rot-140	106.0	46.1	56.5	-13.5	-32.4	22.3	35.8±31.2
rot-160	106.9	47.6	55.5	-16.0	-30.0	19.7	37.0±32.4
rot-unsym1	108.1	54.0	50.0	-10.7	-24.3	3.0	34.7±37.4
rot-unsym2	104.4	55.6	46.7	-17.4	-28.9	16.3	43.7±33.8

the symmetrical rotation cases, the long-axis shortening ratio at ES ($t = 0.2\,s$) increases with increasing myofibre rotation angle from case rot-80 (5.0%) to case rot-160 (-17.4%). Interestingly, for cases rot-80 and rot-100, due to the small rotation angle, the long-axis shortening ratio is positively increasing in the early systole rather than shortening compared with other cases. This long axial elongation during systole suggests that the LV does not contract longitudinally, which is not physiologically accurate. In addition, the long-axis shortening of the case rot-80 remains positive during systole. The radial-axis shortenings of the seven cases all have the same trends as shown in Fig. 3.15 (c). The differences in the radial-axis shortenings are moderate. The radial-axis shortenings at ES are from -24.3% to -33.8%. Fig. 3.15 (d) plots apex twist angles of the LV. The apex twist angles at ES are from 34.2° in case rot-80 to 19.7° in case rot-160. In general, the larger the rotation angle of the myofibre, the smaller the apex twist angle.

The two unsymmetrical rotation cases, case rot-unsym1 and case rot-unsym2, have the same total rotation angle as case rot-120. As shown in Fig. 3.14, the myofibre rotation angle is large at the endocardial layers in the case rot-unsym1 but large at the epicardial layers in the case rot-unsym2. Compared with case rot-120 with an EF of 55.6%, both unsymmetrical cases have reduced cardiac outputs as shown in Table 3.4. EF of the case rot-unsym1 is 50.0% and EF of the case rot-unsym2 is 46.7%. This is mainly caused by the enlarged ESV of the two unsymmetrical rotation cases. Compared with case rot-120, the EDVs of the two unsymmetric cases change slightly but the ESVs of the two unsymmetric cases are significantly larger. Small myofibre angle at the endocardium in case rot-unsym2

achieves both higher radial (Fig. 3.15 (c)) and long-axis shortening (Fig. 3.15 (b)) compared to case rot-unsym1, whilst they both experience less circumferential contraction and larger longitudinal contraction compared to case rot-120, which may be explained by more longitudinally aligned myofibres in those two unsymmetric cases. Furthermore, the unsymmetrical myofibre rotation significantly reduces the apex twist as shown in Fig. 3.15 (d), in which the apex twist angle at ES is 3.0° for case rot-unsym1 and 16.3° for case rot-unsym2, much less than that of case rot-120 (25.8°).

LV shapes and distributions of the myofibre stresses (σ_{ff}) at ES of the seven cases are shown in Fig. 3.16, and corresponding volumetric-averaged myofibre stress are listed in Table 3.4. For the symmetrical rotation cases, it can be found that the long-axis shortenings increase from case rot-80 to case rot-160. The average myofibre stress $\bar{\sigma}_{\mathrm{ff}}$ also increases from case rot-80 (33.8±31.1 kPa) to case rot-160 (37.0±32.4 kPa). Compared with cases rot-120/140/160, higher myofibre stress can be found at the basal regions of the LV in cases rot-80, rot-100, and rot-unsym2 with more heterogeneous stress distributions. Corresponding statistic density distributions of σ_{ff} are shown in Fig. 3.17. It can be found that case rot-unsym1 and case rot-unsym2 both have more heterogeneous stress distributions compared with other cases. Case rot-120 has the least standard deviation suggesting the least heterogeneous distribution.

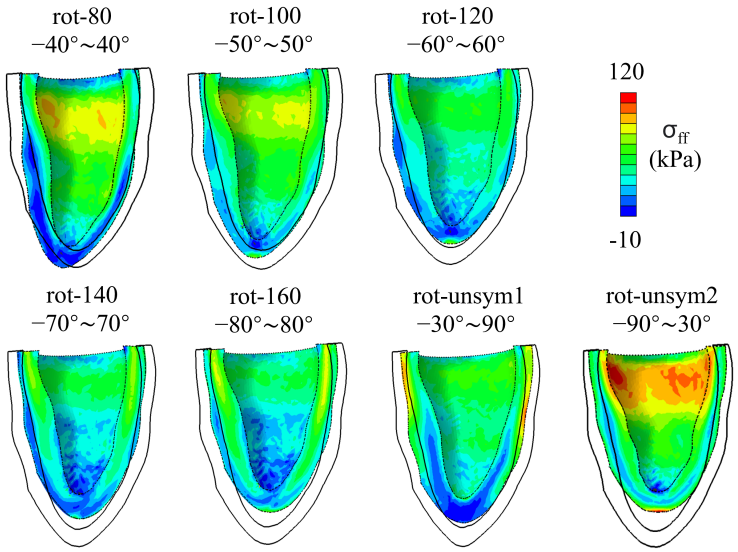

Figure 3.16: Distributions of myofibre stress σ_{ff} in seven fibre rotation cases at the end of systole. The solid curves outline the corresponding end-diastolic boundary of the cutting plane of the left ventricle.

In summary, changes in myofibre rotation angles can significantly alter LV cardiac functions. In general, a myofibre structure with a larger total rotation angle, i.e. case rot-140, yields greater EF and longitudinal contraction, but less apex twist angle. For the human LV model, it shows that the myofibre rotation angle in a range of $120° \sim 140°$ can

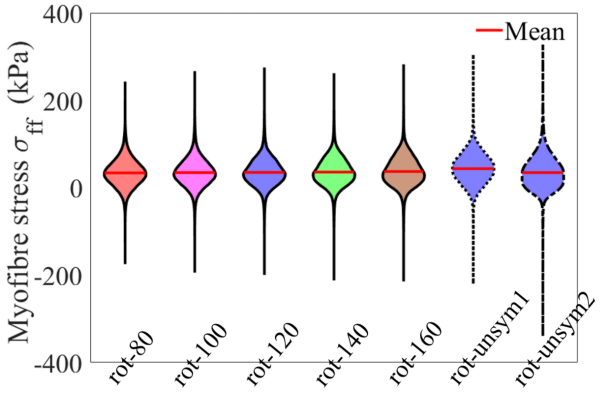

Figure 3.17: Violion plot of the stress along myofibre direction (σ_{ff}) over the whole left ventricle wall when using different myofibre rotation structures.

achieve a more physiologically accurate pump function, i.e. EF>50%. In fact, the myofibre rotation angle from 60° to -60° is the most widely used range in the literature (Wang et al., 2013; Gao et al., 2014, 2017), and also within the range reported by experimental studies (Sommer et al., 2015).

3.6 Effects of fibre dispersion on cardiac functions

As described in Section 3.2.4, the active stress considering fibre dispersion is

$$\boldsymbol{\sigma}^{a}_{\mathrm{Dpf}} = n_{\mathrm{f}} T_{\mathrm{a}} \mathbf{f}_0 \otimes \mathbf{f}_0 + n_{\mathrm{s}} T_{\mathrm{a}} \mathbf{s}_0 \otimes \mathbf{s}_0 + n_{\mathrm{n}} T_{\mathrm{a}} \mathbf{n}_0 \otimes \mathbf{n}_0, \tag{3.74}$$

where n_{f}, n_{s}, and n_{n} are proportions of the active tension in the fibre, sheet, and sheet-normal directions, respectively. Guan et al. (2020a) has shown that $n_{\mathrm{s}} = 0.008$ based on Sommer et al.'s measurements from human myocardium (Sommer et al., 2015) and $n_{\mathrm{s}} = 0.0009$ based on Ahmad et al.'s measurements from neonatal porcine myocardium (Ahmad et al., 2018a). Both values are very close to zero, thus we assumed that the active tension along sheet direction is negligible so that $n_{\mathrm{s}} = 0$. According to Eq. (3.64), value of n_{s} drops to less than 0.01 for any b_1 when $b_2 \geq 16$, thus we set $b_2 = 16$, whilst values of n_{f} and n_{n} are determined by b_1. Finally, five cases of myofibre dispersion are designed as follows:

- case f10n0: $n_{\mathrm{f}} = 1.0$, and $n_{\mathrm{n}} = 0.0$, corresponding to no-dispersion;
- case f8n2: $n_{\mathrm{f}} = 0.8$, and $n_{\mathrm{n}} = 0.2$, ($b_1 = 2.9$, and $b_2 = 16$);
- case f6n4: $n_{\mathrm{f}} = 0.6$, and $n_{\mathrm{n}} = 0.4$, ($b_1 = 1.35$, and $b_2 = 16$);
- case f5n5: $n_{\mathrm{f}} = 0.5$, and $n_{\mathrm{n}} = 0.5$, ($b_1 = 0.85$, and $b_2 = 16$);
- case f4n6: $n_{\mathrm{f}} = 0.4$, and $n_{\mathrm{n}} = 0.6$, ($b_1 = 0.35$, and $b_2 = 16$).

The corresponding myofibre dispersion distributions (b_1 and b_2 in Eq. (3.54)) are determined according to the values of n_{f}, n_{s} and n_{n}. Myofibre structures of the above five cases are the same as that of case rot-120 ($-60^{\circ} \sim 60^{\circ}$) in Section 3.5 but with different in-plane and out-of-plane dispersion.

Fig. 3.18 (a) shows the PV loops of the LV model with different dispersed active tension, and the related EDV, ESV, and EF are summarised in Table 3.5. Overall, the more the active contraction along the sheet-normal direction, the smaller the ESV and the larger the EDV. For instance, the ESV of case f4n6 is 31.6 ml, which is much smaller than that of case f10n0 which has an ESV of 45.9 ml. Similarly, the long-axis shortening is greater with increasing n_{n} as shown in Fig. 3.18 (b). Long-axis shortening ratios at ES are negative for all cases, from -8.1% in case f10n0 to -39.2% in case f4n6. Conversely, the radial-axis shortening is smaller when there is more active tension along the sheet-normal direction, from -34.3% in case f10n0 to -27.0% in case f4n6 as shown in Fig. 3.18 (c). It also can be found that the sheet-normal contraction can prevent long-axis elongation during systole in case f10n0.

Apex twist angle is significantly influenced by the sheet-normal active tension as shown in Fig. 3.18 (d). When n_{f} is greater than n_{n}, the apex twist angle increases to the peak value quickly at early systole and then decreases slightly at late systole, while the larger n_{n} in cases f5n5 and f4n6 lead to continuously increased apex twist in systole.

Table 3.5: Cardiac pump functions with different myofibre dispersion distributions.

Dispersion case	EDV (ml)	ESV (ml)	EF (%)	L_r^{ES} (%)	R_r^{ES} (%)	θ_r^{ES} (°)	$\bar{\sigma}_{\mathrm{ff}} \pm \vartheta$ (kPa)
f10n0	104.0	45.9	55.9	-8.1	-34.3	27.8	38.5±33.4
f8n2	105.2	45.3	57.0	-12.2	-33.8	23.3	30.7±28.8
f6n4	107.0	41.2	61.3	-25.0	-31.6	7.5	23.1±31.7
f5n5	107.4	32.9	69.4	-35.3	-28.1	10.6	17.9±40.2
f4n6	108.1	31.6	70.8	-39.2	-27.0	37.4	4.5±41.8

Although a very strong pump function is achieved in case f5n5/f4n6 according to the PV loops in Fig. 3.18 (a), excessive longitudinal contraction with compressed myofibres around the endocardium can be found in Fig. 3.19. Case f8n2 and f6n4 have more homogeneous stress distributions at the base with better EF and greater long-axis shortening. Fig.3.20 shows the statistics of the myofibre stress in all elements for the five cases, in which case f8n2 has the most homogeneous myofibre stress distribution. Case f6n4 achieves a better pump function with smaller myofibre stress than case f10n0 and case f8n2 while high positive σ_{ff} locates at the middle layer of the LV wall and prevents the

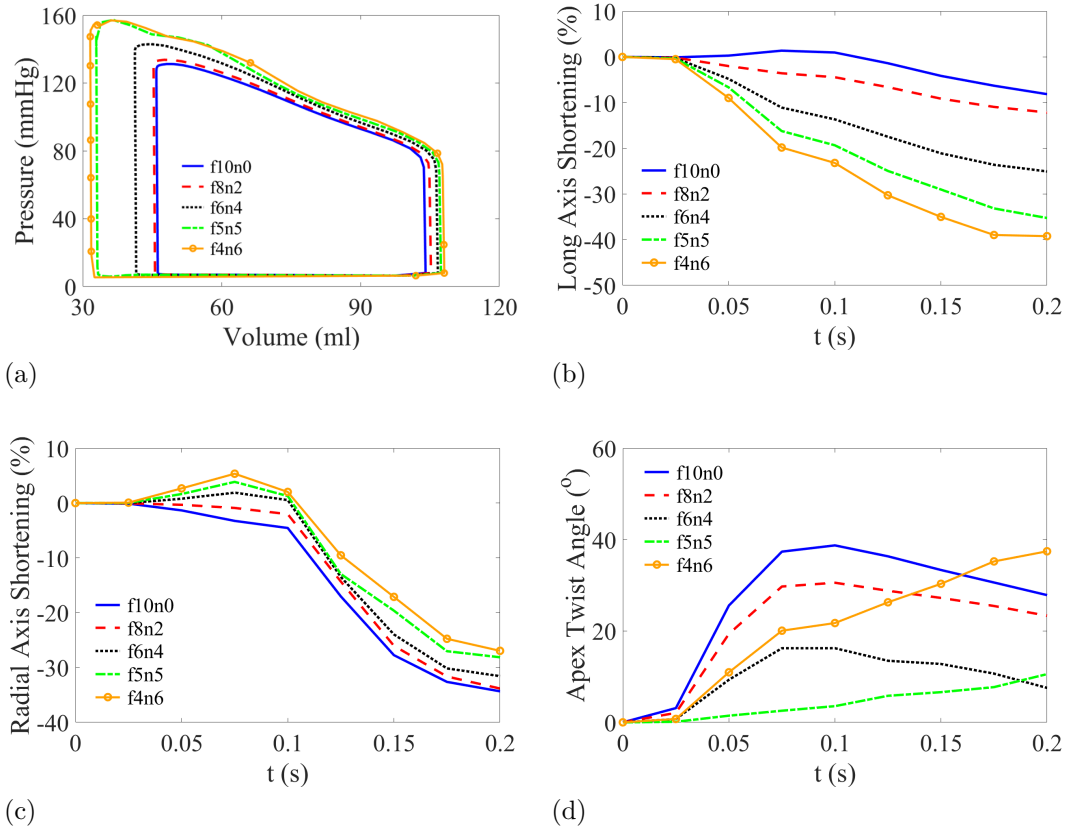

Figure 3.18: Using different sheet-normal active tension in the left ventricle model, pressure-volume loops (a), long-axis shortening (b), radial axis shortening (c), and apex twist angle (d).

myofibre compression in case f4n6 and case f5n5. Mean values of σ_{ff} of the whole heart at ES are summarised in Table 3.5. The myofibre stress σ_{ff} reduces dramatically from 38.5 kPa in case f10n0 to 4.5 kPa in case f4n6 (Fig. 3.20), which is presumably because the active tension aligns more along the sheet-normal direction and less along the myofibre direction.

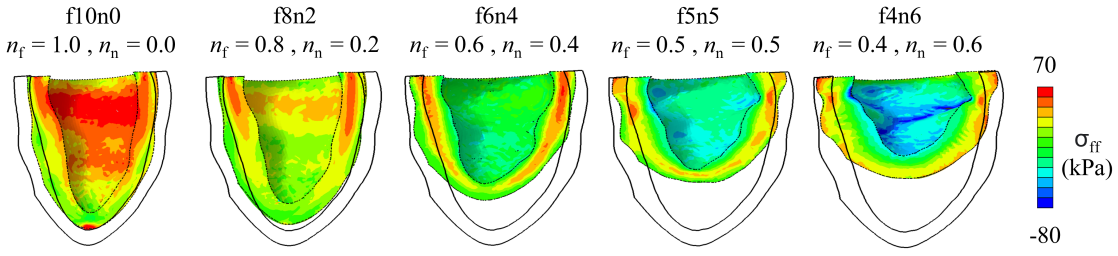

Figure 3.19: Distributions of myofibre stress σ_{ff} in five fibre dispersion cases at the end of systole. The solid curves outline the corresponding end-diastolic boundary of the cutting plane of the left ventricle.

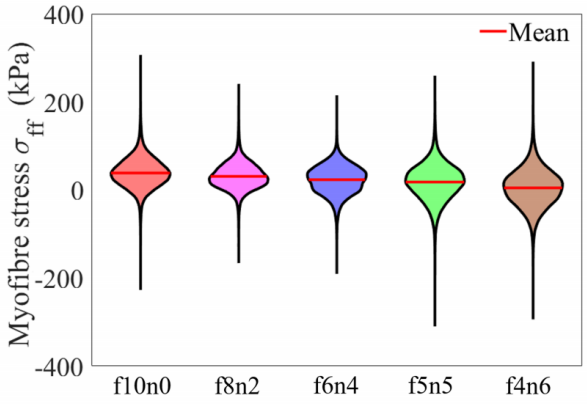

Figure 3.20: Violin plot of myofibre stress (σ_{ff}) in all elements of the left ventricle when using different dispersed active tension.

In summary, we find that increasing $n_{\mathrm{n}} > 0$ can lead to better cardiac output, greater long-axis contraction, and much-reduced myofibre stress during systole. However, with larger n_{n}, i.e. $n_{\mathrm{n}} \geq 0.4$, excessive long-axis contraction occurs and the stress distribution may be not physiologically correct.

3.7 Summary

This chapter outlined the formulation, implementation, and result of a FE model of the LV. Patient-specific geometry was utilised, and a rule-based myofibre architecture was employed in constructing the LV model. The passive response of the myocardium was modelled using the HO model, while the active response was modelled using the time-varying elastance model. To simulate boundary conditions within a cardiac cycle, a lumped parameter system was utilised. The LV model was implemented in ABAQUS, and the explicit solver was utilised to solve the system. Results, including pressure and volume curves, as well as stress analysis of a baseline case, were presented in Section 3.4. Additionally, the impact of different myofibre rotations and myofibre dispersions on cardiac functions was explored.

This chapter aimed to develop a realistic model of the LV that can be used to simulate pressures in the LV and aorta as well as the stress distribution in the LV wall. These pieces of information can next be utilised to interact with the coronary model developed in Chapter 2. The results obtained from our LV model, as presented in Section 3.4, showed that the computed LV pressure and aortic pressure fall within the reported ranges for healthy subjects. Additionally, the ejection fraction of the LV agreed with published data. Furthermore, in the stress analysis sections, we compared the myofibre stress distribution with that reported in other studies. It was observed that stress along the myofibre direction is dominant.

Effects of the myofibre rotation and myofibre dispersion on cardiac functions of the LV were further investigated. Both myofibre rotation and myofibre dispersion can affect significantly cardiac pump functions by redistributing the active tension circumferentially and longitudinally. For example, a myofibre structure with a larger total rotation angle, i.e. case rot-140, yielded greater EF and longitudinal contraction, but less apex twist angle. For the myofibre rotation, we found that a myofibre rotation angle within a range of $120^\circ \sim 140^\circ$ achieved a more physiologically accurate pump function. For the myofibre dispersion, we found that increasing $n_\mathrm{n} > 0$ can yield better cardiac output, greater long-axis contraction, and much-reduced myofibre stress during systole. However, when larger n_n was utilised, i.e. $n_\mathrm{n} \geq 0.4$, the excessive long-axis contraction was observed and the resulting stress distribution may not be physiologically accurate.

There are several limitations of the LV model developed in this chapter. Firstly, a lumped parameter model was used to represent the systemic circulation, which provides physiologically accurate LV pressure boundary conditions. However, the lumped parameter model can further be replaced by a more sophisticated lumped parameter model or 1D model to account for fluid-structure interactions. Secondly, we assumed that all myocytes contract simultaneously. Although this assumption may be valid for healthy hearts, it is not able to investigate the interactions between electrical and mechanical activities of the heart and fails to account for the variations in conduction velocities that are often present in diseased hearts (Göktepe and Kuhl, 2010; Verzicco, 2022). To address this issue, an electromechanical model can be employed, but such a model would significantly increase the complexity of the modelling process, including the incorporation of the Purkinje fibre network and the challenge of parameter calibration. Thirdly, the development of more advanced constitutive law for the myocardium is a key area of focus. For instance, anisotropic poroelastic response in the large strain regime remains a relatively under-explored area in the field of biomedical engineering applications (Lee et al., 2016). Lastly, we assumed that the LV epicardial surface is free to move. However, this simplified boundary condition does not represent the complex physiological conditions of the heart, particularly in the context of the pericardium's presence. Recently, Pfaller et al. (2019) have demonstrated that using a parallel spring and dashpot acting in the normal direction to the epicardium as pericardium boundary conditions can result in more realistic simulations of cardiac mechanics.

Chapter 4

One-way coupling of the coronary flow model and left ventricle model

There has been a growing focus in recent years on incorporating multiphysical modelling into the study of the complete cardiac processes and functions, including blood flow, myocardial contraction, and electrophysiology. This has resulted in the creation of fully integrated electro-mechano-fluidic heart models that incorporate highly detailed mechanical models of the heart, models of blood flow, and the relationship between the ventricles and the coronary flow (Hunter and Smaill, 1988; Wang et al., 2013; Baillargeon et al., 2014; Quarteroni et al., 2017; Sack et al., 2018; Gray and Pathmanathan, 2018; Niederer et al., 2019). These models are being increasingly personalised to the individual patient, providing a more comprehensive understanding of the interactions between various physical processes within the heart.

In this chapter, a one-way coupling framework between the coronary flow model and the left ventricle (LV) model is developed. The coronary flow model, introduced in Chapter 2, depends on the time-varying elastance model for generating its boundary conditions, namely the aortic pressure and the intramyocardial pressure (IMP), which was assumed to be homogeneous in three regions. With the implementation of the LV model developed in Chapter 3, more physiologically accurate aortic pressure and IMP can be substituted, allowing for the one-way coupling between the two models to be established. The possibility of a two-way coupling, allowing for feedback from the coronary flow model to the LV model, will be briefly explored in Chapter 6.

To achieve the one-way coupling, the LV model needs to be fine-tuned to provide physiologically accurate aortic pressure and IMP. Although obtaining the aortic pressure is straightforward as the LV model includes a lumped parameter system representing the systemic circulation, determining the IMP calculation requires further examination. Additionally, the general locations of the coronary arteries within the myocardium are investigated. The goal of the one-way coupling is to examine the feasibility of the interaction

between the LV model and the coronary flow model in order to study the resulting flow in the human coronary circulation. The results of this chapter show that the one-way coupling model produces physiologically correct coronary flow, as evidenced by comparison with experimental data. This chapter also presents the effects of different IMP on coronary flow. Lastly, this chapter reports myocardial perfusion calculated from the one-way coupling framework, which is found to be in good agreement with published data.

This chapter is organised into five sections. First, the network of the coronary blood vessels is reconstructed based on existing literature. Secondly, the effect of IMP and its calculations in the literature is discussed. Thirdly, simulated coronary flow using two different globally averaged IMPs is presented, followed by a recommendation regarding the preferable IMP formula to utilise. Fourthly, 17 segments of the LV wall suggested by the American Heart Association (AHA) (Cerqueira et al., 2002) and the assignment of the coronary arteries to the AHA segments are investigated. Simulated coronary flow results using regionally averaged IMP based on AHA segments are also presented. Finally, in Section 4.5, myocardial perfusion calculated from the one-way coupling framework is studied.

4.1 Reconstructed network of coronary vasculature for the coronary flow model

In Chapter 2, we have described the mathematical basis of the coronary flow model, along with a comparison of coronary flow outcomes with experimental data using assumed IMP. Before replacing the assumed IMP with the IMP generated by the LV model, in this section, we reconstruct the simplified computational network introduced in Chapter 2 (as shown in Fig. 2.1), with a particular focus on incorporating additional blood vessels into the right coronary artery branch based on data from Duanmu et al. (2019) and the reconstruction of the venous system based on existing literature. As per the methodology described in Chapter 2, the coronary vasculature is categorised into three segments: the epicardial coronary arteries, the epicardial coronary veins, and all other vessels within the heart wall.

4.1.1 Reconstructed right coronary arteries

As shown in Fig. 2.10, the coronary flow in the right coronary arteries is found to be impeded more when compared with published experimental data. To achieve a more realistic flow in the right coronary branch, we reconstruct elaborate right coronary arteries based on geometrical data from literature and data from Duanmu et al. (2019). As previously mentioned in Chapter 2, the network derived from Duanmu et al. (2019) consisted of only

three blood vessels in the right coronary artery branch: right coronary artery (RCA), posterolateral ventricular branch (PLA), and posterior descending artery (PDA). However, the literature typically divides the RCA into proximal, middle, and distal segments (Douglas et al., 1988; Skowronski et al., 2018; Hirai et al., 2020). For instance,

- In a study conducted by Douglas et al. (1988), a total of 35 participants, including 23 men and 12 women with an average age of 47±18 years, were subjected to ultrasonographic examination. Their findings revealed that the proximal RCA had an average length of approximately 2.7 cm, with an average diameter of 3.1 mm. The middle RCA had an average length of around 3.6 cm, with an average diameter of 3.1 mm. Lastly, the distal RCA had an average length of approximately 2.9 cm, with an average diameter of 2.7 mm.

- Skowronski et al. (2018) conducted a study using CT angiography to measure the diameter of the RCA in 201 subjects (124 women and 77 men) with an average age of 50 ± 13 years. They found that the diameters of the proximal, middle, and distal RCA for women were 3.9 mm, 3.4 mm, and 3.2 mm, respectively, while for men, the diameters were 4.1 mm, 3.5 mm, and 3.3 mm, respectively.

- Hirai et al. (2020) conducted a study on 50 individuals, including 21 women and 29 men with an average age of 60.5±16.0 years, using contrast-enhanced coronary artery magnetic resonance angiography. Their result showed that the proximal RCA, middle RCA, and distal RCA had lengths of 3.6 cm, 3.5 cm, and 3.5 cm, respectively, with an average diameter of 4.0 mm.

A summary of the length and radius of the segments of the RCA reported in the above three studies (Douglas et al., 1988; Skowronski et al., 2018; Hirai et al., 2020) is provided in Table 4.1. Specifically, the length of the whole RCA was measured to be 9.2 cm by Douglas et al. (1988) and 10.6 cm by Hirai et al. (2020). The average radius of the RCA was reported as 0.148 cm and 0.200 cm by Douglas et al. (1988) and Hirai et al. (2020), respectively. In accordance with Duanmu et al. (2019), the RCA's length, top radius, and bottom radius were measured to be 10.9 cm, 0.151 cm, and 0.148 cm, respectively. Thus, the dimensions reported by Duanmu et al. (2019) align with the reported values in the literature.

Due to the intricate and variable nature of coronary vasculature, and the limited availability of data, it is challenging to establish a definitive pattern for the length and radius ratio of the proximal, middle, and distal RCA segments. As a result, one possible approach is to divide the RCA into three segments of equal length. Alternatively, given that our study relies on the total RCA length reported by Duanmu et al. (2019), which is 10.9 cm, closely resembling the value (10.6 cm) from (Hirai et al., 2020), we opted to maintain the identical proportionality of 36:35:35. Consequently, the RCA is subdivided

into three segments measuring 3.7 cm, 3.6 cm, and 3.6 cm, respectively. For the radius of the RCA segments, we assume that the radius decreases by 0.001 cm along each segment from a top radius of 0.151 cm to a bottom radius of 0.148 cm.

Based on the RCA branches described in (Angelini, 2007; Dowe et al., 2013), we incorporate additional vessels into our model, including the conus vessel originating from the middle of the proximal RCA, the RV branch vessel originating from the end of the proximal RCA, and the acute marginal vessel originating from the end of the middle RCA. The length of these vessels is assumed to be 3.3 cm, with a top radius of 0.112 cm and a bottom radius of 0.108 cm, which are the averages of the length and radius of the corresponding left anterior descending artery (LAD) branches.

Table 4.1: The dimensions (length l and radius r) of the proximal, middle, and distal segments of the right coronary artery (RCA), as well as those of the left main coronary artery (LMCA), proximal and middle segments of the left anterior descending artery (LAD), and proximal and middle segments of the left circumflex artery (LCX), reported in the literature. NA indicates that data are not available.

Branch	l (cm)	r (cm)	l (cm)	r (cm) Women	r (cm) Men	l (cm)	r(cm)
	(Douglas et al., 1988)		(Skowronski et al., 2018)			(Hirai et al., 2020)	
Proximal RCA	2.7	0.155	NA	0.195	0.205	3.6	0.200
Middle RCA	3.6	0.155	NA	0.170	0.175	3.5	0.200
Distal RCA	2.9	0.135	NA	0.160	0.165	3.5	0.200
LMCA	NA	NA	NA	0.25	0.27	NA	NA
Proximal LAD	4.2	0.245	NA	0.190	0.205	3.7	0.180
Middle LAD	1.9	0.23	NA	0.135	0.145	3.6	0.180
Proximal LCX	1.1	0.19	NA	0.175	0.195	3.5	0.160
Middle LCX	NA	NA	NA	0.165	0.180	3.2	0.160

4.1.2 Reconstructed venous system

The coronary veins play a crucial role in coronary circulation by collecting the blood that has circulated through the myocardium and returning it to the right atrium. Given the higher degree of morphological variability displayed by coronary veins compared to arteries (Ldinghausen, 2012; Saremi and Muresian, 2012; Chen et al., 2014), there is currently a scarcity of literature and geometric data available on the former. As a result, rather than

focusing on the dimensions of the coronary veins, we aim to gather more general information about their branching patterns and locations. As shown in Fig. 4.1, the coronary veins are normally divided into two main systems (Ldinghausen, 2012; Saremi and Muresian, 2012) including the greater cardiac venous system (GCVS), which collects approximately 70% of the deoxygenated blood, and the smaller cardiac venous system (SCVS), which is responsible for the remaining 30%. A detailed volume drainage distribution of the canine heart was reported by Hammond and Austen (1967), indicating that the coronary sinus (CS) drained 49%, the right atrium drained 24%, the right ventricle (RV) drained 22%, and the LV drained 5% of a total coronary flow of 171 ml/min.

The GCVS comprises both CS tributaries and non-CS tributaries. Almost all vessels of the GCVS empty into the right atrium. The CS tributaries consist mainly of the CS, great cardiac vein (GCV), left posterior and left marginal veins (PMVs), and small cardiac vein (SCV), which drain most of the LV wall and part of the RV wall, as illustrated in Fig. 4.1. The non-CS tributaries are primarily composed of the anterior cardiac veins (ACVs) and drain most of the RV wall. On the other hand, the SCVS consists of Thebesian vessels, which are embedded in the subendocardial part of the myocardium of all four chambers of the heart. The Thebesian vessels provide direct vascular communications between the coronary arteries and the chambers of the heart, mainly the right atrium and RV.

Therefore, we consider four veins (GCV, PMVs, SCV, and ACVs) in this study. The GCV, with a radius of 0.2-0.7 cm, crosses the branches of the LAD and thus collects blood from the LAD. The PMVs, with radii ranging from 0.05-0.28 cm, drain the posterior and lateral walls of the LV and usually course superficial to the marginal branch of the left circumflex artery (LCX). The SCV, with a radius of less than 0.5 cm, drains the posterolateral wall of the RV into the CS. The ACVs, with radii ranging from 0.025-0.15 cm, drain two-thirds of the RV wall, including the anterior and anterolateral walls.

The CS tributaries are drained by the CS, which is the largest venous vessel in the posterior of the heart that receives most of the deoxygenated blood from the coronary veins and empties it into the right atrium. The GCV marks the origin of the CS, and downstream the PMVs and the SCV drain into the CS. Table 4.2 shows that the average length of the CS is between 3.5 and 6.3 cm, with an average radius of 0.353 to 0.590 cm according to the three literature sources (Shah et al., 2012; Mlynarski et al., 2015; Mehra et al., 2016). From these sources, we obtain an average length of 4.0 cm and an average radius of 0.478 cm for the CS. Given the parallel course of coronary veins with arteries, the dimensions of the other coronary veins are equivalent to those of their corresponding arterial counterparts.

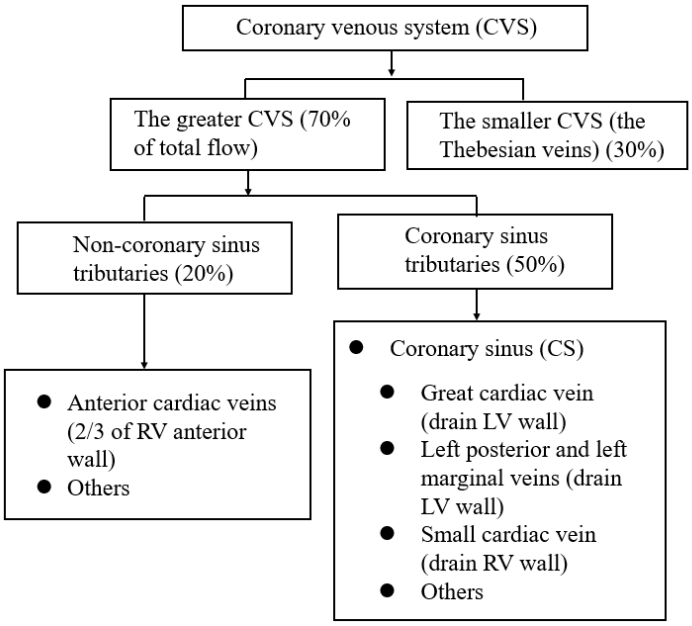

Figure 4.1: Classification of the venous systems, adapted from Saremi and Muresian (2012).

Table 4.2: Length (l) and radius (r) of the human coronary sinus (CS) reported in the literature.

Branch	l (cm)	r (cm)	l (cm)	r (cm)	l (cm)	r (cm)
	(Shah et al., 2012)		(Mlynarski et al., 2015)		(Mehra et al., 2016)	
CS	4.5-6.3	0.353	4.0	0.491	3.5	0.590

4.1.3 Reconstructed coronary network

Based on the dimensions of the coronary arteries obtained from (Duanmu et al., 2019), as well as the branching patterns of the RCA and the coronary venous system presented in the previous two sections, we reconstruct a more detailed coronary network, as shown in Fig. 4.2. The LAD and LCX branches in this network are consistent with those in Chapter 2, but additional blood vessels are present in the RCA branch. The newly reconstructed network also includes four outlets, with the ACVs directly draining into the right atrium.

Dimensions of the blood vessels in this network are summarised in Table 4.3. It should be noted that the dimensions of the LAD and LCX branches are directly obtained from Duanmu et al. (2019). Additionally, we compare these dimensions with the dimensions reported in the literature. For instance, the length of the LAD in our study is 9.6 cm, within 8.34±1.78 cm reported by Kumar et al. (2018). The radius of the LAD is 0.145 cm,

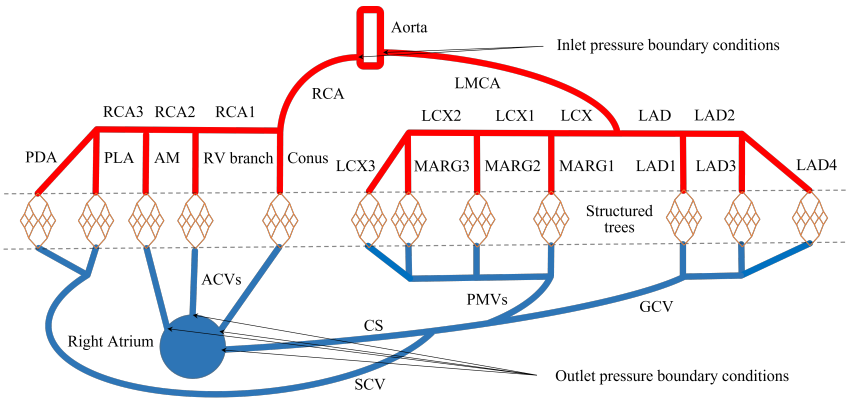

Figure 4.2: Diagram of a simplified network of the human coronary vasculature. The dimensions employed in this representation are derived from CT angiography by Duanmu et al. (2019), with additional reference to general information provided by Hirai et al. (2020); Dowe et al. (2013); Saremi and Muresian (2012). The key elements illustrated in the diagram include LMCA: Left main coronary artery; LAD, LAD1, LAD2, LAD3, and LAD4: Left anterior descending arteries; LCX, LCX1, LCX2, and LCX3: Left circumflex arteries; MARG1, MARG2, and MARG3: Marginal arteries; RCA: Right coronary artery; RCA1, RCA2, and RCA3: Proximal, middle, and distal segments of the right coronary artery, respectively; RV branch: Right ventricular branch; AM: Acute marginal branch; PLA: Posterolateral ventricular branch; PDA: Posterior descending artery; CS: Coronary sinus; GCV: Great cardiac vein; PMVs: Left posterior and left marginal veins; SCV: Small cardiac vein; ACVs: Anterior cardiac veins. The epicardial coronary arteries are highlighted in red, while the epicardial coronary veins are depicted in blue. Additionally, the diagram shows the structured trees representing the intramyocardial blood vessels.

which is 19% smaller than 0.180±0.050 cm reported by Dodge Jr et al. (1992). The length of the LCX is 5.7 cm, which agrees with 4.46±1.79 cm reported by Kumar et al. (2018). The radius of LCX is 0.132 cm, which is 22% smaller than 0.170±0.050 cm reported by Dodge Jr et al. (1992).

Furthermore, we compare our reconstructed human coronary network with a porcine network created by Jay Mackenzie in our group, which is based on data from Kassab's study (Kassab et al., 1993). Table 4.4 summarises the dimensions of the blood vessels from both sources. Our reconstructed human network looks more realistic compared to Mackenzie's network. This is because, in Kassab's study, all porcine coronary vessels were classified into 1-11 orders, and therefore, vessels of the same order have the same length and radius. For instance, the large coronary vessels are categorised into orders 10 and 11. As a result, the proximal, middle, and distal RCA all have the same length. The same holds for the blood vessels in the LCX branches. Additionally, it can be found that Mackenzie's network has incomplete LAD branches, which can be completed in a similar way to the LCX branches.

Moreover, Kassab et al. (1993) measured coronary dimensions from 3-4 month-old porcine hearts rather than adult porcine hearts, which may be the reason why the length

of the porcine vessels is smaller than that of the human vessels, as shown in Table 4.4. However, the radius of the porcine vessels is comparable to that of the human vessels. For example, our reconstructed network shows that the middle RCA has a top radius of 0.150 cm and a bottom radius of 0.149 cm, whereas Mackenzie's network shows that the middle RCA has a top radius of 0.160 cm and a bottom radius of 0.150 cm. Similarly, our network indicates that the LMCA has a top radius of 0.188 cm and a bottom radius of 0.179 cm, while Mackenzie's network shows that the LMCA has a top radius of 0.190 cm and a bottom radius of 0.180 cm.

4.2 Intramyocardial pressure (IMP)

In this section, we will first discuss the impact of IMP on coronary blood flow. Subsequently, we will provide an overview of the existing literature on the experiments and calculation of IMP.

As outlined in Chapter 2, the structured-tree coronary flow model involves the division of the coronary blood vessels into two main components: the epicardial blood vessels, consisting of both the epicardial arteries and veins, which are situated on the surface of the heart; and the intramyocardial blood vessels, which are located within the heart wall and include arterioles, capillaries, and venules. The primary mechanism of interaction between the myocardium and the coronary flow occurs through the intramyocardial blood vessels.

Specifically, according to the tube law given by Eq. (2.34), the cross-sectional areas of the intramyocardial blood vessels are influenced by the transmural pressure (the difference between blood pressure and the IMP). The blood pressure refers to the pressure inside the blood vessels, while the IMP is the pressure exerted by the surrounding myocardial tissue on the outer surfaces of the intramyocardial blood vessels. During each heartbeat, the IMP fluctuates, resulting in corresponding changes in the cross-sectional areas of the coronary blood vessels. In particular, during systole, the IMP increases, causing the intramyocardial blood vessels to constrict, reducing the volume of the vascular bed. The reduction in volume forces the blood into both the arterial and venous coronary blood vessels. As a result, despite the high aortic pressure during systole, the flows in the left coronary arteries are impeded or even reversed in healthy individuals (Gregg and Green, 1940; Goodwill et al., 2011), while the corresponding venous outflows increase. Consequently, the blood pressure gradient from upstream to downstream (the driving force of the coronary flow) is not the sole determinant of coronary blood flow; the IMP also plays a crucial role in determining the dynamics of coronary blood flow. An increase in IMP counteracts the driving force and inhibits the coronary flow (Porter, 1898; Krams et al., 1989; Goodwill et al., 2011).

The impact of the IMP on coronary blood flow was first described through the 'vascular waterfall' phenomenon by Downey and Kirk (1974). This phenomenon is illustrated by an abrupt pressure drop at the outflow regions of a tube with a collapsed segment at its end. Downey and Kirk (1974) proposed that the coronary flow is dependent on the difference between arterial pressure and tissue pressure (IMP), which was supported by their experimental study of the transmural distribution of left coronary blood flow across the canine heart wall during systole. They found a gradient of systolic blood flow from the epicardium to the endocardium. In further support of their hypothesis, Downey and Kirk (1975) tested the pressure-flow characteristics in coronary circulation by designing a lumped parameter model consisting of numerous parallel channels, with an IMP that varies from zero at the epicardium to peak left ventricular pressure at the endocardium. They also conducted experiments on mongrel dogs to measure the pressure and flow of a branch of the left coronary artery. Their model produced results similar to the experimental results, supporting the assumption that the formation of vascular waterfalls impedes systolic coronary flow. Additionally, they concluded that the IMP does not significantly exceed peak ventricular pressure.

Experiments have been conducted to measure the IMP in various animal hearts such as dogs and cats (Brandi and McGregor, 1969; Hamlin et al., 1982; Heineman and Grayson, 1985). Kirk and Honig (1964) measured the IMP in open-chest anesthetised dogs using No. 26 curved needles and found a transmural gradient of the IMP from the epicardium to the endocardium, with the peak IMP being twice the peak LV pressure recorded in the inner half of the wall. Nematzadeh et al. (1984) employed four different methods to measure the IMP in anesthetised dogs. In their experiments, collapsible tubes passing through the LV wall by utilising a surgical suture or needle placed at a specific depth within the LV wall were used to detect IMP. A linear gradient of the IMP from the epicardium to the endocardium was demonstrated, although the estimated magnitude of the gradient varied based on the technique used. A normalised factor (the slope of the regression line relating the IMP to LVP) was used to show the transmural gradient of the IMP. The magnitude of the gradient was 1.13, 1.21, 0.99, and 0.85 for the four different techniques. It should be noted that these gradients were much higher than the values estimated in other studies (Salisbury et al., 1962; Pifarre, 1968), while the peak systolic IMP did not exceed the LV ventricular pressure measured by Heineman and Grayson (Heineman and Grayson, 1985). The discrepancy can be explained by the differences in the size and material properties of their equipment, physical manipulation of the LV wall during the experiment, and techniques of data analysis. They concluded that IMP measured by needles was less invasive and more reliable, in which IMP exceeded the LV ventricular pressure (LVP) by about 8 % in the subendocardial layer. Mihailescu and Abel (1994) measured IMP in working and non-working isolated cat hearts. Glass micropipettes with

a diameter of 20-24 µm were placed inside the LV wall to measure the IMP. The systolic transmural IMP gradient was also reported in their research. In the working cat hearts, IMP exceeded LVP by 11-18 % in the endocardial layer. The mean systolic IMP to LVP radio in the epicardial layer was about 0.36-0.39.

Table 4.3: Dimensions of the reconstructed network of the human coronary vasculature using experimental data from Duanmu et al. (2019) and information from relevant literature.

Branch	Length (cm)	Top radius (cm)	Bottom radius (cm)	Justification and comparison with existing research
Proximal RCA	3.7	0.151	0.150	The ratio between these three branches follows that from (Hirai et al., 2020);
Middle RCA	3.6	0.150	0.149	Length of RCA is 10.9 cm which is within 10.6±0.7 cm (Hirai et al., 2020);
Distal RCA	3.6	0.149	0.148	Radius of RCA is 0.150 cm which is within 0.17±0.035 cm (Skowronski et al., 2018).
Conus	3.3	0.112	0.108	Given the lack of data, it is assumed that these three blood vessels have an average length and radius comparable to that of the LAD branches.
RV branch	3.3	0.112	0.108	
AM	3.3	0.112	0.108	
PLA	4.2	0.128	0.125	The lengths and radii of these blood vessels were directly obtained from data provided by Duanmu et al. (2019);
PDA	3.7	0.108	0.105	
LMCA	3.2	0.188	0.179	
LAD	2.7	0.151	0.145	The length of the LAD (LAD+LAD2) is 9.6 cm which is within 8.34±1.78 cm (Kumar et al., 2018); The radius of the LAD is 0.145 cm which is smaller than 0.180±0.050 cm (Dodge Jr et al., 1992);
LAD1	2.9	0.146	0.145	
LAD2	6.9	0.138	0.106	
LAD3	4.7	0.103	0.103	
LAD4	2.2	0.088	0.077	
LCX	2.1	0.148	0.147	The length of the LCX (LCX+LCX1+LCX2) is 5.7 cm which is within 4.46±1.79 cm (Kumar et al., 2018); The radius of the LCX is 0.132 cm which is smaller than 0.170±0.050 cm (Dodge Jr et al., 1992).
LCX1	1.6	0.132	0.129	
LCX2	2.0	0.115	0.114	
MARG1	3.5	0.116	0.108	
MARG2	3.0	0.098	0.096	
MARG3	3.7	0.102	0.100	
LCX3	3.9	0.102	0.099	

Table 4.4: Comparison of dimensions of human coronary arteries and porcine coronary arteries. The left ones are human coronary arteries, based on data from Duanmu et al. (2019), whereas the right ones are porcine coronary arteries, constructed from data by Kassab et al. (1993).

Branch	Length (cm)	Top radius (cm)	Bottom radius (cm)	Length (cm)	Top radius (cm)	Bottom radius (cm)
Proximal RCA	3.7	0.151	0.150	2.1	0.170	0.160
Middle RCA	3.6	0.150	0.149	2.1	0.160	0.150
Distal RCA	3.6	0.149	0.148	2.1	0.150	0.140
Conus	3.3	0.112	0.108	1.6	0.070	0.070
RV branch	3.3	0.112	0.108	1.6	0.070	0.070
Acute marginal	3.3	0.112	0.108	1.6	0.070	0.070
PLA	4.2	0.128	0.125	1.6	0.070	0.070
PDA	3.7	0.108	0.105	1.6	0.070	0.070
LMCA	3.2	0.188	0.179	1.2	0.190	0.180
LAD	2.7	0.151	0.145	5.0	0.140	0.110
LAD1	2.9	0.146	0.145	NA	NA	NA
LAD2	6.9	0.138	0.106	NA	NA	NA
LAD3	4.7	0.103	0.103	NA	NA	NA
LAD4	2.2	0.088	0.077	NA	NA	NA
LCX	2.1	0.148	0.147	1.2	0.180	0.160
LCX1	1.6	0.132	0.129	1.2	0.160	0.140
LCX2	2.0	0.115	0.114	1.2	0.140	0.130
LCX3	3.9	0.102	0.099	1.6	0.070	0.070
MARG1	3.5	0.116	0.108	1.6	0.070	0.070
MARG2	3.0	0.098	0.096	1.6	0.070	0.070
MARG3	3.7	0.102	0.100	1.6	0.070	0.070

Table 4.5: Experimental intramyocardial pressure (IMP) as well as calculation of IMP from lumped parameter models in the literature.

Experimental IMP at transmural position of LV heart wall

Literature and method	Experimental result						Conclusion
(Kirk and Honig, 1964): curved needle inserted into heart wall of anesthetised dogs	Wall thickness	0	25	50	75	100	Gradient of IMP from epi to endo Peak IMP twice peak LVP
	SIMP	NA	30	90	180	NA	
(Nematzadeh et al., 1984): butterfly needle placed into heart wall of anesthetised dogs	Wall thickness	0	25	50	75	100	Four methods were employed Needle (recommended) is less invasive than tube method Peak IMP exceeds peak LVP by 8 %
	SIMP	23	44	65	87	108	
(Mihailescu and Abel, 1994): glass micropipette placed into working isolated heart wall of cats	Wall thickness	0	25	50	75	100	Peak IMP exceeds peak LVP by 11-18 %
	SIMP	38	63	78	117	100	
Gradient of IMP from epi to endo is observed by experiments; The radio of peak IMP and peak LVP varies with different experiments							

Lumped parameter models of IMP

Literature and method	IMP formula	Conclusion
(Downey and Kirk, 1975) (Arts and Reneman, 1985): CEP to explain impeding effect of IMP on flow during systole	$\mathrm{IMP} = \mathrm{IMP}_{\mathrm{CEP}} = \alpha\ \mathrm{LVP}$, where α is 0 at epi and 1 at endo	Experimental pressure-flow relationship of dogs Coronary vasculature represented by parallel channels Simulated pressure-flow curves similar to experimental ones
(Algranati et al., 2010): five combinations of CEP, SIP and VE	$\mathrm{IMP} = \mathrm{IMP}_{\mathrm{CEP}} + \mathrm{IMP}_{\mathrm{SIP}}$ or $\mathrm{IMP} = \mathrm{IMP}_{\mathrm{CEP}} + \mathrm{IMP}_{\mathrm{VE}}$	Flow features of five combinations of CEP, VE and SIP Coronary vasculature reconstructed from morphometric data of (Kassab et al., 1993) Experimental pressure-flow relationship of dogs (Toyota et al., 2005) Only combined method provides good agreement with the majority of measurements
(Munneke et al., 2022): CEP + VE	$\mathrm{IMP} = \mathrm{IMP}_{\mathrm{CEP}} + \mathrm{IMP}_{\mathrm{VE}}$	Cardiac-coronary model based on the CircAdapt model (Arts et al., 2005) Experimental flow velocity of humans (Davies et al., 2006) Model-predicted waveforms of global epicardial flow velocity were compared with reported data
(Fan et al., 2020): CEP + VE + SIP	$\mathrm{IMP} = \mathrm{IMP}_{\mathrm{CEP}} + \mathrm{IMP}_{\mathrm{VE}} + \mathrm{IMP}_{\mathrm{SIP}}$	Cardiac-coronary model based on (Namani et al., 2018) Experimental flow velocity of swine (Davies et al., 2006) Model-predicted waveforms of LAD and LCX were compared with their data
IMP is assumed; Flow waveforms are validated with experimental data, not IMP		

IMP = intramyocardial pressure; LVP = left ventricular pressure; Percent wall thickness is 0 of epicardium to 100 of endocardium; Normalised SIMP = $\frac{\text{systolic IMP}}{\text{systolic LVP}} \times 100$
CEP = ventricular cavity-induced extracellular pressure; SIP = the muscle shortening-induced intracellular pressure; VE = the time-varying elasticity-induce pressure
σ is the Cauchy stress tensor, and $\sigma_{\mathrm{ff}}, \sigma_{\mathrm{ss}}, \sigma_{\mathrm{nn}}$ are stress in myofibre, sheet, and normal direction, respectively

Arts and Reneman (1977) analysed the role of the IMP through the use of computational models consisting of two different materials. In their models, the LV was represented as a thick-walled cylinder composed of eight concentric cylinders of muscle material, along with a force-length-time relation and a depolarization pattern. One of the models was based on isotropic muscle material, while the other model was based on anisotropic muscle material. The cylindrical geometry used to represent the LV resulted in the calculation of the IMP using the radial component of Cauchy stress. The IMP at the endo-layer was found to be equal to the LV pressure and zero at the epi-layer, leading to a negative IMP gradient from the subendocardial layers to the subendocardial layers. Furthermore, the systolic IMP in the subendocardial layer was found to be equal to the LV pressure, indicating that the systolic IMP never exceeded the LV pressure. The authors also evaluated the reliability of the existing methods for measuring the IMP. They concluded that the measurements of the IMP at that time were not reliable, as the IMP measured directly or indirectly from a fluid-filled cavity surrounding the tissue was dependent on the shape and position of the fluid-filled cavity, leading to errors. The details of this study can be found in (Arts, 1978).

Spaan et al. (1981) utilised the lumped parameter model introduced by Arts (1978) to analyse their experimental data on coronary flow obtained from 5 mongrel dogs. They found that the normal forward systolic coronary flow included a significant reverse flow caused by the contraction of the heart. In other words, they proposed that the myocardium should be considered as a pump during systole that actively pumps coronary blood in both a backward direction towards the arterial side and a forward direction towards the venous side. This conclusion explained the low coronary flow rates and even negative flow during systole observed in their experimental results, which could not be explained by the 'vascular waterfall' model (Downey and Kirk, 1974, 1975).

A summary of experimental IMP in literature can be found in Table 4.5. Despite advancements in the measurement technique, the accurate spatial and temporal distribution of the IMP from cardiac tissue remains elusive due to the complexities of cardiac motion, the potential for uncontrolled distortion of the tissue microstructure by the pipette tip, and the heterogeneous nature of the pressure in various microcompartments (Westerhof et al., 2006; Algranati et al., 2010; Fan et al., 2021). As a result, while various methods have been developed for calculating the IMP in recent modelling studies (Smith et al., 2005; Fan et al., 2021; Algranati et al., 2010; Munneke et al.), most of these models only validate their flow rate results against experimental data, not the IMP itself.

4.2.1 IMP determined through lumped-parameter models

Due to the challenges associated with obtaining accurate experimental measurements of the IMP (Algranati et al., 2010), lumped-parameter models were initially utilised to esti-

mate the IMP based on cardiac outputs. The most basic method of estimating the IMP is using the LV cavity pressure, under the assumption that the IMP equates to the LV pressure at the endocardium and decreases linearly to the environmental pressure at the epicardium (Downey and Kirk, 1975; Arts and Reneman, 1977, 1985). This results in the average IMP across the entire LV wall being equal to half of the LV ventricular pressure. However, it has been acknowledged that relying solely on the LV pressure is insufficient for predicting the IMP, leading to the development of models that take microstructural properties into account for a more accurate calculation of the IMP. For instance, the varying elastance model (Suga et al., 1973; Vis et al., 1997a, 1995, 1997b) considers the cardiac muscle's stiffness as the primary factor affecting coronary flow, while the muscle shortening and thickening model (Willemsen et al., 2001) takes into account the effect of diameter changes in the muscle on the vasculature volume. Algranati et al. (2010) conducted an investigation of combinations of the aforementioned IMP models. They considered seven experimental observations, including transmural perfusion, total flow impediment, and velocity waveforms, among others, to evaluate the results of five combinations of the Ventricular Cavity-Induced Extracellular Pressure (CEP), Time-Varying Elasticity-Induced Pressure (VE), and Muscle Shortening-Induced Intracellular Pressure (SIP). They showed that none of CEP, VE, and SIP alone could produce results that were consistent with the majority of the measurements. The comparison was made using experimental data of blood flow velocities in subendocardial and subepicardial coronary arterioles of in vivo beating canine hearts (Toyota et al., 2005). Recently, Fan et al. (2020) adopted a combination of the three models to compute the IMP, which is further imposed on branches of the LAD and LCX, i.e.

$$\mathrm{IMP} = \mathrm{IMP}_{\mathrm{CEP}} + \mathrm{IMP}_{\mathrm{VE}} + \mathrm{IMP}_{\mathrm{SIP}}, \tag{4.1}$$

in which

$$\mathrm{IMP}_{\mathrm{CEP}} = \alpha \mathrm{P}_{\mathrm{LV}}, \quad \mathrm{IMP}_{\mathrm{VE}} = \beta \mathrm{E}_{\mathrm{es}} e, \quad \mathrm{IMP}_{\mathrm{SIP}} = \gamma(1 - \lambda_{\mathrm{f}}), \tag{4.2}$$

where $\alpha = 0.8$, $\beta = 5$ and $\gamma = 20$ are prescribed parameters to produce physiological flow results that agree with published data, P_{LV} is the LV cavity pressure, E_{es} is the maximal chamber elastance, e is a time-varying elastance function, and λ_{f} is the myocardial stretch. The baseline value of γ is 14 mmHg per shortening, implying a systolic extravascular pressure of 14 mmHg in the intact tissue (Algranati et al., 2010). In their simulation, the peak IMP is about 90 mmHg while the peak pressure of the LV cavity is 120 mmHg. Instead of considering three terms in Eq. (4.1), Munneke et al. (2022) used only the first two terms to calculate the IMP, i.e.

$$\mathrm{IMP} = \mathrm{IMP}_{\mathrm{CEP}} + \mathrm{IMP}_{\mathrm{VE}}, \tag{4.3}$$

in which

$$\mathrm{IMP}_{\mathrm{CEP}} = (rP_1 + (1-r)P_2), \quad \text{and} \quad \mathrm{IMP}_{\mathrm{VE}} = \gamma\sigma_{\mathrm{f}}, \tag{4.4}$$

where P_1 is the LV pressure, P_2 is the pressure on the epicardium, $r = 1/6, 3/6, 5/6$ is the radial positions of three layers (subepi-layer, mid-layer, and subendo-layer) of the myocardial wall, and $\gamma = 0.06$ is a prescribed scaling parameter. For the mid-layer, the peak IMP imposed on the RCA branch is 58 mmHg, on the LAD branch is 81 mmHg, and on the LCX branch is 79 mmHg.

4.2.2 IMP determined by the Cauchy stress

As an alternative to utilising lumped-parameter models to estimate the IMP, Smith et al. (2005) calculated the IMP by

$$\mathrm{IMP} = \frac{1}{2}(\sigma_{\mathrm{ss}} + \sigma_{\mathrm{nn}}), \tag{4.5}$$

where σ_{ss} and σ_{nn} are the force per unit area acting on a surface with the unit vectors of the sheet direction and sheet-normal direction, respectively. This formula requires the assumption that the coronary capillaries are aligned parallel to the myofibres, which was suggested by May-Newman et al. (1994). In their study, Smith et al. (2005) coupled a coronary flow model that consisted of the first six generations of a coronary arterial tree with a biventricular heart model, with the aim of analysing the distribution of metabolic work of the myofibres and the resultant coronary blood flow. However, the values for the IMP were not included in their results.

As shown in the last section, some lumped-parameter models (Willemsen et al., 2001; Algranati et al., 2010) suggested that the shortening of the myocyte affects the IMP. In conjunction with Eq. (4.5), Namani et al. (2020) recently calculated the IMP by

$$\mathrm{IMP} = \frac{1}{2}(\sigma_{\mathrm{ss}} + \sigma_{\mathrm{nn}}) + \alpha(1 - \lambda_{\mathrm{f}}), \tag{4.6}$$

where α is set to be 0.14 mmHg per percent shortening, and λ_{f} is the myofibre stretch. In their study, anatomically realistic subtrees of the LCX, each made up of 8,634 vessels, were utilised to model the regional coronary flow. These subtrees were then integrated into a coupled model that consisted of lumped models of the systemic circulation and an LV model. Detailed IMP curves in the basal, middle, and apical regions can be found in their work.

In fact, the hydrostatic pressure that enforces the incompressibility of the myocardium, i.e. the Lagrange multiplier in Eq. (3.45) (Griffith and Patankar, 2020), can also be employed to calculate the IMP, which is

$$\mathrm{IMP} = \frac{1}{3}\mathrm{trace}(\sigma) = \frac{1}{3}(\sigma_{\mathrm{ff}} + \sigma_{\mathrm{ss}} + \sigma_{\mathrm{nn}}), \tag{4.7}$$

where σ is the Cauchy stress, σ_{ff}, σ_{ss} and σ_{nn} are the Cauchy stress components in the myofibre, sheet, and sheet-normal direction, respectively. The three IMP formulas mentioned above have been tabulated for easy reference in Table 4.6.

Table 4.6: Intramyocardial pressure (IMP) determined by the Cauchy stress in the literature.

Method and reference	IMP formula	Assumption
Method 1 (Smith et al., 2005)	$\mathrm{IMP} = \frac{1}{2}(\sigma_{\mathrm{ss}} + \sigma_{\mathrm{nn}})$	Intramyocardial blood vessels are oriented parallel to the myofibres;
Method 2 (Namani et al., 2020)	$\mathrm{IMP} = \frac{1}{2}(\sigma_{\mathrm{ss}} + \sigma_{\mathrm{nn}}) + \alpha(1 - \lambda_{\mathrm{f}})$	Based on the method 1 and considering the effect of the shortening of the myocyte;
Method 3 (Griffith and Patankar, 2020)	$\mathrm{IMP} = \frac{1}{3}(\sigma_{\mathrm{ff}} + \sigma_{\mathrm{ss}} + \sigma_{\mathrm{nn}})$	Hydro-static pressure.

σ is the Cauchy stress tensor, and $\sigma_{\mathrm{ff}}, \sigma_{\mathrm{ss}}, \sigma_{\mathrm{nn}}$ are the stresses in the myofibre, sheet, and sheet-normal direction, respectively. α is a scaling factor and λ_{f} is the myofibre stretch.

4.2.3 Comparison between two IMP formulas

In this section, a comparison is made between two formulas for calculating the IMP in a single cardiac cycle, utilising the LV model established in Chapter 3. The IMP calculated by Eq. (4.5) is denoted as IMP^1, while the IMP calculated by Eq. (4.6) is denoted as IMP^2, and the IMP calculated by Eq. (4.7) is denoted as IMP^3. Since the value of the IMP^2 is within that of IMP^1 and IMP^3, we omit results of IMP^2. Following the method to calculate the volumetric-averaged myofibre stress in the entire LV wall, we calculate the volumetric-averaged IMP by

$$\mathrm{IMP}^k = \frac{\sum_{i=1}^{n} (\mathrm{IMP}_i^k)\, V^i}{\sum_{i=1}^{n} V^i}, \quad k = 1, 2, 3, \tag{4.8}$$

where IMP_i^k is the IMP at the centroid of i^{th} element which can be calculated by IMP^1, IMP^2, or IMP^3, respectively, V^i is the volume of i^{th} element, n is the total number of elements occupied by the LV wall.

Fig. 4.3 (a) shows the average IMP^1 over the entire LV wall during one cardiac cycle. At 0.48 s, the maximum IMP^1 of 15.0 mmHg is attained, while the minimum IMP^1 of -8.0 mmHg occurs at 0.36 s. It is worth noting that negative IMP^1 values are observed

from late diastole to early systole, as also reported by (Namani et al., 2020). An average IMP^3 over the entire LV wall during one cardiac cycle is shown in Fig. 4.3 (b). The peak IMP^3 is observed at 0.42 s and has a value of 87.8 mmHg, which is in good agreement with the maximum value of 90.2 mmHg reported by Fan et al. (2020). Due to the predominance of stress in the myofibre direction (σ_{ff}) during systole, as opposed to the stresses in the other two directions, σ_{ss} and σ_{nn}, as shown before in Fig. 3.7, the IMP calculated using Eq. (4.7) during systole is much larger than that obtained using Eq. (4.5). The maximum IMP^3 is 485.3% higher than that of IMP^1.

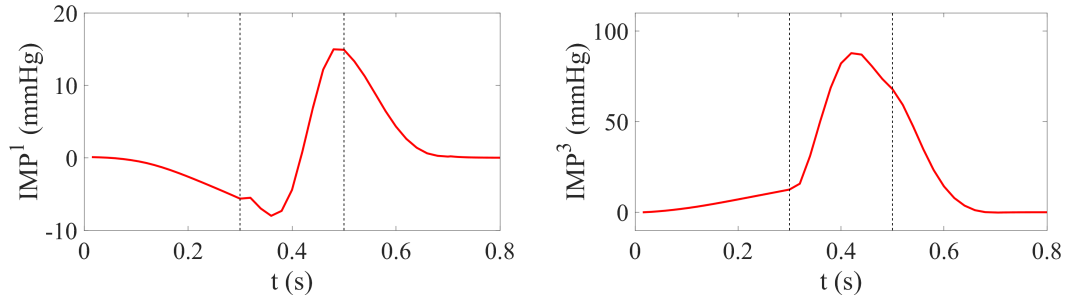

(a) (b)

Figure 4.3: The average IMP^1 (a) and average IMP^3 (b) over the entire left ventricle wall during one cardiac cycle, with the systolic phase occurring between the two vertical dashed lines at 0.30 s and 0.52 s.

4.3 Coronary flow simulations using different IMP

In this section, the coronary flow model developed in Chapter 2 is employed to simulate coronary flow with different IMP calculated from the LV model as shown in Fig. 4.3. The coronary network is shown in Fig. 4.2. The simulated inlet pressure is obtained from the LV model, as described in Chapter 3 and displayed in Fig. 3.6 (a). The outlet pressure is set at 3 mmHg, which is typically the mean right atrial pressure ranging between 0 and 5 mmHg.

4.3.1 Simulated coronary flow without imposing IMP

When no IMP is imposed, the resulting simulated pressures and flow rates at the terminal arteries (LAD1, LAD3, LAD4, MARG1, MARG2, MARG3, LCX3, Conus, RV branch, AM, PLA, and PDA) are illustrated in Fig. 4.4. In the absence of any imposed IMP, the pressure difference between the inlet pressure from the aortic root and the outlet pressure at the venous side drives the coronary flow. As shown in Fig. 4.4 (a, c, e), all pressures have the same trend as the aortic pressure. However, pressure drops occur along the LAD,

LCX, and RCA branches. In contrast to clinical observations and published results which suggest reduced or even reversed flow in the coronary arteries during systole (Mynard et al., 2014; Goodwill et al., 2011; Duanmu et al., 2019), as shown in Fig. 4.4 (b, d, f), the simulated peak flow rates of the terminal arteries are observed in systole. These results highlight the importance of imposing IMP.

4.3.2 Simulated coronary flow using globally averaged IMP[1]

In the subsequent two sections, we will identify the suitable formula for further analyses based on the simulated coronary flow outcomes when provided with two different IMPs (IMP[1] and IMP[3]). In our past simulations, we also used IMP[2] to simulate coronary flow. However, it is important to note that the results of using IMP[2] were not representative, as the IMP values obtained using IMP[2] fell within the range of IMP[1] and IMP[3].

At first, the calculated IMP[1] from the LV model for blood vessels perfusing the LV wall is shown in Fig. 4.3 (a). IMP[1] in the RV wall is assumed to be one-third of that in the LV wall, as the IMP in the RV wall is not available. Applying this IMP to the coronary model, we obtain the flow rates and pressures of all blood vessels. Here, we present a comparison of the pressures and flow rates in the LCX, LAD, and RCA with previously published results (Duanmu et al., 2019; Mynard et al., 2014; Fan et al., 2020), as shown in Fig. 4.5.

As shown in Fig. 4.5 (a,c,e), simulated pressures of LCX, LAD, and RCA using globally averaged IMP[1] exhibit a trend similar to experimental human data from Duanmu et al. (2019), with both the simulated and experimental pressures reaching their maximum values during systole. The simulated LCX pressure ranges from 75.8 mmHg to 114.8 mmHg, whereas the experimental LCX pressure ranges from 59.6 mmHg to 105.3 mmHg. Similarly, the simulated LAD pressure is from 75.7 mmHg to 114.8 mmHg, while the experimental LAD pressure is from 67.3 mmHg to 118.2 mmHg. It is noteworthy that the simulated LAD pressure and LCX pressure are very close to each other. The simulated RCA pressure is from 64.6 mmHg to 99.0 mmHg, while the experimental RCA pressure is from 80.3 mmHg to 119.3 mmHg.

However, the flow rates of LCX and LAD using globally averaged IMP[1], as shown in Fig. 4.5 (b,d), are distinct from the flow rates of LCX and LAD reported in (Duanmu et al., 2019; Mynard et al., 2014; Fan et al., 2020). The simulated LCX and LAD flow rates are dominant during systole which contradicts clinical observations and experimental data where these flow rates are impeded or even reversed during systole. Additionally, a discrepancy can be observed in the time course of the flow rates: while the simulated LCX and LAD flow rates increase from 0.0 to 0.37 s, the experimental data shows a decrease during this period, albeit with some fluctuations. Due to these differences, the IMP[1] is not appropriate to calculate the IMP in terms of our simulated coronary flow result.

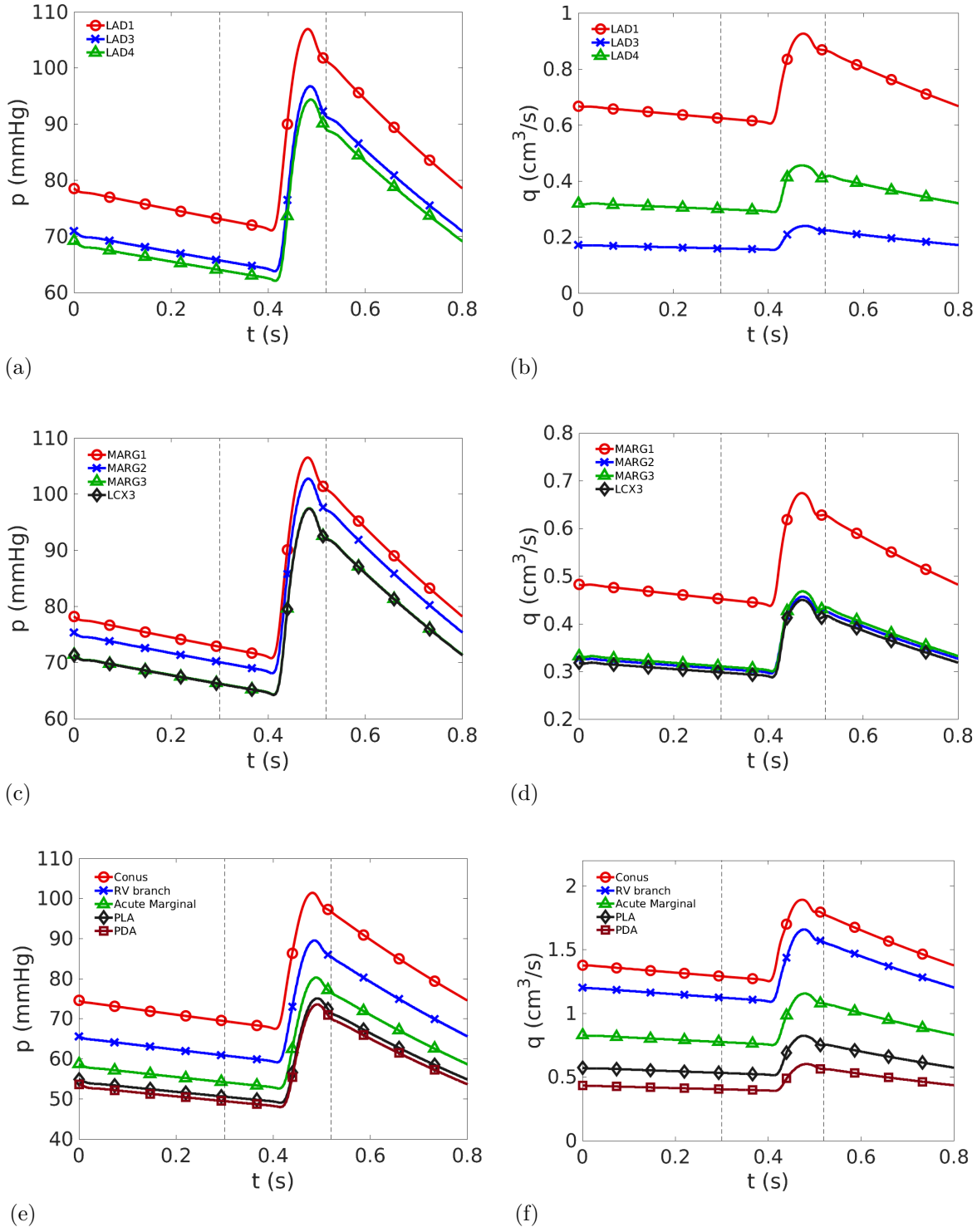

Figure 4.4: Simulated pressures and flow rates of the terminal arteries (LAD1, LAD3, LAD4, MARG1, MARG2, MARG3, LCX3, Conus, RV branch, Acute Marginal, PLA, and PDA) without imposing IMP.

As shown in Fig. 4.5 (f), the simulated RCA flow rate exhibits a good agreement with the experimental RCA flow rate reported in Duanmu et al. (2019), both in terms of their

values and trend. The peak value appears in systole. This is because the IMP[1] yields an even lower value in the RV wall than in the LV wall, resulting in even less impedance to flow during systole.

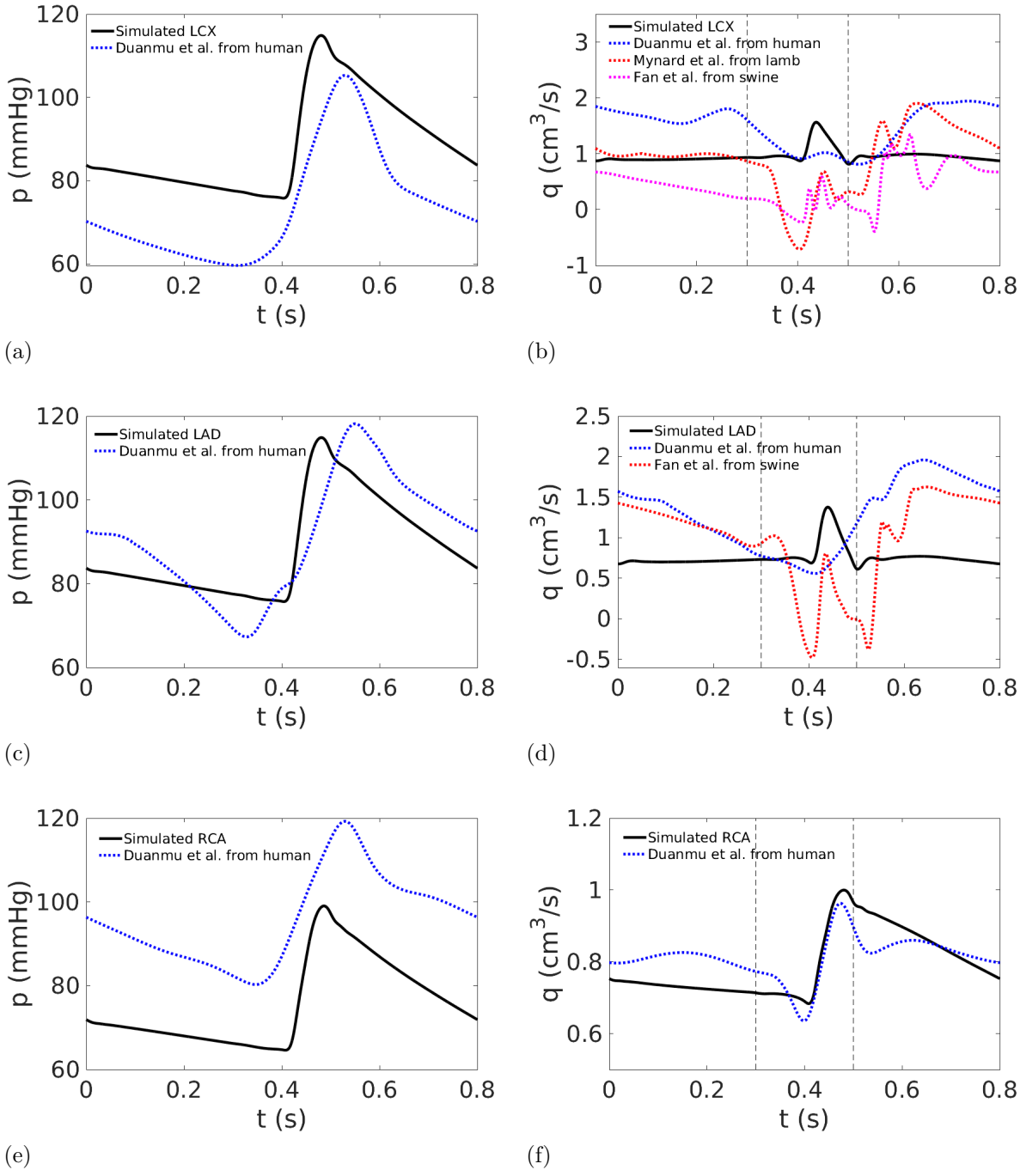

Figure 4.5: Using globally averaged IMP[1], simulated pressures and flow rates of LCX, LAD, and RCA, with a comparison with experimental data from Duanmu et al. (2019); Mynard et al. (2014); Fan et al. (2020).

4.3.3 Simulated coronary flow using globally averaged IMP^3

The globally averaged IMP^3 over the entire LV wall is shown in Fig. 4.3 (b). IMP^3 in the RV wall is assumed to be one-third of that in the LV wall. Applying IMP^3 to the coronary flow model, we obtain the flow rates and pressures of all blood vessels in the coronary network. Same to the previous section, we present a comparison of the pressures and flow rates in the LCX, LAD, and RCA with previously published results (Duanmu et al., 2019; Mynard et al., 2014; Fan et al., 2020), as shown in Fig. 4.6. The simulated pressures of LCX, LAD, and RCA are comparable with experimental human data from Duanmu et al. (2019), as shown in Fig. 4.6 (a, c, e). These pressures are also comparable to the simulated pressures of LCX, LAD, and RCA using globally averaged IMP^1. However, the flow rates of LCX and LAD simulated using the globally averaged IMP^3 exhibit a similar trend to the experimental data obtained by Duanmu et al. (2019); Mynard et al. (2014); Fan et al. (2020) as shown in Fig. 4.6 (b,d,f). It should be noted that using the globally averaged IMP^1 is not an appropriate method for achieving these results.

Specifically, regarding the LCX pressure shown in Fig. 4.6 (a), our simulated LCX pressure ranges from 78.9 mmHg to 118.4 mmHg, while the experimental LCX pressure from Duanmu et al. (2019) ranges from 59.6 mmHg to 105.3 mmHg. As shown in Fig. 4.6 (b), our simulated LCX flow ranges from -0.49 cm^3/s to 0.98 cm^3/s. In comparison, the experimental LCX flow obtained by Duanmu et al. (2019) from a male patient ranges from 0.82 cm^3/s to 1.81 cm^3/s, while the experimental LCX flow obtained by Mynard et al. (2014) from 9 newborn lambs ranges from -0.71 cm^3/s to 1.90 cm^3/s. The experimental LCX flow obtained by Fan et al. (2020) from 3 domestic swine ranges from -0.39 cm^3/s to 1.35 cm^3/s. Notably, the experimental LCX flow reported by Duanmu et al. (2019) is larger than the other two results.

During the period of 0 - 0.32 s, the simulated LCX flow decreases, which is consistent with the experimental data from Mynard et al. (2014) and Fan et al. (2020). However, the experimental data from Duanmu et al. (2019) show a peak during this period, which may be attributed to the measurement error. The decrease in LCX flow during this period is attributed to the decrease in aortic pressure. The mean simulated LCX flow during this period is 1.1 cm^3/s, which falls within the range of the mean experimental values of 0.5-1.6 cm^3/s reported by Duanmu et al. (2019); Mynard et al. (2014); Fan et al. (2020). After 0.3 s, the systolic phase begins and the IMP compresses the blood vessels within the heart wall, leading to the initial minimum value (P1) for all four curves shown in Fig. 4.6 (b). This happens when the IMP reaches its maximum value. This is consistent with previous discussions on the impeding effect of IMP, and our simulation results demonstrate this effect. As the IMP starts to decrease during late systole, the LCX flow rate increases during 0.41 s - 0.46 s as shown in Fig. 4.6 (b). At around 0.46 s, corresponding to the occurrence of the maximum aortic pressure, all four curves attain their respective local

peaks (P2). After the peak P2, the LCX flow gradually decreases along with the decrease of the aortic pressure. At around 0.5 s, there is a local minimum point (P3) observed in all four flow rate curves. However, given that the coronary network reconstructed in our study is less complex than an in vivo network, the experimental data exhibits more variability than our simulation results, with more fluctuations in flow.

The trend of pressure and flow rate in the LAD is similar to that of the LCX, primarily due to their shared origin from the LMCA and similar morphology. As shown in Fig. 4.6 (c), our simulated LAD pressure ranges from 78.8 mmHg to 118.4 mmHg, while the experimental LAD pressure from Duanmu et al. (2019) ranges from 67.3 mmHg to 118.2 mmHg. As shown in Fig. 4.6 (d), our simulated LAD flow ranges from -0.36 cm^3/s to 0.75 cm^3/s. In comparison, the experimental LAD flow obtained by Duanmu et al. (2019) from a male patient ranges from 0.56 cm^3/s to 1.96 cm^3/s, while the experimental LAD flow obtained by Fan et al. (2020) from swine ranges from -0.47 cm^3/s to 1.63 cm^3/s. Both the simulated LAD flow and experimental LAD flow from Fan et al. (2020) exhibit the three local extremes (P1, P2, and P3), however, these local extremes are not apparent in the experimental LAD flow from Duanmu et al. (2019).

The pressure and flow rate trends in the RCA are similar to those of the LCX and LAD. However, it is important to note that the flow rate in the RCA is not impeded to the same extent as in the LCX and LAD. As shown in Fig. 4.6 (f), the RCA flow rate reaches its maximum value during systole. This can be attributed to the fact that the magnitude of the IMP in the RV wall is one-third that of the LV wall.

In summary, the flow simulation results obtained using IMP^3 are in good agreement with the experimental data. Henceforth, the hydro-static pressure, i.e. Eq. (4.7), will be used to compute the IMP in the LV model for subsequent investigations.

4.4 Coronary flow simulation using AHA regionally averaged IMP

4.4.1 AHA segments of the left ventricle and assignment of coronary arteries to the AHA segments

Although there is substantial variation in the coronary blood vasculature, it is considered appropriate to allocate LV regions to specific coronary artery territories. This is mainly because the majority of myocardial segments receive blood supply from a particular coronary artery (Cerqueira et al., 2002). Recognizing the correlation between coronary artery territories and myocardial segments is crucial for diagnosing and treating cardiovascular disease since the segments can be evaluated for wall motion abnormalities, perfusion defects, and viability during imaging studies such as echocardiography, CMR, and nuclear

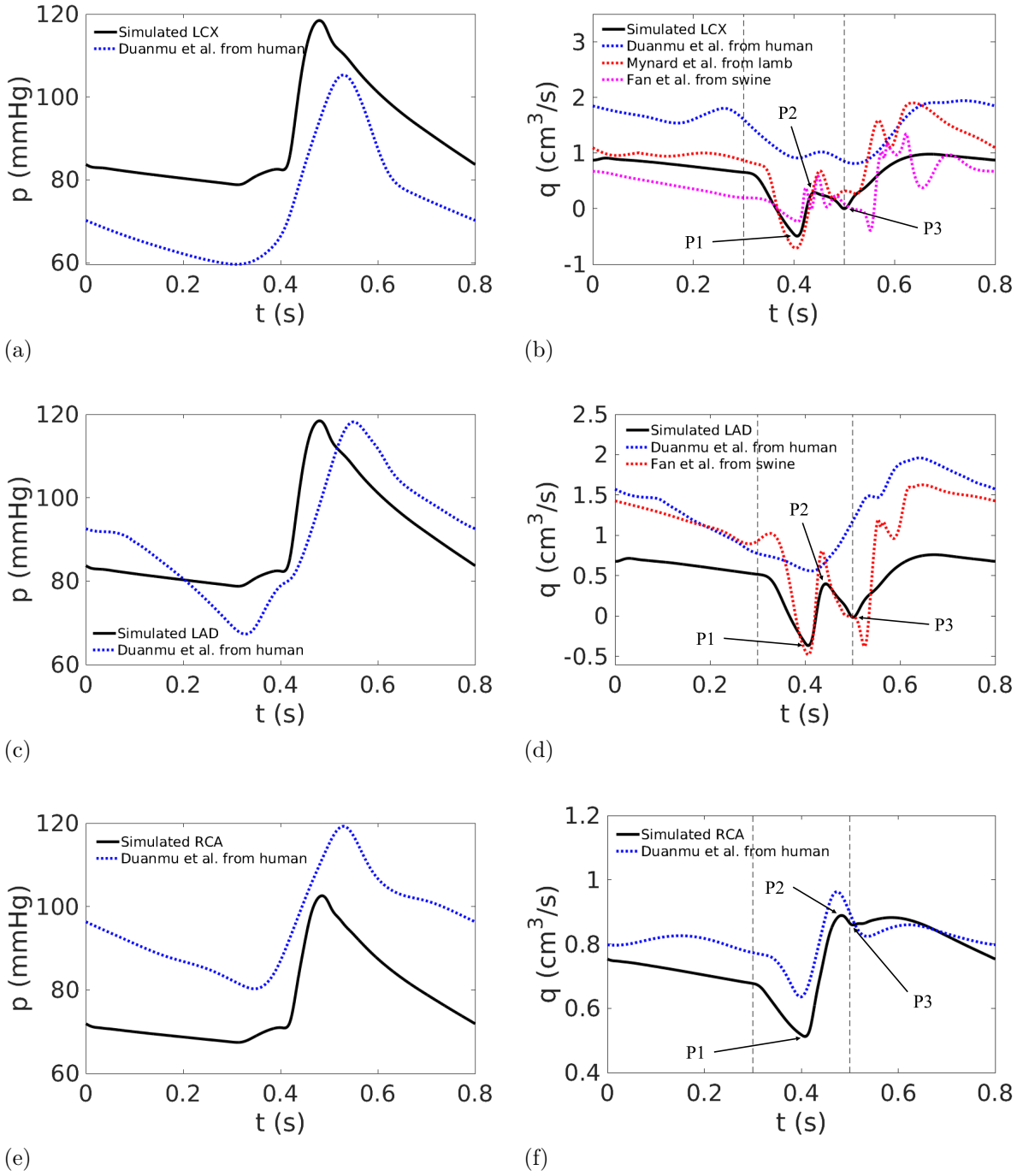

Figure 4.6: Using globally averaged IMP^3, simulated pressures and flow rates of LCX, LAD, and RCA, with a comparison with experimental data from Duanmu et al. (2019); Mynard et al. (2014); Fan et al. (2020). During systole, indicated by the two vertical dashed lines, three local extremes (P1, P2, and P3) are labeled.

medicine scans.

The AHA (Cerqueira et al., 2002) recommends a 17-segment model for the assessment of myocardial perfusion and functions. As shown in Fig. 4.7, the 17-segment model divides the LV wall into three regions: the basal, mid-cavity, and apical regions which occupy 35%,

35%, and 30% of the total LV mass, respectively. The segments are numbered sequentially from 1 to 17. The basal region includes 1-6 segments, the mid-cavity region includes 7-12 segments, and the apical region includes 13-17 segments. Each segment is named according to its anatomical location within the LV wall. For example, the basal segment of the anterior region is designated the basal anterior segment, which is segment 1. A full list of the names of all 17 segments can be found in Table 4.7.

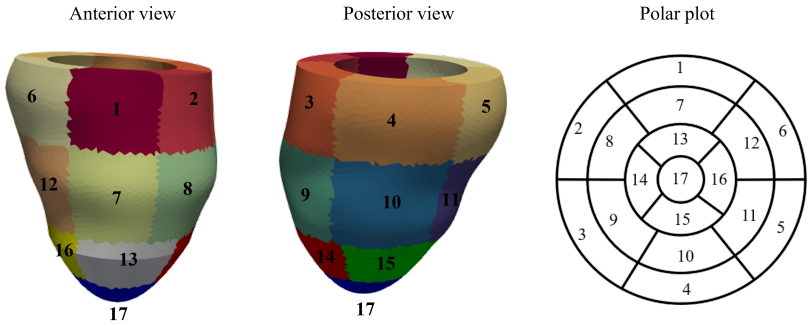

Figure 4.7: Anterior, posterior, and polar view of 17 segments of the left ventricle wall recommended by the American Heart Association (Cerqueira et al., 2002). The segments are numbered sequentially from 1 to 17.

Table 4.7: Names of the 17 segments of the left ventricle wall as recommended by the American Heart Association (Cerqueira et al., 2002).

Name	Segment number	Name	Segment number
Basal anterior	1	Mid inferoseptal	9
Basal anteroseptal	2	Mid inferior	10
Basal inferoseptal	3	Mid inferolateral	11
Basal inferior	4	Mid anterolateral	12
Basal inferolateral	5	Apical anterior	13
Basal anterolateral	6	Apical septal	14
Mid anterior	7	Apical inferior	15
Mid anteroseptal	8	Apical lateral	16
		Apex	17

Due to morphological variability, the assignment of the coronary arteries to the 17 LV segments should be patient-specific. However, the current standardised assignment of coronary arteries to specific myocardial segments is based on empirical assumptions. For

example, according to the guidelines established by Cerqueira et al. (2002), the assignment of the 17 LV segments to one of the three major coronary arteries, i.e. LAD, LCX, and RCA, is illustrated in Fig. 4.8. Segments 1, 2, 7, 8, 13, 14, and 17 are typically ascribed to the LAD branch. In general, 35% of the LV blood supply is provided by the LAD branch, and this is depended on the length of the LAD (Cerci et al., 2012; Separham et al., 2019). Segments 5, 6, 11, 12, and 16 are generally attributed to the LCX branch, while segments 3, 4, 9, 10, and 15 are associated with the RCA branch in instances where it is right dominant.

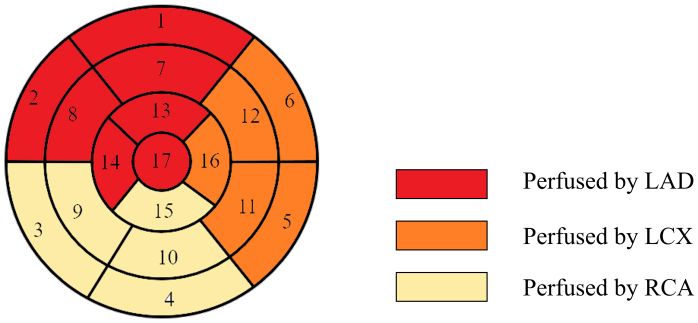

Figure 4.8: Assignment of the 17 left ventricle segments to the left anterior descending artery (LAD), left circumflex coronary artery (LCX), and right coronary artery (RCA) according to (Cerqueira et al., 2002).

The coronary anatomy presents normal variations, one of which is known as cardiac dominance. Cardiac dominance can be categorised into left dominance, right dominance, or codominance and is determined by which of the three major arteries gives rise to the PDA and perfuses the inferior wall, as illustrated in Fig. 4.9. The PDA traverses along the posterior interventricular sulcus to the apex of the heart. When the PDA arises from the LCX, it is termed left dominance, while if it originates from the RCA, it is referred to as right dominance. Codominance is used to describe instances where the PDA arises from both the LCX and RCA (Das et al., 2010; Sakamoto et al., 2013; Khwansang and Chentanez, 2018). Approximately 60% of the general population have right dominance hearts, 25% have codominance hearts, and 15% have left dominant hearts (Vasko et al., 1961; O'Rouke and Fuster, 2001; Kaimkhani et al., 2005).

Several studies have proposed different correspondences between the 17 LV segments and the three major coronary arteries, reflecting the normal variability of coronary anatomy (Cerqueira et al., 2002; Pereztol-Valdés et al., 2005; Ortiz-Pérez et al., 2008; Cerci et al., 2012; Donato et al., 2012). According to the AHA guidelines (Cerqueira et al., 2002), the segment with the greatest variability in myocardial blood supply is the apical cap, segment 17, which can be supplied by any of the three major arteries. However, Pereztol-Valdés et al. (2005) reported that the LAD is the primary vessel perfusing the apex in most of their patients, which may be related to the three anatomical types of the LAD: type A

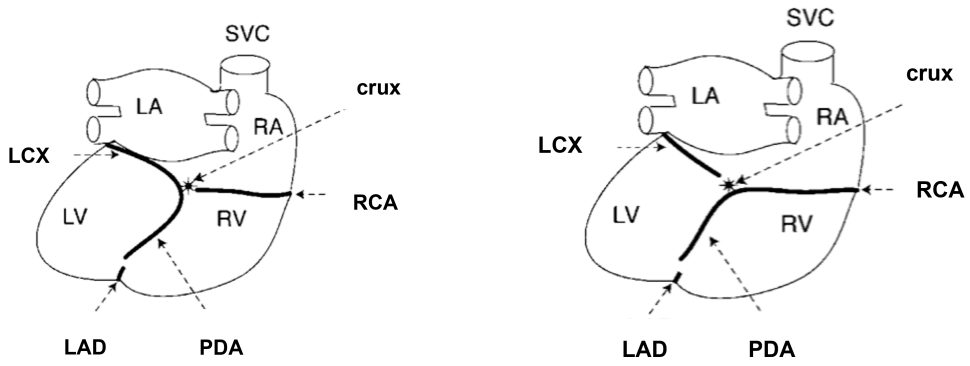

(a) (b)

Figure 4.9: The left (a) and right (b) dominance of the human heart from a posterior view. Three major coronary arteries are the left anterior descending (LAD), left circumflex artery (LCX), and right coronary artery (RCA). In the left dominant heart, the posterior descending artery (PDA) originate from the LCX. In the right dominant heart, the PDA is a continuation of the RCA. The left ventricle (LV), left atrium (LA), right ventricle (RV), and right atrium (RA) are labeled, along with the superior vena cava (SVC). The point at which the plane of the interventricular septum intersects that of the atrioventricular groove is referred to as curx. The figure is adapted from (Katz, 2010).

(LAD terminating before the apex), type B (LAD reached the apex), and type C (LAD wrapping around the apex). Type C of the LAD is often found in left-dominant hearts (Hadi et al., 2018; Separham et al., 2019). The LAD termination point is distal to the apex in 60-82% of cases (Pereztol-Valdés et al., 2005).

Using single-photon emission computed tomography (SPECT) images, Pereztol-Valdés et al. (2005) found that segments 1, 2, 7, 8, 13, 14, 16, and 17 corresponded to the LAD, while segment 6 corresponded to the LCX. Segments 3, 9, and 15 could correspond to either the LAD or RCA, segments 4, 5, 10, and 11 could correspond to either the RCA or LCX, and segment 12 could correspond to either the LAD or LCX. Using CMR imaging in 93 subjects following acute myocardial infarction treated with primary percutaneous coronary intervention, Ortiz-Pérez et al. (2008) found that the LAD territory was larger than the 17-segment model proposed by the AHA and thus was most often responsible for myocardial infarctions involving the mid-anterolateral and all apical segments. They recommended that the LAD perfuses segments 1, 2, 7, 8, 12, 13, 14, 15, 16, and 17, while the LCX perfuses segments 5, 6, and 11, and the RCA perfuses segments 3, 4, 9, and 10. In contrast to the AHA guidelines, their data suggest that the greatest variability occurs at the apical lateral wall, specifically at segment 16 instead of segment 17, which can be supplied by any of the three major coronary arteries. A study conducted by Donato et al. (2012) using multi-detector computed tomography also suggested that the LAD territory

was larger than the AHA-proposed 17-segment model, with the most specific segments located at the anterior wall and supplied exclusively by LAD. In addition, they proposed that no specific segment could be exclusively attributed to RCA or LCX. In some cases, the LCX can be the most important artery for the blood supply of the inferior wall, even if the origin of the PDA is from the RCA.

In order to determine the assignment of the terminal branches (LAD1, LAD3, LAD4, LCX3, MARG1, MARG2, MARG3, PDA) of the three major coronary arteries in the reconstructed network of coronary blood vessels shown in Fig. 4.2 to the 17 LV segments shown in Fig. 4.7, spatial information is needed in this study. However, since such information is not provided in the data from Duanmu et al. (2019), we first map the branches in Fig. 4.2 to a coronary artery segmentation model with 19 segments Scanlon et al. (1999); Wang et al. (2004); Miller et al. (2009); Cerci et al. (2012), as shown in Fig. 4.10 (a). According to the general positions provided by this coronary artery segmentation model, we assign the terminal branches of our network to the 17 LV segments as follows:

- The LAD1 and LAD4 refer to diagonal branches of the LAD that supply blood to the anterior and anterolateral walls. Given that the LAD1 is the first diagonal branch along the LAD, it is assigned to perfuse the basal segments 1 and 2 as well as the mid-cavity segment 8, whereas the LAD4 is assigned to perfuse the mid-cavity segment 7;

- The LAD3 is a distal branch that is assigned to perfuse the apical segments 13, 14, and 17;

- The MARG1, MARG2, and MARG3 are the first, second, and third obtuse marginal branches of the LCX. They curve toward the posterior surface of the heart, so they are assigned to perfuse the LV segments 4, 5, 6, 10, 11, 12, 15, and 16 accordingly;

- The LCX3 is the left posterior descending branch and it is the distal branch of the LCX, so it is responsible for perfusing the apical segment 16;

- The PDA originates from the RCA in the dataset provided by Duanmu et al. (2019) and it is responsible for blood supply to the posterior one-third of the interventricular septum. Thus, the PDA perfuses the LV segments 3 and 9.

A diagram showing the assignment of the terminal branches to the 17 LV segments is depicted in Fig. 4.10 (d). A summary of the assignments is also included in Table 4.8. This assignment allows us to investigate myocardial perfusion.

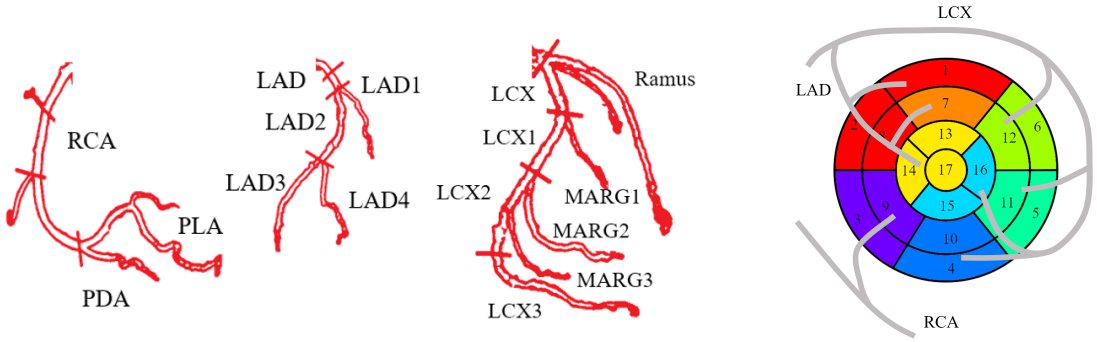

(a) (b)

Figure 4.10: A 19-segment model of coronary arteries (a) proposed by Cerci et al. (2012), and a diagram (b) of a mapping of coronary arteries to the 17 segments of the left ventricle.

Table 4.8: Assignment of coronary arteries to the left ventricle segments.

Coronary arteries (Duanmu et al., 2019)	19-segment model of coronary arteries (Cerci et al., 2012)	AHA 17-segment model of the LV (Cerqueira et al., 2002)
LAD1	First diagonal branch	1, 2, 8
LAD4	Second diagonal branch	7
LAD3	Distal LAD	13, 14, 17
MARG1	First obtuse marginal branch	6, 12
MARG2	Second obtuse marginal branch	5, 11
MARG3	Third obtuse marginal branch	15, 16
LCX3	Left posterior descending branch	4, 10
PDA	Posterior descending artery	3, 9

4.4.2 Regionally averaged IMP^3 in the 17 AHA segments

In the previous sections, our analysis of simulated coronary flow considered the globally averaged IMP. In this section, we aim to explore the effects of regionally averaged IMP by dividing the LV geometry into 17 AHA segments (Cerqueira et al., 2002), as illustrated in Fig. 4.7. The regionally averaged IMP can be calculated in each segment by substituting the volume of the corresponding segment into Eq. (4.8). This approach allows us to examine the impact of IMP at a more localised level and may provide insight into regional variations in coronary flow.

Regionally averaged IMP^3 in 17 AHA segments of the LV are shown in Fig. 4.11. The

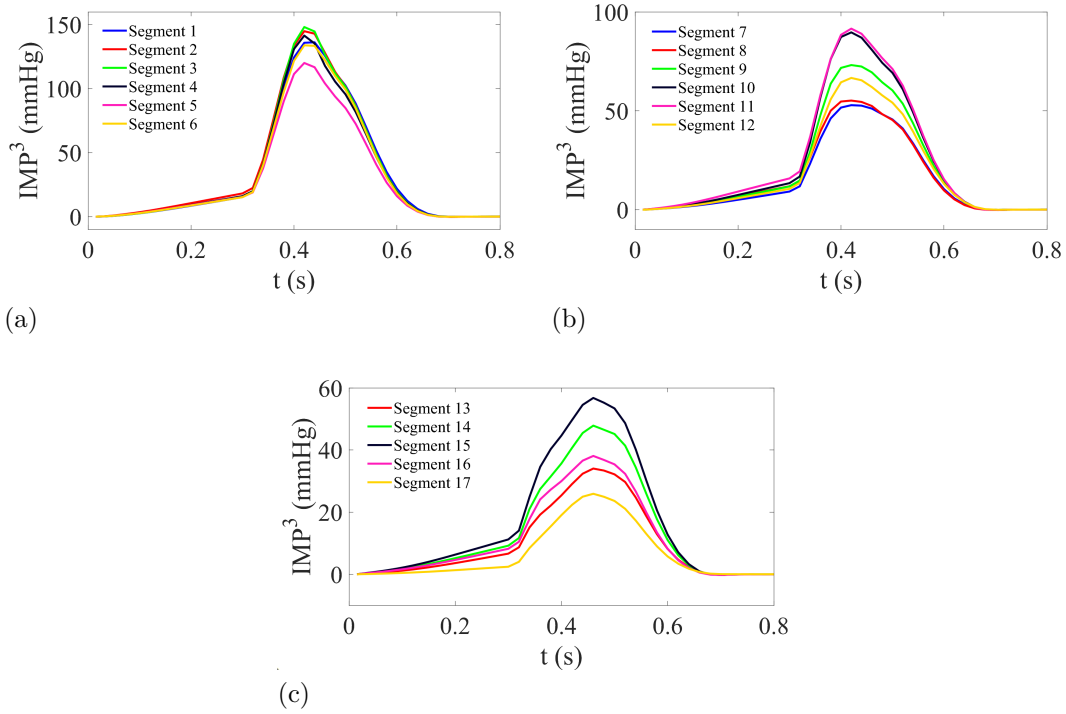

Figure 4.11: Intramyocardial pressure (IMP) in the 17 AHA segments of the left ventricle (Cerqueira et al., 2002), including six basal segments (a), six mid-cavity segments (b), and five apical segments (c). The IMP^3 indicates that the IMP is calculated by Eq. (4.7).

IMP values in all segments exhibit a slow increase from 0 to 0.3 s, followed by a rapid rise to their maximums during systole, and then gradually decrease to zero at approximately 0.7 s. And then, all the IMP values remain zero until 0.8 s. The maximum IMP^3 values in the 6 basal segments range from 120.1 mmHg in segment 5 to 148.2 mmHg in segment 3, with their peaks occurring approximately at 0.42 s. In the 6 mid-cavity segments, the maximum IMP^3 ranges from 52.8 mmHg in segment 7 to 91.5 mmHg in segment 11, with their peaks occurring at approximately 0.42 s. Lastly, in the 5 apical segments, the maximum IMP^3 ranges from 25.9 mmHg in segment 17 to 56.8 mmHg in segment 15, with their peaks occurring at approximately 0.46 s. Therefore, there is a decreasing trend in regionally averaged IMP^3 from basal regions to apical regions. However, there is no specific pattern observed within each region. The maximum values are observed in segments 3, 11, and 15, while the minimum value appears in segments 5, 7, and 17. It is noteworthy that the maximum IMP^3 values in the apical segments are reached at 0.46 s, whereas in the other segments, they are reached at 0.42 s.

4.4.3 Simulated coronary flow using regionally averaged IMP^3

Based on the assignment of coronary arteries to the 17 AHA segments of the LV presented in Table 4.8, we can determine the regionally averaged IMPs for the intramyocardial blood

vessels in regions supplied by the LAD1, LAD4, LAD3, MARG1, MARG2, MARG3, LCX3, and PDA. These regionally averaged IMPs are illustrated in Fig. 4.12. The peak values of regionally averaged IMPs in the LV wall vary from 36.4 mmHg in the region perfused by the LAD3 to 114.9 mmHg in the region perfused by the LCX3. It should be noted that the globally averaged IMP[3] in the LV wall has a peak value of 88.5 mmHg. Therefore, regionally averaged IMPs in regions perfused by the LCX3, PDA, MARG2, LAD1, and MARG1 are higher than the globally averaged IMP, while those in regions perfused by the LAD4, MARG3, and LAD3 are lower. Again, the regionally averaged IMP for the regions perfused by the PLA (one RCA branch to perfuse the RV wall) is assumed to be one-third of the globally averaged IMP in the LV wall.

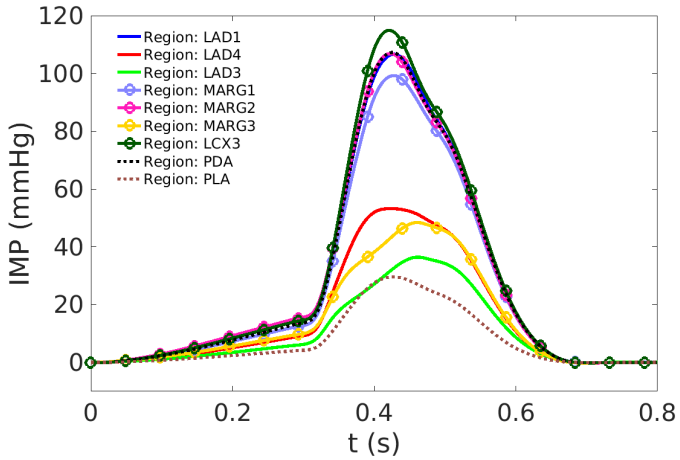

Figure 4.12: Regionally averaged IMPs in regions perfused by the terminal arteries LAD1, LAD4, LAD3, MARG1, MARG2, MARG3, LCX3, and PDA. It should be noted that PLA is included here to demonstrate the assumed IMP of the RV wall.

Applying the regionally averaged IMPs to the coronary flow model, we can obtain the flow rates and pressures of all blood vessels in the reconstructed network. Fig. 4.13 shows a comparison between our simulated pressures and flow rates of LCX, LAD, and RCA to the experimental results. The results are similar to those obtained by using globally averaged IMP as discussed in Section 4.3.3. It is noteworthy that the flow in the left coronary arteries is impeded during systole, whereas this is not the case for the right coronary arteries. For completeness, the figures are presented here, but since similar figures have already been explained in Section 4.3.3, they are not elaborated on again.

In order to compare the differences in simulated coronary flow when using globally averaged IMP and regionally averaged IMP, Fig. 4.14 plots the pressures and flow rates of LCX, LAD, and RCA for both cases. It is observed that, with the exception of the flow rate in the LCX and LAD, there are no significant differences between the results of the two cases. For the flow rates in LCX, during diastole, the LCX flow rate using regionally averaged IMP is higher than that using globally averaged IMP, but during

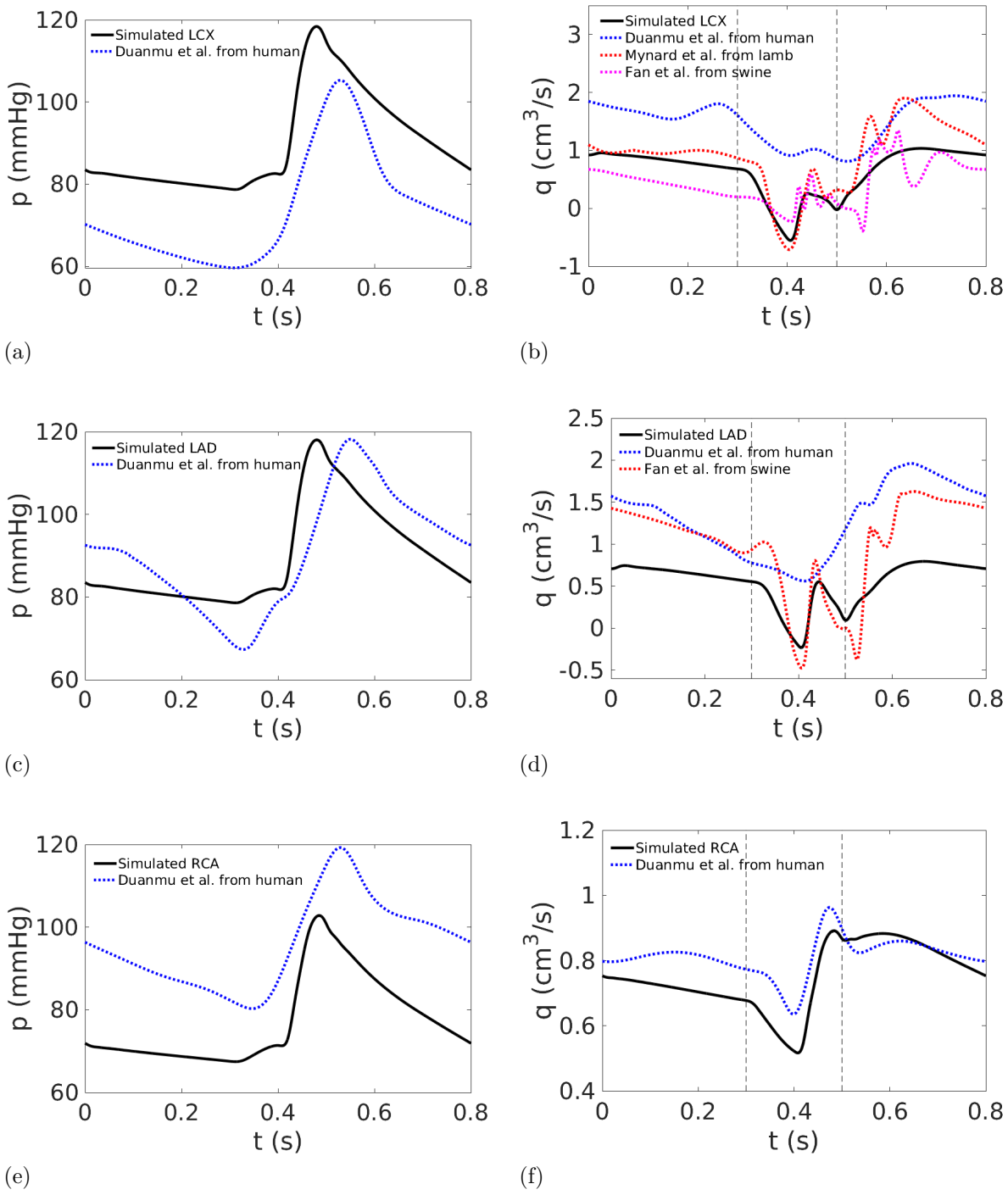

Figure 4.13: Using regionally averaged IMP[3], simulated pressures and flow rates of LCX, LAD, and RCA, with a comparison with experimental data from Duanmu et al. (2019); Mynard et al. (2014); Fan et al. (2020).

systole, it is lower. However, during both systole and diastole, the flow rate in the LAD is higher when using regionally averaged IMP compared to globally averaged IMP. The flow rates in the LAD exhibit the most variation between the two cases. These findings suggest that the use of globally averaged IMP can produce a satisfactory coronary flow in

the proximal coronary arteries such as LCX, LAD, and RCA. Additionally, it is observed that the pressures of the LCX, LAD, and RCA are similar regardless of whether globally averaged IMP, regionally averaged IMP, or no IMP is applied. However, the flow rates of these arteries exhibit considerable differences depending on the imposition of IMP.

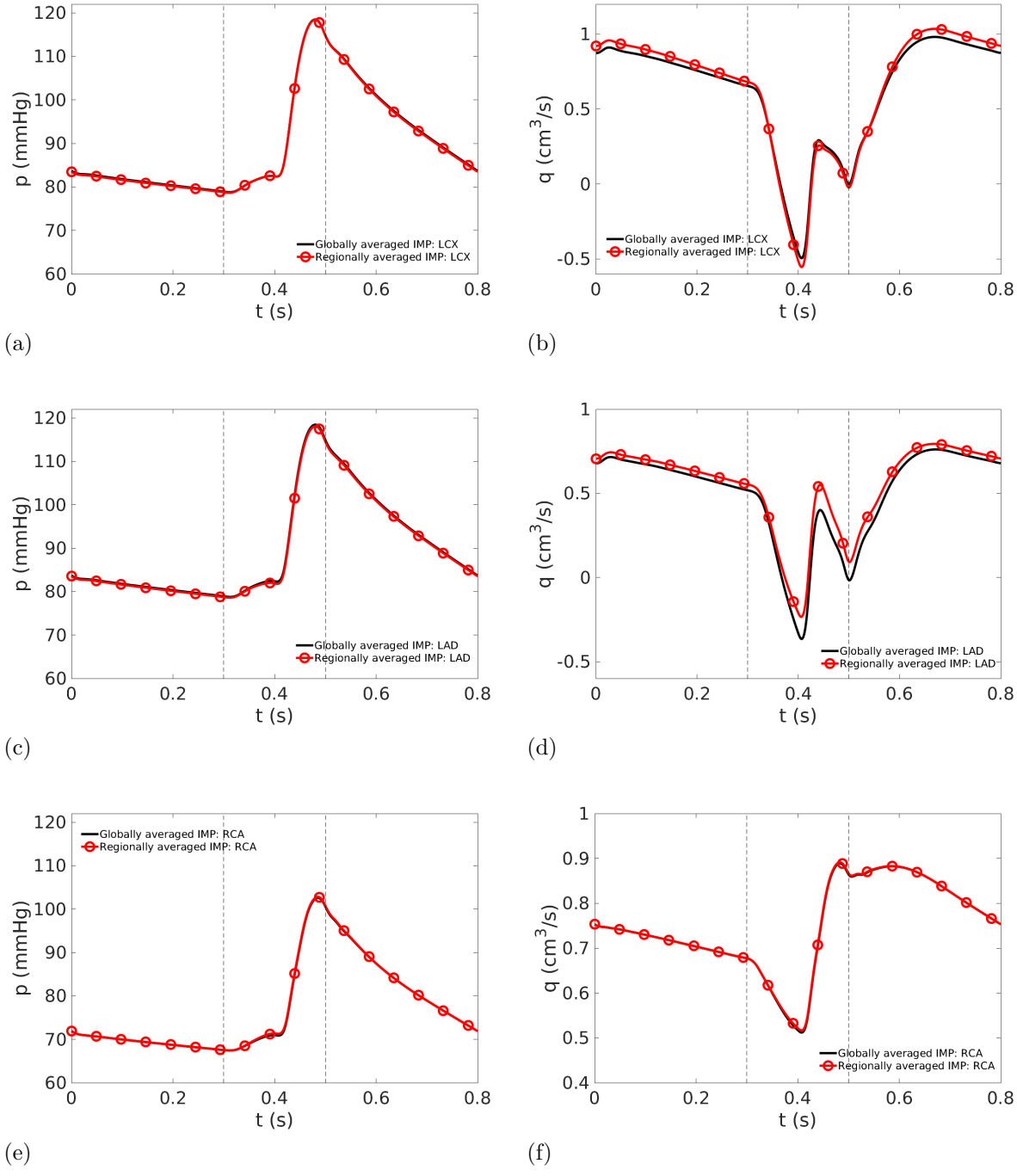

Figure 4.14: Comparison between the simulated pressures and flow rates of LCX, LAD, and RCA when using globally averaged IMP and AHA regionally averaged IMP.

While there are minimal differences in the simulated pressures and flow rates of the LCX, LAD, and RCA between the use of globally averaged IMP and regionally averaged

IMP, the results of the simulations for the distal coronary arteries, namely the terminal vessels (MARG2, MARG3, LCX3, LAD1, LAD4, LAD3, AM, PLA, and PDA), show substantial differences, as shown in Fig. 4.15 (a-f). These figures present a relative comparison of the simulated pressures and flow rates of the terminal arteries of the LCX branches (MARG2, MARG3, and LCX3), the LAD branches (LAD1, LAD4, and LAD3), and the RCA branches (AM, PLA, and PDA) using both the globally averaged IMP and the AHA regionally averaged IMP.

The pressures of the three terminal vessels in the LCX branch, namely the MARG2, MARG3, and LCX3, exhibit little difference during diastole when using either globally or regionally averaged IMP, as illustrated in Fig. 4.15 (a). However, during systole, the difference in the IMP affects the pressures of these vessels. For instance, the maximum pressure of the MARG3 decreases from 117.5 mmHg with globally averaged IMP to 115.2 mmHg with regionally averaged IMP. Similarly, the difference in the IMP has a major influence on the flow rates of these vessels in systole other than diastole. As shown in Fig. 4.15 (b), when globally averaged IMP is used, the flow rates of these three vessels overlap with each other. However, when regionally averaged IMP is used, their flow rates become distinct. Specifically, the regionally averaged IMP applied to the structured tree connected to the MARG3 is the smallest, leading to the least impedance to the flow rate of the MARG3 during systole. In contrast, the regionally averaged IMP applied to the structured tree connected to the LCX3 is the highest, resulting in the greatest impedance to the flow rate of the LCX3 during systole.

The impact of the globally averaged and regionally averaged IMP on the pressures and flow rates of the three terminal vessels in the LAD branches, including the LAD1, LAD4, and LAD3, is comparable to that observed in the LCX branches. The pressures and flow rates of these vessels exhibit greater variation during systole than during diastole, as depicted in Fig. 4.15 (c, d). The reason for the minimal difference in the pressure and flow rates during diastole between the two cases is that the only variable being changed is the IMP. During diastole, when the IMPs gradually rise from zero to a relatively low value, the pressures and flow rates of all vessels are primarily determined by the inlet and outlet pressures, which are identical in both cases.

The figures shown in Fig. 4.15 (e, f) indicate that the variations in the pressures and flow rates of the three vessels (AM, PLA, and PDA) in the RCA branches between using globally and regionally averaged IMP are not as significant as those observed in the LCX and LAD branches. The flow rates in the AM and PLA demonstrate no significant differences, which can be explained by the identical IMPs in the RV wall in the two cases. On the other hand, the regionally averaged IMP of the region perfused by the PDA is substantially higher than the globally averaged IMP, and thus, the flow rate in the PDA is more significantly impeded using the regionally averaged IMP.

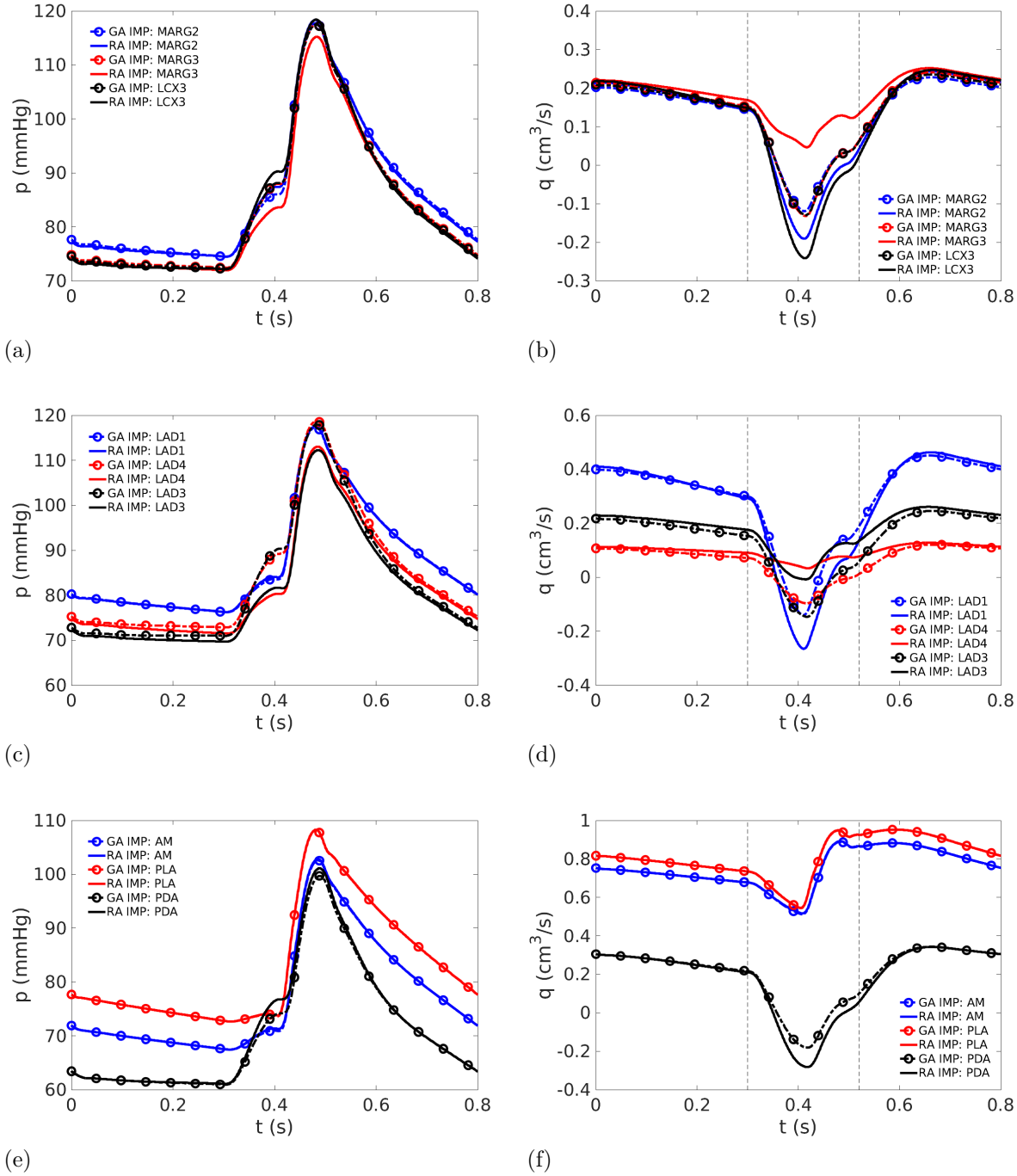

Figure 4.15: Comparison between the simulated pressures and flow rates of the terminal arteries of the LCX branches (MARG2, MARG3, and LCX3) in (a), the LAD branches (LAD1, LAD4, and LAD3) in (b), and the RCA branches (AM, PLA, and PDA) in (c) using both the globally averaged IMP and the AHA regionally averaged IMP. The abbreviations 'GA IMP' and 'RA IMP' represent globally and AHA regionally averaged IMP, respectively.

To summarise, the results of simulating coronary flow using regionally averaged IMP are comparable to experimental data, with slight differences in pressures and flow rates of

the LCX, LAD, and RCA compared to globally averaged IMP. However, the variation in IMP from globally to regionally averaged significantly affects the pressures and flow rates of terminal vessels, especially during systole. During diastole, the differences between the two IMPs are minor, resulting in overlapping pressures and flow rates of the terminal vessels in the two cases. Nonetheless, during systole, when IMP increases, the flow is impeded more, whereas a decrease in IMP results in less impeded flow.

4.5 Myocardial perfusion

As presented in the previous sections, even though the coronary flows in the proximal arteries such as LCX, LAD, and RCA are identical, the coronary flows in the distal arteries namely the terminal vessels can be different. To further evaluate the coronary flow, in this section, we introduce myocardial perfusion. Myocardial perfusion refers to the blood flow that supplies oxygen and nutrients to the heart. Myocardial perfusion can provide more accurate and key information for the diagnosis and management of various cardiovascular diseases. For instance, impaired myocardial perfusion, resulting from various pathological conditions such as coronary artery disease, can lead to ischemia, which may ultimately lead to myocardial infarction and heart failure.

Positron emission tomography (PET), computerised tomography (CT), and CMR are currently being used to assess myocardial perfusion in terms of myocardial blood flow (MBF, ml/min/g) (Larghat et al., 2013; Brown et al., 2018; Fair et al., 2015; Knott et al., 2020). PET represents the gold standard for the non-invasive quantification of MBF and the detection of ischemia. PET has the advantage of being able to provide absolute quantification of MBF and the ratio of stress to rest MBF, known as the myocardial perfusion reserve or coronary flow reserve, which is valuable for the prognostic evaluation of chronic coronary syndromes and cardiomyopathy. PET has been validated against invasive techniques such as fractional flow reserve (FFR) and the index of microcirculatory resistance. CMR also offers an alternative to PET for the quantification of MBF. CMR has several advantages over PET, including a lack of ionizing radiation, higher spatial resolution, and the added value of providing comprehensive data on left ventricular size, function, and scar within a single study. The assessment of myocardial perfusion using CMR has been validated against microspheres, PET, and invasive FFR measurements in several small-scale studies. However, the wider adoption of quantitative perfusion CMR has been limited by the need for time-consuming, off-line processing, and poor repeatability (Larghat et al., 2013; Brown et al., 2018). There is a growing body of research (Fair et al., 2015; Brown et al., 2018; Knott et al., 2020) aimed at enhancing the efficiency and reproducibility of CMR, with the ultimate goal of facilitating the integration of CMR-based perfusion mapping into routine clinical practice.

Table 4.9 summarises the reported values of MBF in human subjects in the literature. The reported values of MBF provide valuable information on the normal range of MBF in healthy subjects at rest and at stress. Specifically, Brown et al. (2018) recruited 42 healthy subjects (23 female, median age 23 years), and found that the mean global MBF at rest was 0.64±0.15 ml/g/min and the mean global MBF at stress was 2.55±0.57 ml/g/min. Kotecha et al. (2019) recruited 54 patients and 15 control subjects, and reported that the global stress MBF of control subjects was 3.17±0.65 ml/g/min, and the global rest MBF was 0.78±0.18 ml/g/min. Myocardial regions with obstructive coronary artery disease had a mean stress MBF of 1.47 ml/g/min and a myocardial perfusion reserve of 1.75. Knott et al. (2019) recruited 50 patients (7 female, mean age 58.2 years) and 24 healthy volunteers (12 female, mean age 37.3 years), and found that mean stress MBF in healthy volunteers was 3.07 ml/g/min and 2.00 ml/g/min in the myocardium of patients with diameter stenosis (DS) DS<50%. The mean rest MBF was 0.86 ml/g/min for healthy volunteers and 0.77 ml/g/min for patients with ischemic myocardium.

Table 4.9: Reported myocardial blood flow (MBF) values in the literature for healthy subjects.

Reference	Number of healthy subjects	MBF (ml/g/min) at rest	MBF (ml/g/min) at stress
(Brown et al., 2018)	42	0.64±0.15	2.55±0.57
(Kotecha et al., 2019)	15	0.78±0.18	3.17±0.65
(Knott et al., 2019)	24	0.86	3.07

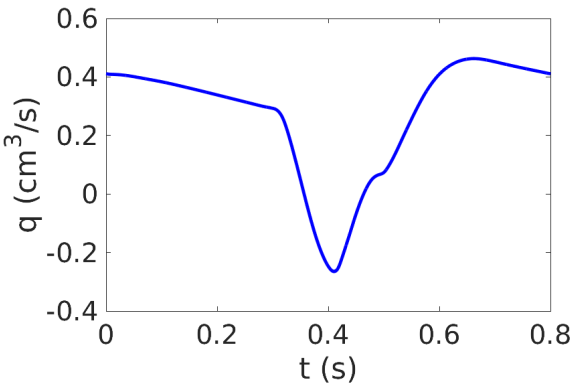

Figure 4.16: Flow rate at the distal point of the LAD1 during one cardiac cycle.

The coronary flow model proposed in this thesis can be readily applied to assess

myocardial perfusion. The MBF can be calculated by

$$\mathrm{MBF} = \frac{\int_0^T q \, \mathrm{d}t}{T \, m_{\mathrm{myo}}}, \tag{4.9}$$

where q is the coronary flow rate measured at the end (truncation point where it enters the myocardium) of one terminal artery, T represents the temporal duration of a single cardiac cycle, and m_{myo} is the myocardial mass of the regions perfused by the terminal artery. For instance, the flow rate at the end of the LAD1 during one cardiac cycle is shown in Fig. 4.16. The integration of the flow rate q over one period is computed to be 0.211 ml. The duration of one cardiac cycle, T, is 0.8 s, which is equivalent to 0.013 min. The regions perfused by LAD1 comprise AHA segments 1, 2, and 8, as listed in Table 4.8. The total volume of these three segments is 12.015 ml, with a density of 1.055 g/ml. Thus, MBF in the regions perfused by LAD1 is

$$\mathrm{MBF}_{\mathrm{LAD1}} = \frac{0.211\,\mathrm{ml}}{0.013\,\mathrm{min} \times 12.015\,\mathrm{ml} \times 1.055\,\mathrm{g/ml}} \approx 1.281\,\mathrm{ml/g/min}, \tag{4.10}$$

The simulated myocardial perfusion of the regions perfused by the terminal vessels (LAD1, LAD4, LAD3, MARG1, MARG2, MARG3, LCX3, PDA, and PLA) using globally averaged and AHA regionally averaged IMP are shown in Fig. 4.17 (a, b). Moreover, Fig. 4.18 displays the perfusion maps of the two simulation cases and a healthy volunteer as reported by Knott et al. (2019), presented in bull's eye plots. Our coronary flow model yields perfusion values ranging from 0.676 ml/g/min to 1.377 ml/g/min when using globally averaged IMP, and from 0.659 ml/g/min to 1.281 ml/g/min when using regionally averaged IMP. These values are comparable to the reported resting MBF values of a healthy subject by Knott et al. (2019) of 0.56 ml/g/min to 1.17 ml/g/min. Furthermore, the mean MBF calculated using globally averaged IMP is 0.981 ml/g/min, and the mean MBF calculated using regionally averaged IMP is 1.043 ml/g/min, both of them are slightly higher than the value of 0.78±0.18 ml/g/min reported by Kotecha et al. (2019).

It can be further observed that the perfusion distribution obtained by utilising regionally averaged IMP is comparatively more uniform than that achieved by utilising globally averaged IMP. Finally, it is expected that the myocardial perfusion obtained from our coronary flow model can be used to inform clinical decisions on the management of cardiovascular diseases, such as the selection of appropriate revascularization strategies.

4.6 Summary

In this chapter, we have investigated the one-way coupling between the coronary flow model and the LV model with a focus on obtaining more accurate coronary flow. We

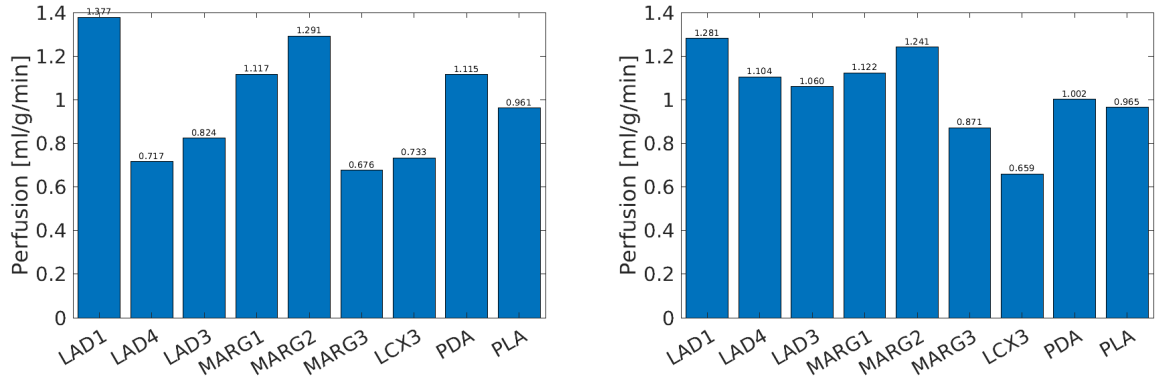

(a) (b)

Figure 4.17: Simulated myocardial perfusion in the regions perfused by the terminal vessels LAD1, LAD4, LAD3, MARG1, MARG2, MARG3, LCX3, PDA, and PLA, while using globally averaged IMP (a) and AHA regionally averaged IMP (b).

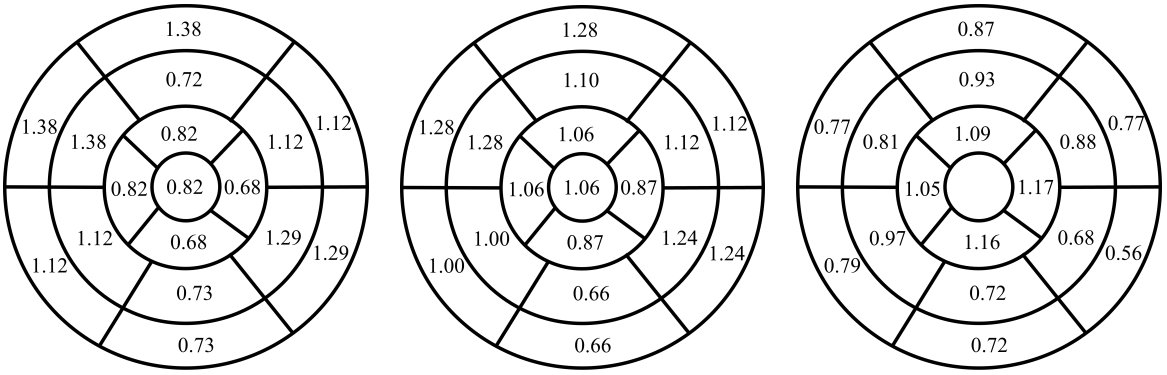

(a) (b) (c)

Figure 4.18: Perfusion maps of the left ventricle using two different IMP averaging methods and measured from a healthy volunteer: Globally averaged IMP (a), regionally averaged IMP (b), and reported by Knott et al. (2019) (c), all presented in bull's eye plots.

have improved several aspects of the coronary flow model compared with that in Chapter 2, including the coronary network reconstruction, IMP calculation, and assignment of the coronary arteries to the segments of the LV wall. Specifically, firstly, the coronary vasculature network was reconstructed by including additional blood vessels in the RCA branch, and a detailed description of the venous system was provided. The morphology and dimensions of the coronary blood vessels were summarised and compared with other published data. Next, a review of the literature was conducted to gather experimental data for the IMP, as well as IMP calculation from lumped parameter models and 3D heart models. We analysed two IMP formulas based on the Cauchy stress calculated from the LV model and applied them to the coronary flow model. Our simulated results showed that employing globally averaged hydro-static pressure as the IMP yielded reasonable coronary flow results. We also compared the simulated flow rates with experimentally

measured flow rates from humans, lambs, and swines. As a consequence of the heart's cyclic contractions, the flow rates in the LAD and LCX were impeded during systole, leading to the identification of three local extremes in the flow rate profiles of the LAD and LCX. In general, there is a direct correlation between the IMP and impediment of coronary flow, with higher IMP leading to greater impeding effects. Thirdly, the influence of the regionally averaged IMP was examined. The LV wall was partitioned into 17 AHA segments, and the assignment of the coronary arteries to these segments was presented. Surprisingly, the simulated pressures and flow rates in the LCX, LAD, and RCA were found to be nearly identical between the globally averaged IMP and the application of the regionally averaged IMP. However, notable discrepancies in the pressures and flow rates of the terminal blood vessels were observed when comparing the results obtained using the two types of average IMP. Finally, we calculated myocardial perfusion in the AHA regions in the last section. Both globally and regionally averaged IMP was used, and the results agreed well with published data. It was found that regionally averaged IMP produced more uniform myocardial perfusion.

Overall, this chapter provides a thorough investigation of the coronary flow model and its one-way coupling with the LV model, as well as a detailed examination of the effects of IMP on coronary blood flow. The coupling of the LV model allows for obtaining a more precise distribution of the IMP, enabling analysis using globally or regionally averaged IMP. Compared with the simulated coronary flow using the assumed IMP in Chapter 2, a more accurate coronary flow is achieved as shown in Fig. 4.6. The calculation of myocardial perfusion can also aid in evaluating interventions and guiding treatment decisions.

It is necessary to acknowledge the limitations of this chapter. Firstly, the lack of experimental data for IMP comparison is a common challenge in modelling IMP. To address this issue, more precise non-invasive imaging techniques and more efforts to translate medical information into computational models are required (Niederer et al., 2019). Secondly, the LV geometry and coronary vasculature used in this chapter were not from the same individual, although the methodology presented in this chapter can be adjusted to incorporate diverse heart geometries and coronary vasculature. Thirdly, we did not consider the autoregulation of coronary flow, which ensures that the heart receives adequate oxygen and nutrients to meet its metabolic demands. Lastly, LV remodelling in diseased conditions, and variations in preload and afterload under different physiological conditions can impact coronary flow results and need further investigation.

Chapter 5

A human bi-ventricle model for modelling pulmonary regurgitation

In the previous chapters, our focus has been on exploring physiological simulations of coronary flow and myocardial mechanics. In this chapter, our objective is to construct a bi-ventricle model and demonstrate its capabilities in simulating disease scenarios. This chapter follows the format of a journal article and has been published. The bi-ventricle model can be further coupled to the coronary flow model developed in Chapter 2 to investigate myocardial perfusion under disease cases.

5.1 Introduction

Pulmonary regurgitation (PR) occurs when the pulmonary valve does not function properly and the blood will flow back to the right ventricle (RV) during diastole. A slight amount of PR was reported in 40-78% of patients with normal pulmonary valves (Lancellotti et al., 2010). Mild-to-moderate PR is often seen in patients with pulmonary hypertension (Berger et al., 1985; Mutlak et al., 2009; Topilsky et al., 2012). Severe PR is a common complication in patients with repaired pulmonary valve (Rebergen et al., 1993; Bouzas et al., 2005), especially after treatments of tetralogy of Fallot which occurs in some infants born with congenital heart disease (Shinebourne et al., 2006; Chaturvedi and Redington, 2007; Frigiola et al., 2008). Severe PR leads to RV overload, bi-ventricle dysfunction, arrhythmias, and associated morbidity and mortality (Gatzoulis et al., 2000; Geva et al., 2004; Puchalski et al., 2008; Mongeon et al., 2019). Thus, assessment of the severity of PR is important to clinical decisions and treatments. Cardiac magnetic resonance (CMR) imaging and Doppler echocardiography are currently the two main techniques to evaluate PR, given their ability to quantify volumes and flow (Li et al., 2004; Puchalski et al., 2008; Lancellotti et al., 2010; Mercer-Rosa et al., 2012). However, standards for the quantification of PR are not well-established and it remains difficult to measure and assess

the impact of PR on cardiac functions due to limitations and challenges in the imaging techniques (Silversides et al., 2003; Geva et al., 2004; Davlouros et al., 2004; Wald et al., 2009; Lancellotti et al., 2010; Mercer-Rosa et al., 2012).

There have been a number of computational models for simulating and predicting the mechanical behaviours of the heart, by virtue of developments in the continuum mechanics and the finite element method (Walker et al., 2005; Szilágyi et al., 2011; Wang et al., 2013; Baillargeon et al., 2014; Sack et al., 2018; Guan et al., 2020b). Wang et al. (2013) developed a finite element human LV model which incorporated the passive material model proposed by Holzapfel and Ogden (2009) and a rule-based myofibre structure. Baillargeon et al. (2014) developed a computational model (the living heart project) to simulate the behaviour of a human heart with all four chambers in a whole cardiac cycle. During systole, an active stress component is added to the total Cauchy stress by a phenomenological representation of active contraction (Guccione and McCulloch, 1993; Guccione et al., 1993; Walker et al., 2005; Göktepe and Kuhl, 2010). In addition, they adopted lumped parameter systems to provide a natural coupling of pressures between the four chambers. Their simulated long-axis shortening and pressure-volume loops agreed well with clinical observations. Moreover, Sack et al. (2018) constructed and validated subject-specific biventricular finite element swine heart models in healthy and diseased states. Their simulated stroke volume, ejection fraction, and strains agreed well with experimental data. Furthermore, reference stress and strain values at multiple time points in one cardiac cycle were reported in their study. Using a finite element computational model of the bi-ventricular porcine heart, Guan et al. (2020b) found that sheet-normal active contraction enhanced the ventricular contraction. They further investigated the effects of myofibre structure, including myofibre rotation angle and myofibre dispersion, on cardiac passive and active responses (Guan et al., 2022b,c). Reviews on cardiac modelling can be found in (Quarteroni et al., 2017; Mangion et al., 2018; Peirlinck et al., 2021).

Recently, Wisneski et al. (2020) employed the four-chamber human heart model developed by Baillargeon et al. (2014) to investigate the impact of aortic stenosis on myofibre stress. They adopted closed-loop lumped parameter models coupled to the heart geometry to simulate the pulmonary and systemic circulatory systems. The degree of aortic stenosis was achieved by tuning the resistance of the aortic valve. Furthermore, they developed patient-specific LV models to study the effect of low-flow and low-gradient aortic stenosis on LV biomechanics (Wisneski et al., 2022), where globally reduced LV stress was observed compared with stress in the idealised LV geometry. However, to the best knowledge of the authors, there yet is no application of the finite element computational heart model to simulations of PR.

To address the need for assessment of the influence of PR on cardiac functions, we have developed the following finite element model of the human bi-ventricle heart and

simulated five cases of different degrees of PR severity to analyse the effect of PR on the bi-ventricle pump functions. This work is built on the previous research on computational LV heart modelling (Guan et al., 2022c). By incorporating a patient-specific bi-ventricle geometry and tuning backflow from the main pulmonary artery to the RV, this bi-ventricle model is constructed to achieve realistic cardiac performance under different degrees of PR. We validate the model with regard to the ejection fractions of the LV and RV of the baseline case, and the pressure ranges of the main pulmonary artery and the aorta. RV dilation in the PR disease cases is compared with reported MRI data. Furthermore, the long-axis and short-axis views of the LV and RV and the motion of the septum are compared with the literature. This is the first 3D computational bi-ventricle model to investigate the effect of PR on cardiac functions and interactions of the RV and LV. Our model offers promise for predicting and assessing PR pathophysiology.

5.2 Methods

Our three-dimensional bi-ventricle human heart model is shown in Fig. 5.1 (c). This model includes a patient-specific bi-ventricle geometry, a commonly used myofibre structure, an up-to-date passive myocardium constitutive law, a modified active tension model for active contraction, an open-loop lumped parameter model for systemic circulation, and an open-loop lumped parameter model for the pulmonary circulation.

The subject-specific human bi-ventricle mesh is obtained from the previous studies (Gao et al., 2017; Guan et al., 2022c) by including both the LV and RV, as shown in Fig. 5.1 (a). The bi-ventricle mesh consists of 173,974 tetrahedral elements and 35,841 nodes. The layered myofibre architecture (Fig. 5.1 (b)) is generated using a rule-based method (RBM) (Guan et al., 2020b), and the myofibre rotation angles vary linearly from -60° at the epicardium to 60° at the endocardium (Wang et al., 2013).

The LV cavity and the RV cavity are connected to simplified open-loop lumped parameter systems representing the systemic circulation and the pulmonary circulation, respectively, as shown in Fig. 5.1 (c). These lumped parameter systems provide physiologically accurate LV and RV cavity pressures. Such lumped parameter systems correspond to the two-element Windkessel model (Westerhof et al., 2009). Details of the two lumped parameter systems can be found in the previous chapters. As shown in Fig. 5.1 (c), there is an additional valve controlling the one-way leakage from the main pulmonary artery to the RV. Different PR severity was achieved by tuning the resistance $R^{\mathrm{L}}_{\mathrm{MP}}$. In this study, five cases are considered:

- $R^{\mathrm{L}}_{\mathrm{MP}} = 1000\,\mathrm{MPa}\cdot\mathrm{s/m^3}$ for the baseline case;
- $R^{\mathrm{L}}_{\mathrm{MP}} = 60\,\mathrm{MPa}\cdot\mathrm{s/m^3}$ for the mild case;

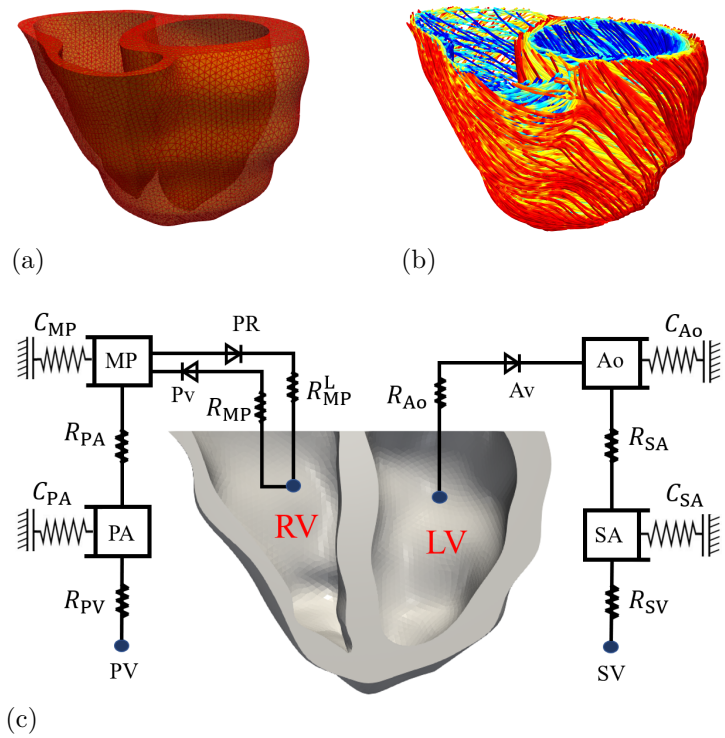

Figure 5.1: The human bi-ventricle mesh (a) with 173,974 linear tetrahedral elements and 35,841 nodes, and the rule-based myofibre structure (b) where the myofibre angle varies from $-60°$ at the epicardium to $60°$ at the endocardium. Schematic illustration (c) of the bi-ventricle model coupled with systemic and pulmonary circulations represented by lumped parameter models. LV is the left ventricle. Ao is the aorta. SA is the systemic arteries. SV is the systemic veins. RV is the right ventricle. MP is the main pulmonary artery. PA is the pulmonary arteries. PV is the pulmonary veins. Pv is the pulmonary valve and Av is the aortic valve, they are represented by the Diode symbols to indicate the unidirectional flow. Note that the severity of the pulmonary regurgitation is controlled by the resistance $R^{\mathrm{L}}_{\mathrm{MP}}$. R_{MP} is the pulmonary valve resistance in healthy condition. R_{PA} is the resistance of the pulmonary arteries. R_{PV} is a trivial resistance allowing drainage of the flow in the pulmonary circulation. R_{Ao} is the aortic valve resistance. R_{SA} is the resistance of the systemic arteries. R_{SV} is a trivial resistance allowing drainage of the flow in the systemic circulation. C_{Ao} is the aortic compliance. C_{SA} is the compliance of the systemic arteries. C_{MP} is the compliance of the main pulmonary artery. C_{PA} is the compliance of the pulmonary arteries.

- $R^{\mathrm{L}}_{\mathrm{MP}} = 35\,\mathrm{MPa}\cdot\mathrm{s/m}^3$ for the moderate 1 case;
- $R^{\mathrm{L}}_{\mathrm{MP}} = 25\,\mathrm{MPa}\cdot\mathrm{s/m}^3$ for the moderate 2 case;
- $R^{\mathrm{L}}_{\mathrm{MP}} = 15\,\mathrm{MPa}\cdot\mathrm{s/m}^3$ for the severe case.

5.2.1 Passive constitutive law

The anisotropic hyperelastic material property proposed by Holzapfel and Ogden (so-called the HO model) (Holzapfel and Ogden, 2009) has been widely used in the computational cardiology community (**?**Sack et al., 2018; Guan et al., 2020a; Wisneski et al., 2022). The invariant-based strain energy function of the HO model can be written as

$$\Psi = \Psi_{\mathrm{g}} + \Psi_{\mathrm{aniso}}, \tag{5.1}$$

where Ψ_{g} is the strain energy of the ground matrix, and Ψ_{aniso} accounts for the strain energy associated with the myofibre direction and the sheet direction as well as their interactions, specifically,

$$\begin{aligned} \Psi_{\mathrm{g}} &= \frac{a_{\mathrm{g}}}{2b_{\mathrm{g}}}\{\exp[b_{\mathrm{g}}(I_1-3)]\}, \\ \Psi_{\mathrm{aniso}} &= \Psi_{\mathrm{aniso}}^{I_{4\mathrm{f}}} + \Psi_{\mathrm{aniso}}^{I_{4\mathrm{s}}} + \Psi_{\mathrm{aniso}}^{I_{8\mathrm{fs}}}, \end{aligned} \tag{5.2}$$

where

$$\begin{aligned} \Psi_{\mathrm{aniso}}^{I_{4\mathrm{f}}} &= \frac{a_{\mathrm{f}}}{2b_{\mathrm{f}}}\{\exp[b_{\mathrm{f}}(I_{4\mathrm{f}}-1)^2]-1\}\,\mathcal{H}(I_{4\mathrm{f}}-1), \\ \Psi_{\mathrm{aniso}}^{I_{4\mathrm{s}}} &= \frac{a_{\mathrm{s}}}{2b_{\mathrm{s}}}\{\exp[b_{\mathrm{s}}(I_{4\mathrm{s}}-1)^2]-1\}\,\mathcal{H}(I_{4\mathrm{s}}-1), \\ \Psi_{\mathrm{aniso}}^{I_{8\mathrm{fs}}} &= \frac{a_{\mathrm{fs}}}{2b_{\mathrm{fs}}}[\exp(b_{\mathrm{fs}}I_{8\mathrm{fs}}^2)-1], \end{aligned} \tag{5.3}$$

in which $a_{(\mathrm{g,\ f,\ s,\ fs})}, b_{(\mathrm{g,\ f,\ s,\ fs})}$ are constant material parameters, $\mathcal{H}(\cdot)$ is the Heaviside step function to ensure that only stretched fibres can bear the load, e.g., $\mathcal{H}(I_{4\mathrm{f}}-1)=1$ when $I_{4\mathrm{f}}-1>0$, otherwise $\mathcal{H}(I_{4\mathrm{f}}-1)=0$. The invariants $I_{(1,\ 4\mathrm{f},\ 4\mathrm{s},\ 8\mathrm{fs})}$ are calculated by the right Cauchy-Green tensor $\mathbf{C}=\mathbf{F}^{\mathrm{T}}\mathbf{F}$ from the deformation gradient tensor $\mathbf{F}$, i.e.

$$I_1 = \mathrm{trace}(\mathbf{C}), \quad I_{4\mathrm{f}} = \mathbf{f}_0\cdot(\mathbf{C}\mathbf{f}_0), \quad I_{4\mathrm{s}} = \mathbf{s}_0\cdot(\mathbf{C}\mathbf{s}_0), \quad I_{8\mathrm{fs}} = \mathbf{f}_0\cdot(\mathbf{C}\mathbf{s}_0), \tag{5.4}$$

where $\mathbf{f}_0, \mathbf{s}_0, \mathbf{n}_0$ are the unit myofibre direction, the unit sheet direction, and the unit sheet-normal direction in the reference configuration, respectively.

5.2.2 Active stress model

During myocardial contraction, the active tension (T_{a}) generated by myocytes is determined by a well-established time-varying elastance model (Guccione and McCulloch, 1993; Sack et al., 2018; Wisneski et al., 2020)

$$T_{\mathrm{a}}(t,l) = \frac{T_{\max}}{2}\,\frac{\mathrm{Ca}_0^2}{\mathrm{Ca}_0^2+\mathrm{ECa}_{50}^2(l)}\,(1-\cos(\omega(t,l))), \tag{5.5}$$

where $T_{\max}$ is the maximum isometric active tension, Ca_0 is the peak intracellular calcium, t is the time, and the length-dependent calcium sensitivity (ECa_{50}) is given by

$$\mathrm{ECa}_{50}(l) = \frac{\mathrm{Ca}_{0\max}}{\sqrt{e^{B(l-l_0)}-1}}, \tag{5.6}$$

in which B and $\mathrm{Ca}_{0\max}$ are constants, l_0 is the minimum sarcomere length to produce active stress, and l is the deformed sarcomere length

$$l = l_r\sqrt{2E_{\mathrm{ff}}+1}, \tag{5.7}$$

where l_r is the stress-free sarcomere length, and $E_{\mathrm{ff}} = \frac{1}{2}(\mathbf{f}_0 \cdot (\mathbf{C}\mathbf{f}_0) - 1)$ is the Lagrange strain in the myofibre direction. The time function after onset of contraction in Eq. (5.5) is

$$\omega(t,l) = \begin{cases} 2\pi\,\frac{t}{t_0} & \text{for} \quad 0 \leqslant t \leqslant t_{\mathrm{Iso}}, \\ \pi + \frac{(t-t_0)(\pi - 2\pi t_{\mathrm{Iso}}/t_0)}{t_0 - t_{\mathrm{Iso}}} & \text{for} \quad t_{\mathrm{Iso}} < t \leqslant t_0, \\ \pi\,\frac{t-t_0+t_r}{t_r} & \text{for} \quad t_0 < t \leqslant t_0 + t_r, \\ 0 & \text{for} \quad t > t_0 + t_r, \end{cases} \tag{5.8}$$

where $t_{\mathrm{Iso}} = 0.05\,\mathrm{s}$, t_0 is the time to peak tension, and t_r is the duration of relaxation, i.e.

$$t_r(l) = ml + b, \tag{5.9}$$

where m and b are constants. Note that the piecewise time function, $\omega(t,l)$, consists of four pieces of linear functions, instead of three pieces (Walker et al., 2005; Sack et al., 2018; Guan et al., 2020b). The original three-piece function $\omega(t,l)$ is introduced by Tözeren (Tözeren, 1985) to incorporate the influence of the activating calcium ions on myofibre contraction. Both the active tensions generated by the two $\omega(t,l)$ are comparable with experimental data from Janssen and de Tombe (1997). However, our modification increases the ascent rate of the active tension during the isovolumetric contraction phase so that the isovolumetric contraction time is decreased. Moreover, it can help to prolong the ejection time if needed.

Finally, the total Cauchy stress is

$$\boldsymbol{\sigma} = \mathbf{F}\frac{\partial \Psi}{\partial \mathbf{F}} + T_{\mathrm{a}}\hat{\mathbf{f}} \otimes \hat{\mathbf{f}} - p\mathbf{I}, \tag{5.10}$$

where $\hat{\mathbf{f}}$ is the unit vector of the myofibre direction in the current configuration, and p is the Lagrange multiplier to enforce incompressibility. Given this total Cauchy stress, the

dynamics of the bi-ventricle mesh are governed by

$$\begin{cases} \nabla \cdot \boldsymbol{\sigma} = 0, & \text{within the bi-ventricle wall domain,} \\ \boldsymbol{\sigma} \cdot \mathbf{n} = -P\mathbf{n}, & \text{on the endocardial surface,} \\ \boldsymbol{\sigma} \cdot \mathbf{n} = 0, & \text{on the epicardial surface,} \\ u_\theta = 0 \quad \text{and} \quad u_z = 0, & \text{on the LV basal surface,} \\ u_z = 0, & \text{on the RV basal surface,} \end{cases} \tag{5.11}$$

where P is the LV or the RV cavity pressure, $\mathbf{n}$ is the unit vector normal to the endocardial or the epicardial surface, u_θ and u_z are displacement along the θ-axis and the z-axis (the long axis direction of the heart) of the global cylinder coordinate system, respectively. The RV wall is thinner and more deformable than the LV wall, thus, different boundary conditions are imposed on the LV and RV basal planes. Note that the RV wall in this study refers to the RV-free wall, and the LV wall includes the septum wall and the LV-free wall.

5.2.3 Implementation

The above bi-ventricle model is solved by the finite element method via ABAQUS 2018 (Dassault Systemes, Johnston RI, USA). The constitutive models are implemented in ABAQUS through the VUMAT user subroutine. The fluid cavity and fluid exchange modulus provided by ABAQUS are used to implement the lumped parameter circulatory systems.

The period of one cardiac cycle is considered to be 0.9 s (67 beats per minute). The run-time for 5 repeated cardiac cycles is approximately 80 hours on a Linux workstation with 8 cores of 2.3 GHz CPU (Intel(R) Xeon(R) CPU E5-2699 v3) and 128 GB memory. In Section 5.3, we will show the convergent results of the third cycle. The parameter values of the passive and active models are summarised in Table 5.1, which are adopted from the previous study (Guan et al., 2022c).

The end-diastolic pressure (EDP), end-systolic pressure (ESP), end-diastolic volume (EDV), and end-systolic volume (ESV) are determined by the pressure and volume of the fluid cavities representing the LV and the RV, respectively. Some cardiac function indicators are calculated following studies in (Wald et al., 2009; Harrild et al., 2010; Lee et al., 2012). Specifically, the ejection fraction (EF) is calculated by

$$\text{EF} = (\text{EDV - ESV})/\text{EDV}. \tag{5.12}$$

The PR volume (PRV) is calculated as the increase of the volume in the RV during diastole when the pressure of the RV drops (Bove et al., 2014). The PR fraction (PRF) is calculated

Table 5.1: Parameter values of the passive and active models adopted by the bi-ventricle model.

Passive constitutive law (Guan et al., 2022c)								
	a_{g} (kPa)	b_{g} -	a_{f} (kPa)	b_{f} -	a_{s} (kPa)	b_{s} -	a_{fs} (kPa)	b_{fs} -
LV	0.1731	5.1207	1.9344	0.2199	0.2143	0.0005	0.2665	2.5505
RV	0.3917	5.1207	4.400	0.2199	0.4850	0.0005	0.6031	2.5505
Active tension model (Guan et al., 2022c)								
	m ($\mathrm{s}\,\mu\mathrm{m}^{-1}$)	b (s)	l_0 (μ m)	B ($\mu\mathrm{m}^{-1}$)	Ca_0 (μM)	$\mathrm{Ca}_{0\mathrm{max}}$ (μM)	T_{max} (kPa)	l_r (μm)
LV	1.0489	-1.429	1.58	4.750	4.35	4.35	130	1.85
RV	1.0489	-1.429	1.58	4.750	4.35	4.35	90	1.85

as the retrograde flow divided by the net antegrade flow (Rebergen et al., 1993; Harrild et al., 2010), i.e.

$$\mathrm{PRF} = \mathrm{PRV}/(\mathrm{RVEDV} - \mathrm{RVESV} - \mathrm{PRV}). \tag{5.13}$$

The RV end-diastolic volume indexed by the body surface area (RVEDVi) is calculated as

$$\mathrm{RVEDVi} = \mathrm{RVEDV}/\mathrm{BSA}, \tag{5.14}$$

where the body surface area (BSA) is $1.55\,\mathrm{m}^2$ for this bi-ventricle geometry (obtained through email communication with the data holder).

5.3 Results

Simulated pressures of the aorta, the main pulmonary artery, the LV cavity, and the RV cavity of the baseline case are shown in Fig. 5.2. As shown in Fig. 5.2 (a), the aortic pressure of the baseline case is from 69.2 mmHg to 109.6 mmHg, which agrees well with the normal range of the aortic pressure from 70.0 mmHg to 120.0 mmHg (Erbel et al., 2001; Reymond et al., 2012). As shown in Fig. 5.2 (b), our simulated pulmonary pressure is from 6.1 mmHg to 27.8 mmHg, which is comparable with the normal range of the pulmonary pressure from 5 mmHg to 25 mmHg (McQuillan et al., 2001; McLaughlin et al., 2009;

Noordegraaf et al., 2019). In Fig. 5.2 (c, d), the peak pressures in the LV and RV are 110.5 mmHg and 29.0 mmHg, respectively. The ejection phases of the LV and RV at baseline are marked by the vertical lines in Fig. 5.2. The ejection phase of the LV at baseline is from the time 0.43 s to 0.59 s, and the ejection phase of the RV is from the time 0.41 s to 0.60 s. The ejection time of the RV is longer than that of the LV, which has been reported by Hirschfeld et al. (1975).

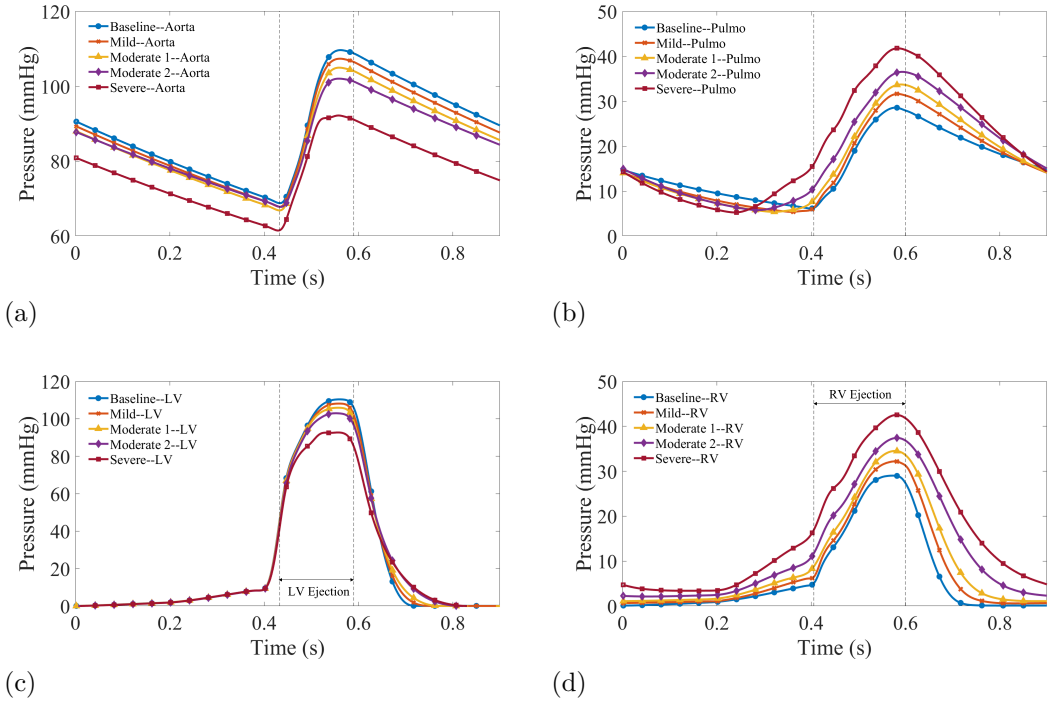

Figure 5.2: Simulated pressures of five cases of different degrees of pulmonary regurgitation in the aorta (a), the main pulmonary artery (Pulmo) (b), the left ventricle cavity (LV) (c), and right ventricle cavity (RV) (d). The two vertical dashed lines in (a, c) mark the ejection phase of the LV of the baseline case, and the two vertical lines in (b, d) mark the ejection phase of the RV of the baseline case.

Fig. 5.2 also shows pressure profiles of the four PR disease cases in the aorta, the main pulmonary artery, the LV cavity, and the RV cavity. Overall, the pressures change greatly from the baseline case to the disease cases. The RV pressure and pulmonary pressure increase due to PR, but LV pressure and aortic pressure are decreased. Specifically, in Fig. 5.2 (a), the aortic pressure continues to decrease from the baseline case to the severe case. The maximum aortic pressure of the severe case is 92.2 mmHg, which is 15.9% less than the maximum aortic pressure of the baseline case (109.6 mmHg). The minimum aortic pressure of the severe case is 61.5 mmHg, which is 11.1% less than that of the baseline case (69.2 mmHg). The decrease in the aortic pressure is caused by the drop in the peak pressure of the LV cavity as shown in Fig. 5.2 (c). The maximum LV pressure of the severe case is 92.5 mmHg, which is 16.3% less than the maximum LV pressure of the

baseline case. Contrary to changes in the LV pressure, as shown in Fig. 5.2 (d), the RV pressure is increased greatly from the baseline case to the severe case. The maximum RV pressure of the severe PR case is 42.5 mmHg, 46.6% higher than that of the baseline case (29.0 mmHg). The increase in the RV pressure leads to an increase in the peak pressure of the main pulmonary artery. As shown in Fig. 5.2 (b), the maximum pulmonary pressure of the severe case is 41.8 mmHg, which is 50.4% higher than that of the baseline case. Due to the largest backflow in the severe case, the pressure of the main pulmonary artery drops quickly to the least at 0.24 s, although its peak pressure is the highest. Note that the pulmonary valve in the severe case opens the earliest, because of its lowest pulmonary pressure and highest RV pressure. In addition, the earliest opening of the pulmonary valve in the severe case yields the longest ejection phase from the time 0.25 s to 0.60 s, which is 84.2% longer than that of the baseline case.

PV loops of the LV and RV of the five cases are shown in Fig. 5.3. For the baseline case, the simulated LV EDV is 115.6 mL and the LV ESV is 45.6 mL, with an EF of 60.5% which is within the reported physiological range for healthy subjects from 50% to 65% (Kumar et al., 2014; Mahadevan et al., 2008; Dokainish et al., 2011; Feher, 2017; Lang et al., 2015). The simulated RV EDV is 132.5 mL and the RV ESV is 63.8 mL, with an EF of 51.8% which is within 52.3±6.2% (N=365) reported by (Pfisterer et al., 1985).

Both PV loops of the LV and of the RV change greatly with different degrees of PR severity as shown in Fig. 5.3. Specifically, the PV loop of the LV shifts leftwards from the baseline case to the severe case, while the PV loop of the RV shifts rightwards. Such behaviour is a result of the increasing dilation of the RV caused by PR. RV dilation for patients with PR has been reported in many studies (Davlouros et al., 2004; Frigiola et al., 2008; Wald et al., 2009). In our simulations, the RV EDV is the largest in the severe case, in the meantime, the LV EDV is the least and is squeezed the most. The RV EDV in the severe case is increased by 50.3% compared with that of the baseline case, while the LV EDV in the severe case is decreased by 18.1% compared with that of the baseline case. Despite different values, all the PV loops of the LV have similar shapes. The isovolumetric contraction and the isovolumetric relaxation periods are clearly indicated by the vertical lines at ED and at ES, respectively. However, for the RV, the shapes of the PV loops in the disease cases are different from that of the baseline case. The isovolumetric relaxation period disappears, thus the RV volume increases as its pressure falls at the beginning of diastole. In addition, the isovolumetric contraction period is shortened and further vanishes. These characteristics of the PV loop have been reported in patients with PR (Redington et al., 1988; Chaturvedi et al., 1997; Yerebakan et al., 2009).

Cardiac pump functions of the LV and RV in the five cases are summarised in Table 5.2, including EDP, ESP, EDV, ESV, EF, PRV, and PRF of the LV and RV, respectively. The LV EDP changes little, but the RV EDP is increased largely. RV EDP of the

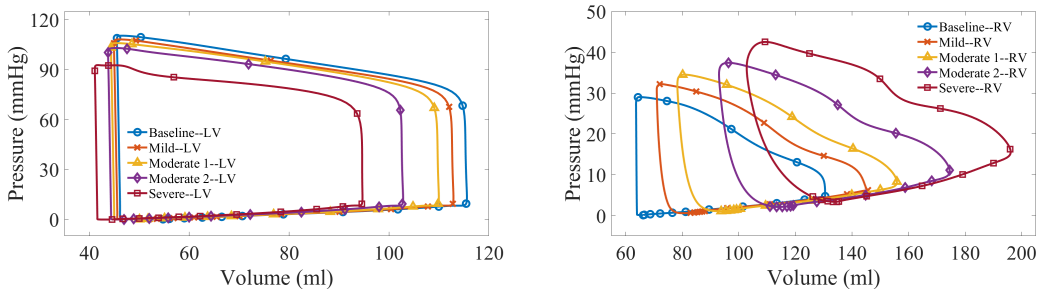

(a) (b)

Figure 5.3: Simulated pressure-volume loops of five cases of different degrees of pulmonary regurgitation of the left ventricle (LV) (a) and of the right ventricle (RV) (b).

severe case is 232.6% higher than that of the baseline case. The LV ESP of the severe case decreases by 20.0% from the baseline case, while the RV ESP increases by 50.9%. Both the LV EF and the RV EF drop in the disease cases, which agree well with (Abd El Rahman et al., 2000; Davlouros et al., 2002). The LV EF decreases by 6.9% from 60.5% of the baseline case to 56.3% of the severe case, and the RV EF decreases by 9.7% from 51.8% of the severe case to 46.8% of the severe case. Comparing the moderate PR-2 case and the severe case, their RV EFs are the same although the RV EDV of the severe case is 12.1% larger than that of the moderate PR-2 case. The PRVs of the four disease cases are 9.3 mL, 15.3 mL, 22.2 mL, and 30.8 mL, respectively, and the PRFs of the four disease cases are 14.3%, 24.4%, 37.2%, and 50.6%.

The simulated RVEDVi with respect to PRF is plotted in Fig. 5.4 with a comparison to magnetic resonance imaging (MRI) data from Harrild et al. (2010) and Lee et al. (2012). RVEDVis of the five cases are within the range of the reported MRI data. For instance, the RVEDVi of the severe case is 126.5 $\mathrm{mL/m^2}$, which is within 110.0 $\mathrm{mL/m^2}$ to 215.3 $\mathrm{mL/m^2}$ reported by Lee et al. (2012). Note that the MRI data are from 41 patients in (Harrild et al., 2010) and 66 patients in (Lee et al., 2012).

The long-axis and short-axis views of the bi-ventricle geometry can be found in Fig. 5.5, showing LV and RV shapes and myofibre stress distributions in the five cases at ED and at ES, respectively. From the long-axis views at ED as shown in Fig. 5.5 (a), the increase of the RV cavity can be clearly observed when PR becomes severe. The increase in the RV cavity is associated with increased backflow (PRV) and pressure in the RV cavity. In addition, the motion of the interventricular septum can be observed. The septum has a right convexity at the baseline case (Méndez et al., 2011). With the increase of PRV, the septum is forced to bulge toward the LV, hence causing the squeeze of the LV. For the short-axis views at ED as shown in Fig. 5.5 (b), the shape of the LV cross-sectional cut plane is nearly circular in the baseline case, but it changes into a flattening D-shape in the severe PR case. At ED, the distance between the septum and the LV-free wall is

Table 5.2: Simulated cardiac pump functions of the left ventricle (LV) and the right ventricle (RV) in five cases of different degrees of pulmonary regurgitation.

Ventricles	Cases	EDP (mmHg)	ESP (mmHg)	EDV (mL)	ESV (mL)	EF	PRV (mL)	PRF
LV	Baseline	9.2	106.5	115.6	45.7	60.5%	-	-
	Mild	9.2	102.8	112.6	45.1	59.9%	-	-
	Moderate 1	9.1	104.3	110.0	44.6	59.5%	-	-
	Moderate 2	9.1	101.8	102.7	44.1	58.6%	-	-
	Severe	9.1	91.6	94.7	41.4	56.3%	-	-
RV	Baseline	4.6	27.7	132.5	63.8	51.8%	-	-
	Mild	6.2	31.4	145.5	71.1	51.1%	9.3	14.3%
	Moderate 1	7.5	33.8	156.4	78.5	49.8%	15.3	24.4%
	Moderate 2	10.0	37.0	175.0	93.1	46.8%	22.2	37.2%
	Severe	15.3	41.8	196.1	104.4	46.8%	30.8	50.6%

EDP = end-diastolic pressure; ESP = end-systolic pressure; EDV = end-diastolic volume; ESV = end-systolic volume; EF = ejection fraction; PRV = pulmonary regurgitation volume; PRF = pulmonary regurgitation fraction.

reduced by 28.0% from the baseline case to the severe case, while the distance between the septum and the RV-free wall is increased by 29.4%. Although the shapes of the LV, the septum, and the RV change greatly at ED from the baseline case to the severe PR case, changes in the shapes of the bi-ventricle are modest at ES. The septum is not clearly bulging toward the LV, from the long-axis views at ES as shown in Fig. 5.5 (c). However, from the short-axis views at ES as shown in Fig. 5.5 (d), RV dilation and the flattening of the LV cross-sectional cut plane can again be observed when PR becomes severe. At ES, the distance between the septum and the LV-free wall is reduced by 5.7% from the baseline case to the severe case, while the distance between the septum and the RV-free wall is increased by 49.6%. The motion of the septum and the flattening of the LV cross-sectional cut plane from the short-axis views have been reported in patients with PR or RV overload (Louie et al., 1992; Sheehan et al., 2008; Méndez et al., 2011; Naeije and Badagliacca, 2017; Mauger et al., 2021).

We used the Menger curvature (Léger, 1999) to quantitatively measure the motion of the septum. As shown in Fig. 5.6 (a), three points are selected (C_1, C_2, C_3) from the long-axis cut plane (in the middle of the bi-ventricle geometry), and the other two points

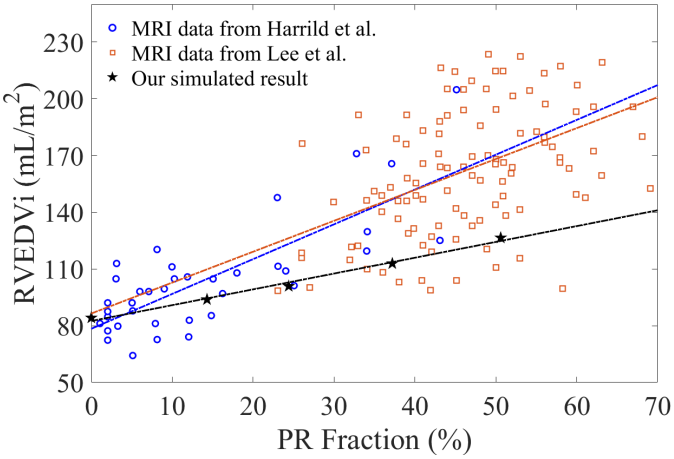

Figure 5.4: Simulated end-diastolic volume of the right ventricle indexed by the body surface area (RVEDVi) versus pulmonary regurgitation (PR) fraction, compared with magnetic resonance imaging (MRI) data from (Harrild et al., 2010; Lee et al., 2012). The blue dashed line (RVEDVi = 1.77× PRF + 78.0, R = 0.79, p<0.001) is the linear regression of data from (Harrild et al., 2010). The orange dashed line (RVEDVi = 1.68× PRF + 84.2, R = 0.47, p<0.001) is the linear regression of data from (Lee et al., 2012). Linear regression of our result is RVEDVi = 0.84× PRF + 82.5 with R = 0.99 and p<0.001.

(C_4, C_5) from the short-axis cut plane (at the equator plane of the bi-ventricle geometry). Specifically, C_1 was picked at the middle part of the septum in the base, C_2 at the intersection of the long-axis cut plane and the short-axis cut plane, C_3 near the apex, C_4 and C_5 near the junctions of the septum and the LV-free wall. These points provide us with a measurement of the curvature of the septum from the long-axis view and from the short-axis view, respectively. The Menger curvature of the septum of the long-axis view is calculated by

$$\frac{4A}{|C_1 - C_2||C_2 - C_3||C_3 - C_1|}, \tag{5.15}$$

where A is the area of the triangle spanned by the three points and $|\cdot|$ is the Euclidean distance. The Menger curvature of the septum of the short-axis view is calculated as

$$\frac{4A}{|C_4 - C_2||C_2 - C_5||C_5 - C_4|}. \tag{5.16}$$

The calculated long-axis and short-axis Menger curvature of the septum are shown in Fig. 5.6 (b). At ED, the long-axis Menger curvature increases by 61.5% from 0.013 at the baseline case to 0.021 at the severe case. The short-axis Menger curvature decreases by 55.2% from 0.029 at the baseline case to 0.013 at the severe case. At ES, the long-axis Menger curvature decreases by 28.6% from 0.007 at the baseline case to 0.005 at the severe case. The short-axis Menger curvature decreases by 29.5% from 0.061 at the baseline case to 0.043 at the severe case.

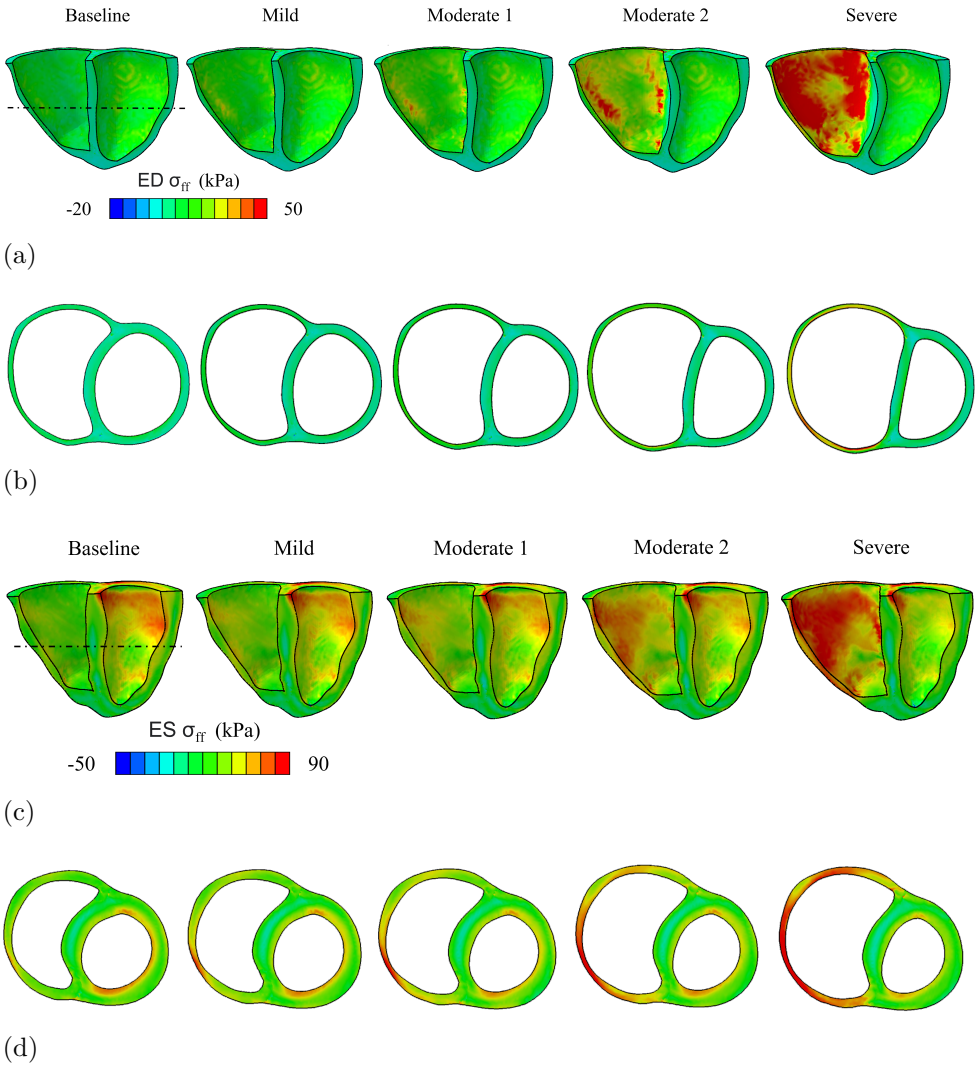

Figure 5.5: Long-axis views (half cuts along the long-axis of the bi-ventricle geometry) showing LV and RV shape and myofibre stress (σ_{ff}) distribution of five cases of different degrees of pulmonary regurgitation at the end of diastole (ED) (a) and at the end of systole (ES) (c). The dashed lines in (a, c) indicate the position of the short-axis cut planes. Short-axis views (cross-sectional cuts at the equator plane of the bi-ventricle geometry) at ED (b) and at ES (d).

Myofibre stress distributions in the five cases at ED and at ES are shown in Fig. 5.5. Myofibre stress on the endocardial surface of the RV increases significantly from the baseline case to the severe case, at both ED and ES, as shown in Fig. 5.5 (a, c). Furthermore, in Fig. 5.5 (d), the increase of the myofibre stress is greater at the thinner part of the RV wall. Finally, the globally averaged myofibre stress ($\bar{\boldsymbol{\sigma}}_{\mathrm{ff}}$) and globally averaged myofibre stretch $\overline{\lambda}_{\mathrm{f}}$ at ED and at ES are calculated by averaging over all elements of the LV or RV wall and weighted by the volume of the elements. For instance, the averaged myofibre stretch is calculated as

$$\overline{\lambda}_{\mathrm{f}} = \frac{\sum_{i=1}^{n} (\lambda_{\mathrm{f}}^{i})\, V^{i}}{\sum_{i=1}^{n} V^{i}}, \tag{5.17}$$

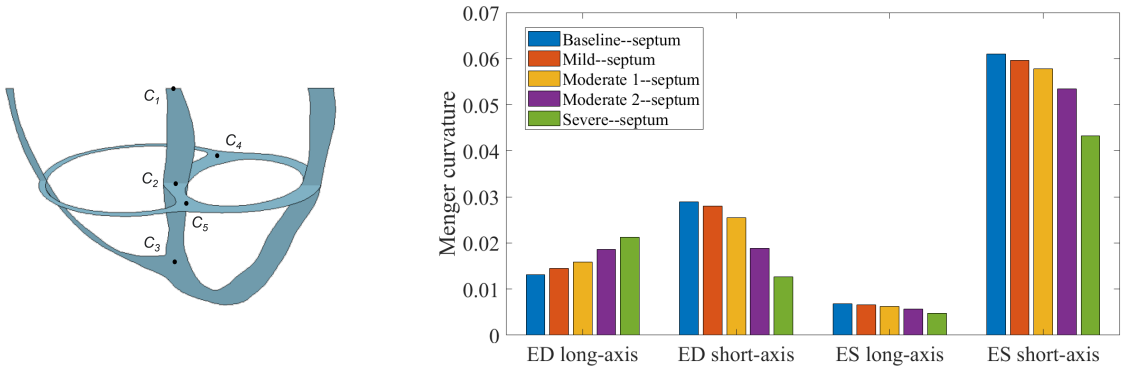

(a) (b)

Figure 5.6: Five selected points (a) of the septum from the long-axis cut plane and the short-axis cut plane to determine the Menger curvature. All points are selected from the midline of the septum. The long-axis and short-axis Menger curvature (b) of the septum at the end of diastole (ED) and at the end of systole (ES) of five cases of different degrees of pulmonary regurgitation.

where $\lambda_{\mathrm{f}}^{i} = \sqrt{2E_{\mathrm{ff}}^{i}+1}$ is the myofibre stretch at the centroid of i^{th} element, E_{ff}^{i} is the Lagrange strain in the myofibre direction at the centroid of i^{th} element, V^{i} is the volume of i^{th} element, n is the total number of elements occupied by the LV wall or RV wall. Analogously, the averaged myofibre stress is calculated by the Cauchy stress.

The globally averaged myofibre stress ($\bar{\boldsymbol{\sigma}}_{\mathrm{ff}}$) and myofibre stretch ($\overline{\lambda}_{\mathrm{f}}$) at ED and at ES are summarised in Table 5.3. At ED, the averaged LV myofibre stress increases by 16.2% from 3.7 kPa to 4.3 kPa, while the averaged RV myofibre stress increases by 303.7% from 2.7 kPa to 10.9 kPa. Back to Fig. 5.5 (a), the RV myofibre stress in the severe case is significantly higher than that of the LV. At ES, the averaged LV myofibre stress decreases by 16.2% from 37.7 kPa to 31.6 kPa, while the averaged RV myofibre stress increases by 105.3% from 24.6 kPa to 50.5 kPa. As shown in Fig. 5.5 (c), the decrease of the LV myofibre stress and the increase of the RV myofibre stress can be clearly observed as PR becomes severe. The averaged LV myofibre stretches change slightly both at ED and at ES. The averaged RV myofibre stretches increase by 8% at ED from 1.12 to 1.21 and 10% at ES from 0.94 to 1.03.

5.4 Discussion

Our study has shown the advantages of modelling PR by the computational model. Realistic cardiac functions were achieved by employing the up-to-date myocardial constitutive law and the open-loop lumped parameter models representing the systemic circulation and the pulmonary circulation. For the baseline case, pressures in the aorta and in the main pulmonary artery and EF of the LV and RV were all within the reported normal

Table 5.3: Averaged myofibre stress ($\bar{\boldsymbol{\sigma}}_{\mathrm{ff}}$) and myofibre stretch ($\bar{\lambda}_{\mathrm{f}}$) in the left ventricular wall (LV wall) and the right ventricular wall (RV wall) in five cases of different degrees of pulmonary regurgitation.

Positions	Cases	$\bar{\boldsymbol{\sigma}}_{\mathrm{ff}}$ (kPa)		$\bar{\lambda}_{\mathrm{f}}$	
		ED	ES	ED	ES
LV wall	Baseline	3.7±18.1	37.7±31.4	1.18±0.07	0.92±0.03
	Mild	3.8±18.5	36.9±31.4	1.18±0.07	0.92±0.03
	Moderate 1	3.8±18.7	36.1±31.4	1.18±0.07	0.92±0.02
	Moderate 2	3.8±19.2	35.4±31.7	1.17±0.08	0.92±0.03
	Severe	4.3±20.3	31.6±32.0	1.17±0.09	0.92±0.03
RV wall	Baseline	2.7±12.1	24.6±28.4	1.12±0.07	0.94±0.06
	Mild	3.7±14.5	30.2±30.1	1.15±0.08	0.96±0.07
	Moderate 1	5.0±17.3	34.8±32.1	1.16±0.09	0.98±0.08
	Moderate 2	7.3±21.4	42.6±36.3	1.18±0.10	1.01±0.11
	Severe	10.9±26.5	50.5±41.7	1.21±0.11	1.03±0.12

Results are presented with standard deviations. ED = at the end of diastole; ES = at the end of systole. The RV wall is the RV-free wall, and the LV wall includes both the septum wall and the LV-free wall. The stress and stretch are volumetric-averaged over the LV wall or RV wall, respectively.

ranges of healthy subjects (Pfisterer et al., 1985; Erbel et al., 2001; McQuillan et al., 2001; McLaughlin et al., 2009; Reymond et al., 2012; Mahadevan et al., 2008). Four disease cases were designed to simulate different degrees of PR severity. Our simulated RVEDVi under different PR cases agreed well with published MRI data (Harrild et al., 2010; Lee et al., 2012), see Fig. 5.4. In addition, the motion of the septum and shapes of the LV and RV cut planes were comparable with the literature (Sheehan et al., 2008; Méndez et al., 2011; Naeije and Badagliacca, 2017; Mauger et al., 2021). The validation of this model allowed us to analyse the effect of PR on cardiac functions from a mathematical aspect.

Determining an optimal and easy-obtained indicator for assessing the severity of PR is important for patients after right ventricular outflow tract surgeries, especially after tetralogy of Fallot repair (Li et al., 2004; Redington, 2006; Wald et al., 2009). Previous studies (Abd El Rahman et al., 2000; Vliegen et al., 2002; Geva et al., 2004; Davlouros et al., 2004; Frigiola et al., 2008; Wald et al., 2009; Harrild et al., 2010) have demonstrated

the correlation between PR and RV dilation, especially the close relationship between PRF and RVEDVi. This relationship has supported the quantitative assessment of RV volume obtained by MRI scans as a standard for determining the pulmonary valve replacement of patients with severe PR (Wald et al., 2009; El-Harasis et al., 2018). A nearly linear relationship between the RVEDVi and the PRF was obtained from our model. However, the PRV for different degrees of PR in our simulations were not as large as reported values by Wald et al. (2009) who suggested that PRV provides a more accurate reflection of PR severity than PRF. They reported that the median PRV of 64 patients was $19\,\mathrm{mL/m^2}$ (range 0 - $63\,\mathrm{mL/m^2}$) and the PRF was 29% (range 0-58)%, considering a body surface area of $2.05\,\mathrm{m^2}$. Nevertheless, because of the large variation of normal RV EDV for different subjects (113 to 225 mL) (Kovalova et al., 2006; Eastman et al., 2008), the PRV might not be solely used as an indicator.

The RV dilation led to a large deformation of the septum and a further squeeze of the LV. The motion of the septum at ED can be clearly observed in both the long-axis views and short-axis views as shown in Fig. 5.5 (a, b). For the long-axis views, severe PR forced the septum to bulge toward the LV. For the short-axis views, the LV cross-sectional cut plane had a circular profile for the baseline case. However, it was forced to a flattened D-shaped profile in the PR disease cases. These characteristics agreed with previous findings in (Louie et al., 1992; Sheehan et al., 2008; Méndez et al., 2011; Naeije and Badagliacca, 2017; Mauger et al., 2021). Given the easy access to the short-axis scans by MRI, it might be an easy-obtained indicator for assessing PR severity (Zoghbi et al., 2003; Méndez et al., 2011). The Menger curvature further showed that a 50.6% PRF caused a 43.9% decrease in the short-axis curvature of the septum and a 61.5% increase in the long-axis curvature. Note that we used the Menger curvature, which can be easily calculated from three points and might be useful in clinical practice. Moreover, it can measure two curvatures from the long-axis cut planes and the short-axis cut planes, respectively, since the long-axis curvature and short-axis curvature may have different clinical implications.

The existence of PR can be easily identified by the PV loop of the RV. A normal PV loop of the RV or the LV should contain two vertical lines representing the isovolumetric contraction and isovolumetric relaxation because of that the pulmonary valve and the aortic valve close fully without leaking. However, the isovolumetric relaxation period disappeared in the PR disease cases due to the dysfunction of the pulmonary valve. The vertical line representing the isovolumetric relaxation changed to an oblique slanting line, which indicated a backflow from the pulmonary arteries to the RV during diastole. In the meantime, the isovolumetric contraction period was shortened and further vanished when PR became severe. These characteristics of the PV loop of the RV have been reported in patients with PR (Redington et al., 1988; Chaturvedi et al., 1997; Yerebakan et al., 2009), which also appeared in the PV loop of the LV for patients with aortic regurgitation

(Gaemperli et al., 2013; Paul and Das, 2017; Bastos et al., 2020). As shown in Fig. 5.3, the PV loop of the LV shifts leftwards from the baseline case to the severe case, while the PV loop of the RV shifts rightwards. This is mostly because of the change in the volume of the LV and RV during the dilation of the RV and the squeeze of the LV. The notable change in the LV and RV PV loops may provide useful information for the assessment of PR because PR becomes severe as patients age and arrhythmia and RV failure occur over time. In addition, cardiac outputs (EF) of the LV and RV were both reduced in the PR disease cases, which agreed with previous studies (Niezen et al., 1996; Abd El Rahman et al., 2000; Davlouros et al., 2002). The LV EF decreased by 6.9% from the baseline case to the severe case, and the RV EF decreased by 9.7%.

There have been studies (Geva et al., 2004; Frigiola et al., 2004; El-Harasis et al., 2018) which suggested that the RV wall stress with PR is increased significantly. Our results agreed with this finding. The RV EDP of the severe PR case in our simulation was 223.4% higher than that of the baseline case. This greatly increased RV pressure is related to RV dilation and overload. Moreover, the averaged RV myofibre stress of the severe case at ED was 303.7% higher than that of the baseline case. This significantly high myofibre stress would contribute to high intramyocardial pressure, and then the increased intramyocardial suppresses coronary flow and may lead to a shortage of the perfusion of the RV wall, which is supported by studies of the coronary flow circulation (Hoffman, 1978; Westerhof et al., 2006; Goodwill et al., 2011; Kassab, 2019; Fan et al., 2022).

5.5 Summary

In this chapter, the effects of different degrees of PR severity on cardiac functions and mechanical behaviours have been investigated using a computational human bi-ventricle model. The model consisted of a patient-specific biventricular geometry and commonly used myofibre structure, as well as passive and active models for mechanical properties of the myocardium. This bi-ventricle model further incorporated open-loop systemic circulation and pulmonary circulation. Flow leakage from the pulmonary arteries back to the RV was introduced to simulate disease cases of PR. The validation of our model was extensive. The baseline case of the model was validated by comparison of the ejection fractions of the LV and RV with normal ranges of healthy subjects in the literature. Pressures of the main pulmonary artery and the aorta were also within reported normal ranges. Furthermore, our simulated RV end-diastolic volumes in the disease cases were comparable to reported CMR data. The motion of the interventricular septum agreed with the literature, which was also reflected by the Menger curvature of the septum. RV dilation secondary to PR at the end of diastole was observed in the long-axis and short-axis views. The RV end-diastolic volume was increased by 50.3% from the baseline case to the severe PR case.

Severe PR also led to reduced ejection fractions of both the LV and RV. Moreover, severe PR caused significantly high myofibre stress in the RV wall. Agreement of our simulated results with reported data illustrated the success of the development of the model and its application to diseased hearts with but not limited to PR. In conclusion, this chapter provided a computational way to investigate and better understand the influence of PR on biventricular functions. Further simulations and adaptations of our model can be applied to the clinical assessment of PR and medical decisions for treatments of patients with severe PR. Moreover, the significantly high myofibre stress in the RV wall under the severe PR case may lead to a shortage of myocardial perfusion, which will be investigated in our future studies with the coupling of the coronary flow model developed in Chapter 2.

There are a number of limitations that should be addressed in the future. Firstly, although this model employed patient-specific geometry, the myofibre structure is not unique for the geometry. The myofibre arrangement, dispersion, and remodelling may alter the results (Mojica et al., 2020; Guan et al., 2022c), especially as the RV wall deforms largely. The next update of this work is replacing the open-loop lumped parameter systems with closed-loop systems. In addition, lumped parameter models to synthesise clinical inputs have been developed in (Liu et al., 2021; Gusseva et al., 2021; Zuo et al., 2022), providing more sophisticated ways to represent circulatory systems. Another important concern is to include a realistic 3D pulmonary valve. The pulmonary valve is comprised of three equally sized semilunar cusps. A review of the clinical impact of computational heart valve models is referred to (Toma et al., 2022), and related computational models can be found in (Caiazzo et al., 2016; Shen et al., 2018; Feng et al., 2021; Loke et al., 2022). However, simulations involving the pulmonary valve can be very challenging since fluid-structure interaction analysis would be needed for such a model.

Chapter 6

Conclusion

The primary objective of this thesis is to study physiologically accurate pressure and flow waveforms in human coronary arteries as well as the corresponding myocardial perfusion, by coupling a one-dimensional (1D) coronary flow model with a realistic three-dimensional (3D) left ventricle (LV) model. We have improved and extended a 1D structured-tree coronary flow model by (Olufsen, 1998; Qureshi, 2013) and a 3D finite element (FE) hyperelastic LV model by (Guan et al., 2020a). In Section 1.4, we described some specific aims, which have been successfully achieved. In the following sections, we provide a summary of our findings and observations throughout this thesis. Additionally, we discuss some limitations of this study, which will guide future work in this area.

6.1 Summary of achievements

To simulate pressure and flow waveforms in epicardial human coronary arteries, we have established a network consisting of epicardial arteries, epicardial veins, and intramyocardial blood vessels based on experimental data from (Duanmu et al., 2019). This network enabled us to simulate physiological pressure and flow along the complete path of coronary vasculature from the aortic root to the right atrium, as well as the corresponding blood perfusion to the myocardium. The waveforms in the epicardial coronary vessels were obtained by numerical solutions to the non-linear, cross-sectionally averaged, 1D Navier-Stokes equations combined with a tube law, given inlet and outlet pressure conditions. On the other hand, the linearised Navier-Stokes equations with the same tube law were analytically solved for the intramyocardial vessels based on the representation of the structured trees.

An important observation regarding the coronary arterial flow is that the majority of the flow occurs during diastole, while during systole, the flow may slow down or even reverse (Gregg and Green, 1940; Westerhof et al., 2006; Goodwill et al., 2011). This is related to the periodic contraction of the heart and distinct to the blood flow in the

systemic and pulmonary circulation. Hence, to account for the time-varying nature of intramyocardial pressure (IMP) and its impact on coronary flow, an analysis was performed in the coronary flow model. In Chapter 2, a lumped parameter heart model was used to generate the IMP, which was validated for the accuracy of our method. In Chapter 4, a 3D FE LV model was employed to incorporate a more precise IMP into the coronary flow model. The simulated results of the pressure and flow waveforms accurately reflected normal physiological patterns and values, agreeing with experimental data reported in (Mynard et al., 2014; Duanmu et al., 2019; Fan et al., 2020). Our simulations demonstrated that the flow waveforms were significantly altered when different IMPs were imposed. Generally, in order to impede the coronary flow during systole, the IMP must be sufficiently high.

Specifically, in Chapter 4, a physiologically accurate simulation of coronary blood flow was accomplished through a one-way coupling of the 1D coronary flow model with the 3D LV model, which allowed for a detailed investigation of the interaction between the motion of the LV and the coronary blood flow. Chapter 4 described the reconstruction of the coronary network, the calculation of the IMP, and the assignment of the coronary arteries to the 17 segments of the LV which is recommended by the American Heart Association (AHA). Detailed morphology and dimensions of the coronary vasculature and a summary of existing literature on IMP calculations were presented. Coronary flow simulations using various IMPs were further conducted, and it was found that regionally averaged IMPs produced more uniform myocardial perfusion. It is important to note that the calculated myocardial perfusion values were consistent with reported values and can assist in the evaluation of interventions. Overall, the coronary flow model developed in this thesis is a promising tool for further studies of coronary circulation.

The computational LV model developed in Chapter 3 has provided physiologically realistic boundary conditions to simulate the coronary flow, including IMP and aortic pressure. This LV model was developed based on a patient-specific LV geometry and implemented in ABAQUS. The Holzapfel-Ogden model (Holzapfel and Ogden, 2009) was utilised to describe the passive constitutive law of the anisotropic hyperelastic myocardium, and a time-varying elastance model (Guccione and McCulloch, 1993) was employed to model the active force generated by the myocardium during systole. The simulated pressure and volume of the LV cavity in repeated cardiac cycles, as well as the ejection fraction, were all within physiological ranges. Moreover, the stress distributions within the LV wall were also consistent with existing literature (Genet et al., 2014; Sack et al., 2016, 2018).

Although the LV model was initially developed to provide realistic boundary conditions for coronary flow simulations, it is ready to be adapted for studying the dynamics of the heart in various settings. For instance, in Chapter 3, we adopted the LV model to investigate the effects of myofibre rotation and dispersion on LV pump functions. It was

found that the LV pump functions can be significantly affected by both the myofibre rotation and myofibre dispersion, which was attributed to the redistribution of active tension in both the circumferential and longitudinal directions. Further research is necessary to explore how the changes in the LV pump functions caused by the myofibre arrangement may affect coronary blood flow.

Moreover, the same modelling approach was utilised to develop a bi-ventricular model to study the effect of pulmonary regurgitation (PR) on cardiac functions in Chapter 5. The validation of the outcomes from the bi-ventricular model was extensive and provided a computational way to investigate and better understand the influence of PR on biventricular functions. We found that the predicted end-diastolic volume (EDV) of the right ventricle (RV) under different degrees of PR was comparable with the reported magnetic resonance imaging data (Harrild et al., 2010; Lee et al., 2012). Additionally, RV dilation and the motion of the interventricular septum from the baseline case to the severe case were clearly observed via long-axis and short-axis views of the biventricular geometry. Further simulations and adaptations of the bi-ventricular model can be applied to help the clinical assessment of PR and the medical decision-making process for patients with severe PR. Additionally, in future work, this biventricular model can be utilised for coupling with the coronary flow model, which allows for the investigation of how the interaction between the LV and RV affects coronary flow.

6.2 Future work

The present study involved the development of a 1D flow model to simulate the dynamics of coronary blood flow in physiological conditions. The simulations were successful in predicting pressure and flow in the human coronary network and showed qualitative agreement with observed features of coronary flow. Furthermore, we developed 3D models of the LV and bi-ventricle to simulate cardiac dynamics and functions under physiological conditions. The simulations predicted cardiac outputs and mechanical behaviours and showed qualitative agreement with published results in both normal and diseased physiological conditions. Nonetheless, there are limitations to the models, and further improvement is required from both modelling and application perspectives.

To begin with, it is important to note that the models developed in this thesis are not fully patient-specific, mainly because the validation was based on physiological ranges in the literature rather than patient-specific experimental data. In the case of the coronary flow model, only the geometries of the left and right coronary arteries were adopted from in vivo data through computed tomography (CT) angiography (Duanmu et al., 2019). Given that vessel dimensions have an impact on local hemodynamics, improving the coronary flow model should involve incorporating geometries of both coronary arteries and

veins. Additionally, while we compared the coronary flow results with published pressure and flow waveforms, further model tuning would be valuable by measuring waveforms throughout the cardiac cycle for the same individual with the corresponding coronary vessel geometries. Regarding the LV and bi-ventricle models, the geometries of the LV wall and bi-ventricle wall were obtained from in vivo CMR scans (Gao et al., 2017). However, model validation was sought from the literature rather than the measured data at the individual level. For the LV model, we compared normal physiological ranges of the LV pressure, LV volume, ejection fraction, aortic pressure, and volumetric-averaged myofibre stress in one cardiac cycle with published data. For the bi-ventricle model, we also compared normal ranges of RV pressure, RV volume, and pulmonary pressure, as well as end-diastolic volumes of the RV in different PR cases. Therefore, to improve these two ventricular models, the first step would be to make them completely patient-specific by obtaining comprehensive data at the individual level.

The lack of experimental data highlights the need for computational modelling studies to improve the translation of clinical imaging measurements into patient-specific computational models (Niederer et al., 2019). Developing improved techniques for converting preclinical measurements into patient-specific models would significantly improve our ability to construct models of various physiological conditions. As a result, we would be able to use this information with greater confidence and reliability to guide clinical decisions. Nevertheless, as discussed by Niederer et al. (2019), it should be further noted that while this approach is crucial to ensure that models accurately reflect available clinical information, it may not be feasible for certain clinical scenarios where relevant data is unattainable or lacks adequate precision. For example, vascular network parameterization presents additional difficulties in this regard due to its limited accessibility.

Secondly, we would like to mention some limitations in terms of the methods of our models. Regarding the coronary flow model, our focus was on the pressure and flow waveforms in the epicardial vessels, while the rest of the intramyocardial vessels were modelled by structured trees. The structured trees aimed to include the intramyocardial arteries, arterioles, capillaries, venules, and intramyocardial veins. Nonetheless, it is essential to note that the fluid dynamics of the flow in the structured trees are not suitable for simulating blood flow at the capillary level. This is due to the interweaving structure of the capillary bed, and the blood at the capillary level behaves as a non-Newtonian fluid (Pedley, 2003). Therefore, the constant viscosity assumption of the blood becomes invalid and does not provide accurate predictions. There are several possible ways to improve this, including modelling the capillaries with different structured tree parameters and fluid dynamics as well as utilising the existing theory of sheet flow in lung alveoli presented by Fung (1998).

In relation to the ventricular models, the selection of an appropriate constitutive law is of perhaps the most importance. In this study, we utilised the Holzapfel-Ogden model

(Holzapfel and Ogden, 2009), which treats the myocardium as a solid continuum, to describe the mechanical behaviour of the myocardium. It can further be incorporated into the poroelasticity framework (Lee et al., 2016; Richardson et al., 2021), which considers the myocardium as a fluid-solid mixture. However, such models demand intensive computational resources and their response in the large strain regime is currently a sparsely explored area in the field of biomedical engineering applications (Lee et al., 2016). The constitutive law of active stress is another important aspect. We utilised the active stress approach, as described in previous studies by Baillargeon et al. (2014) and Sack et al. (2018), and determined the active stress using a well-established time-varying elastance model by Guccione et al. (1993). However, more precise active stress models can also be employed, such as the new hybrid active contraction model proposed by Guan et al. (2022a), which abstracts the myocardial dynamics from sarcomeres by combining the phenomenologically active-stress-based Hill model and the micro-structurally motivated active strain approach.

Furthermore, we acknowledge the limitations of the boundary conditions employed in our model. The boundary conditions only restricted the long-axis displacement of the RV basal plane. Additionally, we have imposed a θ-axis constraint on the LV basal surface to prevent unrealistic deformation of the septum. However, these simplified boundary conditions do not fully represent the complex physiological conditions of the heart, particularly in light of the presence of the pericardium and upper chambers. Asner et al. (2017) have discussed such simplified boundary conditions and proposed novel boundary conditions that introduce data-driven boundary energy terms. Moreover, Pfaller et al. (2019) have demonstrated that using a parallel spring and dashpot acting in the normal direction to the epicardium as pericardium boundary conditions can result in more realistic cardiac mechanics simulations.

Lastly, the current thesis has only achieved a one-way coupling between the coronary flow model and the LV model, which primarily focuses on the investigation of IMP's effect on coronary flow. To establish a complete coupling, the next step involves exploring how coronary flow affects cardiac pump functions such as myocardial work or contractility. To achieve this, an initial idea is to relate cardiac pump functions to myocardial blood flow by balancing myocardial oxygen supply and demand. Smith et al. (2005) proposed a one-way coupling model that combined a hyperelastic bi-ventricle heart model with a detailed 1D coronary flow model that covers the six largest generations of the arterial coronary tree. They calculated the myocardial work of the heart by integrating the product of active tension and myofibre strain during one cardiac cycle. The relationship between the regional work of the myocardium and coronary perfusion can be used as a second step toward complete coupling. However, they found the correlation between the regional work and the coronary perfusion was weak which can be attributed to the lack of an autoregu-

lation model where the coronary network adjusts resistance to meet metabolic demands. Recently, Fan et al. (2020) proposed a relationship between myocardial contractility and coronary flow that considers two regimes: an ischemic and a non-ischemic regime. In the ischemic regime, the myocardial contractility varies linearly with the corresponding total coronary flow, while in the non-ischemic regime, the myocardial contractility remains constant, and the coronary flow has no effect on the contractility. The contractility in their model was determined by the maximal chamber elastance, which in our model can be determined by the scaling factor, $T_{\max}$, in the active contraction model. Also, the myocardial blood flow (MBF) can be quantitatively calculated by the coronary flow model. Therefore, incorporating the aforementioned relationships into our model will enable a complete coupling between the coronary flow model and the LV model. Nonetheless, the development of such a model requires additional effort and investigation to elucidate the interaction between myocardial mechanics and coronary blood flow.

In summary, this thesis is a step forward in our comprehension of coronary circulation from a computational modelling perspective. The presented models of the human heart and the coronary blood flow, as well as their coupling, demonstrate promising capabilities to provide accurate predictions of normal cardiac motion and coronary flow. Moreover, the bi-ventricle heart model demonstrates to have valuable clinical applications in PR disease conditions. By further integrating the heart models and the coronary flow model developed in this study, a deeper understanding of the underlying mechanisms of various heart and coronary artery diseases could be achieved.

Bibliography

MY Abd El Rahman, H Abdul-Khaliq, M Vogel, V Alexi-Meskishvili, M Gutberlet, and PE Lange. Relation between right ventricular enlargement, QRS duration, and right ventricular function in patients with tetralogy of Fallot and pulmonary regurgitation after surgical repair. *Heart*, 84(4):416–420, 2000.

II Abubakar, Taavi Tillmann, and Amitava Banerjee. Global, regional, and national age-sex specific all-cause and cause-specific mortality for 240 causes of death, 1990-2013: a systematic analysis for the global burden of disease study 2013. *Lancet*, 385(9963): 117–171, 2015.

F Ahmad, S Soe, N White, R Johnston, I Khan, J Liao, M Jones, R Prabhu, I Maconochie, and Peter Theobald. Region-specific microstructure in the neonatal ventricles of a porcine model. *Annals of biomedical engineering*, 46(12):2162–2176, 2018a.

Faizan Ahmad, Jun Liao, Shwe Soe, Michael D Jones, Jonathan Miller, Parker Berthelson, Daniel Enge, Katherine M Copeland, Samar Shaabeth, Richard Johnston, et al. Biomechanical properties and microstructure of neonatal porcine ventricles. *Journal of the mechanical behavior of biomedical materials*, 88:18–28, 2018b.

M Alam, C Höglund, and C Thorstrand. Longitudinal systolic shortening of the left ventricle: an echocardiographic study in subjects with and without preserved global function. *Clinical physiology*, 12(4):443–452, 1992.

Dotan Algranati, Ghassan S Kassab, and Yoram Lanir. Mechanisms of myocardium-coronary vessel interaction. *American Journal of Physiology-Heart and Circulatory Physiology*, 298(3):H861–H873, 2010.

Wesley D Anderson, Bettina G Anderson, and Randolph J Seguin. Microvasculature of the bear heart demonstrated by scanning electron microscopy. *Cells Tissues Organs*, 131(4):305–313, 1988.

Paolo Angelini. Coronary artery anomalies: an entity in search of an identity. *Circulation*, 115(10):1296–1305, 2007.

Matheus Gijsbertus Jozef Arts. A mathematical model of the dynamics of the left ventricle and the coronary circulation. 1978.

MGJ Arts and RS Reneman. Analysis of intramyocardial pressure (IMP): a model study. *Bibliotheca anatomica*, 15:103–107, 1977.

T Arts and RS Reneman. Interaction between intramyocardial pressure (IMP) and myocardial circulation. 1985.

Theo Arts, Tammo Delhaas, Peter Bovendeerd, Xander Verbeek, and Frits W Prinzen. Adaptation to mechanical load determines shape and properties of heart and circulation: the circadapt model. *American Journal of Physiology-Heart and Circulatory Physiology*, 288(4):H1943–H1954, 2005.

Liya Asner, Myrianthi Hadjicharalambous, Radomir Chabiniok, Devis Peressutti, Eva Sammut, James Wong, Gerald Carr-White, Reza Razavi, AP King, Nicolas Smith, et al. Patient-specific modeling for left ventricular mechanics using data-driven boundary energies. *Computer Methods in Applied Mechanics and Engineering*, 314:269–295, 2017.

Guido Avanzolini, Paolo Barbini, Angelo Cappello, and Gabriele Cevenini. Cadcs simulation of the closed-loop cardiovascular system. *International journal of bio-medical computing*, 22(1):39–49, 1988.

Reza Avazmohammadi, João S Soares, David S Li, Samarth S Raut, Robert C Gorman, and Michael S Sacks. A contemporary look at biomechanical models of myocardium. *Annual review of biomedical engineering*, 21:417–442, 2019.

AP Avolio. Multi-branched model of the human arterial system. *Medical and Biological Engineering and Computing*, 18:709–718, 1980.

Brian Baillargeon, Nuno Rebelo, David D Fox, Robert L Taylor, and Ellen Kuhl. The living heart project: a robust and integrative simulator for human heart function. *European Journal of Mechanics-A/Solids*, 48:38–47, 2014.

Brian Baillargeon, Ivan Costa, Joseph R Leach, Lik Chuan Lee, Martin Genet, Arnaud Toutain, Jonathan F Wenk, Manuel K Rausch, Nuno Rebelo, Gabriel Acevedo-Bolton, et al. Human cardiac function simulator for the optimal design of a novel annuloplasty ring with a sub-valvular element for correction of ischemic mitral regurgitation. *Cardiovascular engineering and technology*, 6(2):105–116, 2015.

ACL Barnard, WA Hunt, WP Timlake, and E Varley. A theory of fluid flow in compliant tubes. *Biophysical journal*, 6(6):717–724, 1966.

Peter J Basser, James Mattiello, and Denis LeBihan. MR diffusion tensor spectroscopy and imaging. *Biophysical journal*, 66(1):259–267, 1994.

Marcelo B Bastos, Daniel Burkhoff, Jiri Maly, Joost Daemen, Corstiaan A den Uil, Koen Ameloot, Mattie Lenzen, Felix Mahfoud, Felix Zijlstra, Jan J Schreuder, et al. Invasive left ventricle pressure–volume analysis: overview and practical clinical implications. *European heart journal*, 41(12):1286–1297, 2020.

Jason D Bayer, Robert C Blake, Gernot Plank, and Natalia A Trayanova. A novel rule-based algorithm for assigning myocardial fiber orientation to computational heart models. *Annals of biomedical engineering*, 40(10):2243–2254, 2012.

Roy Beigel, Bojan Cercek, Huai Luo, and Robert J Siegel. Noninvasive evaluation of right atrial pressure. *Journal of the American Society of Echocardiography*, 26(9):1033–1042, 2013.

Alberto Benchimol and Joseph G Ellis. A study of the period of isovolumic relaxation in normal subjects and in patients with heart disease. *The American Journal of Cardiology*, 19(2):196–206, 1967.

Marvin Berger, Azriel Haimowitz, Andrew Van Tosh, Russell L Berdoff, and Emanuel Goldberg. Quantitative assessment of pulmonary hypertension in patients with tricuspid regurgitation using continuous wave Doppler ultrasound. *Journal of the American College of Cardiology*, 6(2):359–365, 1985.

Robert M Berne. Cardiovascular physiology. *Annual Review of Physiology*, 43(1):357–358, 1981.

Lorena Bociu, Giovanna Guidoboni, Riccardo Sacco, and Justin T Webster. Analysis of nonlinear poro-elastic and poro-visco-elastic models. *Archive for Rational Mechanics and Analysis*, 222:1445–1519, 2016.

Beatriz Bouzas, Philip J Kilner, and Michael A Gatzoulis. Pulmonary regurgitation: not a benign lesion. *European heart journal*, 26(5):433–439, 2005.

Thierry Bove, Kristof Vandekerckhove, Stefaan Bouchez, Patrick Wouters, Pamela Somers, and Guido Van Nooten. Role of myocardial hypertrophy on acute and chronic right ventricular performance in relation to chronic volume overload in a porcine model: relevance for the surgical management of tetralogy of Fallot. *The Journal of Thoracic and Cardiovascular Surgery*, 147(6):1956–1965, 2014.

Giorgio Brandi and Maurice McGregor. Intramural pressure in the left ventricle of the dog. *Cardiovascular Research*, 3(4):472–475, 1969.

Louise AE Brown, Sebastian C Onciul, David A Broadbent, Kerryanne Johnson, Graham J Fent, James RJ Foley, Pankaj Garg, Pei G Chew, Kristopher Knott, Erica Dall'Armellina, et al. Fully automated, inline quantification of myocardial blood flow with cardiovascular magnetic resonance: repeatability of measurements in healthy subjects. *Journal of Cardiovascular Magnetic Resonance*, 20(1):1–12, 2018.

Rebecca AB Burton, Gernot Plank, Jürgen E Schneider, Vicente Grau, Helmut Ahammer, Stephen L Keeling, Jack Lee, Nicolas P Smith, David Gavaghan, Natalia Trayanova, et al. Three-dimensional models of individual cardiac histoanatomy: tools and challenges. *Annals of the New York Academy of Sciences*, 1080(1):301–319, 2006.

Alfonso Caiazzo, Romain Guibert, and Irene E Vignon-Clementel. A reduced-order modeling for efficient design study of artificial valve in enlarged ventricular outflow tracts. *Computer methods in BiomeChaniCs and BiomediCal engineering*, 19(12):1314–1318, 2016.

Colin Gerald Caro, Timothy J Pedley, RC Schroter, and WA Seed. *The mechanics of the circulation*. Cambridge University Press, 2012.

Rodrigo J Cerci, Armin Arbab-Zadeh, Richard T George, Julie M Miller, Andrea L Vavere, Vishal Mehra, Kihei Yoneyama, John Texter, Courtney Foster, Wei Guo, et al. Aligning coronary anatomy and myocardial perfusion territories: an algorithm for the core320 multicenter study. *Circulation: Cardiovascular Imaging*, 5(5):587–595, 2012.

Manuel D Cerqueira, Neil J Weissman, Vasken Dilsizian, Alice K Jacobs, Sanjiv Kaul, Warren K Laskey, Dudley J Pennell, John A Rumberger, Thomas Ryan, et al. Standardized myocardial segmentation and nomenclature for tomographic imaging of the heart: a statement for healthcare professionals from the cardiac imaging committee of the council on clinical cardiology of the American heart association. *Circulation*, 105 (4):539–542, 2002.

Dominique Chapelle, J-F Gerbeau, J Sainte-Marie, and IE Vignon-Clementel. A poroelastic model valid in large strains with applications to perfusion in cardiac modeling. *Computational Mechanics*, 46(1):91–101, 2010.

Rajiv R Chaturvedi and Andrew N Redington. Pulmonary regurgitation in congenital heart disease. *Heart*, 93(7):880–889, 2007.

Rajiv R Chaturvedi, Philip J Kilner, Paul A White, Andrew Bishop, Richard Szwarc, and Andrew N Redington. Increased airway pressure and simulated branch pulmonary artery stenosis increase pulmonary regurgitation after repair of tetralogy of Fallot: real-time analysis with a conductance catheter technique. *Circulation*, 95(3):643–649, 1997.

Yingming Amy Chen, Elsie T Nguyen, Carole Dennie, Rachel M Wald, Andrew M Crean, Shi-Joon Yoo, and Laura Jimenez-Juan. Computed tomography and magnetic resonance imaging of the coronary sinus: anatomic variants and congenital anomalies. *Insights into imaging*, 5(5):547–557, 2014.

Serkan Çimen, Ali Gooya, Michael Grass, and Alejandro F Frangi. Reconstruction of coronary arteries from x-ray angiography: A review. *Medical image analysis*, 32:46–68, 2016.

AN Cookson, J Lee, C Michler, R Chabiniok, E Hyde, DA Nordsletten, M Sinclair, M Siebes, and NP Smith. A novel porous mechanical framework for modelling the interaction between coronary perfusion and myocardial mechanics. *Journal of biomechanics*, 45(5):850–855, 2012.

Kevin D Costa, Jeffrey W Holmes, and Andrew D McCulloch. Modelling cardiac mechanical properties in three dimensions. *Philosophical transactions of the Royal Society of London. Series A: Mathematical, physical and engineering sciences*, 359(1783):1233–1250, 2001.

Hirak Das, Geeta Das, Dipak Chandra Das, and Kunjalal Talukdar. A study of coronary dominance in the population of assam. *Journal of Anatomical Society of India*, 59(2): 187–191, 2010.

Systèmes Dassault. Abaqus analysis user's guide (6.13). *Providence, Rhode Island, United States: Simulia Corp*, 2014.

Justin E Davies, Zachary I Whinnett, Darrel P Francis, Charlotte H Manisty, Jazmin Aguado-Sierra, Keith Willson, Rodney A Foale, Iqbal S Malik, Alun D Hughes, Kim H Parker, et al. Evidence of a dominant backward-propagating "suction" wave responsible for diastolic coronary filling in humans, attenuated in left ventricular hypertrophy. *Circulation*, 113(14):1768–1778, 2006.

Periklis A Davlouros, Philip J Kilner, Tim S Hornung, Wei Li, Jane M Francis, James CC Moon, Gillian C Smith, Tri Tat, Dudley J Pennell, and Michael A Gatzoulis. Right ventricular function in adults with repaired tetralogy of Fallot assessed with cardiovascular magnetic resonance imaging: detrimental role of right ventricular outflow aneurysms or akinesia and adverse right-to-left ventricular interaction. *Journal of the American College of Cardiology*, 40(11):2044–2052, 2002.

Periklis A Davlouros, Ageliki A Karatza, Michael A Gatzoulis, and Darryl F Shore. Timing and type of surgery for severe pulmonary regurgitation after repair of tetralogy of Fallot. *International journal of cardiology*, 97:91–101, 2004.

Scott J Denardo, Ramavathi Nandyala, Gregory L Freeman, Gary L Pierce, and Wilmer W Nichols. Pulse wave analysis of the aortic pressure waveform in severe left ventricular systolic dysfunction. *Circulation: Heart Failure*, 3(1):149–156, 2010.

Jean-Marie Dieudonné. The left ventricle as confocal prolate spheroids. *The bulletin of mathematical biophysics*, 31(3):433–439, 1969.

Abaqus Documentation and User Manual. Version 6.14-2. *Dassault systemes*, 2014.

J Theodore Dodge Jr, B Greg Brown, Edward L Bolson, and Harold T Dodge. Lumen diameter of normal human coronary arteries. influence of age, sex, anatomic variation, and left ventricular hypertrophy or dilation. *Circulation*, 86(1):232–246, 1992.

Hisham Dokainish, John S Nguyen, Jaromir Bobek, Rajiv Goswami, and Nasser M Lakkis. Assessment of the American society of echocardiography-european association of echocardiography guidelines for diastolic function in patients with depressed ejection fraction: an echocardiographic and invasive haemodynamic study. *European journal of echocardiography*, 12(11):857–864, 2011.

Socrates Dokos, Bruce H Smaill, Alistair A Young, and Ian J LeGrice. Shear properties of passive ventricular myocardium. *American Journal of Physiology-Heart and Circulatory Physiology*, 283(6):H2650–H2659, 2002.

Paulo Donato, P Coelho, C Santos, A Bernardes, and F Caseiro-Alves. Correspondence between left ventricular 17 myocardial segments and coronary anatomy obtained by multi-detector computed tomography: an ex vivo contribution. *Surgical and radiologic anatomy*, 34(9):805–810, 2012.

Pamela S Douglas, John Fiolkoski, Barbara Berko, and Nathaniel Reichek. Echocardiographic visualization of coronary artery anatomy in the adult. *Journal of the American College of Cardiology*, 11(3):565–571, 1988.

David A Dowe, Massimo Fioranelli, and Paolo Pavone. *Imaging coronary arteries*. Springer, 2013.

James M Downey and Edward S Kirk. Distribution of the coronary blood flow across the canine heart wall during systole. *Circulation Research*, 34(2):251–257, 1974.

James M Downey and Edward S Kirk. Inhibition of coronary blood flow by a vascular waterfall mechanism. *Circulation research*, 36(6):753–760, 1975.

Zheng Duanmu, Weiwei Chen, Hao Gao, Xilan Yang, Xiaoyu Luo, and Nicholas A Hill. A one-dimensional hemodynamic model of the coronary arterial tree. *Frontiers in physiology*, 10:853, 2019.

Alexander L Eastman, David A Rosenbaum, and Erwin Thal. *The Parkland Trauma Handbook E-Book: Mobile Medicine Series*. Elsevier Health Sciences, 2008.

Majd A El-Harasis, Heidi M Connolly, William R Miranda, Muhammad Y Qureshi, Nandini Sharma, Mohamad Al-Otaibi, Christopher V DeSimone, and Alexander Egbe. Progressive right ventricular enlargement due to pulmonary regurgitation: clinical characteristics of a "low-risk" group. *American Heart Journal*, 201:136–140, 2018.

R Erbel, F Alfonso, C Boileau, O Dirsch, B Eber, A Haverich, H Rakowski, J Struyven, K Radegran, U Sechtem, et al. Diagnosis and management of aortic dissection: task force on aortic dissection, european society of cardiology. *European heart journal*, 22 (18):1642–1681, 2001.

Thomas SE Eriksson, Anton J Prassl, Gernot Plank, and Gerhard A Holzapfel. Modeling the dispersion in electromechanically coupled myocardium. *International journal for numerical methods in biomedical engineering*, 29(11):1267–1284, 2013.

Merlin J Fair, Peter D Gatehouse, Edward VR DiBella, and David N Firmin. A review of 3d first-pass, whole-heart, myocardial perfusion cardiovascular magnetic resonance. *Journal of Cardiovascular Magnetic Resonance*, 17(1):1–25, 2015.

Francesco Fulvio Faletra, Jagat Narula, and Siew Yen Ho. *Atlas of Non-Invasive Imaging in Cardiac Anatomy*. Springer, 2020.

Lei Fan, Ravi Namani, Jenny S Choy, Ghassan S Kassab, and Lik Chuan Lee. Effects of mechanical dyssynchrony on coronary flow: insights from a computational model of coupled coronary perfusion with systemic circulation. *Frontiers in physiology*, 11:915, 2020.

Lei Fan, Ravi Namani, Jenny S Choy, Ghassan S Kassab, and Lik Chuan Lee. Transmural distribution of coronary perfusion and myocardial work density due to alterations in ventricular loading, geometry and contractility. *Frontiers in physiology*, page 2105, 2021.

Lei Fan, Yuexing Sun, Jenny S Choy, Ghassan S Kassab, and Lik Chuan Lee. Mechanism of exercise intolerance in heart diseases predicted by a computer model of myocardial demand-supply feedback system. *Computer Methods and Programs in Biomedicine*, 227: 107188, 2022.

Yiling Fan, William Ronan, Irvin Teh, Jurgen E Schneider, Claudia E Varela, William Whyte, Peter McHugh, Sean Leen, and Ellen Roche. A comparison of two quasi-static computational models for assessment of intra-myocardial injection as a therapeutic

strategy for heart failure. *International journal for numerical methods in biomedical engineering*, 35(9):e3213, 2019.

Paul WM Fedak, Subodh Verma, Richard D Weisel, and Ren-Ke Li. Cardiac remodeling and failure: from molecules to man (part II). *Cardiovascular Pathology*, 14(2):49–60, 2005.

Joseph J Feher. *Quantitative human physiology: an introduction*. Academic press, 2017.

Liuyang Feng, Hao Gao, Nan Qi, Mark Danton, Nicholas A Hill, and Xiaoyu Luo. Fluid–structure interaction in a fully coupled three-dimensional mitral–atrium–pulmonary model. *Biomechanics and Modeling in Mechanobiology*, 20(4):1267–1295, 2021.

Xiaobing Feng, Zhihao Ge, and Yukun Li. Analysis of a multiphysics finite element method for a poroelasticity model. *IMA Journal of Numerical Analysis*, 38(1):330–359, 2018.

Pedro F Ferreira, Philip J Kilner, Laura-Ann McGill, Sonia Nielles-Vallespin, Andrew D Scott, Siew Y Ho, Karen P McCarthy, Margarita M Haba, Tevfik F Ismail, Peter D Gatehouse, et al. In vivo cardiovascular magnetic resonance diffusion tensor imaging shows evidence of abnormal myocardial laminar orientations and mobility in hypertrophic cardiomyopathy. *Journal of Cardiovascular Magnetic Resonance*, 16(1):1–16, 2014.

Carissa G Fonseca, Michael Backhaus, David A Bluemke, Randall D Britten, Jae Do Chung, Brett R Cowan, Ivo D Dinov, J Paul Finn, Peter J Hunter, Alan H Kadish, et al. The cardiac atlas project—an imaging database for computational modeling and statistical atlases of the heart. *Bioinformatics*, 27(16):2288–2295, 2011.

Luca Formaggia, Alfio Quarteroni, and Allesandro Veneziani. *Cardiovascular Mathematics: Modeling and simulation of the circulatory system*, volume 1. Springer Science & Business Media, 2010.

O Frank. Die grundform des arteriellen pulses [basic shape of the arterial pulse]. *Zeitschrift-für Biologie*, 37:483–526, 1899.

A Frigiola, AN Redington, S Cullen, and M Vogel. Pulmonary regurgitation is an important determinant of right ventricular contractile dysfunction in patients with surgically repaired tetralogy of Fallot. *Circulation*, 110(11_suppl_1):II–153, 2004.

Alessandra Frigiola, Victor Tsang, Johannes Nordmeyer, Philipp Lurz, Carin van Doorn, Andrew M Taylor, Philipp Bonhoeffer, and Mark de Leval. Current approaches to pulmonary regurgitation. *European Journal of Cardio-Thoracic Surgery*, 34(3):576–581, 2008.

Hidekatsu Fukuta and William C Little. The cardiac cycle and the physiologic basis of left ventricular contraction, ejection, relaxation, and filling. *Heart failure clinics*, 4(1): 1–11, 2008.

Yuan-Cheng Fung. Biomechanics: circulation. *Shock*, 9(2):155, 1998.

Oliver Gaemperli, Patric Biaggi, Remo Gugelmann, Martin Osranek, Jan J Schreuder, Ines Bühler, Daniel Sürder, Thomas F Lüscher, Christian Felix, Dominique Bettex, et al. Real-time left ventricular pressure-volume loops during percutaneous mitral valve repair with the mitraclip system. *Circulation*, 127(9):1018–1027, 2013.

Hao Gao, Huiming Wang, Colin Berry, Xiaoyu Luo, and Boyce E. Griffith. Quasi-static image-based immersed boundary-finite element model of left ventricle under diastolic loading. *International Journal for Numerical Methods in Biomedical Engineering*, 30 (11):1199–1222, 2014.

Hao Gao, Andrej Aderhold, Kenneth Mangion, Xiaoyu Luo, Dirk Husmeier, and Colin Berry. Changes and classification in myocardial contractile function in the left ventricle following acute myocardial infarction. *Journal of The Royal Society Interface*, 14(132): 20170203, 2017.

T Christian Gasser, Ray W Ogden, and Gerhard A Holzapfel. Hyperelastic modelling of arterial layers with distributed collagen fibre orientations. *Journal of the royal society interface*, 3(6):15–35, 2006.

Michael A Gatzoulis, Seshadri Balaji, Steven A Webber, Samuel C Siu, John S Hokanson, Christine Poile, Mark Rosenthal, Makoto Nakazawa, James H Moller, Paul C Gillette, et al. Risk factors for arrhythmia and sudden cardiac death late after repair of tetralogy of Fallot: a multicentre study. *The Lancet*, 356(9234):975–981, 2000.

Martin Genet, Lik Chuan Lee, Rebecca Nguyen, Henrik Haraldsson, Gabriel Acevedo-Bolton, Zhihong Zhang, Liang Ge, Karen Ordovas, Sebastian Kozerke, and Julius M Guccione. Distribution of normal human left ventricular myofiber stress at end diastole and end systole: a target for in silico design of heart failure treatments. *Journal of applied physiology*, 117(2):142–152, 2014.

Tal Geva, Bryan M Sandweiss, Kimberlee Gauvreau, James E Lock, and Andrew J Powell. Factors associated with impaired clinical status in long-term survivors of tetralogy of Fallot repair evaluated by magnetic resonance imaging. *Journal of the American College of Cardiology*, 43(6):1068–1074, 2004.

Serdar Göktepe and Ellen Kuhl. Electromechanics of the heart: a unified approach to the strongly coupled excitation–contraction problem. *Computational Mechanics*, 45(2): 227–243, 2010.

Adam G Goodwill, Gregory M Dick, Alexander M Kiel, and Johnathan D Tune. Regulation of coronary blood flow. *Comprehensive Physiology*, 7(2):321–382, 2011.

K Lance Gould and Nils P Johnson. Coronary physiology beyond coronary flow reserve in microvascular angina: Jacc state-of-the-art review. *Journal of the American College of Cardiology*, 72(21):2642–2662, 2018.

Ayush Goyal, Jack Lee, Pablo Lamata, Jeroen van den Wijngaard, Pepijn van Horssen, Jos Spaan, Maria Siebes, Vicente Grau, and Nic P Smith. Model-based vasculature extraction from optical fluorescence cryomicrotome images. *IEEE transactions on medical imaging*, 32(1):56–72, 2012.

Richard A Gray and Pras Pathmanathan. Patient-specific cardiovascular computational modeling: diversity of personalization and challenges. *Journal of cardiovascular translational research*, 11:80–88, 2018.

Donald E Gregg and Harold D Green. Registration and interpretation of normal phasic inflow into a left coronary artery by an improved differential manometric method. *American Journal of Physiology-Legacy Content*, 130(1):114–125, 1940.

Boyce E Griffith and Neelesh A Patankar. Immersed methods for fluid–structure interaction. *Annual review of fluid mechanics*, 52:421–448, 2020.

Debao Guan, Faizan Ahmad, Peter Theobald, Shwe Soe, Xiaoyu Luo, and Hao Gao. On the aic-based model reduction for the general holzapfel–ogden myocardial constitutive law. *Biomechanics and modeling in mechanobiology*, 18(4):1213–1232, 2019.

Debao Guan, Xiaoyu Luo, and Hao Gao. Constitutive modelling of soft biological tissue from ex vivo to in vivo: myocardium as an example. In *International Conference by Center for Mathematical Modeling and Data Science, Osaka University*, pages 3–14. Springer, 2020a.

Debao Guan, Jiang Yao, Xiaoyu Luo, and Hao Gao. Effect of myofibre architecture on ventricular pump function by using a neonatal porcine heart model: from DT-MRI to rule-based methods. *Royal Society Open Science*, 7(4):191655, 2020b.

Debao Guan, Xin Zhuan, William Holmes, Xiaoyu Luo, and Hao Gao. Modelling of fibre dispersion and its effects on cardiac mechanics from diastole to systole. *Journal of Engineering Mathematics*, 128(1):1–24, 2021.

Debao Guan, Hao Gao, Li Cai, and Xiaoyu Luo. A new active contraction model for the myocardium using a modified hill model. *Computers in Biology and Medicine*, 145: 105417, 2022a.

Debao Guan, Yuqian Mei, Lijian Xu, Li Cai, Xiaoyu Luo, and Hao Gao. Effects of dispersed fibres in myocardial mechanics, part i: passive response. *submitted*, 2022b.

Debao Guan, Yingjie Wang, Lijian Xu, Li Cai, Xiaoyu Luo, and Hao Gao. Effects of dispersed fibres in myocardial mechanics, part II: active response. *Mathematical Biosciences and Engineering*, 19(4):4101–4119, 2022c.

JM Guccione and AD McCulloch. Mechanics of active contraction in cardiac muscle: part i—constitutive relations for fiber stress that describe deactivation. *Journal of biomechanical engineering*, 115(1):72–81, 1993.

Julius M Guccione, Andrew D McCulloch, and LK Waldman. Passive material properties of intact ventricular myocardium determined from a cylindrical model. 1991.

Julius M Guccione, LK Waldman, and Andrew D McCulloch. Mechanics of active contraction in cardiac muscle: Part II—cylindrical models of the systolic left ventricle. *Journal of biomechanical engineering*, 115(1):82–90, 1993.

Maria Gusseva, Tarique Hussain, Camille Hancock Friesen, Philippe Moireau, Animesh Tandon, Cécile Patte, Martin Genet, Keren Hasbani, Gerald Greil, Dominique Chapelle, et al. Biomechanical modeling to inform pulmonary valve replacement in tetralogy of Fallot patients after complete repair. *Canadian Journal of Cardiology*, 37(11):1798–1807, 2021.

Arthur C Guyton, Dimitri Polizo, and George G Armstrong. Mean circulatory filling pressure measured immediately after cessation of heart pumping. *American Journal of Physiology-Legacy Content*, 179(2):261–267, 1954.

Arthur C Guyton, John Edward Hall, et al. *Textbook of medical physiology*, volume 548. Saunders Philadelphia, 1986.

Khaleel A Hadi, Issam Tariq Abdul Wahaab, Sherif Abou Gamra, and Fatma Magdy Mohamad Salama. Length of left anterior descending (LAD) coronary artery in relation to right & left dominancy: A retrospective computed tomographic (CT) coronary angiographic study. *The Egyptian Journal of Hospital Medicine*, 71(4):2944–2949, 2018.

Robert L Hamlin, Murina J Levesque, and Mark D Kittleson. Intramyocardial pressure and distribution of coronary blood flow during systole and diastole in the horse. *Cardiovascular research*, 16(5):256–262, 1982.

GL Hammond and WG Austen. Drainage patterns of coronary arterial flow as determined from the isolated heart. *American Journal of Physiology-Legacy Content*, 212(6):1435–1440, 1967.

David M Harrild, Andrew J Powell, Trang X Trang, Tal Geva, James E Lock, Jonathan Rhodes, and Doff B McElhinney. Long-term pulmonary regurgitation following balloon valvuloplasty for pulmonary stenosis: risk factors and relationship to exercise capacity and ventricular volume and function. *Journal of the American College of Cardiology*, 55(10):1041–1047, 2010.

FW Heineman and J Grayson. Transmural distribution of intramyocardial pressure measured by micropipette technique. *American Journal of Physiology-Heart and Circulatory Physiology*, 249(6):H1216–H1223, 1985.

Patrick A Helm, Hsiang-Jer Tseng, Laurent Younes, Elliot R McVeigh, and Raimond L Winslow. Ex vivo 3d diffusion tensor imaging and quantification of cardiac laminar structure. *Magnetic Resonance in Medicine: An Official Journal of the International Society for Magnetic Resonance in Medicine*, 54(4):850–859, 2005.

LaBarron K Hill, John J Sollers III, and Julian F Thayer. Resistance reconstructed: Estimation of total peripheral resistance from computationally-derived cardiac output. *Biomedical sciences instrumentation*, 49:216, 2013.

Kuniaki Hirai, Teruhito Kido, Tomoyuki Kido, Ryo Ogawa, Yuki Tanabe, Masashi Nakamura, Naoto Kawaguchi, Akira Kurata, Kouki Watanabe, Osamu Yamaguchi, et al. Feasibility of contrast-enhanced coronary artery magnetic resonance angiography using compressed sensing. *Journal of Cardiovascular Magnetic Resonance*, 22(1):1–10, 2020.

STEPHEN Hirschfeld, RICHARD Meyer, DAVID C Schwartz, J Korfhagen, and S Kaplan. Measurement of right and left ventricular systolic time intervals by echocardiography. *Circulation*, 51(2):304–309, 1975.

JI Hoffman. Determinants and prediction of transmural myocardial perfusion. *Circulation*, 58(3):381–391, 1978.

Gerhard A Holzapfel and Ray W Ogden. Constitutive modelling of passive myocardium: a structurally based framework for material characterization. *Philosophical Transactions of the Royal Society A: Mathematical, Physical and Engineering Sciences*, 367(1902): 3445–3475, 2009.

Gerhard A Holzapfel, Justyna A Niestrawska, Ray W Ogden, Andreas J Reinisch, and Andreas J Schriefl. Modelling non-symmetric collagen fibre dispersion in arterial walls. *Journal of the royal society interface*, 12(106):20150188, 2015.

Barry L Huey, George A Beller, Donald L Kaiser, and Robert S Gibson. A comprehensive analysis of myocardial infarction due to left circumflex artery occlusion: comparison with infarction due to right coronary artery and left anterior descending artery occlusion. *Journal of the American College of Cardiology*, 12(5):1156–1166, 1988.

JD Humphrey and FCP Yin. On constitutive relations and finite deformations of passive cardiac tissue: I. a pseudostrain-energy function. 1987.

JD Humphrey, RK Strumpf, and FCP Yin. Determination of a constitutive relation for passive myocardium: I. a new functional form. 1990.

Peter J Hunter and Bruce H Smaill. The analysis of cardiac function: a continuum approach. *Progress in biophysics and molecular biology*, 52(2):101–164, 1988.

Yunlong Huo and Ghassan S Kassab. A hybrid one-dimensional/womersley model of pulsatile blood flow in the entire coronary arterial tree. *American Journal of Physiology-Heart and Circulatory Physiology*, 292(6):H2623–H2633, 2007.

Reuben Ilia, Gabriel Rosenshtein, Jean Marc Weinstein, Carlos Cafri, Akram Abu-Ful, and Mosche Gueron. Left anterior descending artery length in left and right coronary artery dominance. *Coronary artery disease*, 12(1):77–78, 2001.

Spencer L James, Degu Abate, Kalkidan Hassen Abate, Solomon M Abay, Cristiana Abbafati, Nooshin Abbasi, Hedayat Abbastabar, Foad Abd-Allah, Jemal Abdela, Ahmed Abdelalim, et al. Global, regional, and national incidence, prevalence, and years lived with disability for 354 diseases and injuries for 195 countries and territories, 1990–2017: a systematic analysis for the global burden of disease study 2017. *The Lancet*, 392 (10159):1789–1858, 2018.

PM Janssen and Pieter P de Tombe. Uncontrolled sarcomere shortening increases intracellular ca2+ transient in rat cardiac trabeculae. *American Journal of Physiology-Heart and Circulatory Physiology*, 272(4):H1892–H1897, 1997.

Zahid Ali Kaimkhani, M Moazzam Ali, and AM Faruqi. Pattern of coronary arterial distribution and its relation to coronary artery diameter. *J Ayub Med Coll Abbottabad*, 17(1):40–3, 2005.

Benjamin Kaimovitz, Yoram Lanir, and Ghassan S Kassab. Large-scale 3-d geometric reconstruction of the porcine coronary arterial vasculature based on detailed anatomical data. *Annals of biomedical engineering*, 33(11):1517–1535, 2005.

Benjamin Kaimovitz, Yoram Lanir, and Ghassan S Kassab. A full 3-d reconstruction of the entire porcine coronary vasculature. *American Journal of Physiology-Heart and Circulatory Physiology*, 299(4):H1064–H1076, 2010.

G Kassab. *Coronary Circulation*. Springer, 2019.

Ghassan S Kassab, Carmela A Rider, Nina J Tang, and Yuan-Cheng Fung. Morphometry of pig coronary arterial trees. *American Journal of Physiology-Heart and Circulatory Physiology*, 265(1):H350–H365, 1993.

GS Kassab and S Molloi. Cross-sectional area and volume compliance of porcine left coronary arteries. *American Journal of Physiology-Heart and Circulatory Physiology*, 281(2):H623–H628, 2001.

Arnold M Katz. *Physiology of the Heart*. Lippincott Williams & Wilkins, 2010.

Nadine Kawel, Evrim B Turkbey, J Jeffrey Carr, John Eng, Antoinette S Gomes, W Gregory Hundley, Craig Johnson, Sofia C Masri, Martin R Prince, Rob J van der Geest, et al. Normal left ventricular myocardial thickness for middle-aged and older subjects with steady-state free precession cardiac magnetic resonance: the multi-ethnic study of atherosclerosis. *Circulation: Cardiovascular Imaging*, 5(4):500–508, 2012.

Natatcha Khwansang and Vilai Chentanez. Anatomic variations of coronary arteries: origins, branching patterns, and abnormalities. *Asian Biomed (Res Rev News)*, 12: 117–123, 2018.

Edward S Kirk and Carl R Honig. An experimental and theoretical analysis of myocardial tissue pressure. *American Journal of Physiology-Legacy Content*, 207(2):361–367, 1964.

Richard Klabunde. *Cardiovascular physiology concepts*. Lippincott Williams & Wilkins, 2011.

Kristopher D Knott, Claudia Camaioni, Anantharaman Ramasamy, Joao A Augusto, Anish N Bhuva, Hui Xue, Charlotte Manisty, Rebecca K Hughes, Louise AE Brown, Rajiv Amersey, et al. Quantitative myocardial perfusion in coronary artery disease: a perfusion mapping study. *Journal of Magnetic Resonance Imaging*, 50(3):756–762, 2019.

Kristopher D Knott, Andreas Seraphim, Joao B Augusto, Hui Xue, Liza Chacko, Nay Aung, Steffen E Petersen, Jackie A Cooper, Charlotte Manisty, Anish N Bhuva, et al. The prognostic significance of quantitative myocardial perfusion: an artificial intelligence–based approach using perfusion mapping. *Circulation*, 141(16):1282–1291, 2020.

Tushar Kotecha, Ana Martinez-Naharro, Michele Boldrini, Daniel Knight, Philip Hawkins, Sundeep Kalra, Deven Patel, Gerry Coghlan, James Moon, Sven Plein, et al. Automated pixel-wise quantitative myocardial perfusion mapping by CMR to detect obstructive coronary artery disease and coronary microvascular dysfunction: validation against invasive coronary physiology. *JACC: Cardiovascular Imaging*, 12(10):1958–1969, 2019.

Sylva Kovalova, Josef Necas, and Jaroslav Vespalec. What is a "normal" right ventricle? *European Journal of Echocardiography*, 7(4):293–297, 2006.

R Krams, PIETER Sipkema, J Zegers, and NICO Westerhof. Contractility is the main determinant of coronary systolic flow impediment. *American Journal of Physiology-Heart and Circulatory Physiology*, 257(6):H1936–H1944, 1989.

A Kumar, ML Ajmani, and PS Klinkhachorn. Morphological variation and dimensions of left coronary artery: a cadaveric study. *MOJ Anat & Physiol*, 5(4):266–270, 2018.

Vinay Kumar, Abul K Abbas, Nelson Fausto, and Jon C Aster. *Pathologic basis of disease, professional edition e-book*, page 530. Elsevier health sciences, 2014.

Pablo Lamata, Steven Niederer, David Nordsletten, David C Barber, Ishani Roy, D Rod Hose, and Nic Smith. An accurate, fast and robust method to generate patient-specific cubic hermite meshes. *Medical image analysis*, 15(6):801–813, 2011.

BC Lampert. Right heart catheterization. 2018.

Patrizio Lancellotti, Christophe Tribouilloy, Andreas Hagendorff, Luis Moura, Bogdan A Popescu, Eustachio Agricola, Jean-Luc Monin, Luc A Pierard, Luigi Badano, Jose L Zamorano, et al. European association of echocardiography recommendations for the assessment of valvular regurgitation. part 1: aortic and pulmonary regurgitation (native valve disease). *European Journal of Echocardiography*, 11(3):223–244, 2010.

Sander Land, Viatcheslav Gurev, Sander Arens, Christoph M Augustin, Lukas Baron, Robert Blake, Chris Bradley, Sebastian Castro, Andrew Crozier, Marco Favino, et al. Verification of cardiac mechanics software: benchmark problems and solutions for testing active and passive material behaviour. *Proceedings of the Royal Society A: Mathematical, Physical and Engineering Sciences*, 471(2184):20150641, 2015.

Roberto M Lang, Luigi P Badano, Victor Mor-Avi, Jonathan Afilalo, Anderson Armstrong, Laura Ernande, Frank A Flachskampf, Elyse Foster, Steven A Goldstein, Tatiana Kuznetsova, et al. Recommendations for cardiac chamber quantification by echocardiography in adults: an update from the American society of echocardiography and the european association of cardiovascular imaging. *European Heart Journal-Cardiovascular Imaging*, 16(3):233–271, 2015.

Abdulghani M Larghat, Neil Maredia, John Biglands, John P Greenwood, Stephen G Ball, Michael Jerosch-Herold, Aleksandra Radjenovic, and Sven Plein. Reproducibility of first-pass cardiovascular magnetic resonance myocardial perfusion. *Journal of magnetic resonance imaging*, 37(4):865–874, 2013.

Michael Ldinghausen. The venous drainage of the human myocardium. *Springer Science and Business Media*, 2012.

Cheul Lee, Yang Min Kim, Chang-Ha Lee, Jae Gun Kwak, Chun Soo Park, Jin Young Song, Woo-Sup Shim, Eun Young Choi, Sang Yun Lee, and Jae Suk Baek. Outcomes of pulmonary valve replacement in 170 patients with chronic pulmonary regurgitation after relief of right ventricular outflow tract obstruction: implications for optimal timing of pulmonary valve replacement. *Journal of the American College of Cardiology*, 60(11): 1005–1014, 2012.

Jack Lee and Nicolas P Smith. The multi-scale modelling of coronary blood flow. *Annals of biomedical engineering*, 40(11):2399–2413, 2012.

Jack Lee, David Nordsletten, Andrew Cookson, Simone Rivolo, and Nicolas Smith. In silico coronary wave intensity analysis: application of an integrated one-dimensional and poromechanical model of cardiac perfusion. *Biomechanics and modeling in mechanobiology*, 15(6):1535–1555, 2016.

Jean Christophe Léger. Menger curvature and rectifiability. *Annals of mathematics*, 149 (3):831–869, 1999.

Ian J LeGrice, BH Smaill, LZ Chai, SG Edgar, JB Gavin, and Peter J Hunter. Laminar structure of the heart: ventricular myocyte arrangement and connective tissue architecture in the dog. *American Journal of Physiology-Heart and Circulatory Physiology*, 269 (2):H571–H582, 1995.

Ian J LeGrice, Peter J Hunter, and BH Smaill. Laminar structure of the heart: a mathematical model. *American Journal of Physiology-Heart and Circulatory Physiology*, 272 (5):H2466–H2476, 1997.

Kewei Li, Ray W Ogden, and Gerhard A Holzapfel. A discrete fibre dispersion method for excluding fibres under compression in the modelling of fibrous tissues. *Journal of The Royal Society Interface*, 15(138):20170766, 2018.

Wei Li, Periklis A Davlouros, Philip J Kilner, Dudley J Pennell, Derek Gibson, Michael Y Henein, and Michael A Gatzoulis. Doppler-echocardiographic assessment of pulmonary regurgitation in adults with repaired tetralogy of Fallot: comparison with cardiovascular magnetic resonance imaging. *American heart journal*, 147(1):165–172, 2004.

Sir James Lighthill. *Mathematical biofluiddynamics*. SIAM, 1975.

Leonard S Lilly. *Pathophysiology of heart disease: An introduction to cardiovascular medicine*. Lippincott Williams & Wilkins, 2020.

DHS Lin and FCP Yin. A multiaxial constitutive law for mammalian left ventricular myocardium in steady-state barium contracture or tetanus. *Journal of biomechanical engineering*, 120(4):504–517, 1998.

Jincheng Liu, Boyan Mao, Yue Feng, Bao Li, Jian Liu, and Youjun Liu. Closed-loop geometric multi-scale heart-coronary artery model for the numerical calculation of fractional flow reserve. *Computer Methods and Programs in Biomedicine*, 208:106266, 2021.

Yue Hin Loke, Francesco Capuano, Elias Balaras, and Laura J Olivieri. Computational modeling of right ventricular motion and intracardiac flow in repaired tetralogy of Fallot. *Cardiovascular engineering and technology*, 13(1):41–54, 2022.

Eric K Louie, Stuart Rich, Sidney Levitsky, and Bruce H Brundage. Doppler echocardiographic demonstration of the differential effects of right ventricular pressure and volume overload on left ventricular geometry and filling. *Journal of the American College of Cardiology*, 19(1):84–90, 1992.

Marios Loukas, Amit Sharma, Christa Blaak, Edward Sorenson, and Asma Mian. The clinical anatomy of the coronary arteries. *Journal of cardiovascular translational research*, 6:197–207, 2013.

G Mahadevan, RC Davis, MP Frenneaux, FDR Hobbs, GYH Lip, JE Sanderson, and MK Davies. Left ventricular ejection fraction: are the revised cut-off points for defining systolic dysfunction sufficiently evidence based? *Heart*, 94(4):426–428, 2008.

Kenneth Mangion, Hao Gao, Dirk Husmeier, Xiaoyu Luo, and Colin Berry. Advances in computational modelling for personalised medicine after myocardial infarction. *Heart*, 104(7):550–557, 2018.

Elaine Nicpon Marieb and Katja Hoehn. *Human anatomy & physiology*. Pearson education, 2007.

Charlène A Mauger, Sachin Govil, Radomir Chabiniok, Kathleen Gilbert, Sanjeet Hegde, Tarique Hussain, Andrew D McCulloch, Christopher J Occleshaw, Jeffrey Omens, James C Perry, et al. Right-left ventricular shape variations in tetralogy of Fallot: associations with pulmonary regurgitation. *Journal of Cardiovascular Magnetic Resonance*, 23(1):1–14, 2021.

Karen May-Newman, Jeffrey H Omens, Richard S Pavelec, and Andrew D McCulloch. Three-dimensional transmural mechanical interaction between the coronary vasculature and passive myocardium in the dog. *Circulation research*, 74(6):1166–1178, 1994.

Vallerie V McLaughlin, Stephen L Archer, David B Badesch, Robyn J Barst, Harrison W Farber, Jonathan R Lindner, Michael A Mathier, Michael D McGoon, Myung H Park, Robert S Rosenson, et al. A report of the american college of cardiology foundation task force on expert consensus documents and the american heart association. *Circulation*, 119(16):2250–2294, 2009.

Brendan M McQuillan, Michael H Picard, Marcia Leavitt, and Arthur E Weyman. Clinical correlates and reference intervals for pulmonary artery systolic pressure among echocardiographically normal subjects. *Circulation*, 104(23):2797–2802, 2001.

Lalit Mehra, Shashi Raheja, Sneh Agarwal, Yashoda Rani, Kulwinder Kaur, and Anita Tuli. Anatomical consideration and potential complications of coronary sinus catheterisation. *Journal of clinical and diagnostic research: JCDR*, 10(2):AC12, 2016.

Cristina Méndez, Rafaela Soler, Esther Rodriguez, Marisol López, Lucia Álvarez, Noela Fernández, and Lorenzo Montserrat. Magnetic resonance imaging of abnormal ventricular septal motion in heart diseases: a pictorial review. *Insights into imaging*, 2(4): 483–492, 2011.

Laura Mercer-Rosa, Wei Yang, Shelby Kutty, Jack Rychik, Mark Fogel, and Elizabeth Goldmuntz. Quantifying pulmonary regurgitation and right ventricular function in surgically repaired tetralogy of Fallot: a comparative analysis of echocardiography and magnetic resonance imaging. *Circulation: Cardiovascular Imaging*, 5(5):637–643, 2012.

LS Mihailescu and FL Abel. Intramyocardial pressure gradients in working and nonworking isolated cat hearts. *American Journal of Physiology-Heart and Circulatory Physiology*, 266(3):H1233–H1241, 1994.

Julie M Miller, Marc Dewey, Andrea L Vavere, Carlos E Rochitte, Hiroyuki Niinuma, Armin Arbab-Zadeh, Narinder Paul, John Hoe, Albert de Roos, Kunihiro Yoshioka, et al. Coronary CT angiography using 64 detector rows: methods and design of the multi-centre trial core-64. *European radiology*, 19(4):816–828, 2009.

Rafal Mlynarski, Agnieszka Mlynarska, Maciej Haberka, Krzysztof S Golba, and Maciej Sosnowski. The thebesian valve and coronary sinus in cardiac magnetic resonance. *Journal of Interventional Cardiac Electrophysiology*, 43(2):197–203, 2015.

Mia Mojica, Mihaela Pop, Maxime Sermesant, and Mehran Ebrahimi. Novel atlas of fiber directions built from ex-vivo diffusion tensor images of porcine hearts. *Computer Methods and Programs in Biomedicine*, 187:105200, 2020.

Francois-Pierre Mongeon, Walid Ben Ali, Paul Khairy, Ismail Bouhout, Judith Therrien, Rachel M Wald, Frederic Dallaire, Pierre-Luc Bernier, Nancy Poirier, Annie Dore, et al.

Pulmonary valve replacement for pulmonary regurgitation in adults with tetralogy of Fallot: a meta-analysis—a report for the writing committee of the 2019 update of the canadian cardiovascular society guidelines for the management of adults with congenital heart disease. *Canadian Journal of Cardiology*, 35(12):1772–1783, 2019.

Rohollah Moosavi Tayebi, Rahmita Wirza, Puteri SB Sulaiman, Mohd Zamrin Dimon, Fatimah Khalid, Aqeel Al-Surmi, and Samaneh Mazaheri. 3d multimodal cardiac data reconstruction using angiography and computerized tomographic angiography registration. *Journal of cardiothoracic surgery*, 10(1):1–25, 2015.

Paul D Morris, Andrew Narracott, Hendrik von Tengg-Kobligk, Daniel Alejandro Silva Soto, Sarah Hsiao, Angela Lungu, Paul Evans, Neil W Bressloff, Patricia V Lawford, D Rodney Hose, et al. Computational fluid dynamics modelling in cardiovascular medicine. *Heart*, 102(1):18–28, 2016.

Anneloes G. Munneke, Joost Lumens, Theo Arts, and Tammo Delhaas. A closed-loop modeling framework for cardiac-to-coronary coupling. *Frontiers in Physiology*, 13, 2022. ISSN 1664-042X. doi: 10.3389/fphys.2022.830925. URL `https://www.frontiersin.org/article/10.3389/fphys.2022.830925`.

Anneloes Geertje Munneke, Joost Lumens, Theo Arts, and Tammo Delhaas. A closed-loop modelling framework for cardiac-to-coronary coupling. *Frontiers in Physiology*, page 183.

JOSEPH P Murgo, NICO Westerhof, JOHN P Giolma, and STEPHEN A Altobelli. Aortic input impedance in normal man: relationship to pressure wave forms. *Circulation*, 62 (1):105–116, 1980.

Cecil D Murray. The physiological principle of minimum work: I. the vascular system and the cost of blood volume. *Proceedings of the National Academy of Sciences*, 12(3): 207–214, 1926a.

Cecil D Murray. The physiological principle of minimum work: II. oxygen exchange in capillaries. *Proceedings of the National Academy of Sciences*, 12(5):299–304, 1926b.

Diab Mutlak, Doron Aronson, Jonathan Lessick, Shimon A Reisner, Salim Dabbah, and Yoram Agmon. Functional tricuspid regurgitation in patients with pulmonary hypertension: is pulmonary artery pressure the only determinant of regurgitation severity? *Chest*, 135(1):115–121, 2009.

Jonathan P Mynard, Daniel J Penny, and Joseph J Smolich. Scalability and in vivo validation of a multiscale numerical model of the left coronary circulation. *American Journal of Physiology-Heart and Circulatory Physiology*, 306(4):H517–H528, 2014.

Robert Naeije and Roberto Badagliacca. The overloaded right heart and ventricular interdependence. *Cardiovascular research*, 113(12):1474–1485, 2017.

Ravi Namani, Ghassan S Kassab, and Yoram Lanir. Integrative model of coronary flow in anatomically based vasculature under myogenic, shear, and metabolic regulation. *Journal of General Physiology*, 150(1):145–168, 2018.

Ravi Namani, Lik C Lee, Yoram Lanir, Benjamin Kaimovitz, Sheikh M Shavik, and Ghassan S Kassab. Effects of myocardial function and systemic circulation on regional coronary perfusion. *Journal of Applied Physiology*, 128(5):1106–1122, 2020.

D Nematzadeh, JC Rose, TH Schryver, HK Huang, and PA Kot. Analysis of methodology for measurement of intramyocardial pressure. *Basic research in cardiology*, 79(1):86–97, 1984.

Steven A Niederer, Joost Lumens, and Natalia A Trayanova. Computational models in cardiology. *Nature Reviews Cardiology*, 16(2):100–111, 2019.

Sonia Nielles-Vallespin, Choukri Mekkaoui, Peter Gatehouse, Timothy G Reese, Jennifer Keegan, Pedro F Ferreira, Steve Collins, Peter Speier, Thorsten Feiweier, Ranil De Silva, et al. In vivo diffusion tensor MRI of the human heart: reproducibility of breath-hold and navigator-based approaches. *Magnetic resonance in medicine*, 70(2):454–465, 2013.

Sonia Nielles-Vallespin, Zohya Khalique, Pedro F Ferreira, Ranil de Silva, Andrew D Scott, Philip Kilner, Laura-Ann McGill, Archontis Giannakidis, Peter D Gatehouse, Daniel Ennis, et al. Assessment of myocardial microstructural dynamics by in vivo diffusion tensor cardiac magnetic resonance. *Journal of the American College of Cardiology*, 69 (6):661–676, 2017.

PM Nielsen, IJ Le Grice, BH Smaill, and PJ Hunter. Mathematical model of geometry and fibrous structure of the heart. *American Journal of Physiology-Heart and Circulatory Physiology*, 260(4):H1365–H1378, 1991.

R Andre Niezen, Willem A Helbing, EE Van der Wall, RJ Van der Geest, Sidney A Rebergen, and A De Roos. Biventricular systolic function and mass studied with MR imaging in children with pulmonary regurgitation after repair for tetralogy of Fallot. *Radiology*, 201(1):135–140, 1996.

Rick A Nishimura, Catherine M Otto, Robert O Bonow, Blase A Carabello, John P Erwin III, Lee A Fleisher, Hani Jneid, Michael J Mack, Christopher J McLeod, Patrick T O'Gara, et al. 2017 AHA/ACC focused update of the 2014 AHA/ACC guideline for

the management of patients with valvular heart disease: a report of the american college of cardiology/american heart association task force on clinical practice guidelines. *Circulation*, 135(25):e1159–e1195, 2017.

Anton Vonk Noordegraaf, Kelly Marie Chin, François Haddad, Paul M Hassoun, Anna R Hemnes, Susan Roberta Hopkins, Steven Mark Kawut, David Langleben, Joost Lumens, and Robert Naeije. Pathophysiology of the right ventricle and of the pulmonary circulation in pulmonary hypertension: an update. *European Respiratory Journal*, 53 (1), 2019.

Ray W Ogden. Nonlinear elasticity with application to material modelling. *Lecture Notes-AMAS*, 2003.

Mette S Olufsen. Structured tree outflow condition for blood flow in larger systemic arteries. *American journal of physiology-Heart and circulatory physiology*, 276(1):H257–H268, 1999.

Mette S Olufsen, Charles S Peskin, Won Yong Kim, Erik M Pedersen, Ali Nadim, and Jesper Larsen. Numerical simulation and experimental validation of blood flow in arteries with structured-tree outflow conditions. *Annals of biomedical engineering*, 28(11): 1281–1299, 2000.

Mette S Olufsen, NA Hill, Gareth DA Vaughan, Christopher Sainsbury, and Martin Johnson. Rarefaction and blood pressure in systemic and pulmonary arteries. *Journal of fluid mechanics*, 705:280, 2012.

Mette Sofie Olufsen. *Modeling the arterial system with reference to an anestesia simulator*. PhD thesis, Roskilde University, 1998.

Alaa Mabrouk Salem Omar, Sharath Vallabhajosyula, and Partho P Sengupta. Left ventricular twist and torsion: research observations and clinical applications. *Circulation: Cardiovascular Imaging*, 8(6):e003029, 2015.

José T Ortiz-Pérez, José Rodríguez, Sheridan N Meyers, Daniel C Lee, Charles Davidson, and Edwin Wu. Correspondence between the 17-segment model and coronary arterial anatomy using contrast-enhanced cardiac magnetic resonance imaging. *JACC: Cardiovascular Imaging*, 1(3):282–293, 2008.

RA O'Rouke and V Fuster. Hurst's the heart [10 (international edition) ed.], 2001.

Anna Pandolfi, Alessio Gizzi, and Marcello Vasta. Coupled electro-mechanical models of fiber-distributed active tissues. *Journal of biomechanics*, 49(12):2436–2444, 2016.

Lazaros Papamanolis, Hyun Jin Kim, Clara Jaquet, Matthew Sinclair, Michiel Schaap, Ibrahim Danad, Pepijn van Diemen, Paul Knaapen, Laurent Najman, Hugues Talbot, et al. Myocardial perfusion simulation for coronary artery disease: a coupled patient-specific multiscale model. *Annals of biomedical engineering*, 49:1432–1447, 2021.

Abhijit Paul and Sucharita Das. Valvular heart disease and anaesthesia. *Indian Journal of Anaesthesia*, 61(9):721, 2017.

Timothy J Pedley. Mathematical modelling of arterial fluid dynamics. *Journal of engineering mathematics*, 47:419–444, 2003.

M Peirlinck, F Sahli Costabal, J Yao, JM Guccione, S Tripathy, Y Wang, D Ozturk, P Segars, TM Morrison, S Levine, et al. Precision medicine in human heart modeling. *Biomechanics and modeling in mechanobiology*, pages 1–29, 2021.

Osvaldo Pereztol-Valdés, Jaume Candell-Riera, César Santana-Boado, Juan Angel, Santiago Aguadé-Bruix, Joan Castell-Conesa, Ernest V Garcia, and Jordi Soler-Soler. Correspondence between left ventricular 17 myocardial segments and coronary arteries. *European heart journal*, 26(24):2637–2643, 2005.

Jean-Marc Peyrat, Maxime Sermesant, Xavier Pennec, Hervé Delingette, Chenyang Xu, Elliot R McVeigh, and Nicholas Ayache. A computational framework for the statistical analysis of cardiac diffusion tensors: application to a small database of canine hearts. *IEEE transactions on medical imaging*, 26(11):1500–1514, 2007.

Martin R Pfaller, Julia M Hörmann, Martina Weigl, Andreas Nagler, Radomir Chabiniok, Cristóbal Bertoglio, and Wolfgang A Wall. The importance of the pericardium for cardiac biomechanics: from physiology to computational modeling. *Biomechanics and modeling in mechanobiology*, 18:503–529, 2019.

ME Pfisterer, A Battler, and BL Zaret. Range of normal values for left and right ventricular ejection fraction at rest and during exercise assessed by radionuclide angiocardiography. *European heart journal*, 6(8):647–655, 1985.

Roque Pifarre. Intramyocardial pressure during systole and diastole. *Annals of Surgery*, 168(5):871, 1968.

William Townsend Porter. The influence of the heart-beat on the flow of blood through the walls of the heart. *American Journal of Physiology-Legacy Content*, 1(2):145–163, 1898.

RF Potter and AC Groom. Capillary diameter and geometry in cardiac and skeletal muscle studied by means of corrosion casts. *Microvascular research*, 25(1):68–84, 1983.

Michael D Puchalski, Bojana Askovich, C Todd Sower, Richard V Williams, L LuAnn Minich, and Lloyd Y Tani. Pulmonary regurgitation: determining severity by echocardiography and magnetic resonance imaging. *Congenital Heart Disease*, 3(3):168–175, 2008.

Alfio Quarteroni and Silvia Quarteroni. *Numerical models for differential problems*, volume 2. Springer, 2009.

Alfio Quarteroni, Toni Lassila, Simone Rossi, and Ricardo Ruiz-Baier. Integrated heart—coupling multiscale and multiphysics models for the simulation of the cardiac function. *Computer Methods in Applied Mechanics and Engineering*, 314:345–407, 2017.

M Umar Qureshi and Nicholas A Hill. A computational study of pressure wave reflections in the pulmonary arteries. *Journal of mathematical biology*, 71(6):1525–1549, 2015.

Muhammad Umar Qureshi. *Simulating the pulse wave in the human pulmonary circulation*. PhD thesis, University of Glasgow, 2013.

Sidney A Rebergen, JG Chin, Jaap Ottenkamp, EE Van der Wall, and A De Roos. Pulmonary regurgitation in the late postoperative follow-up of tetralogy of Fallot. volumetric quantitation by nuclear magnetic resonance velocity mapping. *Circulation*, 88 (5):2257–2266, 1993.

Andrew N Redington. Determinants and assessment of pulmonary regurgitation in tetralogy of Fallot: practice and pitfalls. *Cardiology clinics*, 24(4):631–639, 2006.

ANDREW N Redington, PAUL J Oldershaw, ELLIOT A Shinebourne, and MICHAEL L Rigby. A new technique for the assessment of pulmonary regurgitation and its application to the assessment of right ventricular function before and after repair of tetralogy of Fallot. *Heart*, 60(1):57–65, 1988.

Timothy G Reese, Robert M Weisskoff, R Neil Smith, Bruce R Rosen, Robert E Dinsmore, and Van J Wedeen. Imaging myocardial fiber architecture in vivo with magnetic resonance. *Magnetic Resonance in Medicine*, 34(6):786–791, 1995.

Philippe Reymond, Fabrice Merenda, Fabienne Perren, Daniel Rufenacht, and Nikos Stergiopulos. Validation of a one-dimensional model of the systemic arterial tree. *American Journal of Physiology-Heart and Circulatory Physiology*, 297(1):H208–H222, 2009.

Philippe Reymond, Nico Westerhof, and Nikos Stergiopulos. Systolic hypertension mechanisms: effect of global and local proximal aorta stiffening on pulse pressure. *Annals of biomedical engineering*, 40(3):742–749, 2012.

Scott I Heath Richardson, Hao Gao, Jennifer Cox, Rob Janiczek, Boyce E Griffith, Colin Berry, and Xiaoyu Luo. A poroelastic immersed finite element framework for modelling cardiac perfusion and fluid–structure interaction. *International journal for numerical methods in biomedical engineering*, 37(5):e3446, 2021.

Walter J Rogers Jr, Edward P Shapiro, James L Weiss, Maurice B Buchalter, Frank E Rademakers, Myron L Weisfeldt, and Elias A Zerhouni. Quantification of and correction for left ventricular systolic long-axis shortening by magnetic resonance tissue tagging and slice isolation. *Circulation*, 84(2):721–731, 1991.

Simone Rossi, Toni Lassila, Ricardo Ruiz-Baier, Adélia Sequeira, and Alfio Quarteroni. Thermodynamically consistent orthotropic activation model capturing ventricular systolic wall thickening in cardiac electromechanics. *European Journal of Mechanics-A/Solids*, 48:129–142, 2014.

Kevin L Sack, Brian Baillargeon, Gabriel Acevedo-Bolton, Martin Genet, Nuno Rebelo, Ellen Kuhl, Liviu Klein, Georg M Weiselthaler, Daniel Burkhoff, Thomas Franz, et al. Partial lvad restores ventricular outputs and normalizes lv but not rv stress distributions in the acutely failing heart in silico. *The International journal of artificial organs*, 39 (8):421–430, 2016.

Kevin L Sack, Eric Aliotta, Daniel B Ennis, Jenny S Choy, Ghassan S Kassab, Julius M Guccione, and Thomas Franz. Construction and validation of subject-specific biventricular finite-element models of healthy and failing swine hearts from high-resolution DT-MRI. *Frontiers in physiology*, 9:539, 2018.

Shingo Sakamoto, Saeko Takahashi, Ahmet U Coskun, Michail I Papafaklis, Akihiko Takahashi, Shigeru Saito, Peter H Stone, and Charles L Feldman. Relation of distribution of coronary blood flow volume to coronary artery dominance. *The American journal of cardiology*, 111(10):1420–1424, 2013.

Peter F Salisbury, Cecil E Cross, and P Andre Rieben. Intramyocardial pressure and strength of left ventricular contraction. *Circulation research*, 10(4):608–623, 1962.

Gregory B Sands, Dane A Gerneke, Darren A Hooks, Colin R Green, Bruce H Smaill, and Ian J Legrice. Automated imaging of extended tissue volumes using confocal microscopy. *Microscopy research and technique*, 67(5):227–239, 2005.

Farhood Saremi and Muresian. Coronary veins: comprehensive CT-anatomic classification and review of variants and clinical implications. *Radiographics*, 32(1):E1–E32, 2012.

Akira Sato, Hirokazu Ohigashi, Toshihiro Nozato, Hiroyuki Hikita, Mieko Tamura, Shinsuke Miyazaki, Yoshihide Takahashi, Taishi Kuwahara, Atsushi Takahashi, Michiaki

Hiroe, et al. Coronary artery spatial distribution, morphology, and composition of non-culprit coronary plaques by 64-slice computed tomographic angiography in patients with acute myocardial infarction. *The American journal of cardiology*, 105(7):930–935, 2010.

Patrick J Scanlon, David P Faxon, Anne-Marie Audet, Blase Carabello, Gregory J Dehmer, Kim A Eagle, Ronald D Legako, Donald F Leon, John A Murray, Steven E Nissen, et al. ACC/AHA guidelines for coronary angiography: a report of the American college of cardiology/American heart association task force on practice guidelines (committee on coronary angiography) developed in collaboration with the society for cardiac angiography and interventions. *Journal of the American College of Cardiology*, 33(6):1756–1824, 1999.

H Schmid, MP Nash, AA Young, and PJ Hunter. Myocardial material parameter estimation—a comparative study for simple shear. 2006.

Stanley G Schultz. William harvey and the circulation of the blood: the birth of a scientific revolution and modern physiology. *Physiology*, 17(5):175–180, 2002.

Partho P Sengupta, A Jamil Tajik, Krishnaswamy Chandrasekaran, and Bijoy K Khandheria. Twist mechanics of the left ventricle: principles and application. *JACC: Cardiovascular Imaging*, 1(3):366–376, 2008.

Ahmad Separham, Masoud Nouri-Vaskeh, and Mehdi Maleki. Association between left anterior descending artery length with coronary artery dominance: An angiographic study. *Journal of Cardio-Thoracic Medicine*, 7(3):484–490, 2019.

RALPH Shabetai. Pericardial and cardiac pressure. *Circulation*, 77(1):1–5, 1988.

Sanket S Shah, Shawn D Teague, Jimmy C Lu, Adam L Dorfman, Ella A Kazerooni, and Prachi P Agarwal. Imaging of the coronary sinus: normal anatomy and congenital abnormalities. *Radiographics*, 32(4):991–1008, 2012.

Sheikh Mohammad Shavik, Christopher Tossas-Betancourt, C Alberto Figueroa, Seungik Baek, and Lik Chuan Lee. Multiscale modeling framework of ventricular-arterial bi-directional interactions in the cardiopulmonary circulation. *Frontiers in physiology*, page 2, 2020.

Florence H Sheehan, Shuping Ge, G Wesley Vick III, Kara Urnes, William S Kerwin, Edward L Bolson, Taylor Chung, John P Kovalchin, David J Sahn, Michael Jerosch-Herold, et al. Three-dimensional shape analysis of right ventricular remodeling in repaired tetralogy of Fallot. *The American journal of cardiology*, 101(1):107–113, 2008.

Xiaoqin Shen, Lin Bai, Li Cai, and Xiaoshan Cao. A geometric model for the human pulmonary valve in its fully open case. *PloS one*, 13(6):e0199390, 2018.

Elliot A Shinebourne, Sonya V Babu-Narayan, and Julene S Carvalho. Tetralogy of Fallot: from fetus to adult. *Heart*, 92(9):1353–1359, 2006.

Candice K Silversides, Gruschen R Veldtman, Jane Crossin, Naeem Merchant, Gary D Webb, Brian W McCrindle, Samuel C Siu, and Judith Therrien. Pressure half-time predicts hemodynamically significant pulmonary regurgitation in adult patients with repaired tetralogy of Fallot. *Journal of the American Society of Echocardiography*, 16 (10):1057–1062, 2003.

Jaroslaw Skowronski, Jerzy Pregowski, Gary S Mintz, Mariusz Kruk, Cezary Kepka, Pawel Tyczynski, Ilona Michalowska, Lukasz Kalinczuk, Maksymilian P Opolski, Michal Ciszewski, et al. Measurements of lumen areas and diameters of proximal and middle coronary artery segments in subjects without coronary atherosclerosis. *The American journal of cardiology*, 121(8):917–923, 2018.

Bruce Smaill and Peter Hunter. Structure and function of the diastolic heart: material properties of passive myocardium. *Theory of heart: biomechanics, biophysics, and nonlinear dynamics of cardiac function*, pages 1–29, 1991.

Nicolas Smith, Carey Stevens, and Peter Hunter. Computational modeling of ventricular mechanics and energetics. *Appl. Mech. Rev.*, 58(2):77–90, 2005.

Nicolas P Smith, AJ Pullan, and PJ Hunter. Generation of an anatomically based geometric coronary model. *Annals of biomedical engineering*, 28(1):14–25, 2000.

Gerhard Sommer, Andreas J Schriefl, Michaela Andrä, Michael Sacherer, Christian Viertler, Heimo Wolinski, and Gerhard A Holzapfel. Biomechanical properties and microstructure of human ventricular myocardium. *Acta biomaterialia*, 24:172–192, 2015.

JAE Spaan, NPW Breuls, JD Laird, and A Boekee. Forward coronary flow normally seen in systole is the result of both forward and concealed back flow. *Basic research in cardiology*, 76(5):582–586, 1981.

Anthony James Merrill Spencer. Constitutive theory for strongly anisotropic solids. In *Continuum theory of the mechanics of fibre-reinforced composites*, pages 1–32. Springer, 1984.

Nicholas Sperelakis. *Heart physiology and pathophysiology*. Elsevier, 2000.

Nikos Stergiopulos, Berend E Westerhof, and Nico Westerhof. Total arterial inertance as the fourth element of the windkessel model. *American Journal of Physiology-Heart and Circulatory Physiology*, 276(1):H81–H88, 1999.

JC Stettler, P Niederer, and M Anliker. Theoretical analysis of arterial hemodynamics including the influence of bifurcations: Part i: Mathematical model and prediction of normal pulse patterns. *Annals of biomedical engineering*, 9(2):145–164, 1981.

George Gabriel Stokes. On the theories of the internal friction of fluids in motion, and of the equilibrium and motion of elastic solids. 2007.

Daniel D Streeter Jr and William T Hanna. Engineering mechanics for successive states in canine left ventricular myocardium: I. cavity and wall geometry. *Circulation research*, 33(6):639–655, 1973.

Hiroyuki Suga, Kiichi Sagawa, and Artin A Shoukas. Load independence of the instantaneous pressure-volume ratio of the canine left ventricle and effects of epinephrine and heart rate on the ratio. *Circulation research*, 32(3):314–322, 1973.

Kay Sun, Nielen Stander, Choon-Sik Jhun, Zhihong Zhang, Takamaro Suzuki, Guan-Ying Wang, Maythem Saeed, Arthur W Wallace, Elaine E Tseng, Anthony J Baker, et al. A computationally efficient formal optimization of regional myocardial contractility in a sheep with left ventricular aneurysm. 2009.

Salvatore P Sutera and Richard Skalak. The history of poiseuille's law. *Annual review of fluid mechanics*, 25(1):1–20, 1993.

Sándor M Szilágyi, László Szilágyi, and Zoltán Benyó. A patient specific electro-mechanical model of the heart. *Computer methods and programs in biomedicine*, 101(2):183–200, 2011.

Giuseppe Tarantini, Federico Migliore, Filippo Cademartiri, Chiara Fraccaro, and Sabino Iliceto. Left anterior descending artery myocardial bridging: a clinical approach. *Journal of the American College of Cardiology*, 68(25):2887–2899, 2016.

Namshad Thekkethil, Simone Rossi, Hao Gao, Scott I Heath Richardson, Boyce E Griffith, and Xiaoyu Luo. A stabilized linear finite element method for anisotropic poroelastodynamics with application to cardiac perfusion. *Computer Methods in Applied Mechanics and Engineering*, 405:115877, 2023.

James D Thomas, Frank A Flachskampf, Chunguang Chen, J Luis Guererro, Michael H Picard, Robert A Levine, and Arthur E Weyman. Isovolumic relaxation time varies predictably with its time constant and aortic and left atrial pressures: implications for the noninvasive evaluation of ventricular relaxation. *American heart journal*, 124(5): 1305–1313, 1992.

Milan Toma, Shelly Singh-Gryzbon, Elisabeth Frankini, Zhenglun Wei, and Ajit P Yoganathan. Clinical impact of computational heart valve models. *Materials*, 15(9):3302, 2022.

Yan Topilsky, Amber Khanna, Thierry Le Tourneau, Soon Park, Hector Michelena, Rakesh Suri, Douglas W Mahoney, and Maurice Enriquez-Sarano. Clinical context and mechanism of functional tricuspid regurgitation in patients with and without pulmonary hypertension. *Circulation: Cardiovascular Imaging*, 5(3):314–323, 2012.

Nicolas Toussaint, Christian T Stoeck, Tobias Schaeffter, Sebastian Kozerke, Maxime Sermesant, and Philip G Batchelor. In vivo human cardiac fibre architecture estimation using shape-based diffusion tensor processing. *Medical image analysis*, 17(8):1243–1255, 2013.

Eiji Toyota, Yasuo Ogasawara, Osamu Hiramatsu, Hiroyuki Tachibana, Fumihiko Kajiya, Shinji Yamamori, and William M Chilian. Dynamics of flow velocities in endocardial and epicardial coronary arterioles. *American Journal of Physiology-Heart and Circulatory Physiology*, 288(4):H1598–H1603, 2005.

A Tözeren. Continuum rheology of muscle contraction and its application to cardiac contractility. *Biophysical journal*, 47(3):303–309, 1985.

Wen-Yih I Tseng, Timothy G Reese, Robert M Weisskoff, Thomas J Brady, and Van J Wedeen. Myocardial fiber shortening in humans: initial results of MR imaging. *Radiology*, 216(1):128–139, 2000.

Ken Umetani, Donald H Singer, Rollin McCraty, and Mike Atkinson. Twenty-four hour time domain heart rate variability and heart rate: relations to age and gender over nine decades. *Journal of the American College of Cardiology*, 31(3):593–601, 1998.

HBM Uylings. Optimization of diameters and bifurcation angles in lung and vascular tree structures. *Bulletin of mathematical biology*, 39(5):509–520, 1977.

Fijoy Vadakkumpadan, Hermenegild Arevalo, Can Ceritoglu, Michael Miller, and Natalia Trayanova. Image-based estimation of ventricular fiber orientations for personalized modeling of cardiac electrophysiology. *IEEE transactions on medical imaging*, 31(5): 1051–1060, 2012.

John S Vasko, John Gutelius, and David C Sabiston Jr. A study of predominance of human coronary arteries determined by arteriographic and perfusion technics. *The American journal of cardiology*, 8(3):379–384, 1961.

Gareth DA Vaughan. *Pulse propagation in the pulmonary and systemic arteries*. PhD thesis, University of Glasgow, 2010.

Roberto Verzicco. Electro-fluid-mechanics of the heart. *Journal of Fluid Mechanics*, 941: P1, 2022.

MA Vis, PH Bovendeerd, P Sipkema, and N Westerhof. Effect of ventricular contraction, pressure, and wall stretch on vessels at different locations in the wall. *American Journal of Physiology-Heart and Circulatory Physiology*, 272(6):H2963–H2975, 1997a.

MARTIJN A Vis, PIETER Sipkema, and NICO Westerhof. Modeling pressure-area relations of coronary blood vessels embedded in cardiac muscle in diastole and systole. *American Journal of Physiology-Heart and Circulatory Physiology*, 268(6):H2531–H2543, 1995.

MARTIJN A Vis, PIETER Sipkema, and NICO Westerhof. Modeling pressure-flow relations in cardiac muscle in diastole and systole. *American Journal of Physiology-Heart and Circulatory Physiology*, 272(3):H1516–H1526, 1997b.

Charalambos Vlachopoulos, Michael O'Rourke, and Wilmer W Nichols. *McDonald's blood flow in arteries: theoretical, experimental and clinical principles*. CRC press, 2011.

Hubert W Vliegen, Alexander van Straten, Albert de Roos, Arno AW Roest, Paul H Schoof, Aeilko H Zwinderman, Jaap Ottenkamp, Ernst E van der Wall, and Mark G Hazekamp. Magnetic resonance imaging to assess the hemodynamic effects of pulmonary valve replacement in adults late after repair of tetralogy of Fallot. *Circulation*, 106(13): 1703–1707, 2002.

Zeev Vlodaver, Robert F Wilson, and Daniel Garry. *Coronary heart disease: clinical, pathological, imaging, and molecular profiles*. Springer, 2012.

Rachel M Wald, Andrew N Redington, Andre Pereira, Yves L Provost, Narinder S Paul, Erwin N Oechslin, and Candice K Silversides. Refining the assessment of pulmonary regurgitation in adults after tetralogy of Fallot repair: should we be measuring regurgitant fraction or regurgitant volume? *European heart journal*, 30(3):356–361, 2009.

Joseph C Walker, Mark B Ratcliffe, Peng Zhang, Arthur W Wallace, Bahar Fata, Edward W Hsu, David Saloner, and Julius M Guccione. MRI-based finite-element analysis of left ventricular aneurysm. *American Journal of Physiology-Heart and Circulatory Physiology*, 289(2):H692–H700, 2005.

HM Wang, H Gao, XY Luo, C Berry, BE Griffith, RW Ogden, and TJ Wang. Structure-based finite strain modelling of the human left ventricle in diastole. *International journal for numerical methods in biomedical engineering*, 29(1):83–103, 2013.

Jiun-Jr Wang, Aoife B O'Brien, Nigel G Shrive, Kim H Parker, and John V Tyberg. Time-domain representation of ventricular-arterial coupling as a windkessel and wave system. *American Journal of Physiology-Heart and Circulatory Physiology*, 284(4): H1358–H1368, 2003.

John C Wang, Sharon-Lise T Normand, Laura Mauri, and Richard E Kuntz. Coronary artery spatial distribution of acute myocardial infarction occlusions. *Circulation*, 110 (3):278–284, 2004.

J F Wenk, D Klepach, L C Lee, Z Zhang, L Ge, E E Tseng, A Martin, S Kozerke, J H Gorman, R C Gorman, and J M Guccione. First Evidence of Depressed Contractility in the Border Zone of a Human Myocardial Infarction. *The Annals of Thoracic Surgery*, 93(4):1188–1193, apr 2012.

Nico Westerhof, Christa Boer, Regis R Lamberts, and Pieter Sipkema. Cross-talk between cardiac muscle and coronary vasculature. *Physiological reviews*, 86(4):1263–1308, 2006.

Nico Westerhof, Jan-Willem Lankhaar, and Berend E Westerhof. The arterial windkessel. *Medical & biological engineering & computing*, 47(2):131–141, 2009.

Maurice JJMF Willemsen, Dirk J Duncker, Rob Krams, Marieke A Dijkman, Regis R Lamberts, Pieter Sipkema, and Nico Westerhof. Decrease in coronary vascular volume in systole augments cardiac contraction. *American Journal of Physiology-Heart and Circulatory Physiology*, 281(2):H731–H737, 2001.

Andrew D Wisneski, Yunjie Wang, Tobias Deuse, Arthur C Hill, Salvatore Pasta, Kevin L Sack, Jiang Yao, and Julius M Guccione. Impact of aortic stenosis on myofiber stress: translational application of left ventricle-aortic coupling simulation. *Frontiers in Physiology*, page 1157, 2020.

Andrew D Wisneski, Yunjie Wang, Salvatore Cutugno, Salvatore Pasta, Ashley Stroh, Jiang Yao, Tom C Nguyen, Vaikom S Mahadevan, and Julius M Guccione. Left ventricle biomechanics of low-flow, low-gradient aortic stenosis: A patient-specific computational model. *Frontiers in Physiology*, page 587, 2022.

John R Womersley. An elastic tube theory of pulse transmission and oscillatory flow in mammalian arteries. Technical report, Aerospace Research Labs Wright-Patterson AFB OH, 1957.

Jonathan Wong and Ellen Kuhl. Generating fibre orientation maps in human heart models using poisson interpolation. *Computer methods in biomechanics and biomedical engineering*, 17(11):1217–1226, 2014.

Elizabeth A Woodcock and Scot J Matkovich. Cardiomyocytes structure, function and associated pathologies. *The international journal of biochemistry & cell biology*, 37(9): 1746–1751, 2005.

Robert H Woods. A few applications of a physical theorem to membranes in the human body in a state of tension. *Journal of anatomy and physiology*, 26(Pt 3):362, 1892.

Can Yerebakan, Christian Klopsch, Stephanie Prietz, Johannes Boltze, Brigitte Vollmar, Andreas Liebold, Gustav Steinhoff, and Eugen Sandica. Pressure-volume loops: feasible for the evaluation of right ventricular function in an experimental model of acute pulmonary regurgitation? *Interactive cardiovascular and thoracic surgery*, 9(2):163–168, 2009.

M Zamir and H Chee. Branching characteristics of human coronary arteries. *Canadian journal of physiology and pharmacology*, 64(6):661–668, 1986.

Yongjie Zhang, Xinghua Liang, Jun Ma, Yiming Jing, Matthew J Gonzales, Christopher Villongco, Adarsh Krishnamurthy, Lawrence R Frank, Vishal Nigam, Paul Stark, et al. An atlas-based geometry pipeline for cardiac hermite model construction and diffusion tensor reorientation. *Medical image analysis*, 16(6):1130–1141, 2012.

William A Zoghbi, Maurice Enriquez-Sarano, Elyse Foster, Paul A Grayburn, Carol D Kraft, Robert A Levine, Petros Nihoyannopoulos, Catherine M Otto, Miguel A Quinones, Harry Rakowski, et al. Recommendations for evaluation of the severity of native valvular regurgitation with two-dimensional and Doppler echocardiography. *Journal of the American Society of Echocardiography*, 16(7):777–802, 2003.

Xiaowen Zuo, Zhike Xu, Huaping Jia, Yang Mu, Mingming Zhang, Manli Yuan, and Chengwei Wu. Co-simulation of hypertensive left ventricle based on computational fluid dynamics and a closed-loop network model. *Computer Methods and Programs in Biomedicine*, 216:106649, 2022.

Zygote Media Group and Inc. The Zygote Solid 3D Heart Model. 2013.